Platform and enabling technologies in organic synthesis
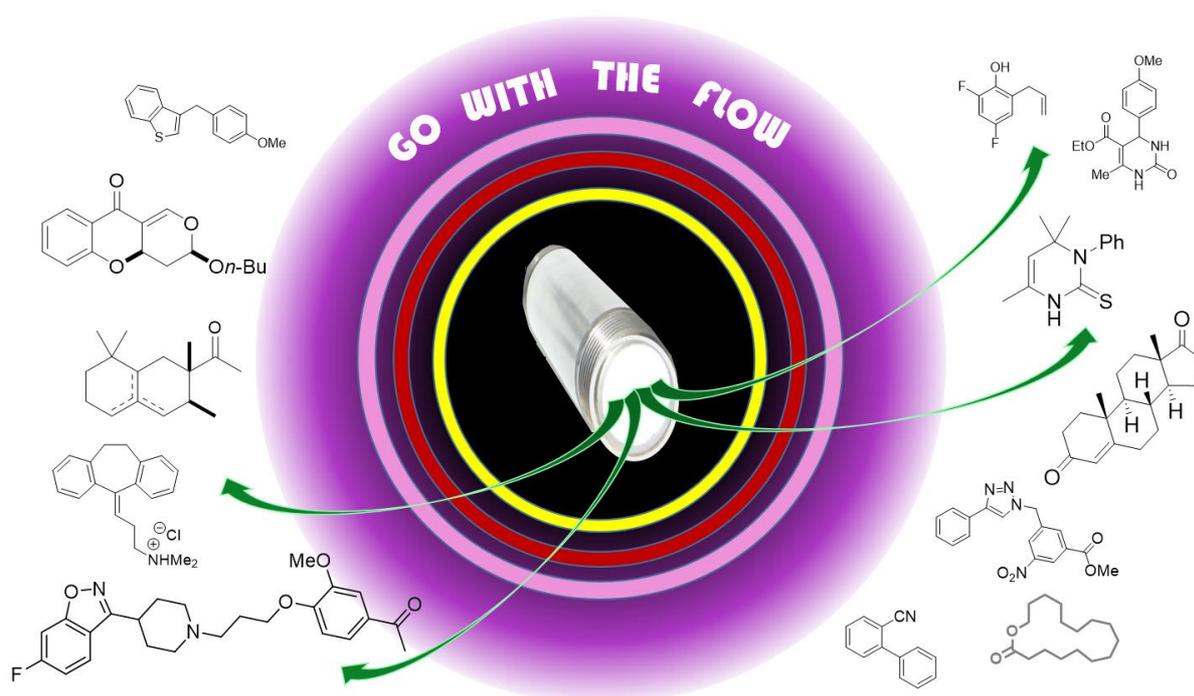
Edited by Philipp Heretsch and Andreas Kirschning

Imprint

Modern flow chemistry – prospect and advantage

Philipp Heretsch

Editorial

Address:
Institute of Organic Chemistry, Leibniz Universität Hannover, Schneiderberg 1B, 30167 Hannover, Germany

Email:
Philipp Heretsch - philipp.heretsch@oci.uni-hannover.de

This article is part of the thematic issue "Platform and enabling technologies in organic synthesis".

Guest Editor: P. Heretsch

Organic chemistry has shaped modern society by fulfilling the basic needs for pharmaceuticals, agrochemicals, fragrances, and many more. Implementation of new and innovative technologies has played a vital role in this mission and has contributed to the opening of new research areas and to pushing the frontiers of existing ones. Among these new technologies, continuous flow chemistry has stepped on the stage in the last decades [1]. Originating from the petrochemical industry, where it enabled high productivity and scalability even for the most standard processes of heating, cracking, and refining of crude oil to bulk chemicals [2], it has since entered the production of pharmaceuticals and other fine chemicals. This has again led to improved scalability, higher purity of products, and eventually decreased manufacturing costs.

From the undisputed role of continuous flow chemistry for process chemists, the advent of this technology in academic research laboratories, especially for method development and natural product synthesis programs [3], has revealed some inadequacies, particularly in view of the equipment and procedures available. These limitations have been slowly overcome with many creative but sometimes highly "academic" solutions.

Thus, recent years witnessed a steady increase in the application of continuous flow technology for academic research, leading to an expansion of synthetic options and generally more sustainable operations. Among the many advantages of performing organic reactions in continuous flow, enhanced heat-, mass- and photon transfer, an improved safety profile, broad scalability, and higher sustainability are the most prevalent ones.

To provide examples and explanation for these claims, "flash chemistry", a term coined by late Yoshida [4] for reactions at the diffusion limit, i.e., reactions completed within milliseconds with proper mixing, showcases the fast heat- and mass transfer of continuous flow reactors. The generation of organolithium species in the presence of carbonyl compounds and their reaction has been facilitated by the extremely fast mixing of reagents and almost instantaneous heat transfer (i.e., cooling) in specifically designed microreactors [5].

Analogously, significantly increased photon transfer in flow reactors has been exploited. Where the molar attenuation coefficient is high, such as in many important photoredox catalysts, most of the irradiation is already absorbed within a thin layer of a few millimeters. Thus, in batch reactors the vast volume of the solution is not irradiated, and the reaction can only take place in the outermost layer [6,7]. This results in an extended reaction time when performing such reactions in bulk and may even lead to increased side reactions. Moving such operations into tubular flow reactors with a small diameter can both accelerate the transformations as well as lead to significantly less side products by continuously removing the products from the irradiation source.

As an example, Noël and co-workers performed efficient irradiation in flow for the $C(sp^3)$–H functionalization of gaseous hydrocarbons [8], wherein photoexcited decatungstate was employed. Decatungstate is an efficient and versatile hydrogen atom transfer (HAT) catalyst with a growing number of applications. The use of decatungstate in a continuous flow setup led to shorter reaction times, increased scalability, and improved safety with pressurized gaseous alkanes employed in the above-mentioned transformations.

Enhanced safety profiles of continuous flow reactors have been widely appreciated in industrial laboratories, while hazardous reactions still tend to be addressed subordinately or are even marginalized in academia [9]. The comparably small dimensions of flow reactors enable explosive, toxic, or otherwise dangerous reactions and reagents to be accumulated only to a much lesser degree, especially when scaling up.

This virtue has been exploited in process chemistry, where in the manufacturing of HIV protease inhibitor nelfinavir mesylate, diazomethane was an inevitable necessity. By moving the generation of this toxic and explosive reagent into a continuous process with manageable amounts present at any given point and continuously stripping the chemical with a stream of nitrogen, safety protocols could be met [10].

Among the disadvantages when moving from batch reactions to a continuous flow regime, dispersion phenomena play a detrimental role. These gradient effects occur when a stream of reagent is introduced into the reactor by pushing it with pure solvent. The reagents with well-defined concentration then leach into the solvent slug, leading to ill-defined stoichiometry and decrease in yield. While this axial dispersion is dependent on flow speed and residence time, only the central part of the reaction stream is under so-called steady-state conditions. To zero out these effects when a process yield is to be determined, pre- and postrun fractions are discarded [6], leading to loss of

reagent and substrate as well as to increased waste. This is even less tolerable when small quantities of precious intermediates from multistep routes are to be employed, as is typically the case in projects of the pharmaceutical industry and academia.

A possible solution to this general problem was reported by Jensen and co-workers, who introduced segmented gas–liquid flow by mixing the reagent stream with an inert carrier gas, forming liquid and gaseous slugs moving through the reactor, and thus insolating liquid compartments from leaching into one another [11]. This concept has been adapted and further refined by Gilmore and co-workers, introducing automated multistep synthesizers [12], as well as Heretsch et al. in a setup optimized for natural products synthesis and late-stage manipulations [13].

To address customized reactor solutions from an engineering perspective, the advent of computer-aided design (CAD) in combination with widely available 3D printing has become a preferred choice. Prototyping aided by these technologies has significantly accelerated the development of novel flow reactor designs [14]. The challenging properties of organic solvents for standard polymers used in commercial 3D printers remain a drawback, while industrial 3D printers remain the much more expensive option. Reactors or other laboratory ware printed in polypropylene are restricted in use to only a few organic solvents or even to a single application, rendering this technology rather a supportive tool than a general solution [15]. Still, having this option available significantly lowers the barrier of inventing novel technological solutions and allows for high-throughput optimization in reactor design. Since different types of reactions typically call for an optimized or even specifically designed reactor built, the modularity of flow reactor is vital for quick reconfiguration and switching between different reactions.

This argument is particularly true when natural product synthesis is to be performed in continuous flow. The need for flexible and modular reactors that address the different demands associated with total synthesis poses particular challenges, among them performing fast reactions at low temperature, slow reactions at elevated temperature, reactions involving reactive gases under pressure, and photochemical reactions. Besides, also scalability is a major prerequisite in these synthetic endeavors, with reactions routinely being performed on a decagram scale in the early stages of a route and on a milligram scale at the end of a sequence. Designing modular reactors that meet these demands will help to overcome existing reservations for continuous flow in academia [13].

As guest editor of this thematic issue, I would like to express my gratitude to all authors for their excellent contributions.

ORCID® iDs

Philipp Heretsch - https://orcid.org/0000-0002-9967-3541

References

1. Guidi, M.; Seeberger, P. H.; Gilmore, K. *Chem. Soc. Rev.* **2020**, *49*, 8910–8932. doi:10.1039/c9cs00832b
2. Luis, S. V.; Garcia-Verdugo, E., Eds. *Chemical Reactions and Processes under Flow Conditions;* RSC Publishing: Cambridge, UK, 2009. doi:10.1039/9781847559739
3. Newton, S.; Carter, C. F.; Pearson, C. M.; de C. Alves, L.; Lange, H.; Thansandote, P.; Ley, S. V. *Angew. Chem., Int. Ed.* **2014**, *53*, 4915–4920. doi:10.1002/anie.201402056
4. Yoshida, J.-i. *Chem. Commun.* **2005**, 4509–4516. doi:10.1039/b508341a
5. Kim, H.; Nagaki, A.; Yoshida, J.-i. *Nat. Commun.* **2011**, *2*, 264. doi:10.1038/ncomms1264
6. Plutschack, M. B.; Pieber, B.; Gilmore, K.; Seeberger, P. H. *Chem. Rev.* **2017**, *117*, 11796–11893. doi:10.1021/acs.chemrev.7b00183
7. Su, Y.; Straathof, N. J. W.; Hessel, V.; Noël, T. *Chem. – Eur. J.* **2014**, *20*, 10562–10589. doi:10.1002/chem.201400283
8. Laudadio, G.; Deng, Y.; van der Wal, K.; Ravelli, D.; Nuño, M.; Fagnoni, M.; Guthrie, D.; Sun, Y.; Noël, T. *Science* **2020**, *369*, 92–96. doi:10.1126/science.abb4688
9. McGarry, K. A.; Hurley, K. R.; Volp, K. A.; Hill, I. M.; Merritt, B. A.; Peterson, K. L.; Rudd, P. A.; Erickson, N. C.; Seiler, L. A.; Gupta, P.; Bates, F. S.; Tolman, W. B. *J. Chem. Educ.* **2013**, *90*, 1414–1417. doi:10.1021/ed400305e
10. Proctor, L. D.; Warr, A. J. *Org. Process Res. Dev.* **2002**, *6*, 884–892. doi:10.1021/op020049k
11. Günther, A.; Khan, S. A.; Thalmann, M.; Trachsel, F.; Jensen, K. F. *Lab Chip* **2004**, *4*, 278–286. doi:10.1039/b403982c
12. Chatterjee, S.; Guidi, M.; Seeberger, P. H.; Gilmore, K. *Nature* **2020**, *579*, 379–384. doi:10.1038/s41586-020-2083-5
13. Kleoff, M.; Schwan, J.; Christmann, M.; Heretsch, P. *Org. Lett.* **2021**, *23*, 2370–2374. doi:10.1021/acs.orglett.1c00661
14. Coakley, M.; Hurt, D. E. *J. Lab. Autom.* **2016**, *21*, 489–495. doi:10.1177/2211068216649578
15. Kitson, P. J.; Rosnes, M. H.; Sans, V.; Dragone, V.; Cronin, L. *Lab Chip* **2012**, *12*, 3267–3271. doi:10.1039/c2lc40761b

High-speed C–H chlorination of ethylene carbonate using a new photoflow setup

Takayoshi Kasakado[‡1], Takahide Fukuyama[*2], Tomohiro Nakagawa[‡3], Shinji Taguchi[‡3] and Ilhyong Ryu[*1,4]

Abstract

We report the high-speed C–H chlorination of ethylene carbonate, which gives chloroethylene carbonate, a precursor to vinylene carbonate. A novel photoflow setup designed for a gas–liquid biphasic reaction turned out to be useful for the direct use of chlorine gas. The setup employed sloped channels so as to make the liquid phase thinner, ensuring a high surface-to-volume ratio. When ethylene carbonate was introduced to the reactor, the residence time was measured to be 15 or 30 s, depending on the slope of the reactor set at 15 or 5°, respectively. Such short time of exposition sufficed the photo C–H chlorination. The partial irradiation of the flow channels also sufficed for the C–H chlorination, which is consistent with the requirement of photoirradiation for the purpose of radical initiation. Near-complete selectivity for single chlorination required the low conversion of ethylene carbonate such as 9%, which was controlled by limited introduction of chlorine gas. At a higher conversion of ethylene carbonate such as 61%, the selectivity for monochlorinated ethylene carbonate over dichlorinated ethylene carbonate was 86%. We found that the substrate contamination with water negatively influenced the performance of the C–H chlorination.

Introduction

The C–H chlorination by molecular chlorine is a highly exothermic reaction that proceeds via a radical chain mechanism as illustrated in Scheme 1 [1-6]. Frequently, photoirradiation is used for radical initiation through homolysis of the Cl–Cl bond to generate chlorine radicals. In a subsequent step, a S_H2 reaction by chlorine radicals at C–H bonds generates alkyl radicals

and HCl. The second S_H2 reaction between alkyl radicals and molecular chlorine then occurs to give the C–H chlorinated product and a chlorine radical, sustaining the radical chain. Chlorine gas is a cheap feedstock since it is formed as a byproduct of the electrolysis of NaCl to produce NaOH in an industrial process [7]. We felt that C–H chlorination would be updated by using scalable flash chemistry [8].

Scheme 1: Radical chain mechanism for a photo-induced C–H chlorination reaction.
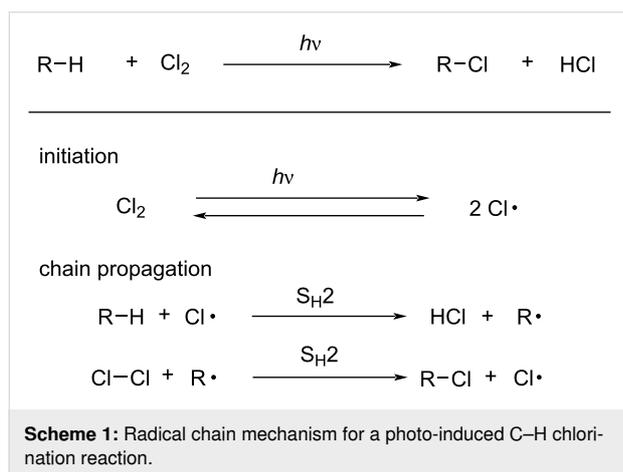
Flow C–H chlorination using a compact flow reactor is highly desirable in terms of efficiency and safety in handling highly toxic gases such as chlorine. In 2002, Jähnisch and co-workers reported the first microflow chlorination of 2,4-diisocyano-1-methylbenzene, which used a falling-film reactor developed by IMM [9]. While the flow rate employed was quite low (0.12 mL/min of toluene), the residence time was less than 14 seconds. More recent studies on flow C–H chlorination reactions focused on the use of Cl_2 gas in situ generated by photolysis of sulfuryl chloride [10] or by acid treatment of NaOCl [11,12]. We thought that if rationally designed scalable photoflow setups were available, flow C–H chlorination reactions using chlorine gas would be able to focus on production. In this study, we tested a novel photoflow setup consisting of quartz-made straight-line reactors, which are provided from MiChS (LX-1, Figure 1a) and a high-power LED (MiChS LED-s, 365 ± 5 nm, Figure 1b) [13]. Each channel track has a 2 mm depth and 557 mm length, while the width varies from 6 or 13 mm depending on the number of channels 7 or 5, respectively. The flow photoreactor is embedded into an aluminum frame equipped with a heat carrier channel. The design concepts including angle settings to ensure a thin liquid layer are summarized in Figure 1.

We chose the C–H chlorination of ethylene carbonate (**1**) as a model reaction (Scheme 2). Chlorinated ethylene carbonate **2** is a precursor to vinylene carbonate (**3**), which is used as an electrolyte additive for Li-ion batteries [14-20]. Vinylene carbonate

also serves as a useful synthetic building block for Diels–Alder reactions [21-25] and polymerization [26-30].

Results and Discussion

Using a PTFE tube and PTFE connectors, we connected the photoflow setup with a chlorine gas cylinder through a floating gas level meter in a fume hood (Figure 2). Since ethylene carbonate (**1**) melts between 34–37 °C, we preheated the container of **1** using an oil bath at 70 °C and pumped it to the photoreactor. In the reactor, hot water (80 °C) was circulated through a hole channel manufactured in an aluminum-made frame to keep the contacted glass reactor warm. The LED lamp was placed on the upper side of the reactor with a 20° angle to the reactor surface. The exiting gases (HCl and unreacted Cl_2) were trapped by an aqueous NaOH solution (1.7 M).

The reactors are set with a slope of 15 or 5° to achieve a thin substrate layer causing a rapid gas/liquid biphasic reaction. The residence time was estimated to be 15 and 30 seconds, respectively (for the measurement, ethylene carbonate was introduced in the absence of chlorine gas). After the experiments, chlorine gas that remained inside the flow setup was flushed with N_2 gas. In general, we used ethylene carbonate (**1**) with the grade containing less than 0.03% of water. The results are summarized in Table 1.

When the reaction of ethylene carbonate (**1**, flow rate: 74.9 mmol/min, containing 0.03% of H_2O) with 0.17 equiv of Cl_2 gas (flow rate: 12.5 mmol/min) was carried out under irradiation by UV-LED (240 W) with a 15° reactor angle, the desired chloroethylene carbonate (**2**) was formed selectively with a 9% conversion of **1** (Table 1, entry 1). When 0.23 equiv of Cl_2 was used, the selectivity became 96% with 12% conversion of **1**, in which a small amount of undesired 1,2-dichloroethylene carbonate (**2'**) was detected by GC (Table 1, entry 2). When 0.45 equiv of Cl_2 was used, the conversion of **1** increased to 21% and the selectivity of **2** became 91% (Table 1, entry 3). The reaction of **1** with one equivalent of Cl_2 gave **2** and **2'** in a ratio of 89:11 with 39% conversion of **1** (Table 1, entry 4). When the reaction mixture was circulated twice, we observed a higher conversion of **1** (87%) and obtained a 74:26 mixture of **2** and **2'** (Table 1, entry 5). Then, we limited the feeding of **1** (flow rate: 46.4 mmol/min) in order to increase conversion, which worked well. The reaction of **1** with 1.97 equiv of Cl_2 resulted in 61% conversion of **1** and an 86:14 ratio of **2** and **2'** (Table 1, entry 6). When a lower feeding of **1** (29.6 mmol/min) and an excess amount of Cl_2 (3.09 equiv) were used, higher conversion of **1** (76%) was attained with the selectivity of 84:16 (Table 1, entry 7). The irradiation at 600 W gave an almost similar result (Table 1, entries 8 and 9), which suggested that 240 W sufficed the reaction. Indeed, when the reaction was

(a) Photoflow Reactor, MiChS LX-1
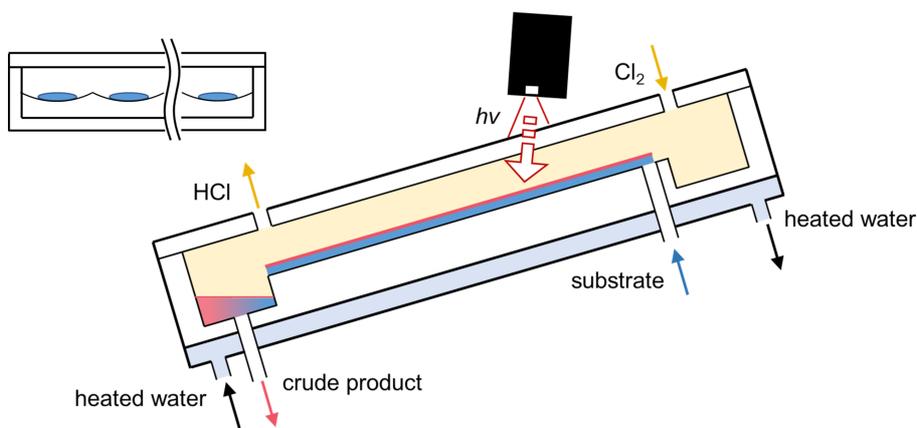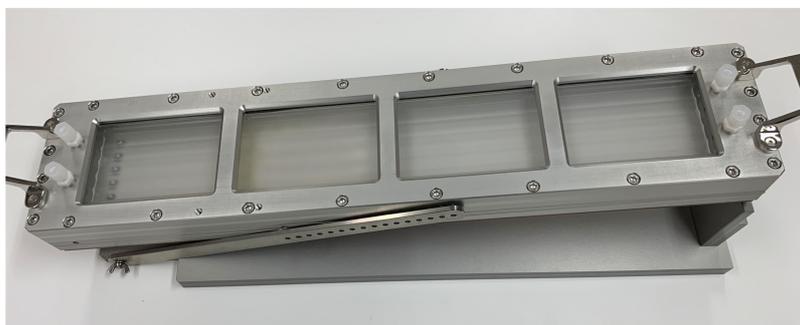
Concepts
• quartz-glass made
• slope setting for thin liquid phase
• minimum use of chlorine gas
• gas outlet for hydrogen chloride
• partial photoirradiation
• heat control function in the aluminum frame

(b) MiChS LED-s
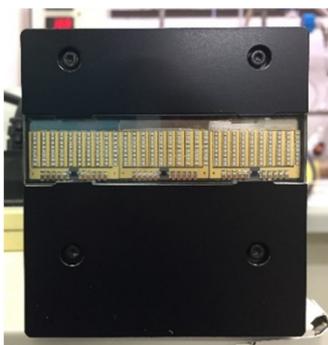
Figure 1: Components for photoflow setup: (a) MiChS LX-1 reactor and (b) MiChS LED-s (365 ± 5 nm, 60–600 W).

carried out with a shallow reactor angle such as 5°, the conversion of **1** increased from 49 to 61% (Table 1, entries 8 and 10). This is due to the extended residence time from 15 to 30 s. Flow gas/liquid reactions are often carried out using a tubular reactor and mixer under slug flow conditions. However, it is not easy to apply such conditions to the present photochlorination reaction since the volume of the Cl$_2$ gas is ca. 400 times larger than that of ethylene carbonate (for entry 8 in Table 1). In addition, a much longer tubular reactor would be required to ensure 15–30 s residence time.
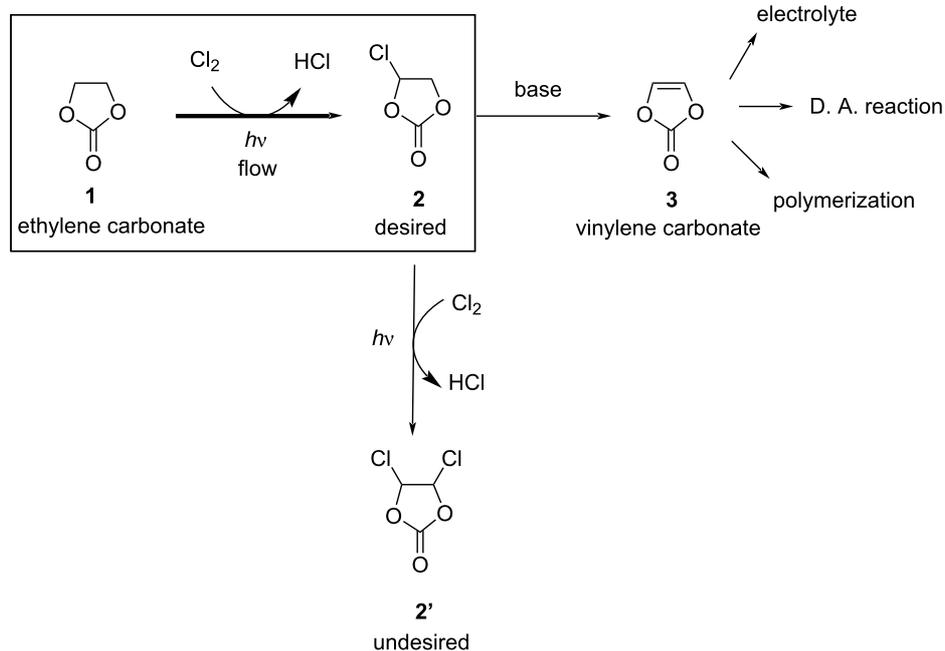
Scheme 2: Model reaction: photoflow C–H chlorination of ethylene carbonate (**1**) to chloroethylene carbonate (**2**).
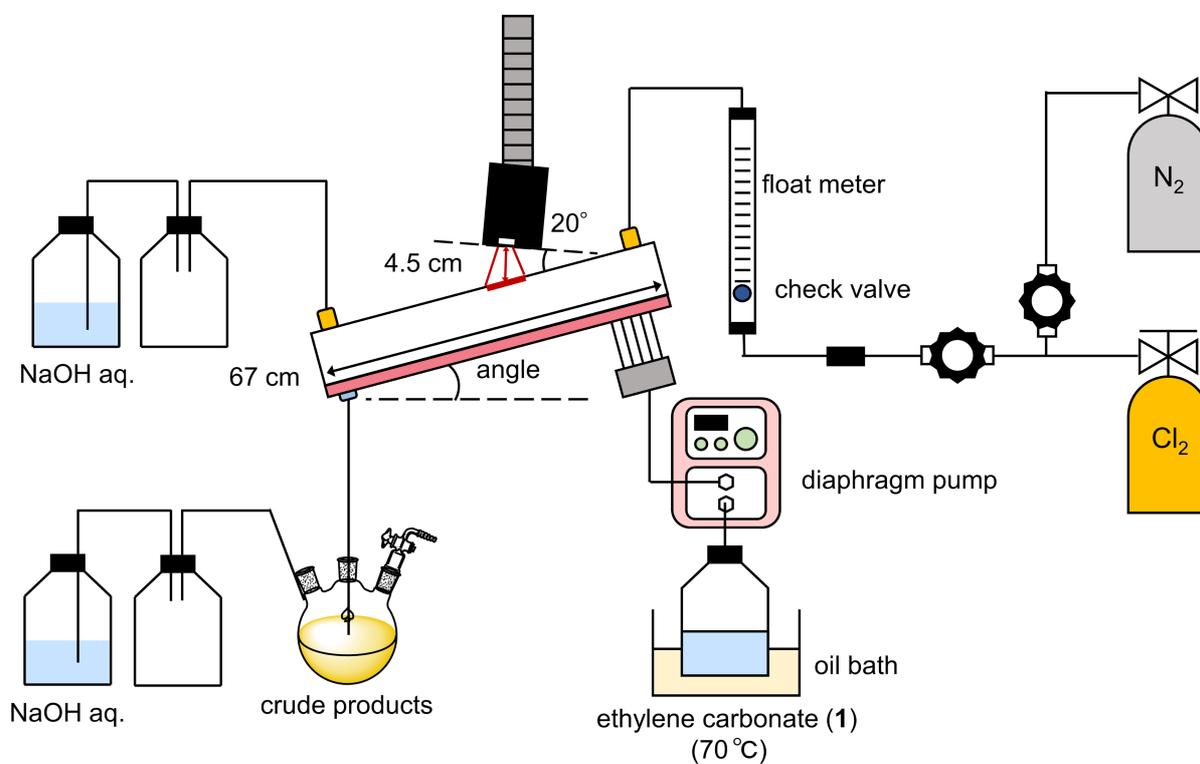
Figure 2: Photoflow setup for the C–H chlorination of ethylene carbonate (**1**).

Table 1: Photoflow C–H chlorination of ethylene carbonate (**1**) to chloroethylene carbonate (**2**).[a]

entry	angle (°)	flow rate		UV-LED (W)	conversion (%)[b]	selectivity (%)[b]	
		1[a] (mmol/min)	Cl$_2$ (mmol/min) (equiv)			**2**	**2'**
1	15	74.9	12.5 (0.17)	240	9	100	0
2	15	74.9	17.4 (0.23)	240	12	96	4
3	15	74.9	33.9 (0.45)	240	21	91	9
4	15	74.9	75.9 (1.01)	240	39	89	11
5[c]	15	74.9	75.9 + 75.9 (2.02)	240	87	74	26
6	15	46.4	91.5 (1.97)	240	61	86	14
7	15	29.6	91.5 (3.09)	240	76	84	16
8	15	117.6	146.5 (1.25)	240	49	78	22
9	15	117.6	143.7 (1.22)	600	47	78	22
10	5	117.6	146.5 (1.25)	240	61	79	21

[a]Reactions were conducted by using LX-1 with a reactor angle of 15° or 5° (entry 10). Photoirradiation was carried out by using LEDs (365 ± 5 nm at the power of 240 or 600 W). Ethylene carbonate (**1**) contains 0.03% of H$_2$O. [b]Determined by GC analysis. [c]Reaction mixture was circulated twice.

We then investigated the effect of contamination with water on the reaction, since Cl$_2$ gas is known to react with H$_2$O under irradiation conditions [31] and the results are summarized in Table 2. The flow rate of **1** and the equivalents of chlorine to **1** were set to be 187 mmol/min and 0.60–0.69, respectively. The reactor angle and light power were 15° and 240 W, respectively. The chlorination reaction using an ordinary grade of the substrate **1** containing 0.03% of water gave a 96:4 ratio of products **2** and **2'** with 26% conversion of **1** (Table 2, entry 1). In contrast, when we used substrate **1** containing 0.15% of water, the conversion decreased to 11% (Table 2, entry 2). With 0.76% of water, the conversion decreased further to 9% (Table 2, entry 3). These results suggest that the reaction has to be carried out carefully under dry conditions.

Conclusion

In this work, we reported that a novel photoflow setup designed for a gas–liquid biphasic reaction turned out to be useful for the C–H chlorination using chlorine gas in flow. Two decades after the first report on the microflow chlorination of a toluene derivative by Jähnisch and co-workers, we propose a new photoflow setup for C–H chlorination using chlorine gas, applicable to

scalable flow C–H chlorination. In our test reaction using C–H chlorination of ethylene carbonate (**1**), chloroethylene carbonate (**2**) was obtained in good to excellent selectivity by tuning the flow rates of **1** and chlorine gas. Partial irradiation of the flow channel is sufficient for the C–H chlorination, consistent with the requirement for light irradiation for the radical initiation step. If we apply the conditions to give 80% selectivity with 60% conversion with 30 s residence time, around 15 kilograms of chloroethylene carbonate (**2**) can be synthesized per day, which suggests the high potential of the present photoflow setup. We also demonstrated that the contamination with water had a negative impact on the reaction and the system should be kept dry for continuous production. We are now investigating some other photo gas–liquid flow reactions, which will be reported in due course.

Experimental

The photoflow setup consisting of a flow photoreactor LX-1 and UV-LEDs were supplied from MiChS Inc., Ltd. (http://www.michs.jp). The angle of the photoflow reactor was set to be 15 or 5° and heated water at 80 °C was circulated in a channel of an aluminum-made frame to avoid solidification of

Table 2: Effect of contamination of water.[a]

entry	water contamination	flow rate		conversion (%)[b]	selectivity (%)[b]	
		1[a] (mmol/min)	Cl$_2$ (mmol/min) (equiv)		**2**	**2'**
1	0.03%	187.0	126.8 (0.68)	26	96	4
2	0.15%	187.0	112.7 (0.60)	11	92	8
3	0.76%	187.0	118.3 (0.63)	9	100	0

[a]Reactions were conducted by using LX-1 with a rector angle of 15° and LEDs (240 W). [b]Measured by GC.

ethylene carbonate (**1**), whose melting point is 34–37 ºC. The UV-LED (365 ± 5 nm) was set with an angle of 20° to the reactor surface. Ethylene carbonate (**1**) preheated to 70 °C was fed into each channel of the flow photoreactor by using a diaphragm pump. At the same time, chlorine gas was fed into the reactor from the top-side inlet. Evolved HCl gas and unreacted Cl_2 gas were trapped by an aqueous 1.7 M NaOH solution. The first eluted solution was discarded for 3 min after which the eluted solution was collected for analysis. GC analysis was performed on a Shimadzu GC-2014 equipped with an FID detector using an Agilent J&W DB-1 column (Ø 0.25 mm × 30 m) under the following conditions: initial oven temperature: 40 °C, temperature change rate of 5 °C/min to 250 °C, hold at this temperature for 10 min. Yields were determined by using the percentage peak area method with compensation for the relative sensitivities of each component. Product **2** and byproduct **2'** were confirmed by ^1H and ^{13}C NMR analysis (see Supporting Information File 1).

Supporting Information

Supporting Information File 1
GC analysis and NMR spectra of the crude reaction mixture for the chlorination of compound **1**.
[https://www.beilstein-journals.org/bjoc/content/supplementary/1860-5397-18-16-S1.pdf]

Acknowledgements

ORCID® iDs
Takahide Fukuyama - https://orcid.org/0000-0002-3098-2987
Ilhyong Ryu - https://orcid.org/0000-0001-7715-4727

Preprint
A non-peer-reviewed version of this article has been previously published as a preprint: https://doi.org/10.3762/bxiv.2021.84.v1

References

1. Ingold, K. U.; Lusztyk, J.; Raner, K. D. *Acc. Chem. Res.* **1990,** *23,* 219–225. doi:10.1021/ar00175a003
2. Fletcher, B.; Suleman, N. K.; Tanko, J. M. *J. Am. Chem. Soc.* **1998,** *120,* 11839–11844. doi:10.1021/ja982289e
3. Sun, N.; Klabunde, K. J. *J. Am. Chem. Soc.* **1999,** *121,* 5587–5588. doi:10.1021/ja990084f
4. Pease, R. N.; Walz, G. F. *J. Am. Chem. Soc.* **1931,** *53,* 3728–3737. doi:10.1021/ja01361a016
5. Brown, H. C.; Kharasch, M. S.; Chao, T. H. *J. Am. Chem. Soc.* **1940,** *62,* 3435–3439. doi:10.1021/ja01869a040
6. Kharasch, M. S.; Berkman, M. G. *J. Org. Chem.* **1941,** *6,* 810–817. doi:10.1021/jo01206a004
7. Wang, Y.; Liu, Y.; Wiley, D.; Zhao, S.; Tang, Z. *J. Mater. Chem. A* **2021,** *9,* 18974–18993. doi:10.1039/d1ta02745j
   See for a recent review.
8. Yoshida, J.-i. *Flash Chemistry: Fast Organic Synthesis in Microsystems;* John Wiley & Sons: Chichester, UK, 2008.
9. Ehrich, H.; Linke, D.; Morgenschweis, K.; Baerns, M.; Jähnisch, K. *Chimia* **2002,** *56,* 647–653. doi:10.2533/000942902777680063
10. Matsubara, H.; Hino, Y.; Tokizane, M.; Ryu, I. *Chem. Eng. J.* **2011,** *167,* 567–571. doi:10.1016/j.cej.2010.08.086
11. Fukuyama, T.; Tokizane, M.; Matsui, A.; Ryu, I. *React. Chem. Eng.* **2016,** *1,* 613–615. doi:10.1039/c6re00159a
12. Strauss, F. J.; Cantillo, D.; Guerra, J.; Kappe, C. O. *React. Chem. Eng.* **2016,** *1,* 472–476. doi:10.1039/c6re00135a
13. Hyodo, M.; Iwano, H.; Kasakado, T.; Fukuyama, T.; Ryu, I. *Micromachines* **2021,** *12,* 1307. doi:10.3390/mi12111307
14. Zhang, S. S. *J. Power Sources* **2006,** *162,* 1379–1394. doi:10.1016/j.jpowsour.2006.07.074
    See for a review on electrolyte additives for lithium ion batteries.
15. Ivanov, S.; Sauerteig, D.; Dimitrova, A.; Krischok, S.; Bund, A. *J. Power Sources* **2020,** *457,* 228020. doi:10.1016/j.jpowsour.2020.228020
16. Michan, A. L.; Parimalam, B. S.; Leskes, M.; Kerber, R. N.; Yoon, T.; Grey, C. P.; Lucht, B. L. *Chem. Mater.* **2016,** *28,* 8149–8159. doi:10.1021/acs.chemmater.6b02282
17. Liu, Y.-H.; Takeda, S.; Kaneko, I.; Yoshitake, H.; Yanagida, M.; Saito, Y.; Sakai, T. *RSC Adv.* **2016,** *6,* 75777–75781. doi:10.1039/c6ra15168j
18. Wang, Y.; Nakamura, S.; Tasaki, K.; Balbuena, P. B. *J. Am. Chem. Soc.* **2002,** *124,* 4408–4421. doi:10.1021/ja017073i
19. Burns, J. C.; Petibon, R.; Nelson, K. J.; Sinha, N. N.; Kassam, A.; Way, B. M.; Dahn, J. R. *J. Electrochem. Soc.* **2013,** *160,* A1668–A1674. doi:10.1149/2.031310jes
20. Xiong, D.; Burns, J. C.; Smith, A. J.; Sinha, N.; Dahn, J. R. *J. Electrochem. Soc.* **2011,** *158,* A1431–A1435. doi:10.1149/2.100112jes
21. Aotake, T.; Tanimoto, H.; Hotta, H.; Kuzuhara, D.; Okujima, T.; Uno, H.; Yamada, H. *Chem. Commun.* **2013,** *49,* 3661–3663. doi:10.1039/c3cc40827b
22. Geiseler, O.; Müller, M.; Podlech, J. *Tetrahedron* **2013,** *69,* 3683–3689. doi:10.1016/j.tet.2013.03.013
23. Revés, M.; Lledó, A.; Ji, Y.; Blasi, E.; Riera, A.; Verdaguer, X. *Org. Lett.* **2012,** *14,* 3534–3537. doi:10.1021/ol301545e
24. Dong, S.; Cahill, K. J.; Kang, M.-I.; Colburn, N. H.; Henrich, C. J.; Wilson, J. A.; Beutler, J. A.; Johnson, R. P.; Porco, J. A., Jr. *J. Org. Chem.* **2011,** *76,* 8944–8954. doi:10.1021/jo201658y
25. Taffin, C.; Kreutler, G.; Bourgeois, D.; Clot, E.; Périgaud, C. *New J. Chem.* **2010,** *34,* 517–525. doi:10.1039/b9nj00536f
26. Huang, X.; Wu, J.; Wang, X.; Tian, Y.; Zhang, F.; Yang, M.; Xu, B.; Wu, B.; Liu, X.; Li, H. *ACS Appl. Energy Mater.* **2021,** *4,* 9368–9375. doi:10.1021/acsaem.1c01570
27. Zhang, Y.; Chen, S.; Chen, Y.; Li, L. *Mater. Chem. Front.* **2021,** *5,* 3681–3691. doi:10.1039/d1qm00004g
28. Li, H.; Yang, J.; Xu, Z.; Lu, H.; Zhang, T.; Chen, S.; Wang, J.; NuLi, Y.; Hirano, S.-i. *ACS Appl. Energy Mater.* **2020,** *3,* 8552–8561. doi:10.1021/acsaem.0c01173

29. Chai, J.; Liu, Z.; Zhang, J.; Sun, J.; Tian, Z.; Ji, Y.; Tang, K.; Zhou, X.;
Cui, G. *ACS Appl. Mater. Interfaces* **2017**, *9*, 17897–17905.
doi:10.1021/acsami.7b02844

30. Zhao, H.; Zhou, X.; Park, S.-J.; Shi, F.; Fu, Y.; Ling, M.; Yuca, N.;
Battaglia, V.; Liu, G. *J. Power Sources* **2014**, *263*, 288–295.
doi:10.1016/j.jpowsour.2014.04.063

31. Allmand, A. J.; Cunliffe, P. W.; Maddison, R. E. W.
J. Chem. Soc., Trans. **1925**, *127*, 822–840. doi:10.1039/ct9252700822

Flow synthesis of oxadiazoles coupled with sequential in-line extraction and chromatography

Kian Donnelly and Marcus Baumann[*]

Abstract

An efficient continuous flow process is reported for the synthesis of various 1,3,4-oxadiazoles via an iodine-mediated oxidative cyclisation approach. This entails the use of a heated packed-bed reactor filled with solid K_2CO_3 as a base. Using DMSO as solvent, this flow method generates the target heterocycles within short residence times of 10 minutes and in yields up to 93%. Scale-up of this flow process was achieved (34 mmol/h) and featured an integrated quenching and extraction step. Lastly, the use of an automated in-line chromatography system was exploited to realise a powerful flow platform for the generation of the heterocyclic targets.

Introduction

The application of enabling technologies in chemistry has received a surge in interest in recent years [1-4]. At the forefront of this revolution has been the advent of flow chemistry and its increasing utility in synthetic chemistry [5-8]. This is largely driven by the ability to improve reaction efficiency, safety and provide access to chemistry that was not previously possible [9-11]. Carrying out a reaction in continuous flow mode can improve its efficiency in several ways, including decreasing reaction times, increasing yields, or eliminating tedious unit operations by incorporating them in-line in a telescoped

manner. These improvements are typically not limited to the chemistry itself but can also result in the generation of less waste, thus reducing the harmful environmental impact of various processes [12-15]. This has led to a significant development in continuous flow platforms, particularly in industry [16-20].

1,3,4-Oxadiazoles are biologically relevant 5-membered heterocyclic compounds with various favourable pharmacokinetic properties and have been investigated as potential candidates for

antiviral, antifungal and anticancer agents [21-23]. Previous reports of the synthesis of 1,3,4-oxadiazoles in continuous flow focused on the reaction between tetrazoles and carboxylic acids (Huisgen synthesis) [24,25]. Continuous flow technology has also been exploited for the further functionalisation of 1,3,4-oxadiazoles [26]. Various other methods to access this heterocyclic moiety have been reported in the literature, with many focusing on either cyclodehydration or cyclodesulphurisation (Scheme 1) [27]. However, in recent years, there have been a number of oxidative cyclisation protocols reported to access the same 1,3,4-oxadiazole unit [28-33]. In 2012, Guin and co-workers described the iodine-mediated cyclodesulphurisation of thiosemicarbazides, yielding the corresponding 1,3,4-oxadiazoles [32]. Subsequently, Yu and co-workers reported the iodine-mediated oxidative cyclisation of acyl hydrazones to form oxadiazoles [33]. While this method provided the products in high yields, it required the use of super-stoichiometric quantities of iodine, which is potentially toxic and corrosive. This potential toxicity in combination with the requirement for

the subsequent removal of excess iodine and potentially biologically active reaction products, led us to explore the implementation of a continuous flow platform to reduce these hazards, while maintaining the high efficiency of the reaction.

Results and Discussion

We began with the investigation of various oxidative cyclisations of acyl hydrazones to compare the iodine-mediated cyclisation with other oxidative conditions. A range of oxidants was investigated (Table 1), with only *N*-chlorosuccinimide (NCS) [34] and iodine resulting in the formation of product (entries 1 and 2, Table 1). As iodine yielded superior results, we opted to transfer this reaction from batch mode to continuous flow mode.

The use of an insoluble reagent (e.g. K_2CO_3) is generally problematic with continuous flow reactors, due to the high probability of blockages occurring within the reactor tubing. To overcome this, we opted to incorporate a packed bed reactor into the continuous flow setup. The initial setup consisted of a heated

Scheme 1: Methods for accessing 1,3,4-oxadiazoles.
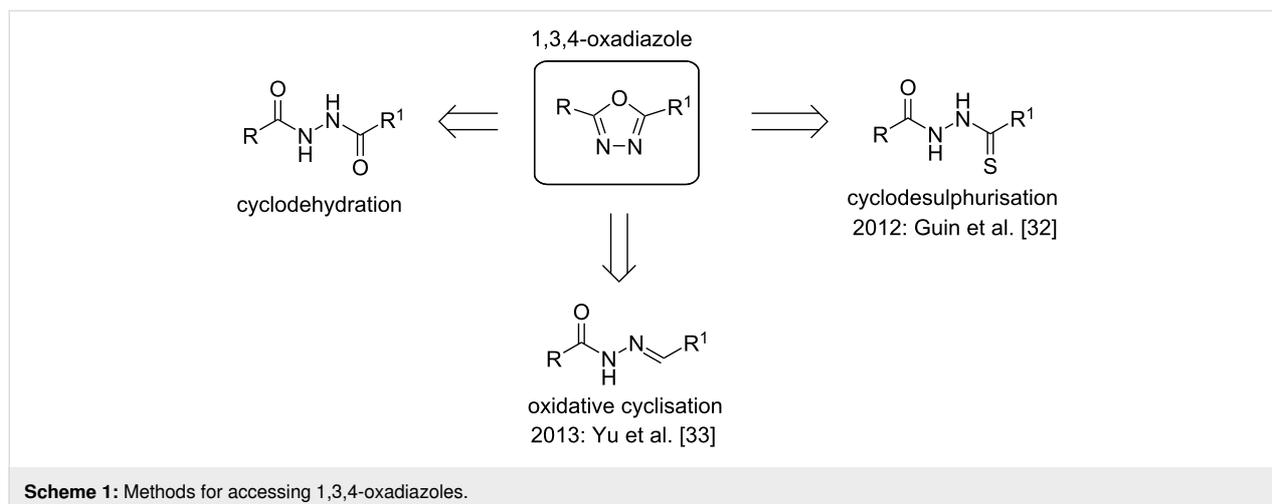
Table 1: Screening of oxidants for cyclisation of acyl hydrazone.

| Entry	Oxidant	Base	Solvent	NMR yield
1	iodine	K_2CO_3	DMSO	57%
2	NCS	DBU	DCM	31%
3	sodium periodate	K_2CO_3	DMSO	n.d.
4	oxone	K_2CO_3	DMSO	n.d.
5	sodium percarbonate	K_2CO_3	DMSO	n.d.

glass column (i.d. 7 mm, length 7 cm), packed with K_2CO_3, through which a solution of acyl hydrazone and iodine were passed. It was anticipated that the larger excess of K_2CO_3 present in the packed bed reactor (when compared to batch mode), in addition to the more efficient heat transfer, would lead to significantly shorter reaction times. Using a flow rate of 0.3 mL/min and a temperature of 100 °C as a starting point (entry 1, Table 2), we began to vary the reaction conditions in view of achieving high yields in short residence times. Through variation of flow rate, we found 0.2 mL/min (approximately 10 minute residence time) to be optimal (entries 1–3, Table 2). Shorter residence times were found to be slightly detrimental to the yield and longer residence times provided no benefit (entries 2 and 3, Table 2). The reaction was found to be sensitive to the quantity of iodine present, with an increase in yield correlating with a larger excess of iodine (entries 4 and 5, Table 2). Variation of reaction temperature identified 100 °C to be optimal, affording the desired product in 90% yield (entry 5, Table 2). A decrease in temperature resulted in a slight decrease in yield, and an increase in decomposition was observed with an increase in temperature despite the short residence times (entries 6 and 7, Table 2). The lack of solubility of the hydrazone substrates limited options with regards to variation in reaction solvent, with adequate solubility only being observed in DMF and DMSO. Despite the slightly lower yield observed using DMF (entry 8, Table 2), it provided the option of a co-solvent system in situations where solubility in DMSO is insufficient.

A variety of acyl hydrazones were subsequently synthesised from the corresponding aldehydes (Scheme 2) and subjected to the optimised flow conditions (Scheme 3). This resulted in full conversion of the substrate in all cases. Both thiophene and pyridine-containing substrates were well tolerated, with slightly higher yields observed in the case of the more electron-deficient CF_3-substituted system (**2a** and **2c** vs **2b** and **2d**). Both electron-rich and electron-deficient acyl hydrazones afforded high yields, with a slight decrease observed with the presence of the electron-withdrawing CF_3 group in the case of the electron poor nitro-substituted substrate **2g**. The reaction was also chemoselective in the presence of other oxidisable moieties such as in the cases of **2i** and **2j**. Additionally, the stereoconfiguration of the styryl moiety was maintained as confirmed via the X-ray structure of **2j** (Scheme 3).

As a potential application of our previously reported synthesis of useful bicyclo[1.1.1]pentane (BCP) building blocks [36], we investigated their use in the oxadiazole-forming reaction. The BCP acid chloride **5** was synthesised from [1.1.1]propellane (**3**) via the photochemical reaction with isopropyl 2-chloro-2-oxoacetate (Scheme 4). The corresponding BCP acyl hydrazone was then obtained following treatment of acid **5** with hydrazine hydrate, followed by hydrazone formation with the corresponding aldehyde. When subjected to the reaction conditions, oxadiazoles **2k** and **2l** were obtained in low yield over this multi-step sequence. While unsuitable for large scale reactions, this methodology may prove useful for accessing small quantities of medicinally interesting BCP-1,3,4-oxadiazole compounds for biological testing. Additionally, the reaction of 1,3-substituted isoxazole **1m** under these conditions was investigated. Despite high degrees of decomposition, it was possible

Table 2: Optimisation of iodine-mediated cyclisation in continuous flow mode.
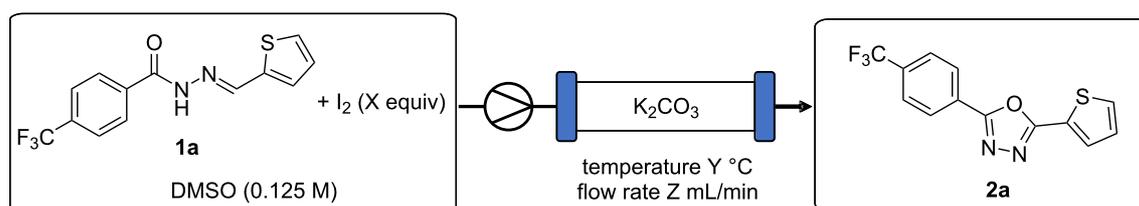
Entry	Flow rate (Z) (mL/min)	Temperature (Y) (°C)	I_2 Equivalents (X)	Yield[a]
1	0.3	100	1.1	76%
2	0.2	100	1.1	79%
3	0.1	100	1.1	78%
4	0.2	100	1.2	76%
5	0.2	100	1.5	90%
6	0.2	80	1.5	87%
7	0.2	120	1.5	81%
8[b]	0.2	100	1.5	81%

[a]Yields were determined by ^1H NMR using 1,3,5-trimethoxybenzene as internal standard. [b]DMF was used in place of DMSO.
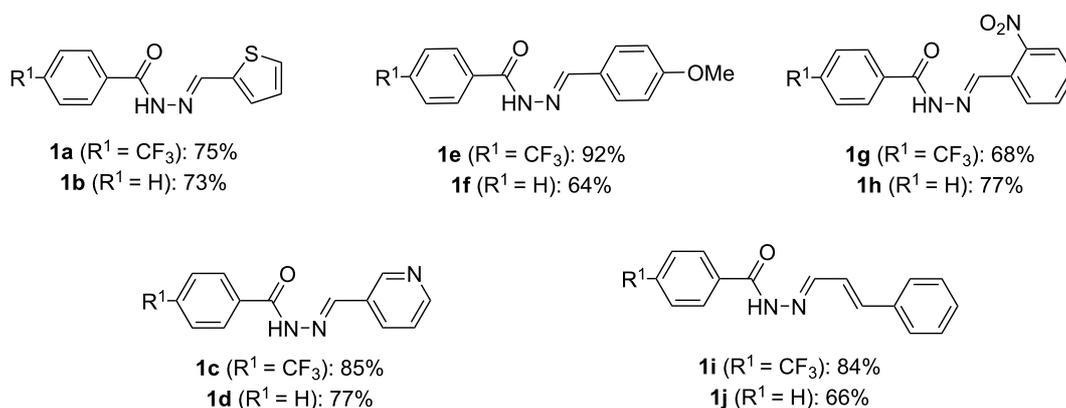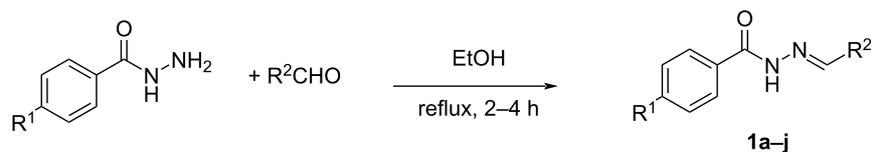
Scheme 2: Synthesis of acyl hydrazones **1a–j**.

1a (R^1 = CF$_3$): 75%
1b (R^1 = H): 73%

1e (R^1 = CF$_3$): 92%
1f (R^1 = H): 64%

1g (R^1 = CF$_3$): 68%
1h (R^1 = H): 77%

1c (R^1 = CF$_3$): 85%
1d (R^1 = H): 77%

1i (R^1 = CF$_3$): 84%
1j (R^1 = H): 66%

2a (R^1 = CF$_3$): 89%
2b (R^1 = H): 86%

2e (R^1 = CF$_3$): 84%
2f (R^1 = H): 83%

2g (R^1 = CF$_3$): 77%
2h (R^1 = H): 85%

2c (R^1 = CF$_3$): 93%
2d (R^1 = H): 77%

2i (R^1 = CF$_3$): 85%
2j (R^1 = H): 70%

2c
CCDC-2129202

2j
CCDC-2129203
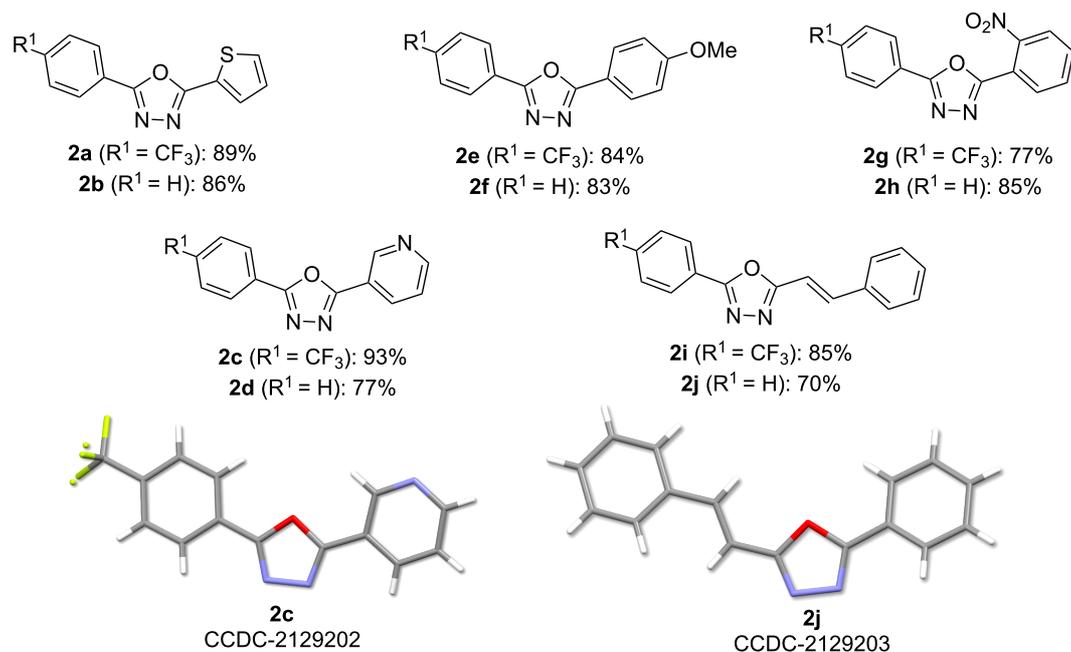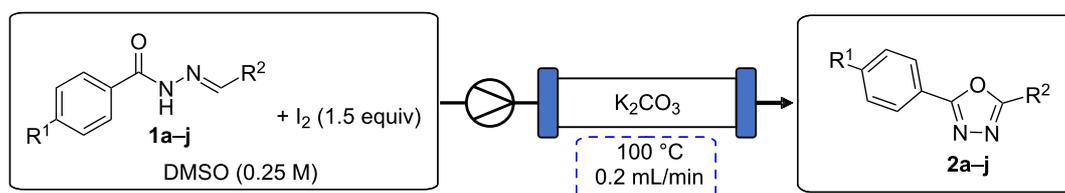
Scheme 3: Iodine-mediated cyclisation of hydrazones **1a–j** yielding oxadiazoles **2a–j**. Reaction conditions: **1a–j** (1 mmol), iodine (1.5 mmol), DMSO (4 mL, 0.25 M), 100 °C, 0.2 mL/min. Reported yields are isolated yields following purification [35].

to isolate the desired poly-heterocyclic compound **2m** in low yield (Scheme 4).

Having investigated the substrate scope in continuous flow mode, we then moved to probe the scalability of the reaction. A primary advantage of carrying out a reaction in continuous flow is the ease of which it can subsequently be scaled-up, without the need for further extensive optimisation. Oxadiazole product **2j** was chosen as the target molecule for the scale-up reaction due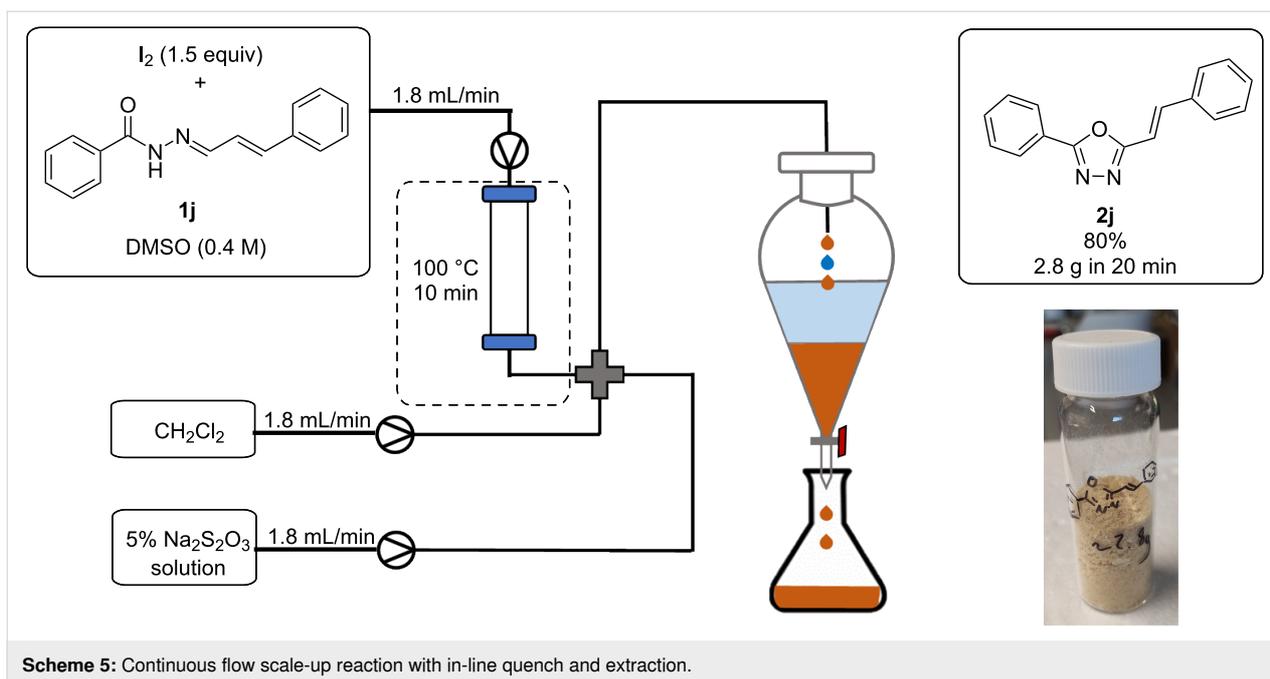 to the potential for further diversification via the embedded alkene. Due to the large quantity of material, an increase in column size was required to house the larger quantity of K_2CO_3. As a result of the increased volume of the reactor column (i.d. 15 mm, length 12 cm) a proportional increase in flow rate was necessary to maintain the residence time consistent with our small-scale experiments.

Following reaction, the excess iodine must be quenched via a wash using sodium thiosulphate solution. To avoid the hazards associated with handling of iodine on multi-gram scale, in addition to eliminating unit operations, an in-line quench and separation was developed. The in-line quench consisted of employing a 4-way mixer, through which sodium thiosulphate solution and an additional organic solvent could be introduced. As the

reaction is carried out in DMSO, which is water soluble, an additional organic solvent was required to isolate the desired product from the aqueous phase. There are various examples of in-line separations published in the literature [37], however, many of them involve the use of expensive and complex membrane filters. To reduce cost and increase simplicity we opted to use a 'home-made' setup to achieve continuous separation which consisted of a laboratory separating funnel, into which we collect the biphasic reaction output following aqueous workup (Scheme 5). Dichloromethane (DCM) was selected as the organic solvent of choice due to its increased density compared to DMSO and water. Separation in a continuous manner could then be simply achieved by adjusting the outlet tap of the separating funnel such that a constant volume is maintained. To improve throughput, substrate concentration was increased to 0.4 M, and using this setup 2.8 g (11.2 mmol, 80%) of oxadiazole product **2j** could be synthesised in just 20 minutes. This corresponds to a productivity of 8.4 g/h (34 mmol/h). The increase in yield when compared to the small-scale reaction is potentially explained by the reaction reaching steady state during this longer run, thus providing a more accurate indication of the yield. This productivity could potentially be further increased, simply by increasing the volume of the glass column reactor.

Scheme 4: Synthesis of complex oxadiazoles.

Scheme 5: Continuous flow scale-up reaction with in-line quench and extraction.
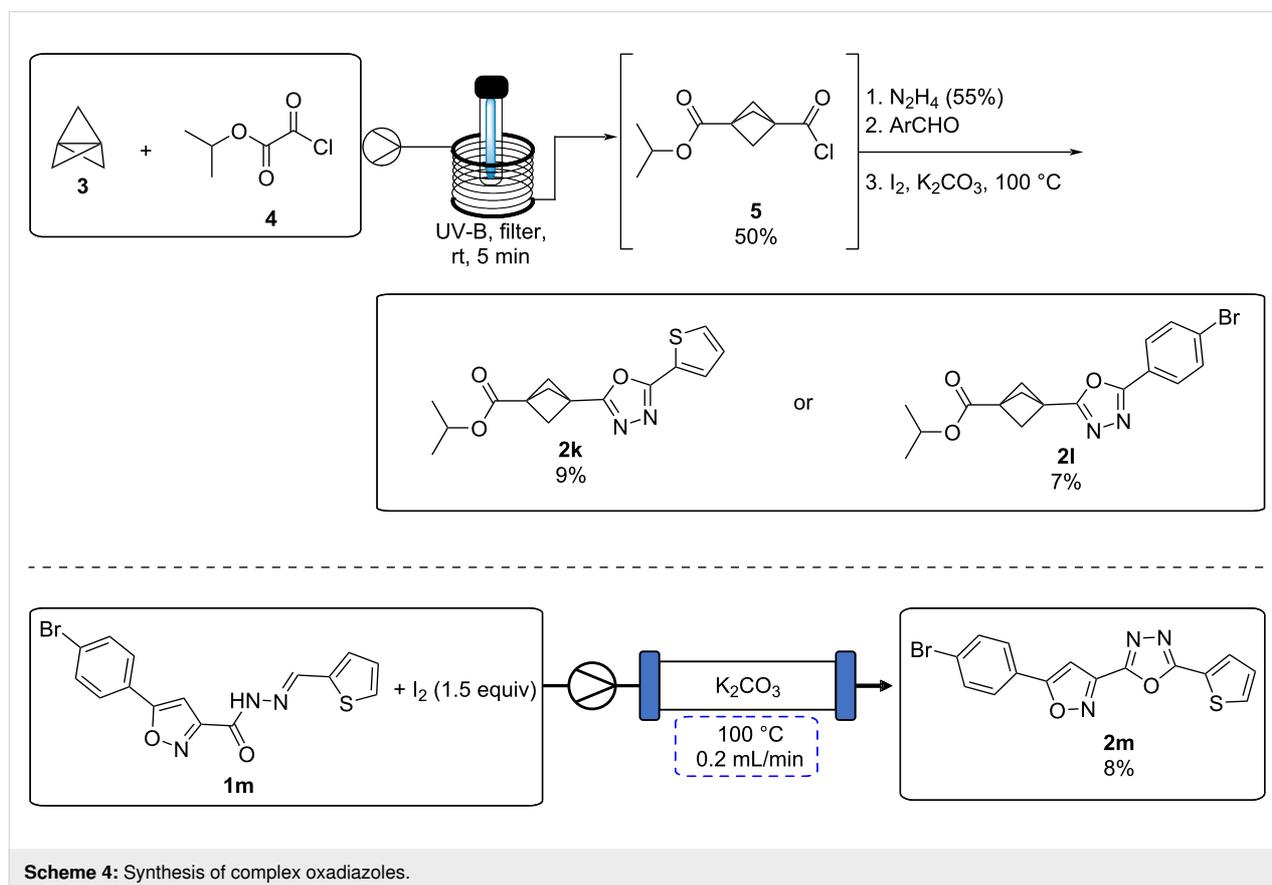
With an in-line extraction system in hand, we envisioned a system which would eliminate a further time-consuming unit operation, product purification. Inspired by recent reports of the incorporation of the Advion puriFlash 5.250 system in a continuous flow system [38], we aimed to apply this system to our flow setup. The puriFlash system is an automated liquid chromatography purification system which is capable of purifying mixtures in a continuous fashion by using alternating sample loops and chromatography columns. Initial experiments proved challenging as clean separation could not be achieved with high concentrations (0.4 M) or with large quantities of highly polar DMSO. After some optimisation, satisfactory separation was achieved by decreasing the reaction concentration to 0.2 M, and the final concentration to approximately 0.1 M, through adjustment of the flow rate of DCM in the separation step. Further improvements were realised by increasing the flow rate of the thiosulphate solution to remove sufficient DMSO in view of satisfactory separation being achieved. Due to the high polarity of the reaction mixture, moderately non-polar chromatographic conditions were required (3% EtOAc, 97% cyclohexane at start), with a gradient method being employed. While these conditions successfully provided the desired products in pure form, it must be noted that a short equilibration period between runs was required, thus slightly reducing the throughput of the system.

With satisfactory chromatography conditions in hand, we moved to test the system using various substrates (Scheme 6). Compounds **2b**, **2f**, and **2h** were all subjected to the reaction conditions and isolated in comparable yields to previous experi-

ments, following in-line quench and in-line purification. In addition to increasing efficiency by removing manual unit operations, the incorporation of the in-line purification system allowed for isolation of pure material in approximately 100 minutes (from substrate vial to pure product) on a 1 mmol scale. To determine the effect of scale on the system, **2j** was processed on a 2 mmol scale (0.5 g) with no loss in efficiency or yield being observed.

While the residence time of the reaction remains constant, incorporating an in-line quench and subsequent purification results in significant reduction in processing times. Typically, performing the quench step manually will take approximately 20–30 minutes when subsequent evaporation of solvent is accounted for. Additionally, manual purification by flash column chromatography can take between 60–120 minutes depending on reaction scale. When added to the reaction time, this results in an estimated total processing time of at least 110 minutes (from substrate vial to pure product) on a 1 mmol scale.

Conclusion

In summary, we have developed a continuous flow platform for the synthesis of 1,3,4-oxadiazoles in high yields and short residence times of 10 minutes. The incorporation of an in-line extraction reduced the risk of contact with toxic and corrosive iodine in addition to eliminating a tedious unit operation. The reaction was demonstrated to be readily scalable with a productivity of 34 mmol/h being achieved for oxadiazole **2j**. Additionally, the implementation of in-line chromatographic purifica-

Scheme 6: Continuous flow setup equipped with in-line extraction and purification.
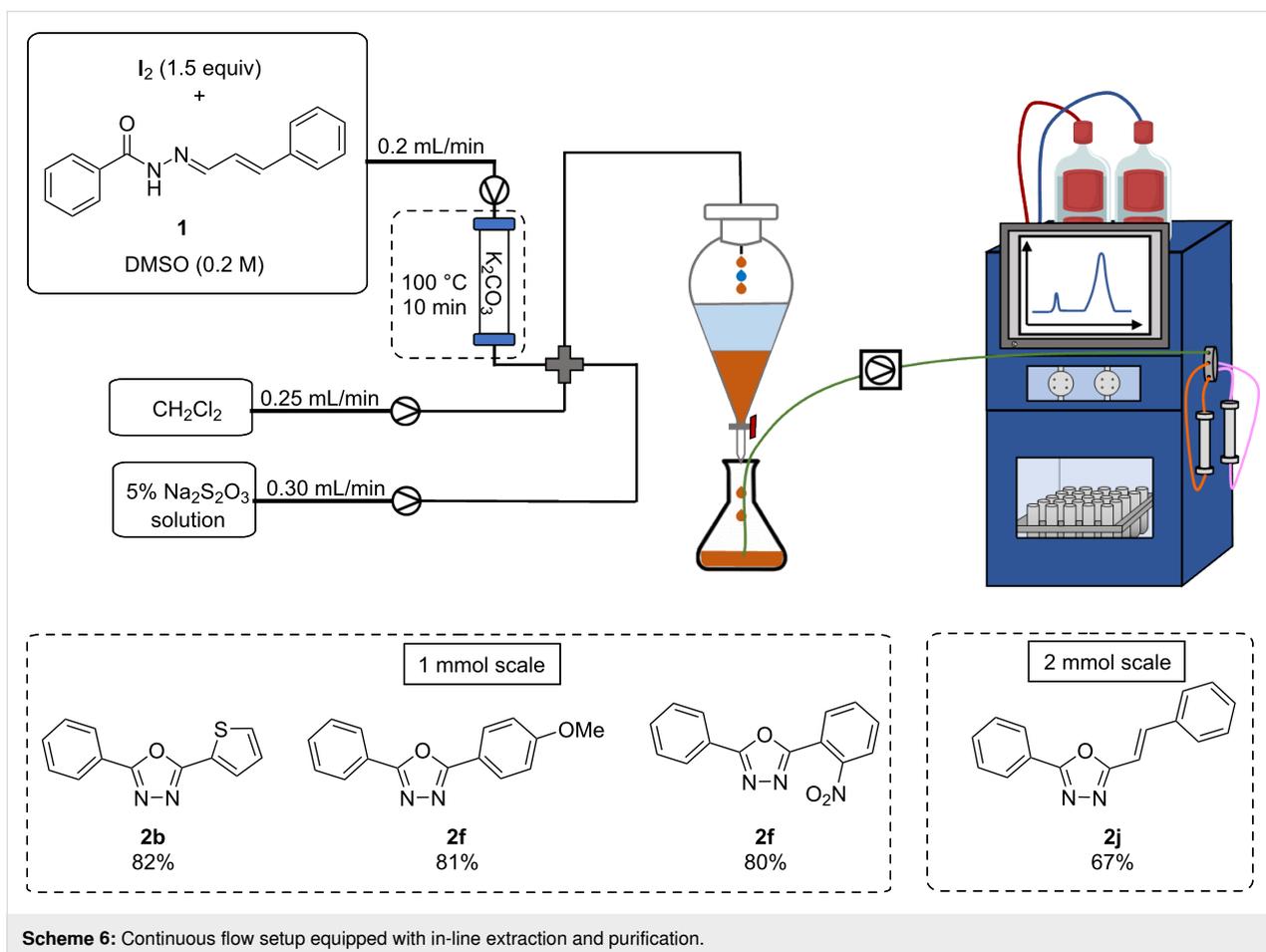
tion provided the desired products in high yields, integrating an additional unit operation and thus increasing efficiency. Through removing two off-line unit operations and carrying out chromatographic purification in-line, further benefits were realised through a reduction in solvent consumption and operator time when compared to the analogous batch process.

Supporting Information

Supporting Information File 1

Experimental section and analytical data.
[https://www.beilstein-journals.org/bjoc/content/supplementary/1860-5397-18-27-S1.pdf]

Acknowledgements

We are very grateful to Colin Banks and Mark Allen (Advion-interchim) for the loan of an Advion puriFlash 5.250 system and fruitful discussions. We are indebted to Dr. Andrew D. Phillips for solving all X-ray structures reported in this article.

Funding

ORCID® iDs

Kian Donnelly - https://orcid.org/0000-0001-5024-4378
Marcus Baumann - https://orcid.org/0000-0002-6996-5893

References

1. Fitzpatrick, D. E.; Battilocchio, C.; Ley, S. V. *ACS Cent. Sci.* **2016**, *2*, 131–138. doi:10.1021/acscentsci.6b00015
2. Wegner, J.; Ceylan, S.; Kirschning, A. *Adv. Synth. Catal.* **2012**, *354*, 17–57. doi:10.1002/adsc.201100584
3. Noël, T.; Cao, Y.; Laudadio, G. *Acc. Chem. Res.* **2019**, *52*, 2858–2869. doi:10.1021/acs.accounts.9b00412
4. Buglioni, L.; Raymenants, F.; Slattery, A.; Zondag, S. D. A.; Noël, T. *Chem. Rev.* **2022**, *122*, 2752–2906. doi:10.1021/acs.chemrev.1c00332
5. Baxendale, I. R.; Brocken, L.; Mallia, C. J. *Green Process. Synth.* **2013**, *2*, 211–230. doi:10.1515/gps-2013-0029

6. Bogdan, A. R.; Dombrowski, A. W. *J. Med. Chem.* **2019**, *62*, 6422–6468. doi:10.1021/acs.jmedchem.8b01760

7. Wegner, J.; Ceylan, S.; Kirschning, A. *Chem. Commun.* **2011**, *47*, 4583–4592. doi:10.1039/c0cc05060a

8. Akwi, F. M.; Watts, P. *Chem. Commun.* **2018**, *54*, 13894–13928. doi:10.1039/c8cc07427e

9. Movsisyan, M.; Delbeke, E. I. P.; Berton, J. K. E. T.; Battilocchio, C.; Ley, S. V.; Stevens, C. V. *Chem. Soc. Rev.* **2016**, *45*, 4892–4928. doi:10.1039/c5cs00902b

10. Ketels, M.; Konrad, D. B.; Karaghiosoff, K.; Trauner, D.; Knochel, P. *Org. Lett.* **2017**, *19*, 1666–1669. doi:10.1021/acs.orglett.7b00460

11. Bonner, A.; Loftus, A.; Padgham, A. C.; Baumann, M. *Org. Biomol. Chem.* **2021**, *19*, 7737–7753. doi:10.1039/d1ob01452h

12. Baumann, M.; Moody, T. S.; Smyth, M.; Wharry, S. *Synthesis* **2021**, *53*, 3963–3976. doi:10.1055/a-1541-1761

13. Newman, S. G.; Jensen, K. F. *Green Chem.* **2013**, *15*, 1456–1472. doi:10.1039/c3gc40374b

14. Brandão, P.; Pineiro, M.; Pinho e Melo, T. M. V. D. *Eur. J. Org. Chem.* **2019**, 7188–7217. doi:10.1002/ejoc.201901335

15. Dallinger, D.; Kappe, C. O. *Curr. Opin. Green Sustainable Chem.* **2017**, *7*, 6–12. doi:10.1016/j.cogsc.2017.06.003

16. Donnelly, K.; Baumann, M. *J. Flow Chem.* **2021**, *11*, 223–241. doi:10.1007/s41981-021-00168-z

17. Ley, S. V.; Chen, Y.; Robinson, A.; Otter, B.; Godineau, E.; Battilocchio, C. *Org. Process Res. Dev.* **2021**, *25*, 713–720. doi:10.1021/acs.oprd.0c00534

18. Baumann, M.; Moody, T. S.; Smyth, M.; Wharry, S. *Org. Process Res. Dev.* **2020**, *24*, 1802–1813. doi:10.1021/acs.oprd.9b00524

19. Hartman, R. L. *Curr. Opin. Chem. Eng.* **2020**, *29*, 42–50. doi:10.1016/j.coche.2020.05.002

20. Gioiello, A.; Piccinno, A.; Lozza, A. M.; Cerra, B. *J. Med. Chem.* **2020**, *63*, 6624–6647. doi:10.1021/acs.jmedchem.9b01956

21. Li, Z.; Zhan, P.; Liu, X. *Mini-Rev. Med. Chem.* **2011**, *11*, 1130–1142. doi:10.2174/138955711797655407

22. Glomb, T.; Szymankiewicz, K.; Świątek, P. *Molecules* **2018**, *23*, 3361. doi:10.3390/molecules23123361

23. Wani, M. Y.; Ahmad, A.; Shiekh, R. A.; Al-Ghamdi, K. J.; Sobral, A. J. F. N. *Bioorg. Med. Chem.* **2015**, *23*, 4172–4180. doi:10.1016/j.bmc.2015.06.053

24. Reichart, B.; Kappe, C. O. *Tetrahedron Lett.* **2012**, *53*, 952–955. doi:10.1016/j.tetlet.2011.12.043

25. Green, L.; Livingstone, K.; Bertrand, S.; Peace, S.; Jamieson, C. *Chem. – Eur. J.* **2020**, *26*, 14866–14870. doi:10.1002/chem.202002896

26. Wong, J. Y. F.; Tobin, J. M.; Vilela, F.; Barker, G. *Chem. – Eur. J.* **2019**, *25*, 12439–12445. doi:10.1002/chem.201902917

27. Patel, K. D.; Prajapati, S. M.; Panchal, S. N.; Patel, H. D. *Synth. Commun.* **2014**, *44*, 1859–1875. doi:10.1080/00397911.2013.879901

28. Majji, G.; Rout, S. K.; Guin, S.; Gogoi, A.; Patel, B. K. *RSC Adv.* **2014**, *4*, 5357–5362. doi:10.1039/c3ra44897e

29. Zhang, G.; Yu, Y.; Zhao, Y.; Xie, X.; Ding, C. *Synlett* **2017**, *28*, 1373–1377. doi:10.1055/s-0036-1588747

30. Yadav, A. K.; Yadav, L. D. S. *Tetrahedron Lett.* **2014**, *55*, 2065–2069. doi:10.1016/j.tetlet.2014.02.022

31. Prakash, O.; Kumar, M.; Kumar, R.; Sharma, C.; Aneja, K. R. *Eur. J. Med. Chem.* **2010**, *45*, 4252–4257. doi:10.1016/j.ejmech.2010.06.023

32. Guin, S.; Rout, S. K.; Ghosh, T.; Khatun, N.; Patel, B. K. *RSC Adv.* **2012**, *2*, 3180–3183. doi:10.1039/c2ra00044j

33. Yu, W.; Huang, G.; Zhang, Y.; Liu, H.; Dong, L.; Yu, X.; Li, Y.; Chang, J. *J. Org. Chem.* **2013**, *78*, 10337–10343. doi:10.1021/jo401751h

34. Pardeshi, S. P.; Patil, S. S.; Bobade, V. D. *Synth. Commun.* **2010**, *40*, 1601–1606. doi:10.1080/00397910903134592

35. X-ray data of compounds **2c** and **2j** were deposited with the Cambridge Crystalographic Data Centre and are available free of charge as CCDC-2129202 and 2129203, respectively from https://www.ccdc.cam.ac.uk/.

36. Donnelly, K.; Baumann, M. *Chem. Commun.* **2021**, *57*, 2871–2874. doi:10.1039/d0cc08124h

37. Weeranoppanant, N.; Adamo, A. *ACS Med. Chem. Lett.* **2020**, *11*, 9–15. doi:10.1021/acsmedchemlett.9b00491

38. Thomson, C. G.; Banks, C.; Allen, M.; Barker, G.; Coxon, C. R.; Lee, A.-L.; Vilela, F. *J. Org. Chem.* **2021**, *86*, 14079–14094. doi:10.1021/acs.joc.1c01151

Shift of the reaction equilibrium at high pressure in the continuous synthesis of neuraminic acid

Jannis A. Reich[‡1], Miriam Aßmann[‡2], Kristin Hölting[2], Paul Bubenheim[1], Jürgen Kuballa[2] and Andreas Liese[*1]

Abstract

The importance of a compound that helps fight against influenza is, in times of a pandemic, self-evident. In order to produce these compounds in vast quantities, many researchers consider continuous flow reactors in chemical industry as next stepping stone for large scale production. For these reasons, the synthesis of *N*-acetylneuraminic acid (Neu5Ac) in a continuous fixed-bed reactor by an immobilized epimerase and aldolase was investigated in detail. The immobilized enzymes showed high stability, with half-life times > 173 days under storage conditions (6 °C in buffer) and reusability over 50 recycling steps, and were characterized regarding the reaction kinetics (initial rate) and scalability (different lab scales) in a batch reactor. The reaction kinetics were studied in a continuous flow reactor. A high-pressure circular reactor (up to 130 MPa) was applied for the investigation of changes in the position of the reaction equilibrium. By this, equilibrium conversion, selectivity, and yield were increased from 57.9% to 63.9%, 81.9% to 84.7%, and 47.5% to 54.1%, respectively. This indicates a reduction in molar volume from *N*-acetyl-ᴅ-glucosamine (GlcNAc) and pyruvate (Pyr) to Neu5Ac. In particular, the circular reactor showed great potential to study reactions at high pressure while allowing for easy sampling. Additionally, an increase in affinity of pyruvate towards both tested enzymes was observed when high pressure was applied, as evidenced by a decrease of K_I for the epimerase and K_M for the aldolase from 108 to 42 mM and 91 to 37 mM, respectively.

Introduction

In times of a pandemic, the importance of substances to enhance the human immune system is self-explanatory. Among them are sialic acids, which are produced and investigated for this reason, as they are found in cell membranes and play an important role in cell adhesion and signaling [1]. They are also studied, for instance, in Covid-19 research [2]. It has been

pointed out that derivatives from Neu5Ac can inhibit viral enzymes [3]. Neu5Ac and its production have been described over the past three decades [4], however, no major breakthrough in its synthesis has been achieved so far [5]. Additionally, some reports underline the importance of sialic acids (rather than Neu5Ac in particular), of which Neu5Ac is the most prominent form [6].

In 2016, Neu5Ac was approved as a food additive in the United States of America and in the European Union and the Republic of China in 2017 [7]. Due to its importance, Neu5Ac production by enzymatic [5,8] or via whole cell production is still under investigation [9-11]. For this study, the enzymatic synthesis was chosen for its simple reaction sequence (Figure 1) and high selectivity.

Different research groups already described the reaction kinetics of the epimerase and aldolase at ambient pressure [5,8]. In this study, the rate expressions from Groher et al. are used [8]. So far, different approaches have been attempted to increase the overall position of an equilibrium by using additional enzymes [12], different temperatures or high concentrations of the substrates [13].

In accordance with the principle of Le Chatelier, pressure can also be used to influence the position of an equilibrium given that the molar volume changes during the reaction [14]. High-pressure processing is gaining increasing attraction for the enhancement of enzymes [15]. It has been shown that pressure can influence enzymatic reactions, either in kinetics [16-18], in enantiomeric excess [19], in stability [20], or in the position of the equilibrium [17,21]. State of the art for high-pressure research is the use of pressurized batch reactors [22,23].

Since continuous production and suitable reactors are receiving more attention [24], and some believe that this will be the next stepping stone for industry [25,26], the aim of this research was to first establish a continuous reactor at high pressure, and then to investigate the influence of pressure on the reaction sequence to produce Neu5Ac. While high-pressure processes that operate semi-continuously already exist in the food industry, continuous reactors containing a high-performance liquid chromatography (HPLC) pump and a fixed-bed reactor at high pressure are still a relatively new concept. The use of a back pressure regulator up to 10 MPa (100 bar) was already demonstrated by Ötvös et al. [27] or reviewed by Plutschack et al. [28]. In the current work pressures up to 130 MPa were achieved by using an ultrahigh-performance liquid chromatography (UHPLC) pump.

Results and Discussion
Immobilization
For the biosynthesis of *N*-acetylneuraminic acid, two enzymes, the epimerase from *Pedobacter heparinus* and the aldolase from *Escherichia coli* K12 were produced in *E. coli* BL21(DE3). Both enzymes were purified and immobilized on different carriers to find for each enzyme the best choice for a stable and active enzyme preparation when applied under high pressure in continuous operation.

For screening purposes, six different carriers were used to immobilize the epimerase and aldolase (Table 1). The carriers differ in their properties (size, hydrophobicity, binding type, and porosity). The quality of immobilization was evaluated in terms of enzyme loading, activity, and reusability in repetitive batch experiments. Furthermore, the most suited carrier with immobilized enzyme was analyzed in long-term studies with respect to the stability of the enzyme preparation.

The enzymes were immobilized on six different carriers according to the instructions of the supplier (Lifetech Purolite, Ratingen, Germany). The loading was quantified by analyzing the protein concentration before and after immobilization using the Bradford assay for protein quantification [29]. Screening experiments showed that both enzymes were successfully immobilized on the carriers (Figure 2). For the immobilized epimerase, a maximal loading of 80 $mg_{enzyme}/g_{carrier}$ was achieved. Two carriers revealed lower yields with enzyme loadings of 30 and 40 $mg_{enzyme}/g_{carrier}$ (epoxy methacrylate, polymethacrylic DVB). The aldolase revealed the highest loadings with 80 $mg_{enzyme}/g_{carrier}$ for the amino methacrylate und macroporous styrene carrier. The other analyzed loadings of the
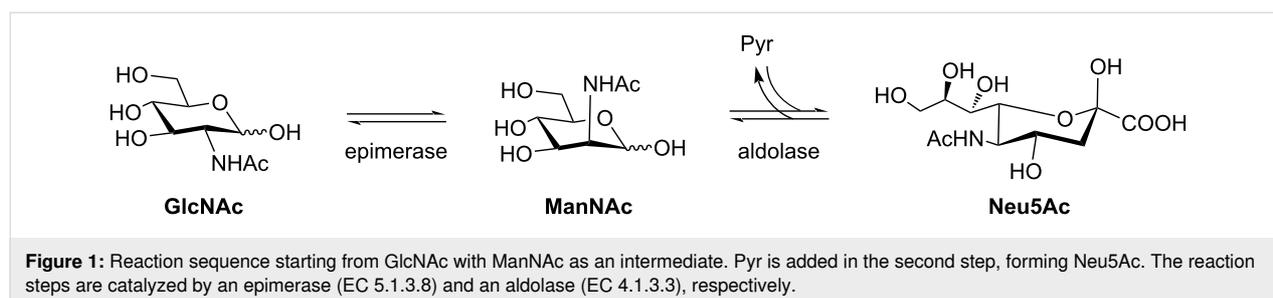
Figure 1: Reaction sequence starting from GlcNAc with ManNAc as an intermediate. Pyr is added in the second step, forming Neu5Ac. The reaction steps are catalyzed by an epimerase (EC 5.1.3.8) and an aldolase (EC 4.1.3.3), respectively.

Table 1: List of carriers used for the screening in this work (Lifetech Purolite).

Carrier	Functional group	Binding type	Hydrophobicity	Size [µm]	Pores [Å]
Lifetech ECR8309F amino methacrylate	amino	covalent	hydrophilic	150–300	600–1200
Lifetech ECR8204F epoxy methacrylate	epoxy	covalent	hydrophilic	150–300	300–600
Lifetech ECR8285 epoxy butyl methacrylate	epoxy	covalent	hydrophobic	250–1000	450–650
Lifetech ECR1030M polymethacrylic DVB	none	adsorption	middle	300–710	220–340
Lifetech ECR8806F octadecyl methacrylate	octadecyl	adsorption	hydrophobic	150–300	400–650
Lifetech ECR1090M macroporous styrene	none	adsorption	hydrophobic	300–710	200–300

Figure 2: Enzyme loading after immobilization of the epimerase and aldolase on different carriers.

Figure 3: Evaluation of immobilized epimerase on different carriers with respect to specific activity. Reaction conditions: 40 °C, pH 8, 100 mM Tris, $U_{shaking}$ = 1400 rpm, V = 1 mL, 100 mM GlcNAc, 1 mM ATP, 1 mM MgCl$_2$, immo epimerase 1% (w/v).
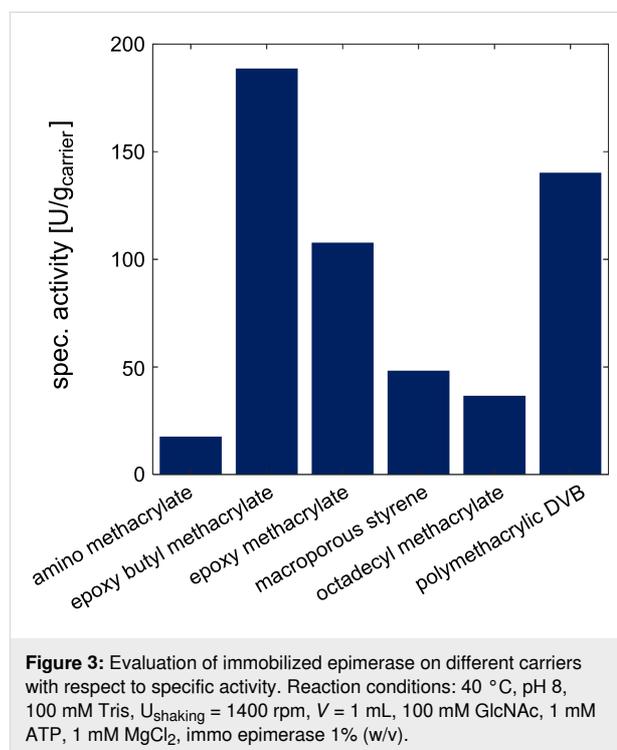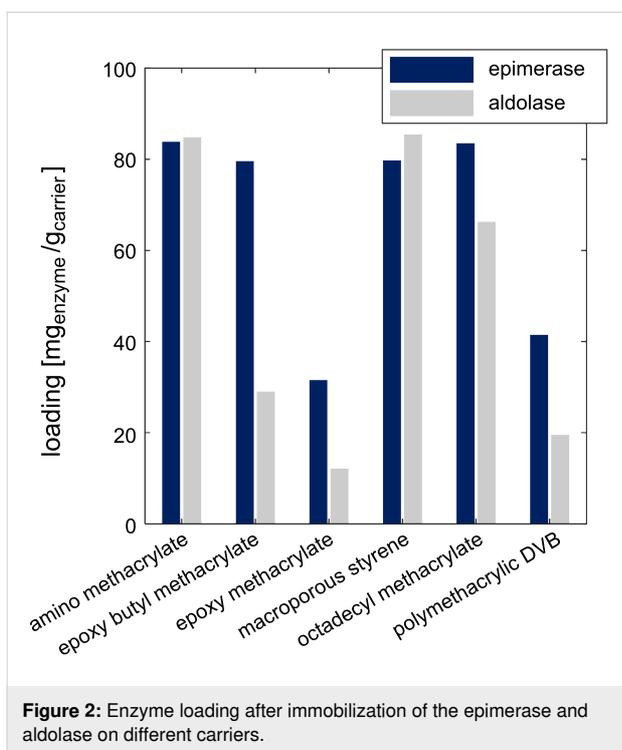
aldolase showed a lower yield of 70 mg$_{enzyme}$/g$_{carrier}$ (octadecyl methacrylate) and between 10–30 mg$_{enzyme}$/g$_{carrier}$ for the other evaluated carriers.

The activity of the immobilized enzymes was analyzed in small scale batch experiments with a reaction volume of 1 mL. The carrier was filtered and a defined amount of each carrier was weighed out for the reaction. After the addition of the substrate, samples were taken over the course of time and the specific activity was calculated (Figure 3 and Figure 4).

The product formation of the immobilized epimerase on amino methacrylate reveals the lowest calculated specific activity com-

pared to other utilized carriers with less than 20 U/g$_{carrier}$. The highest specific activity was achieved with two epoxy-functionalized carriers (epoxy butyl methacrylate and polymethacrylic DVB) with over 100 U/g$_{carrier}$. The aldolase reveals the highest activities immobilized on amino methacrylate with about 25 U/g$_{carrier}$. Compared to this, the results of all other specific activities were lower with less than 10 U/g$_{carrier}$. Here the epoxy butyl methacrylate and the macroporous styrene carrier reveal slightly more activity with more than 5 U/g$_{carrier}$ compared to the others with less than 5 U/g$_{carrier}$.

The selection of the most suitable carrier for the immobilization is important for the loading yield of the enzyme on the

Beilstein J. Org. Chem. **2022**, 18, 567–579.

Figure 4: Evaluation of immobilized aldolase on different carriers with respect to specific activity. Reaction conditions: 40 °C, pH 8, 100 mM Tris, $U_{shaking}$ = 1400 rpm, V = 1 mL, 100 mM *N*-acetyl-D-mannosamine, 250 mM pyruvate, immo aldolase 5% (w/v).

Figure 5: Relative activities in repetitive batch experiments of the immobilized epimerase on polymethacrylate DVB, epoxy methacrylate and epoxy butyl methacrylate. Reaction conditions: 40 °C, pH 8, 100 mM Tris, U_{shaker} = 1400 rpm, V = 1 mL, immo epimerase 1% (w/v), 100 mM *N*-acetyl-D-glucosamine, 1 mM ATP, 1 mM MgCl$_2$.

Figure 6: Relative activities in repetitive batch experiments of the immobilized aldolase on amino methacrylate, epoxy butyl methacrylate, and macroporous styrene. Reaction conditions: 40 °C, pH 8, 100 mM Tris, U_{shaker} = 1400 rpm, V = 1 mL, immo aldolase 5% (w/v), 100 mM *N*-acetyl-D-mannosamine, 250 mM pyruvate.

carrier and the yield of the activity. Both enzymes show the best performance on different materials (epimerase: epoxy butyl methacrylate and aldolase: amino methacrylate). The microenvironment and material surrounding the enzyme have a significant influence on the enzyme activity [30].

For reusability studies, the three most appropriate carriers were selected and analyzed with respect to the activity of the immobilized enzymes. Reusability was investigated by repetitive batch experiments with up to 5% (w/v) carrier, which is within a range of industrial application of immobilized enzymes in a batch mode [31]. The immobilized epimerase showed in the application in repetitive batches the slightest activity loss using the epoxy methacrylate carrier (Figure 5). For the other analyzed activities on the different carriers, the activity loss was much higher, 60% when using epoxy butyl methacrylate and 90% when polymethacrylate DVB was used.

The reusability of the immobilized aldolase was analyzed with amino methacrylate, epoxy butyl methacrylate, and macroporous styrene (Figure 6). All carriers show high suitability for repeated application with the highest loss of activity (35%) for the epoxy butyl methacrylate carrier and macroporous styrene carrier (25%).

Both enzymes showed a suitable reusability in the recycling study. Due to the measured activity, epoxy methacrylate was chosen as carrier for the epimerase and amino methacrylate for the aldolase. The immobilized enzymes were analyzed
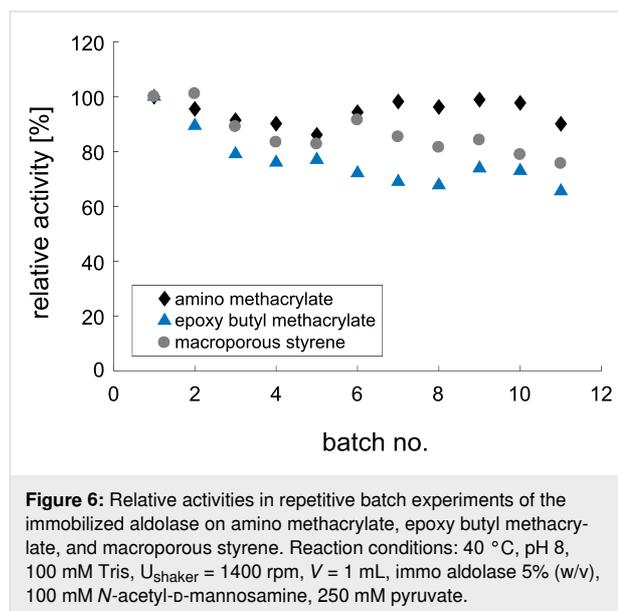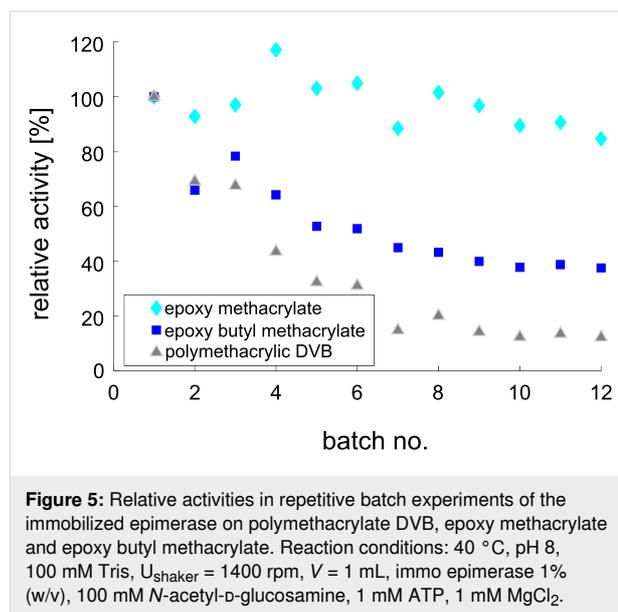
regarding their reusability over a large number of 50 repetitive batches (Figure 7) and for their stability under storage, and reaction conditions (Table 2).

After 50 repetitive batches, both enzymes show almost no loss of activity in the recycling study. The residual activity remains in a range around the initial activity, indicating a high robustness of the selected preparations (Figure 7). The high fluctuation of the relative activity values can be explained by the addition of several measurement errors. Besides the normal standard deviation, a number of other errors affect the results, such as the storage of the immobilized enzymes, the irregularity of carrier washing after the application, the removal of the buffer
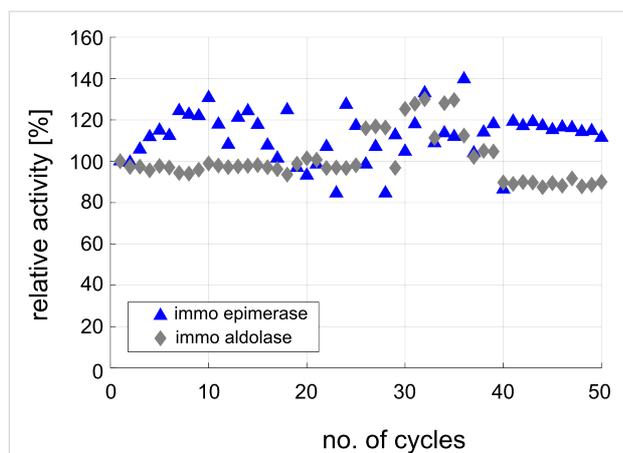
Figure 7: Recycling study of immobilized epimerase and aldolase. Assay conditions: 100 mM Tris, pH 8, 40 °C, shaking with 1000 rpm, V = 1 mL. Between the batches the carrier was washed with 100 mM Tris pH 8 and stored until the next application at 4 °C. Reaction conditions: (i) immo epimerase: 100 mM *N*-acetyl-D-glucosamine, 1 mM ATP, 1 mM MgCl$_2$, 10 g$_{carrier}$/L, loading: 37.6 mg$_{enzyme}$/g$_{carrier}$; (ii) immo aldolase: 100 mM *N*-acetyl-D-mannosamine, 250 mM pyruvate, 70 g$_{carrier}$/L, loading: 95.0 mg$_{enzyme}$/g$_{carrier}$.

Table 2: Storage, temperature, and mechanic stability of immobilized epimerase and aldolase.[a]

Conditions of stability experiment	immo epimerase $\tau_{1/2}$ [d]	immo aldolase $\tau_{1/2}$ [d]
6 °C, w/o buffer	87	>179[a]
6 °C, with buffer	>173[a]	>179[a]
40 °C, with buffer	39	58
40 °C, with buffer and shaking	32	46

[a]No significant loss of activity in the analyzed time of the long-term study.

before application, as well as the sample collection, and sample preparation for the analytics. For further analysis, long-term studies were carried out to analyze the stability in relation to different storage conditions such as the influence of moisture as well as temperature and mechanical stress. The stability of the immobilized enzymes during storage and application is an important criterion for the economic use of the enzyme. Therefore, immobilized enzyme aliquots were stored under four different conditions: filtered and cooled at 6 °C, with buffer at 6 °C, with buffer at 40 °C, and with buffer at 40 °C and shaking at 1000 rpm. During the storage period the activity was measured under standard activity conditions. By calculating of the residual activity, the stability was calculated by exponential fitting [32]. Due to inadequate correlation of the exponential fit to determine the deactivation, a half-life time could not be calculated for all stability tests. In these cases, the loss of activity was minor and a fit by deactivation was not possible. During

the experimental period the activity decreased by less than 50%. For the immobilized enzymes stored in buffer with cooling no significant loss of activity was observed during the investigated period of 179 days (immo aldolase) or 173 days (immo epimerase) (Table 2). For the immobilized aldolase, no difference in stability was detected during storage of the filtered carrier with residual moisture or the wet-stored carrier in buffer (>179 days). For the immobilized epimerase, a high loss of stability was observed up to a half-life of about 87 days without buffer, whereas the wet-stored carrier had a half-life of >173 days. The residual moisture of the carrier after filtration is also dependent on the pore sizes. The smaller pore sizes of the 300–600 nm carrier (ECR8204F), used for epimerase immobilization, may not ensure that the enzyme is surrounded by sufficient liquid for an extended storage period. As a result, the activity of the epimerase gets lost. In contrast, almost no loss of activity was observed for the carrier ECR8309F with larger pore sizes (600–1200 nm) that was used for the aldolase immobilization, suggesting that the residual content of moisture significantly influences the stability of the immobilized enzyme. The strongest influence on the stability is evoked by the heating of the immobilized enzymes. A reduction of the half-life time to 39 days or 58 days for the immobilized epimerase and aldolase, respectively, is observed when a continuous temperature exposure is applied. The mechanical stress of shaking the immobilized enzyme decreases the stability by about 20% compared to the reference study without shaking. From the stability investigations, it can be concluded that both selected enzyme preparations have adequate stability for the continuous application under high pressure.

Kinetics

Reaction kinetics were first measured for the immobilized epimerase. In the absence of inhibitors or backward reactions, the reaction rate can be modelled as a Michaelis–Menten rate expression. The Michaelis–Menten equation was used to fit the reaction rates at different substrate concentrations for different pressures in Figure 8. The resulting kinetic parameters are listed with 95% confidence intervals in Table 3.

The influence of pressure on the inhibition by pyruvate was measured and is shown in Figure 9.

The value for the inhibition constant is in the same order of magnitude as results of other groups, measured at ambient pressure (0.146 ± 0.019 mol/L [5]). Since the K_I value changes with pressure (Table 4), the concentrations were kept constant and only the pressure was varied, resulting in the reactions rates shown in Figure 10 (left). By rearranging the rate expression and inserting the previously calculated kinetic parameters, the inhibition constant was calculated (Figure 10 (right)).

Table 3: Kinetic parameters from experiments with immobilized epimerase.

Pressure [MPa][a]	K_M [mM][b]	a_{sp} [μmol/g$_{carrier}$/min][b]	v_{max} [mol/L/min][b]
1.6 ± 0.1	195 ± 26	1324 ± 77	0.37 ± 0.02
54 ± 3.8	208 ± 34	1400 ± 104	0.41 ± 0.03
110 ± 9.3	193 ± 93	1388 ± 47	0.39 ± 0.01

[a]The error given for pressure is the median average difference. [b]The error given for the kinetic parameters indicates the confidence interval (95%) in the regression.
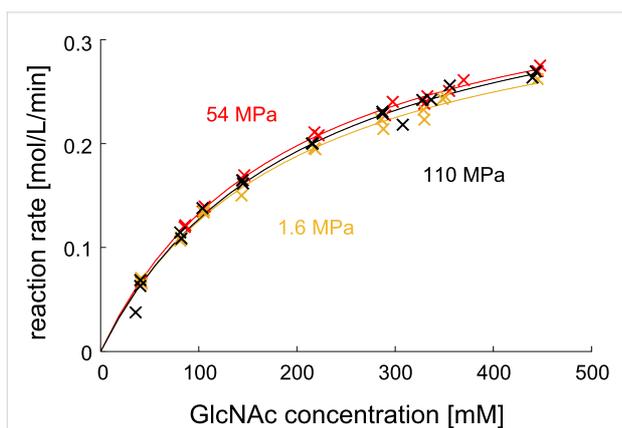

Figure 8: Measured reaction rates of the immobilized epimerase. The dashed line is the fit according to the Michaelis–Menten equation. Conditions: 40 °C, flow rates: 1.6 MPa at 2 mL/min, 54 MPa and 110 MPa at 1.8 mL/min, reactor volume: 0.21 mL, 10 mM potassium phosphate buffer 7.50, 1 mM ATP, 1 mM MgCl$_2$, 55 mg particles loaded with epimerase.
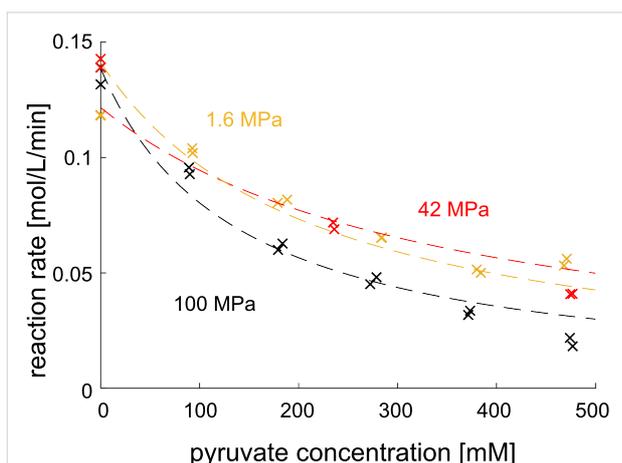

Figure 9: Measured reaction rate of the immobilized epimerase as a function of pyruvate and pressure. Dashed lines are fitted to a competitive inhibition model, 40 °C, volume flow: 2 mL/min, 440 mM GlcNAc, 100 mM buffer, 0.21 mL reactor volume, 2.25 min waited for steady state, 57 mg particles loaded with epimerase.

The change in molar volume introduced by the coupling of pyruvate to the enzyme was calculated by using the exponential fit. The calculated value is −12.9 ± 5.5 mL/mol (the values at

Table 4: Determined inhibition constant for pyruvate for the immobilized epimerase.

Pressure [MPa]	K_I [mM][a]
1.6	108 ± 21
42	67 ± 11
100	43 ± 10

[a]The error given for the kinetic parameter indicates the confidence interval (95%) in the regression.
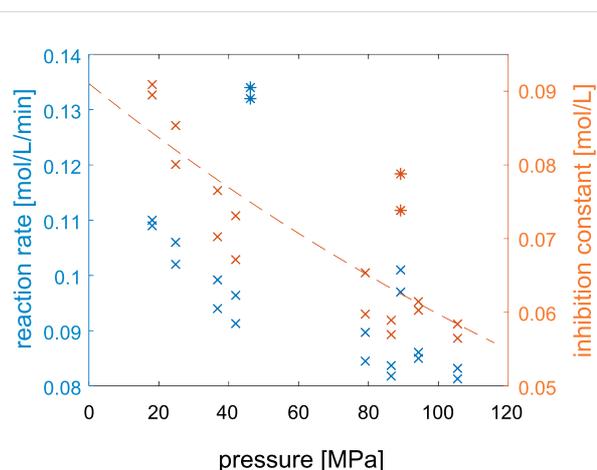
Figure 10: Measured reaction rate (left) and the determined inhibition constant by pyruvate (right) at different pressures. Conditions: 450 mM GlcNAc, 400 mM pyruvate, 2 mL/min, 40 °C, 0.21 mL reactor volume, 57 mg particles loaded with epimerase. Points determined as outliers are marked using asterisks.

50 MPa and 89 MPa were considered as outliers and not included in the calculation).

Kinetic studies of the immobilized aldolase show an increase in affinity of pyruvate towards the enzyme (Figure 11). The calculated K_M values are 91 ± 45 mM and 37 ± 10 mM at 2 MPa and 115 MPa, respectively. A volume change for the binding of pyruvate to the enzyme of 20 mL/mol was calculated from the change in the Michaelis–Menten constant. The calculated kinetic parameters are listed in Table 5. Since Neu5Ac is acidic,

Figure 11: Measured kinetics of the aldolase when varying the pyruvate and ManNAc concentration (given in mM) at different pressures. Reaction conditions: 40 °C, flow rate: 1.5–2 mL/min, reactor volume: 0.70 mL, 100 mM potassium phosphate buffer (pH 7.50), 179.80 mg particles loaded with aldolase. Immobilisate was pestled.

Table 5: Calculated kinetic parameters at ambient and high pressure. Rate expression adopted from Groher et al. [8].

Forward reactions	2 MPa	115 MPa
$a_{sp,max}$ [U/$g_{carrier}$]	650 ± 150	630 ± 130
$K_{M,ManNAc}$ [mM]	230 ± 110	320 ± 120
$K_{M,Pyr}$ [mM]	91 ± 45	37 ± 10
Backward reactions	2.5 MPa	93 MPa
$K_{M,Neu}$ [mM]	650 ± 300	365 ± 260
$a_{sp,max}$ [U/$g_{carrier}$]	743 ± 230	403 ± 170

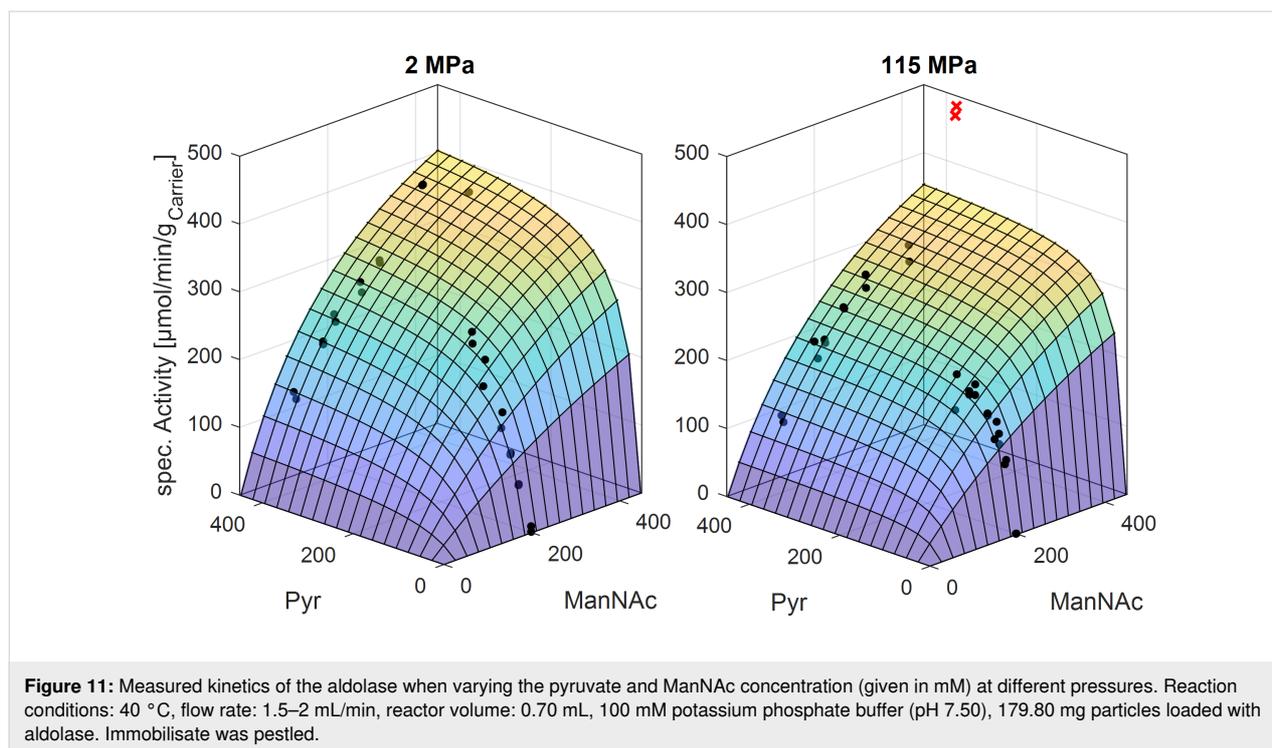200 mM buffer solution with the addition of K_2HPO_4 was used to neutralize the solution to pH 7.2. Using the Haldane relation, the calculated equilibrium constants were 27 L/mol and 48 L/mol at 2 MPa and 115 MPa, respectively.

Circulation reactor

If the position of the equilibrium is to be investigated, high residence times and small flow rates are needed. Since the pressure drop across a capillary depends on the flow rate, it was not possible to build up sufficient pressure when investigating the equilibrium. For this reason, the fixed-bed reactor was changed into a circular reactor (Figure 12). In this set-up the flow rate can be set (almost) freely to achieve the desired pressure (mixing time is affected when the flow rate is low).

Figure 12: Circular reactor, vessel mixing was achieved with a magnetic stirrer and samples were taken directly from the vessel.
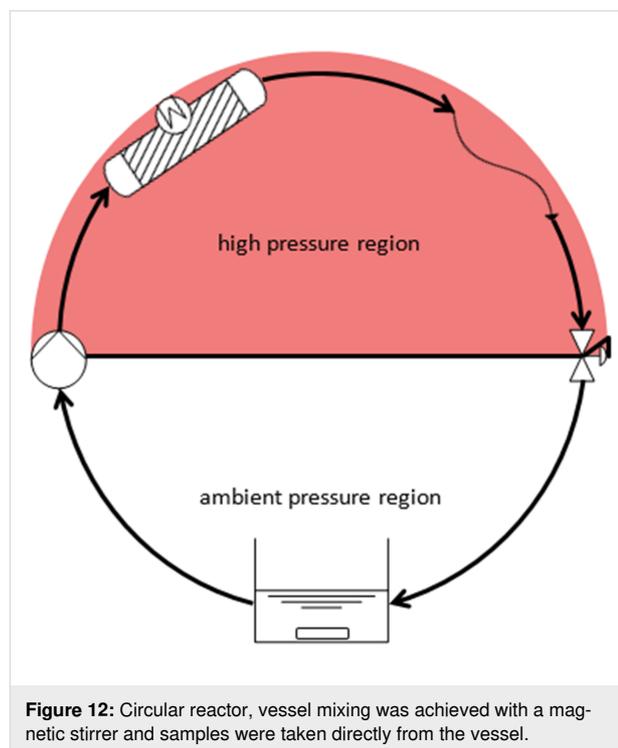
Position of equilibrium

The position of the equilibrium was determined using the circular reactor. The ratio of product and substrates was calculated for each sample and converged to the equilibrium constant under the given conditions.

Figure 13: Aldolase: Change of the equilibrium constant at different pressures. Starting concentrations were varied: 100 mM with 250 mM and 100 mM with 100 mM of ManNAc and pyruvate, respectively. Conditions: 41 °C, reaction time at least 12 h, total working volume 4 mL, flow rate 1.5 mL/min, 272.3 mg particles loaded with aldolase. The used regression is an exponential fit according to Equation 5.

The equilibrium constant for the first reaction (one-to-one) was insensitive to pressure. For the second reaction (aldolase), the calculated equilibrium constant is shown in Figure 13. Since this reaction step is a two-to-one-reaction, a reduction in molar volume was expected, resulting in a positive influence of pressure (principle of Le Chatelier). The change in volume was calculated as −16.0 ± 1.2 mL/mol.

Both immobilisates were added into one reactor and GlcNAc and Pyr were added as substrates to produce Neu5Ac. The resulting progress curve is shown in Figure 14. In order to measure changes in concentration with a high resolution, a high working volume was selected and the enzyme concentrations were reduced, leading to a slower conversion. Pressure was then varied, resulting in a change in substrate and product concentration, indicating that the system was sensitive to pressure.
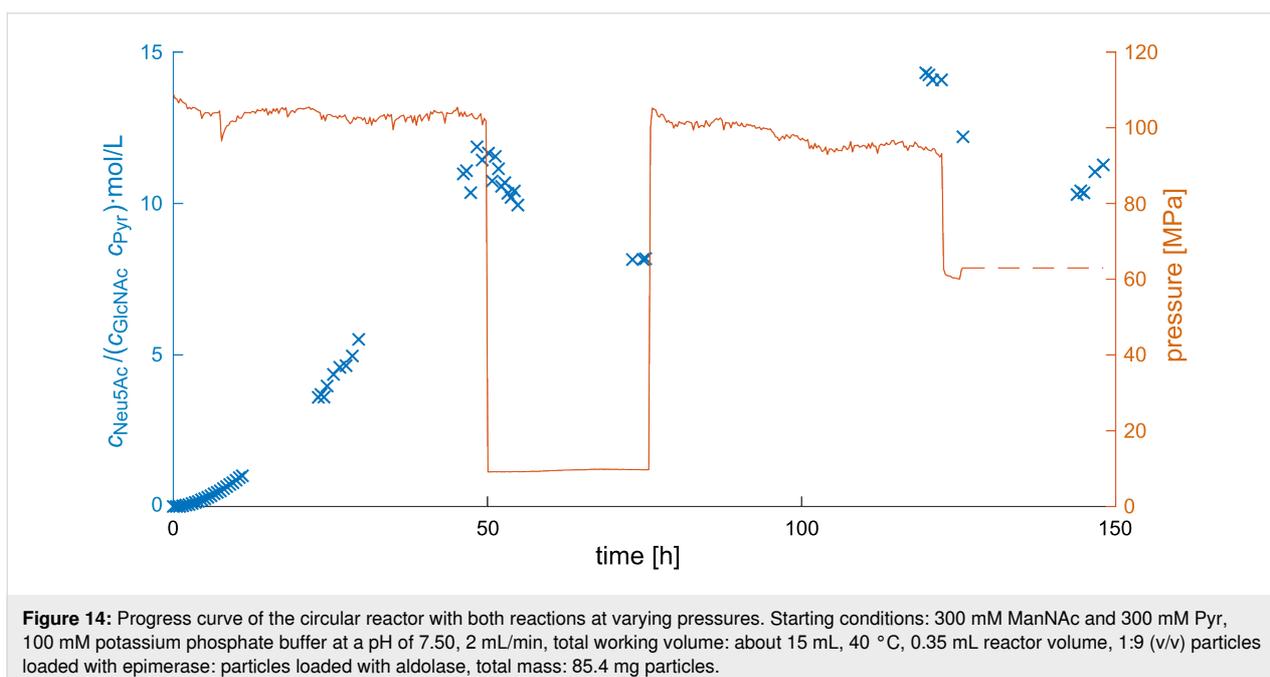
Figure 14 shows the two advantages of the high-pressure circular reactor over a pressurized batch reactor: First, samples can be taken without the use of special pressure valves. Second, the pressure can be changed while the reaction is ongoing. If pressure is only changed up to 30 MPa, the operation can continue. If larger changes in pressure are required, the pump can be shut down, capillaries added or removed and the pump turned on again, resulting in a minimal downtime.

The combined reaction was, like the aldolase reaction, positively influenced by pressure. This was shown by the ratio of product to substrates (with the equilibrium constant K as the asymptote), as well as conversion, selectivity, and yield (Table 6). While the conversion, selectivity, and yield depend on the ratio

Table 6: Changes in conversion, selectivity, and yield at different pressures.

Pressure [MPa]	Conversion [%]	Selectivity [%]	Yield [%]
9.6	57.9	81.9	47.4
60.8	60.4	82.7	50.0
95.0	63.9	84.7	54.1

[a]Same reaction conditions as in Figure 14.

Figure 14: Progress curve of the circular reactor with both reactions at varying pressures. Starting conditions: 300 mM ManNAc and 300 mM Pyr, 100 mM potassium phosphate buffer at a pH of 7.50, 2 mL/min, total working volume: about 15 mL, 40 °C, 0.35 mL reactor volume, 1:9 (v/v) particles loaded with epimerase: particles loaded with aldolase, total mass: 85.4 mg particles.

of substrates, the equilibrium constant can also be used for other ratios.

Conclusion

An epimerase and an aldolase were investigated to continuously produce *N*-acetylneuraminic acid under high pressure. Both enzymes were successfully immobilized with high stability and used to catalyze a reaction starting from *N*-acetyl-D-glucosamine and pyruvate. In addition, pressure up to 130 MPa was used to increase the conversion by 6.0%, the selectivity by 2.8%, and the yield by 6.7% (from 57.9% to 63.9%, 81.9% to 84.7%, and 47.4% to 54.1%, respectively). The increase in the value of the equilibrium constant with pressure suggests a reduction in molar volume. The circular reactor setup allowed for easy sampling and enabled the analysis of the resulting progress curve. The findings for the epimerase indicate that some inconspicuous reactions, such as the inhibition by pyruvate, can be influenced by pressure. In both reactions pyruvate showed increased affinity towards the investigated enzymes. Given the metabolic importance of pyruvate [33-35], it may be of interest to test different pyruvate converting enzymes if this trend is confirmed.

Experimental
Methodology
Genes and expression strains

The gene of the epimerase (*N*-acyl-D-glucosamine 2-epimerase, EC 5.1.3.8) from *Pedobacter heparinus* was ordered as codon optimized gBlocks gene fragment (Integrated DNA Technologies, Leuven, Belgium). The gene for the aldolase (*N*-acetylneuraminate lyase, EC 4.1.3.3) was amplified from the genomic DNA of *Escherichia coli* K12. The genes of the enzymes were cloned into the expression vector pETDuet-1™ (Novagen®, Merck KGaA, Darmstadt, Germany). For expression *E. coli* BL21 (DE3) strains were used.

Enzyme immobilization

For analysis of enzyme immobilization, six different carriers with different properties of a screening kit were used (ECRKIT1, Purolite Lifetech, Duisburg, Germany). Three carriers that bind the enzyme through absorption (ECR1030M, ECR8806F, ECR1090M), two carriers with epoxy functional groups for covalent immobilization (ECR8204F, ECR8806F), and one amino-functionalized carrier for covalent immobilization (ECR8309F). For all immobilizations, a 20 mM sodium phosphate buffer with a pH of 7.4 was used as immobilization buffer. All filtration steps were executed using a membrane pump (Membrane pump ME 2C NT, Vacuubrandt GMBH & Co. KG, Wertheim, Germany) with bottle topper filter (Nalgene™, Thermo Fisher Scientific GmbH, Schwerte, Germany), and membrane filters (3 µm) (Sartorius AG,

Göttingen, Germany). The carriers were equilibrated with immobilization buffer at a carrier to buffer ratio of 1:1 (w/v). For the amino methacrylate carrier (ECR8309F), a further step of activation was performed with 2% glutaraldehyde solution 1:4 (w/v). After addition of the 2% glutaraldehyde solution, the mixture was incubated for 1 h at room temperature under slow rotation at 8 rpm using a sample mixer (MXIC1 sample mixer, Dynal Biotech Ltd., Bromborough, UK). Afterwards, the activated carrier was filtered and carefully washed with immobilization buffer. For immobilization, the buffer of purified enzymes (150 mM imidazol, 300 mM NaCl, 50 mM sodium phosphate buffer pH 7.4) was exchanged to the immobilization buffer using ultracentrifuge units with 10 kDa Cut-off (Sartorius Vivaspin™, Göttingen, Germany). The unbuffered enzymes were mixed with the different carriers (epimerase: 89.5 mg$_{enzyme}$/g$_{carrier}$, aldolase: 83.9 mg$_{enzyme}$/g$_{carrier}$) and incubated at 25 °C under slow rotation at 8 rpm using a sample mixer (MXIC1 sample mixer, Dynal Biotech Ltd., Bromborough, UK). After 18 h the rotation of the immobilization with the epoxide-functionalized carrier (ECR8204F, ECR8806F) was stopped and incubated for further 20 h at 25 °C. The immobilization process for the other carrier was stopped after 18 h (ECR8309F) and 24 h (ECR1030M, ECR8806F, ECR1090M). The carriers with immobilized enzymes were filtered and the filtrate was collected for protein quantification. Afterwards, the carriers were washed twice with immobilization buffer containing 0.5 M NaCl 1:1 (w/v) and three times with immobilization buffer 1:1 (w/v). They were stored afterwards refrigerated at 6 °C.

Activity assays

To compare the activities of both enzymes, a standard activity assay was used for the free and immobilized enzymes. For the epimerase, the reaction conditions were 100 mM Tris, pH 8, 40 °C, 100 mM *N*-acetyl-D-glucosamine, 1 mM adenosine triphosphate, 1 mM MgCl$_2$, and 10 g/L immobilized enzyme or 2.5 mg/L free enzyme, respectively. For the aldolase, the reaction conditions were 100 mM Tris, pH 8, 40 °C, 100 mM *N*-acetyl-D-mannosamine, 250 mM pyruvate, and 50 g/L immobilized enzyme or 100 mg/L free enzyme, respectively.

Repetitive batch study

Reusability was analyzed in 2 mL micro reaction tubes, using 10 mg immobilized epimerase (in triplicate) or 70 mg immobilized aldolase (in duplicate), respectively. The reactions were started by adding 1 mL substrate solution, run for 30 min, and analyzed for product formation. Afterwards, the remaining substrate was removed, and the carriers were washed twice with 100 mM Tris pH 8, and used for the next cycle or stored at 6 °C for the next experiment. For each enzyme, 50 repetitive batches were analyzed.

Stability study

For stability investigations, samples (10 mg immobilized epimerase or 50 mg immobilized aldolase) in 2 mL micro reaction tubes were stored under four different conditions: Storage with residual moisture (immobilized enzyme after filtration under vacuum) at 6 °C. Storage in 20 mM sodium phosphate buffer, pH 7.5 at 6 °C and 40 °C, respectively and storage at 40 °C while shaking at 1000 rpm. Enzyme activity was measured at regular intervals over the storage period. For each measuring point, the initial activity was analyzed using a standard activity assay.

High-performance liquid chromatography (HPLC)

For quantification of the product *N*-acetylneuraminic acid, an Agilent HPLC system connected with a variable wavelength detector at 210 nm was used. Separation was realized with a Nucleogel Sugar 810H column (Macherey Nagel, Düren, Germany). The injection was set to 10 µL and compounds were eluted with an isocratic flow of 0.1% phosphoric acid at 30 °C. The retention order was *N*-acetylneuraminic acid (8.1 min), pyruvate (9.5 min), and *N*-acetylglucosamine (11.1 min).

Enzymatic quantification of *N*-acetyl-ᴅ-mannosamine

The quantification of ManNAc for the epimerase activity was realized with an enzymatic quantification assay as described in Klermund et al. using *N*-acylmannosamine 1-dehydrogenase (ManDH, EC. 1.1.1.233) [36]. The assay was performed in 100 mM Tris-HCl pH 8 containing up to 0.2 mM ManNAc, 2 mM NAD, and 0.05 mL ManDH solution with 3 kU/mL. After starting the reaction, the mixture was incubated at room temperature for 30 minutes. The resulting NADH concentration was measured with an Eppendorf spectrophotometer at 340 nm.

High-pressure set-up

An HPLC pump (Nexera X2 LC-30AD) by Shimadzu Deutschland (Duisburg, Germany) was used in order to generate a steady flow. All given pressures were measured by the pump. For the reactor, an emptied UHPLC column (length 50 mm, ID 3 mm) by ISERA GmbH (Düren, Germany) was filled with immobilized enzymes and pressure was built up via capillaries with a smaller inner diameter (50 µm).

If the position of the equilibrium was investigated, high residence times were required, resulting in low flow rates and pressure built-up. To circumvent this bottle neck, a circular reactor was designed. A flow rate can be chosen in order to achieve the desired pressure (usually 1.7–2 mL/min). Another advantage is the reduction of film diffusion on the carriers.

A key advantage of this setup is that sampling and reaction at high pressure can occur simultaneously and progress curves can be measured in one reactor. Prior publications investigating high-pressure batch reactors required to conduct several experiments and stop the reaction at different times [22,37]. Moreover, the circular reactor allows for a change in pressure via the back pressure regulator. A magnetic stirrer was used to mix the fluid in a vessel from which the pump draws its feed.

Chemicals

All compounds were ordered from Biosynth Carbosynth (United Kingdom) and used without further purification. Buffer preparation: potassium phosphate buffer: 5.3 mL of 0.2 M potassium dihydrogenphosphate (KH_2PO_4) with 94.7 mL of 0.2 M potassium hydrogenphosphate (K_2HPO_4) in 100 mL water resulting in 200 mL of 100 mM solution. The pH was measured and afterwards adjusted to pH 7.50 or 8.00 by adding more potassium dihydrogen- or monohydrogenphophate solution. 1 M Tris buffer: 121.14 g tris(hydroxymethyl)aminomethane was dissolved in 800 mL H_2O, the volume was filled up to 1 L with H_2O, and the pH value adjusted with HCl.

Analytics

For HPLC analysis the method according to Zimmermann [5] was used as a starting point, resulting in the use of a Eurocat H type (KNAUER Wissenschaftliche Geräte GmbH (Berlin, Germany)) in an HPLC system (0.8 mL/min, column temperature 65 °C, 55 °C for refraction index, 5 mM H_2SO_4 as eluent). The retention order was *N*-acetylneuraminic acid (14 min), pyruvate (15.5 min), *N*-acetyl-ᴅ-mannosamine (19 min), and *N*-acetyl-ᴅ-glucosamine (20 min).

Enzymatic bed

The packing of the enzymatic bed was achieved via sedimentation of the particles. First, the reactor was filled with buffer solution. Then, a slurry of particles was prepared in buffer solution (10 or 100 mM KP$_i$ buffer at pH 7.5) and taken up using a syringe. The syringe was then placed on top of the reactor forming a water bridge and allowing the particles to sediment. Once the reactor was filled, it was shaken to allow the bed to settle and refilled, if needed. Once the bed was packed, buffer solution was pumped through to compress the material. The reactor was then opened and new particles were added until the whole space was occupied.

Residence time distribution

In order to verify that this method yields similar packed beds, the residence time distribution (RTD) was measured and compared. The pump, autosampler, and refraction index (RI) detector were used to measure the RDT (HPLC 1100er Series by Agilent). Five µL of a 10 mM buffer were used as a tracer

with an injection rate of 1 mL/min, resulting in a rapid injection. The flow rate was set to 0.1, 0.35, and 0.5 mL/min. The RI was used to measure the refraction approximately twice a second.

The tracer was injected via an autosampler and measured using a RI detector (KNAUER Wissenschaftliche Geräte GmbH, Berlin, Germany). At a flow rate of 0.35 mL/min, a mean residence time of 1.5 ± 0.01 min was calculated. The mean residence time of the system itself needs to be considered and was determined to be 0.801 ± 0.003 min.

The residence time distribution of the reactor was calculated assuming that the cumulative distributions are additive with respect to time. The obtained distribution of the reactor was convoluted with the distribution of the system and a result similar to the measured distribution of both was obtained (Figure 15).

The mean residence time was 0.7 min (as opposed to 1 min, obtained by dividing the whole reactor volume by the flow rate) when particles with the original size distribution were used. Since the diameter of the original particles is 0.5 mm and the inner diameter of the reactor is only 3 mm, wall effects occur [38,39].

When pestled particles were used, the mean residence time was 0.66 min by pumping 0.21 mL/min through a reactor volume of 0.21 mL. When using pestled particles, the residence time distribution is assumed to be narrow because the residence time distribution (RTD) of the system and of the whole setup are

similar in shape and just shifted in time. Integration was conducted using Matlab 2017a and 2018a using the trapz function. The given values for τ do not account for the porosity of the packed bed. They are calculated via Equation 1

$$\tau = \frac{V}{\dot{V}},\tag{1}$$

with V as the volume of the empty reactor and $\dot{V}$ as the volumetric flow rate.

Kinetics

To investigate the influence of pressure on the selected reaction, a continuously operated fixed-bed reactor filled with immobilized enzyme was used (Figure 16). By setting a high flow rate, the determination of the reaction rate is possible via initial rate measurement. The pressure was built up using capillaries with small inner diameters (25 μm and 50 μm according to the law of Hagen–Poiseuille [40]).
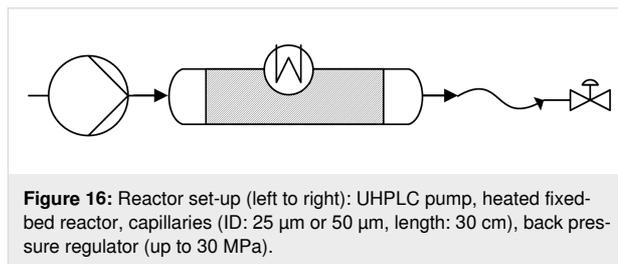

Figure 16: Reactor set-up (left to right): UHPLC pump, heated fixed-bed reactor, capillaries (ID: 25 μm or 50 μm, length: 30 cm), back pressure regulator (up to 30 MPa).

The fixed bed reactor was utilized to investigate the reaction kinetics. The RDT of the fixed bed reactor was calculated
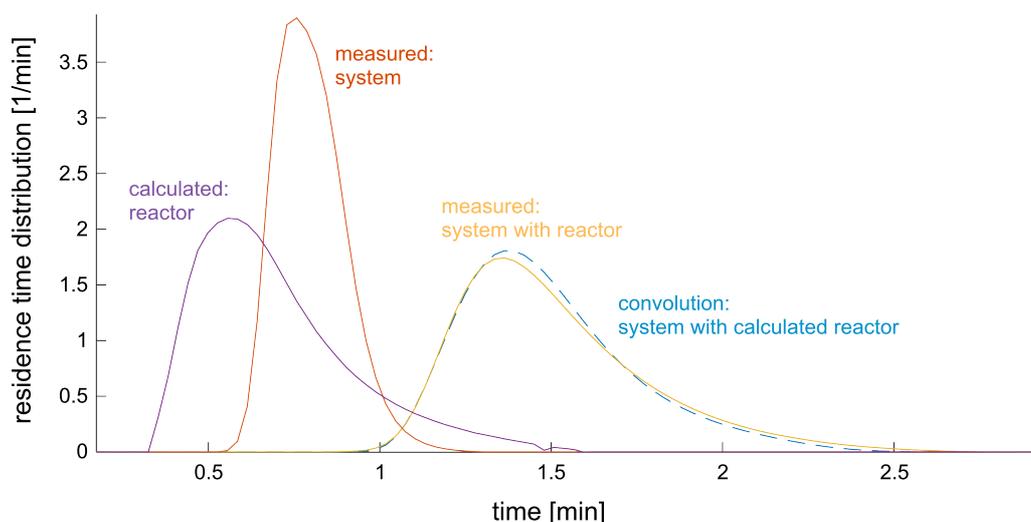

Figure 15: Residence time distributions of the stand-alone system and the reactor integrated into the system. Flow rate: 0.35 mL/min, reactor volume: 0.35 mL, filled with 74 to 80 mg of particles, 5 μL of 10 mM potassium phosphate buffer was used as tracer and injected with a speed of 1 mL/min.

following Equation 2 and used to calculate the mean residence time according to Equation 3.

$$E(t) = \frac{S(t)}{\int S(t)\,dt}, \qquad (2)$$

$$\bar{t} = \int t \cdot E(t)\,dt, \qquad (3)$$

with E as the residence time distribution, S as the signal, and $\bar{t}$ as the mean residence time.

The RDT was measured by placing the reactor into an HPLC, replacing the regular separation column. Hereby, the mean residence time of the reactor was calculated to be 66% of the quotient of reactor volume and flow rate.

When kinetic parameters were calculated by regression, the error given corresponds to the 95% confidence interval. All particles were pestled to remove potential diffusion limitations. All experiments were conducted at 40 °C and in potassium phosphate buffer. Since the pump is intended for UHPLC applications, a mixing chamber was installed for up to four eluents. In this study, the mixing chamber was used to change the concentration of the substrate to measure the reaction rate. A UV detector was used to ensure the homogeneity of the fluid generated by the mixing chamber. The order of concentrations was randomized to avoid systematic carry over to the next experiment.

The reaction rate (v) was calculated according to Equation 4, using the product concentration (c_{ManAc}), the hydraulic residence time (τ), and the volume fraction (f_V).

$$v = \frac{c_{ManAc}}{f_V \cdot \tau} \qquad (4)$$

The volume fraction was determined to be 0.66 for pestled particles (as shown in the section about residence time distribution).

Equilibrium

Equation 5 describes the relationship between the equilibrium constant, change in molar volume, and pressure and was already applied in high-pressure investigations of enzymes [41]:

$$K(p) = K(0\ \text{MPa}) \cdot \exp\left\{-\frac{\Delta V}{RT} \cdot p\right\}, \qquad (5)$$

with K as the equilibrium constant, ΔV as the change in molar volume, R as the ideal gas constant, T as temperature, and p as pressure. Equation 5 was also used for the pressure dependency of the inhibition constant.

Conversion is calculated according to Equation 6 via a closed mass balance with $c_{GlcNAc}(0) = c_{GlcNAc}(t) + c_{ManNAc}(t)$,

$$X(t) = \frac{c_{ManNAc}(t)}{c_{GlcNAc}(t) + c_{ManNAc}(t)}. \qquad (6)$$

For a reaction with different products or a sequence of reactions, selectivity is calculated using the product concentration following Equation 7:

$$S(t) = \frac{c_{Neu5Ac}(t)}{c_{ManNAc}(t) + c_{Neu5Ac}(t)}. \qquad (7)$$

Acknowledgements

Funding

ORCID® iDs

Jannis A. Reich - https://orcid.org/0000-0002-6374-6630
Miriam Aßmann - https://orcid.org/0000-0002-1660-5253
Andreas Liese - https://orcid.org/0000-0002-4867-9935

Preprint

A non-peer-reviewed version of this article has been previously published as a preprint: https://doi.org/10.3762/bxiv.2022.11.v1

References

1. Varki, A. *Trends Mol. Med.* **2008,** *14,* 351–360.
   doi:10.1016/j.molmed.2008.06.002
2. Altalhi, T. A.; Alswat, K.; Alsanie, W. F.; Ibrahim, M. M.; Aldalbahi, A.;
   El-Sheshtawy, H. S. *J. Mol. Struct.* **2021,** *1228,* 129459.
   doi:10.1016/j.molstruc.2020.129459
3. Maru, I.; Ohnishi, J.; Ohta, Y.; Tsukada, Y. *J. Biosci. Bioeng.* **2002,** *93,*
   258–265. doi:10.1016/s1389-1723(02)80026-3
4. Kragl, U. *Reaktionstechnik biokatalytischer Prozesse am Beispiel der
   kontinuierlichen enzymatischen Synthese von N-Acetylneuraminsäure;*
   Forschungszentrum Jülich: Jülich, Germany, 1992.

5. Zimmermann, V.; Hennemann, H.-G.; Daußmann, T.; Kragl, U. *Appl. Microbiol. Biotechnol.* **2007,** *76,* 597–605. doi:10.1007/s00253-007-1033-6

6. Lakdawala, S. S.; Jayaraman, A.; Halpin, R. A.; Lamirande, E. W.; Shih, A. R.; Stockwell, T. B.; Lin, X.; Simenauer, A.; Hanson, C. T.; Vogel, L.; Paskel, M.; Minai, M.; Moore, I.; Orandle, M.; Das, S. R.; Wentworth, D. E.; Sasisekharan, R.; Subbarao, K. *Nature* **2015,** *526,* 122–125. doi:10.1038/nature15379

7. Zhu, W.; Chen, X.; Yuan, L.; Wu, J.; Yao, J. *Molecules* **2020,** *25,* 5141. doi:10.3390/molecules25215141

8. Groher, A.; Hoelsch, K. *J. Mol. Catal. B: Enzym.* **2012,** *83,* 1–7. doi:10.1016/j.molcatb.2012.05.016

9. Lin, B.-X.; Zhang, Z.-J.; Liu, W.-F.; Dong, Z.-Y.; Tao, Y. *Appl. Microbiol. Biotechnol.* **2013,** *97,* 4775–4784. doi:10.1007/s00253-013-4754-8

10. Jennewein Biotechnologie GmbH. Fermentative production of N-acetylneuraminic acid. Eur. Pat. Appl. EP3473644A1, April 24, 2019.

11. Zhu, D.; Zhan, X.; Wu, J.; Gao, M.; Zhao, Z. *Biotechnol. Lett.* **2017,** *39,* 55–63. doi:10.1007/s10529-016-2215-z

12. Abu, R.; Woodley, J. M. *ChemCatChem* **2015,** *7,* 3094–3105. doi:10.1002/cctc.201500603

13. Hussain, M. I.; Zhang, X.; Lv, X.; Basharat, S.; Shahbaz, U.; Li, J.; Du, G.; Liu, L.; Liu, Y. *Syst. Microbiol. Biomanuf.* **2022,** *2,* 130–146. doi:10.1007/s43393-021-00050-y

14. Atkins, P. W.; de Paula, J. *Physikalische Chemie,* 8th ed.; Wiley-VCH: Weinheim, Germany, 2006.

15. Eisenmenger, M. J.; Reyes-De-Corcuera, J. I. *Enzyme Microb. Technol.* **2009,** *45,* 331–347. doi:10.1016/j.enzmictec.2009.08.001

16. Kitahara, R.; Oyama, K.; Kawamura, T.; Mitsuhashi, K.; Kitazawa, S.; Yasunaga, K.; Sagara, N.; Fujimoto, M.; Terauchi, K. *Sci. Rep.* **2019,** *9,* 12395. doi:10.1038/s41598-019-48693-1

17. Luong, T. Q.; Erwin, N.; Neumann, M.; Schmidt, A.; Loos, C.; Schmidt, V.; Fändrich, M.; Winter, R. *Angew. Chem., Int. Ed.* **2016,** *55,* 12412–12416. doi:10.1002/anie.201605715

18. Eyring, H.; Magee, J. L. *J. Cell. Comp. Physiol.* **1942,** *20,* 169–177. doi:10.1002/jcp.1030200205

19. Berheide, M.; Peper, S.; Kara, S.; Long, W. S.; Schenkel, S.; Pohl, M.; Niemeyer, B.; Liese, A. *Biotechnol. Bioeng.* **2010,** *106,* 18–26. doi:10.1002/bit.22650

20. Kaushik, N.; Rao, P. S.; Mishra, H. N. *Food Res. Int.* **2017,** *100,* 885–893. doi:10.1016/j.foodres.2017.07.056

21. Lomelí-Martín, A.; Martínez, L. M.; Welti-Chanes, J.; Escobedo-Avellaneda, Z. *Foods* **2021,** *10,* 878. doi:10.3390/foods10040878

22. Hackbusch, S.; Noirungsee, N.; Viamonte, J.; Sun, X.; Bubenheim, P.; Kostka, J. E.; Müller, R.; Liese, A. *Mar. Pollut. Bull.* **2020,** *150,* 110683. doi:10.1016/j.marpolbul.2019.110683

23. Shkolnikov, H.; Belochvostov, V.; Okun, Z.; Shpigelman, A. *Innovative Food Sci. Emerging Technol.* **2020,** *59,* 102273. doi:10.1016/j.ifset.2019.102273

24. Gambacorta, G.; Sharley, J. S.; Baxendale, I. R. *Beilstein J. Org. Chem.* **2021,** *17,* 1181–1312. doi:10.3762/bjoc.17.90

25. Elliott, M.; Makatsoris, H. *Chim. Oggi* **2020,** *38* (3), 8–9.

26. Vilé, G.; Amann, F.; Bourne, S.; Elliott, M.; Wiles, C.; Houldsworth, S.; Vizza, A.; Gemoets, H.; Ramakrishnan, S.; Bandichhor, R.; Kaaden, A.; Heck, J.; Noel, T.; Nonnenmacher, M.; Loureiro, R.; Kirschneck, D.; Ni, X.-W.; Lovett, D.; Khinast, J.; Dubay, B.; Dapremont, O.; Muldowney, M. *Chim. Oggi* **2020,** *38* (3), 14–30.

27. Ötvös, S. B.; Georgiádes, Á.; Mándity, I. M.; Kiss, L.; Fülöp, F. *Beilstein J. Org. Chem.* **2013,** *9,* 1508–1516. doi:10.3762/bjoc.9.172

28. Plutschack, M. B.; Pieber, B.; Gilmore, K.; Seeberger, P. H. *Chem. Rev.* **2017,** *117,* 11796–11893. doi:10.1021/acs.chemrev.7b00183

29. Bradford, M. M. *Anal. Biochem.* **1976,** *72,* 248–254. doi:10.1006/abio.1976.9999

30. Bolivar, J. M.; Nidetzky, B. *Molecules* **2019,** *24,* 3460. doi:10.3390/molecules24193460

31. Basso, A.; Serban, S. *Mol. Catal.* **2019,** *479,* 110607. doi:10.1016/j.mcat.2019.110607

32. Liese, A.; Hilterhaus, L. *Chem. Soc. Rev.* **2013,** *42,* 6236–6249. doi:10.1039/c3cs35511j

33. Tonin, F.; Arends, I. W. C. E. *Beilstein J. Org. Chem.* **2018,** *14,* 470–483. doi:10.3762/bjoc.14.33

34. Menefee, A. L.; Zeczycki, T. N. *FEBS J.* **2014,** *281,* 1333–1354. doi:10.1111/febs.12713

35. Baik, S. H.; Kang, C.; Jeon, I. C.; Yun, S. E. *Biotechnol. Tech.* **1999,** *13,* 1–5. doi:10.1023/a:1008865212773

36. Klermund, L.; Riederer, A.; Hunger, A.; Castiglione, K. *Enzyme Microb. Technol.* **2016,** *87–88,* 70–78. doi:10.1016/j.enzmictec.2016.04.006

37. Schedler, M.; Hiessl, R.; Valladares Juárez, A. G.; Gust, G.; Müller, R. *AMB Express* **2014,** *4,* 77. doi:10.1186/s13568-014-0077-0

38. Dixon, A. G.; Nijemeisland, M. *Ind. Eng. Chem. Res.* **2001,** *40,* 5246–5254. doi:10.1021/ie001035a

39. Preller, A. C. N. Numerical modelling of flow through packed beds of uniform spheres. Ph.D. Thesis, North-West University, Potchefstroom, South Africa, 2011.

40. Sutera, S. P.; Skalak, R. *Annu. Rev. Fluid Mech.* **1993,** *25,* 1–20. doi:10.1146/annurev.fl.25.010193.000245

41. Bruins, M. E.; Janssen, A. E. M.; Boom, R. M. *J. Mol. Catal. B: Enzym.* **2006,** *39,* 124–127. doi:10.1016/j.molcatb.2006.01.033

Rapid gas–liquid reaction in flow. Continuous synthesis and production of cyclohexene oxide

Kyoko Mandai[1,2], Tetsuya Yamamoto[1], Hiroki Mandai[2] and Aiichiro Nagaki[*1]

Abstract

The enhanced reaction rate in the epoxidation of cyclohexene with air as an oxidant was discovered without any added catalyst utilizing a continuous flow reactor constructed with readily available stainless steel parts and devices. This continuous-flow process demonstrates a significant improvement in reaction time for highly selective epoxide production over the batch process due to the efficient mass transfer between the liquid phase and air. The flow process discovered was operated continuously with good operational stability, evaluated by a constant high yield of cyclohexene oxide, to obtain the desired product with high productivity.

Introduction

From the past to the present, organic synthesis has contributed to the development of science and technology. With the rapid advances in the 21st century, increasing demand for organic synthesis has led to a strong need for faster and more sophisticated methods.

The gas–liquid reaction is one of the organic synthetic methods of importance because gases are one of the promising reagents concerning environmental aspects. Demands for the use of gases for constructing various functional organic materials should be increased if a reliable and powerful technique for gas-liquid reaction is established. In a conventional batch process, a faster reaction with good efficiency should be pursued either by

pressurizing the reaction system filled with gas using an autoclave or by introducing gas into the reaction mixture with bubbling [1]. Thinking about the implementation of gas–liquid reactions, especially at the industrial manufacturing level, the conventional batch technique has irreconcilable limitations.

Cyclohexene oxide is one of the key starting materials for manufacturing various functional organic compounds and materials such as polymers and chiral organic compounds with cyclohexane moiety [2-6]. Thus, an efficient and fast synthetic method for the production of cyclohexene oxide is highly desired to be developed, taking sustainability for the environment and our society into consideration. The general synthetic

procedure for cyclohexene oxide is the epoxidation of cyclohexene [7,8]. Among various oxidizing agents used in the oxidation, a combination of molecular oxygen and aldehydes as a sacrificial agent has been widely studied [9]. However, in general, such a reaction in batch is slow due to the difficulties of performing a gas–liquid reaction in a batch reactor [10]. In addition, even valuable catalysts could not accelerate the reaction with good efficiency [11,12].

The continuous flow technology has brought a dramatic change and new aspects in organic synthesis [13-23] and has been noticed to provide significant improvement in gas–liquid reactions [24,25]. Thus, we envisioned that such a technology should make the gas–liquid-type epoxidation of cyclohexene using air as a green gaseous reagent faster with good efficiency to synthesize important organic compounds. Previous reports on reactions in a flow system using air as a green reactant [26,27] and epoxidations in a flow system using oxidants other than air [28-30] encouraged us to develop a highly productive flow system with air. Herein, we report that rapid gas–liquid oxidation of cyclohexene with air in the presence of isobutyraldehyde as a sacrificial agent to synthesize cyclohexene oxide is successfully achieved by using a flow technique (Scheme 1). Cyclohexene oxide was selectively produced with high yield in our flow oxidation system using air and within only 1.4 min. The fast epoxidation of cyclohexene without added catalyst in the solution was achieved since the solution of cyclohexene and aldehyde in 1,2-dichloroethane and air could react efficiently inside a pressurized microfluidic channel at high temperature in the flow microreactor. It is important to be noted that precise control of reaction temperature and residence time in our flow system are keys to inhibit overreactions in cyclohexene oxidation and decomposition of oxidants generated from air and aldehyde. Furthermore, the fast epoxidation is applicable for the continuous production process of cyclohexene oxide for 1 hour maintaining stable operation.

Scheme 1: Synthesis of cyclochexene oxide via epoxidation with air in the presence of isobutyraldehyde.
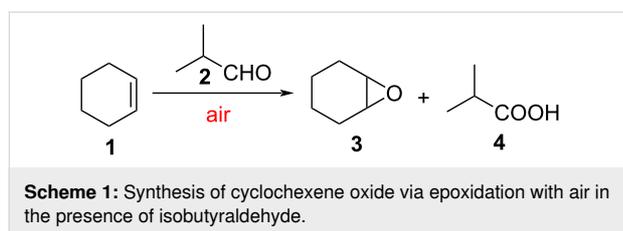
Results and Discussion
Batch experiment of epoxidation of cyclohexene with air
As an initial study, we carried out the oxidation of cyclohexene with air using a typical batch-type apparatus. The similar reaction conditions described in the reference were followed to compare the epoxidation with air to that with oxygen [10]. 3 equivalents of isobutyraldehyde were used and the concentration of cyclohexene in 1,2-dichloroethane was set to 0.065 M (see the reaction scheme in Figure 1). The air was introduced into the reaction mixture by bubbling from an air cylinder under atmospheric pressure. The reaction was investigated at different reaction temperatures of 40, 60, and 80 °C (Figure 1). The experiment was carefully carried out using a pear-shaped flask equipped with a reflux condenser cooled to −15 °C to avoid the loss of relatively volatile organic compounds in the reaction mixture. In the reaction at 40 °C, the reaction was very slow to yield the product in less than 20% yield within 270 min. This indicates that the cyclohexene oxidation with air can be hardly promoted at the temperature although the same reaction using bubbling of oxygen yielded cyclohexene oxide in 84% yield (GC) at 40 °C for 270 min [10]. When the reaction was performed with air at 60 °C, a significant increase in yield of the epoxide was observed to reach about 75% after 270 min but no more improvement was achieved. Then, the reaction was carried out at an elevated temperature of 80 °C, resulting in a decreased yield of the epoxide within 270 min as compared to the reaction at 60 °C. This result stemmed from the lowered solubility of air in a solvent at a high temperature to produce peracid from the reaction of aldehyde and oxygen insufficiently, and the epoxidation was deaccelerated. The experimental results revealed that aerobic epoxidation of cyclohexene in a batch reactor required a longer reaction time than 3 h to reach the maximum yield but a moderate yield of the epoxide.

The reaction under pressure requires an extensive pressurizing reactor such as an autoclave. Safety issues, however, would be unavoidable. Introducing gas as a bubble in the reaction mixture is a well-used method to increase the interfacial contact area [1]. However, thinking about the implementation of gas–liquid reactions at the industrial manufacturing level, the conventional batch technique has irreconcilable limitations.

Consequently, the batch operation has definite limitations to meet the demand to establish a highly productive process for industrial manufacturing.

Investigation of epoxidation of cyclohexene with air in continuous flow system
The flow system for the cyclohexene epoxidation with air was constructed and an investigation of flow conditions, temperature, and residence time was conducted. Subsequently, continuous production of cyclohexene oxide and further investigation to enhance the productivity in the flow system were conducted as described below.
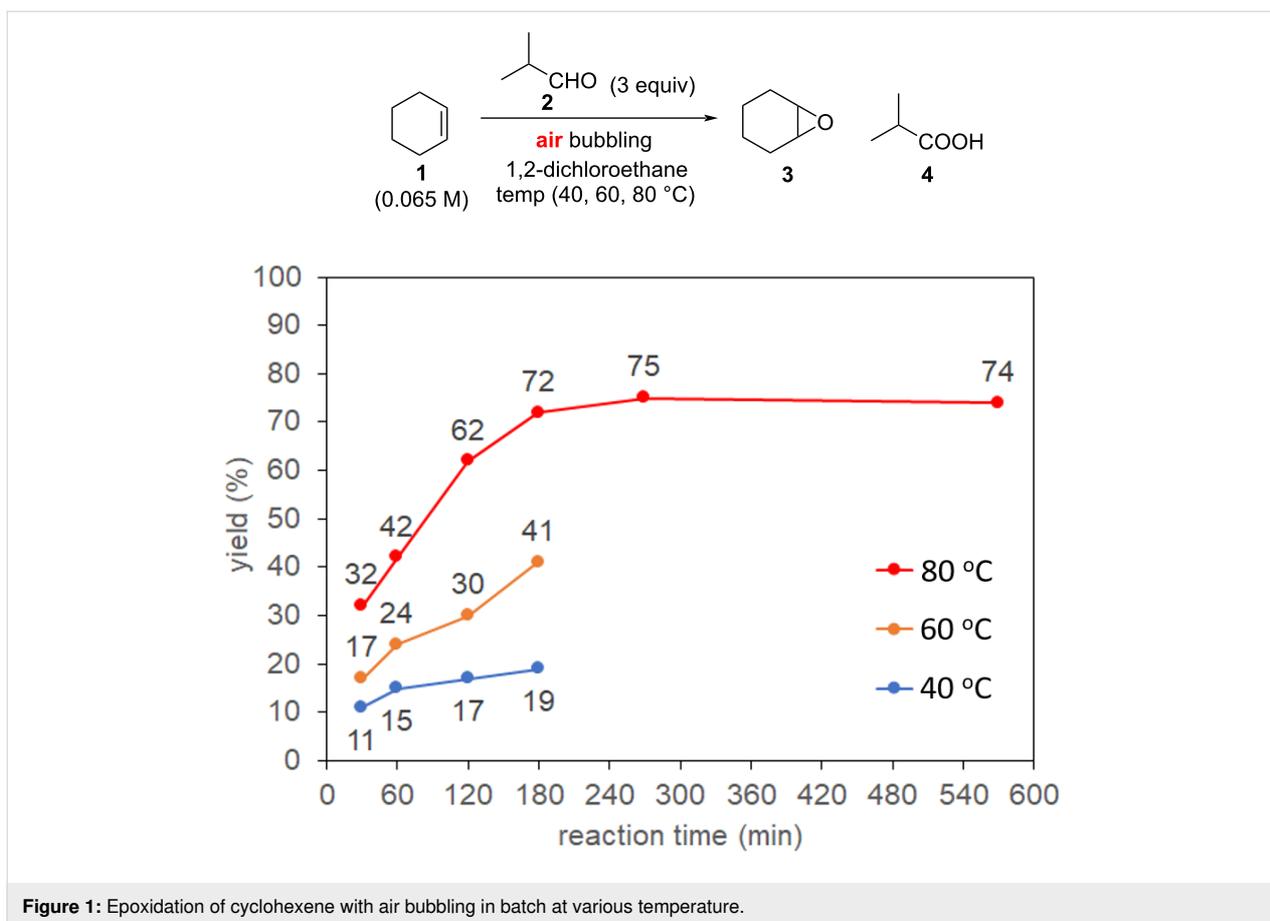
Figure 1: Epoxidation of cyclohexene with air bubbling in batch at various temperature.

Experimental setup

As shown in Figure 2, the system was constructed using commercially available stainless-steel tubing, mixer, joint parts, and devices. For a reactor, widely-used 1/8 inch stainless-steel tubing with a relatively large inner diameter (2.17 mm) was used to establish a readily applicable flow system for industrial use. A solution of cyclohexene and isobutyraldehyde in 1,2-dichloroethane was pumped out by a diaphragm pump. The concentration of cyclohexene in 1,2-dichloroethane was set to 0.065 M for the initial study and three equivalents of isobutyraldehyde were dissolved in the solution. While the solution was sent to the flow reactor at the flow rate of 2.6 mL/min, the air was at the flow rate of 480 mL/min with keeping the molar ratio of aldehyde and oxygen to 1:9. The liquid and gas phases were combined at a T-shaped mixer with a 1 mm inner diameter and flowed through a stainless-steel tube reactor immersed in heated silicon oil for reaction temperature control. The inner pressure was maintained at 0.9 MPa using a back pressure regulator (BPR). The reaction solution was cooled to ambient temperature in a water bath at the position right before BPR and collected in a sample vial. The solution was then immediately diluted with deuterated chloroform for ^{1}H NMR analysis.

Investigation of the temperature effect

Initially, we set out our research by investigating the effect of temperature on the epoxidation reaction at a residence time of 0.35 min (Figure 3). The temperature range tested was from 40 °C to 120 °C at intervals of 20 °C. At 40 °C, no epoxide was produced in spite of about 20% conversion of cyclohexene. When the temperature was elevated from 40 to 100 °C in increments of 20 °C, conversion and yield increased up to 73% and 47%, respectively at 100 °C. The yield was, however, no more improved from 47% at 100 °C by elevating the temperature to 120 °C even with the highest conversion of 90% attained, indicating the undesired reaction could take place to reduce the epoxide output at 120 °C. The efficiency of the reaction towards the desired epoxidation was clearly demonstrated by calculating the ratio of yield over conversion as black dots in Figure 3. As a result, the highest yield/conversion ratio for epoxidation was obtained in the reaction at 100 °C which is the temperature of choice for the following optimization of the flow epoxidation.

Investigation of the residence time

The residence time of the flow epoxidation was examined at 100 °C from 0.35 to 2 min (Figure 4). Both conversion of
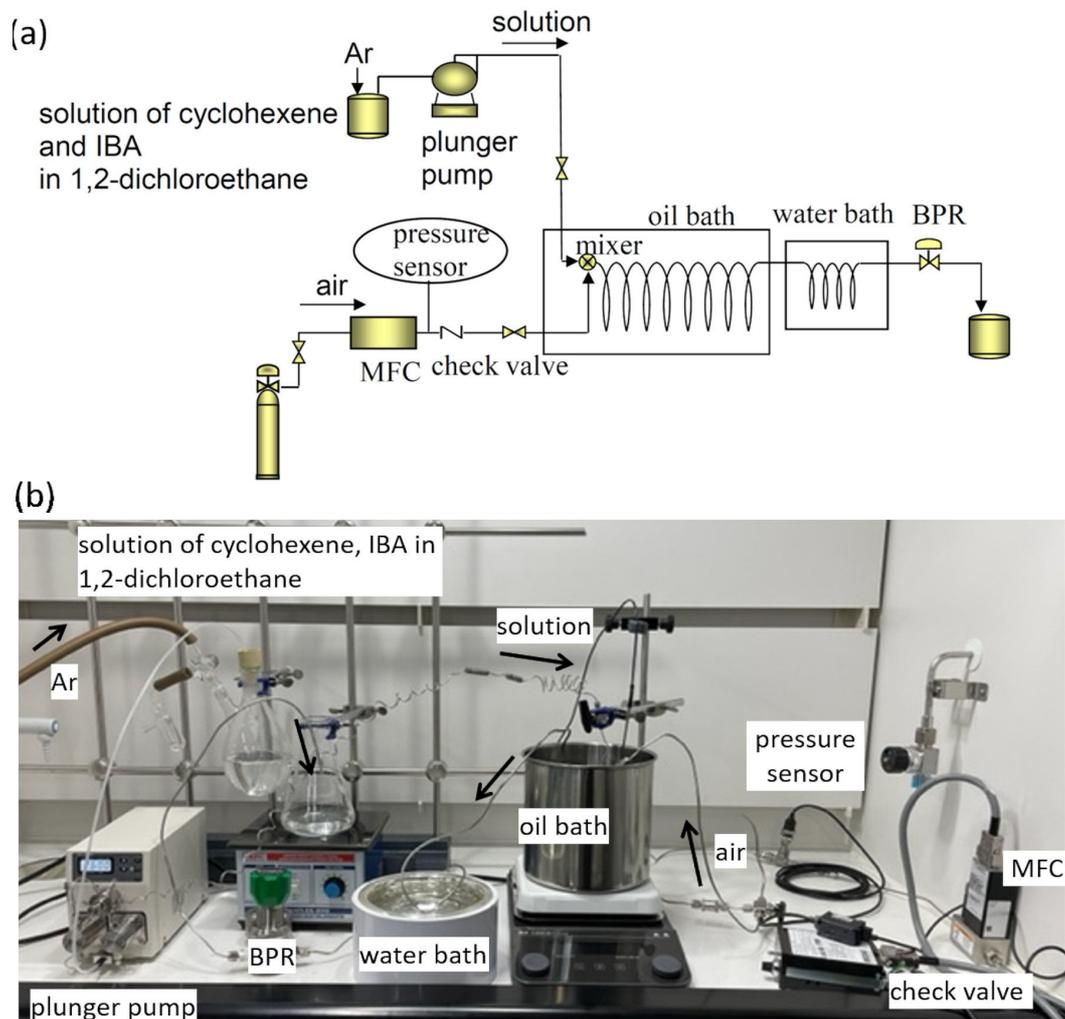
Figure 2: Schematic diagram (a) and photo (b) of the flow reactor used for cyclohexene epoxidation with air. IBA = isobutyraldehyde.
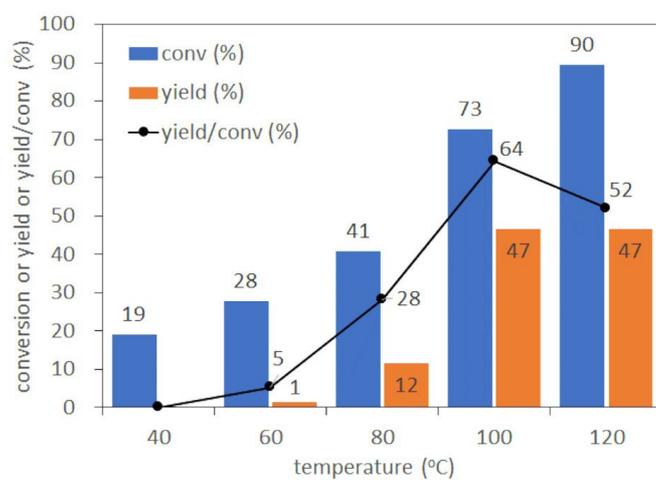

Figure 3: Investigation of reaction temperature in flow epoxidation of cyclohexene at residence time of 0.35 min.
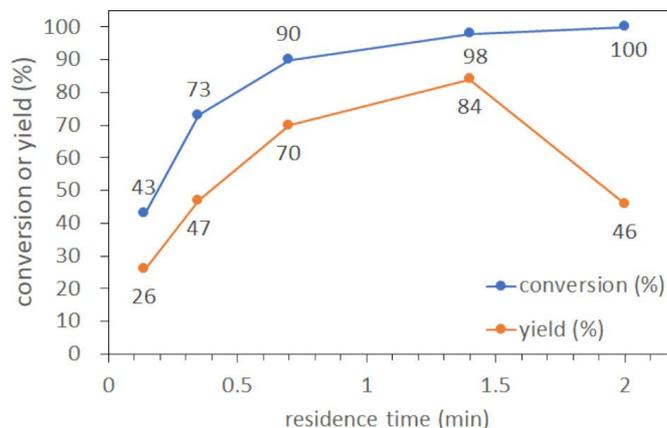
Figure 4: Investigation of residence time in flow epoxidation of cyclohexene at 100 °C.

cyclohexene and yield of cyclohexene oxide increased as residence time elongated from 0.35 to 1.4 min. However, a drastic decrease in both values was observed at a residence time of 2 min. This result indicates that the epoxide was generated efficiently at a proper residence time, which could be explored readily by performing the reaction in a continuous flow system. To the best of our knowledge, this is for the first time to achieve the epoxidation of cyclohexene using air within only 1.4 min by carefully avoiding any unwanted release which could result in a hazardous situation. In our flow conditions, the volume of air is remarkably higher than that of the solution (480 mL/min of air vs 2.6 mL/min of solution). Although we have no clear evidence for now, the solution could form a very thin layer due to plug-type flow. In such a case, the interfacial area is greatly enlarged in the flow reactor due to the high volume-to-surface ratio. Thus, very efficient contact between reactants in solution and air was achieved to enhance the reaction remarkably. Furthermore, the volume and inner pressure of the reactor were

readily and precisely controlled even at the elevated reaction temperature. Consequently, the operation of the gas–liquid oxidation even with air in the flow reactor definitely paved the way for a green and fast oxidation process.

Based on the mechanisms reported in the literature [11,31], we hypothesized the plausible reaction mechanism in our flow system as shown in Scheme 2. Firstly, the peracid **6** was generated via the autoxidation process of aldehyde (reaction 1), which rapidly oxidized coexisting cyclohexene to produce cyclohexene oxide as a major product along with isobutyric acid **4** (reaction 2). Although we did not quantify whether the polymerization of epoxide **3** might proceed when the residence time was elongated, leading to a significant decrease in the yield of cyclohexene oxide (Supporting Information File 1, Figure S2) [32]. Overall, we assume that, in our flow system, the highly efficient contact of acyl radical **5** with oxygen during the autoxidation of aldehyde could produce the peracid **6** very
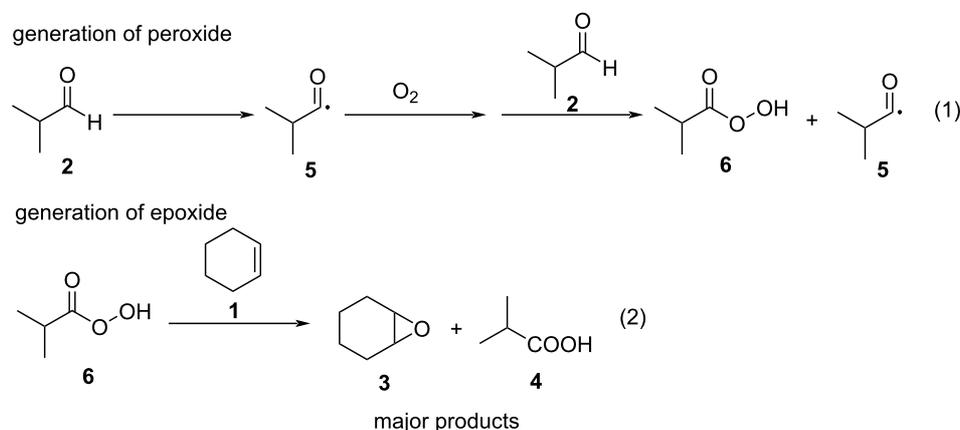
Scheme 2: Plausible reaction pathway of the epoxidation of cyclohexene with air in the flow system.

efficiently, which immediately reacts with cyclohexene to generate cyclohexene oxide selectively. This reaction process might take place smoothly and selectively in the microfluidic channel to achieve a high reaction rate.

Verification of continuous production

The above-mentioned exploitation of optimal conditions for flow cyclohexene epoxidation revealed that continuous flow operation of the reaction provides cyclohexene oxide very fast in the highest yield with the best efficiency using green, inexpensive air. Next, we verified the continuous production of the epoxide with the aim of industrial implementation of this synthetic process (Figure 5). The stability of the continuous flow operation was confirmed during the 1-hour operation as follows. The reaction solution flowing out of the exit was collected every 5 min and analyzed immediately by ^{1}H NMR. Yields and conversions were plotted against the operation time as shown in Figure 5. As demonstrated clearly, the production of cyclohexene oxide was maintained constant and high during 1-hour operation. As a result, the productivity was integrated to reach 3.7 g/h reliably, determined by ^{1}H NMR analysis.

Investigation of the equivalents of isobutyraldehyde and concentration of cyclohexene for further enhancement of cyclohexene productivity

We turned our attention to enhancing the productivity further. It is significantly important for the industrial operation to increase the productivity by reducing the volume of reagents and organic solvents used for safe, low-cost, and environmentally benign

operations. Initially, we decided to maintain the key flow conditions such as the flow rate since it severely affects the fluidic interaction inside a flow reactor and thus the reaction efficiency of this type of gas–liquid reaction. Thus, the flow rate of the solution containing cyclohexene, isobutyraldehyde in 1,2-dichloroethane, and the air was set to 2.6 mL/min and 1920 mL/min, respectively, as used for the above-mentioned continuous operation and no change was made throughout the investigation. The results are displayed in Figure 6. At first, the equivalent of aldehyde was reduced from three to two equivalents and 0.26 M solution of cyclohexene was prepared. As compared to the reaction with a 1:3 ratio of cyclohexene and the aldehyde, the flow epoxidation with a 1:2 ratio of that favorably proceeded to achieve higher levels of yield and productivity (97% yield and 3.9 g/h with a 1:2 ratio of cyclohexene to aldehyde vs 93% yield and 3.3 g/h with 1:3 ratio of cyclohexene and aldehyde). We succeeded in reducing the equivalents of aldehyde without any loss of productivity by our approach. Following is the flow operation with the increased concentration such as 0.52 M and 0.78 M with a 1:2 ratio of cyclohexene and aldehyde. As the concentration increased, the productivity of cyclohexene oxide was amplified up to 11.1 g/h, which is 14-fold that obtained from 0.065 M solution of cyclohexene with 3 equivalents of isobutyraldehyde (0.8 g/h). Consequently, a small change in the equivalents of isobutyraldehyde and concentration of cyclohexene in solution delivered about a 14-fold remarkably large enhancement of productivity. Moreover, using a high concentration solution for flow operation enabled minimization of the volume of reagents used.
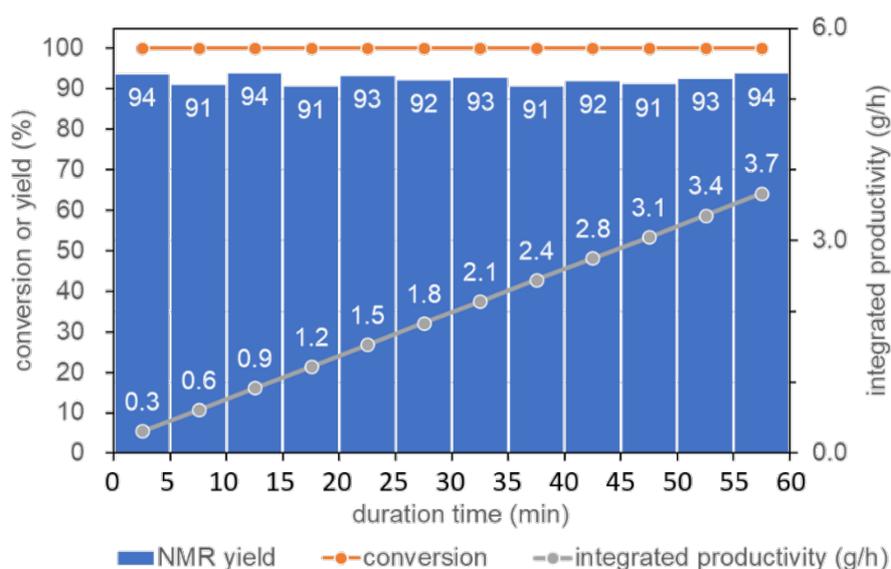

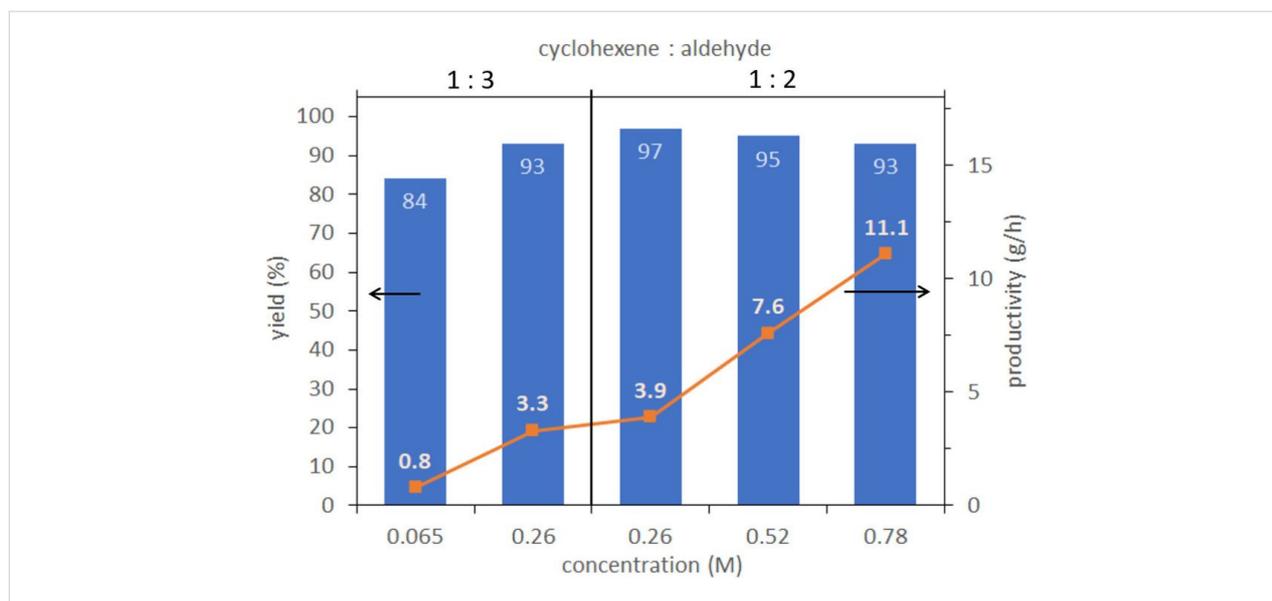**Figure 5:** Continuous production of cyclohexene oxide.

Figure 6: Effect of concentration of cyclohexene and eqivalent of aldehyde.

Conclusion

In the present study, we developed the continuous flow system for the aerobic cyclohexene oxide production based on appropriate temperature and residence time control. Moreover, the production of cyclohexene oxide with high yield and selectivity was achieved under the conditions of a very short timescale such as 1.4 min of residence time without added catalyst. Rapid production of cyclohexene oxide in a continuous flow system could be sustained for at least 1 hour with reliable operation stability. In addition, the use of a higher concentration of cyclohexene (1:2 = cyclohexene/isobutyraldehyde in 0.78 M of cyclohexene in solution) results in a remarkable improvement in productivity (11.1 g/h). Further flow condition search will be conducted for developing a highly productive cyclohexene oxide production and other rapid gas-liquid reactions.

Experimental
Procedure for epoxidation of cyclohexene with air bubbling in a batch reactor

The same procedure as described in the literature was followed [5]. A 100 ml two-necked flask equipped with a cooling condenser through which −15 °C cooling solvent was circulated, a solution of isobutyraldehyde (9.75 mmol) and tridecane (as an internal standard) in 1,2-dichloroethane (45 mL) was stirred vigorously with air bubbling at the reaction temperature for 30 min to initiate the peroxide formation. Then, a solution of cyclohexene (3.25 mmol) in 1,2-dichloroethane (5 mL) was added. The inner pressure was released through a thin needle on the top of the condenser. The reaction

temperature was controlled either in a water bath or an oil bath. At a certain reaction time, 50 µL of the reaction solution was taken out using a gastight syringe and immediately diluted with deuterated chloroform for ^{1}H NMR analysis.

General procedure for epoxidation of cyclohexene with air in the flow microreactor

A flow microreactor system consisting of a T-shaped micromixer, and one microtube reactor was used for epoxidation of cyclohexene with air. A solution of cyclohexene (0.065 M), isobutyraldehyde (0.195 M), and tridecane as an internal standard in 1,2-dichloroethane (flow rate: 2.6 mL/min) exposed to Ar flow was introduced into a mixer by a plunger pump. Air was introduced into the mixer at the flow rate of 480 mL/min. The resulting mixture was passed through the microtube reactor (ϕ = 2.17 mm, L = 20 m, residence time = 1.4 min) which was immersed in an oil bath. The reaction mixture was then passed through the microtube ((ϕ = 2.17 mm, L = 1 m) immersed in a water bath. The resulting solution was collected in a vessel for 1 min, then a small amount of it was immediately diluted with deuterated chloroform and analyzed by ^{1}H NMR to obtain yield and conversion.

Supporting Information

Supporting Information File 1
Experimental and analytical data.
[https://www.beilstein-journals.org/bjoc/content/supplementary/1860-5397-18-67-S1.pdf]

ORCID® iDs

Hiroki Mandai - https://orcid.org/0000-0001-9121-3850
Aiichiro Nagaki - https://orcid.org/0000-0002-8264-6205

References

1. Fujita, H.; Yoshimatsu, H.; Miki, C.; Shirai, T.; Hata, T.; Sakamoto, M. *Chem. Lett.* **2021,** *50,* 1066–1070. doi:10.1246/cl.200958
2. Oral, A.; Tasdelen, M. A.; Demirel, A. L.; Yagci, Y. *J. Polym. Sci., Part A: Polym. Chem.* **2009,** *47,* 5328–5335. doi:10.1002/pola.23581
3. Chang, H.; Li, D.; Cao, T.; Li, Q.; Bu, Z.; Zhao, W.; Lin, T. *Polym. Adv. Technol.* **2018,** *29,* 1870–1874. doi:10.1002/pat.4293
4. Koning, C.; Wildeson, J.; Parton, R.; Plum, B.; Steeman, P.; Darensbourg, D. J. *Polymer* **2001,** *42,* 3995–4004. doi:10.1016/s0032-3861(00)00709-6
5. Muthuraj, R.; Mekonnen, T. *Polymer* **2018,** *145,* 348–373. doi:10.1016/j.polymer.2018.04.078
6. Trost, B. M. *Org. Process Res. Dev.* **2012,** *16,* 185–194. doi:10.1021/op200294r
7. Centi, G.; Cavani, F.; Trifirò, F. Trends and Outlook in Selective Oxidation. *Selective Oxidation by Heterogeneous Catalysis;* Springer US: Boston, MA, U.S.A., 2001; pp 1–24. doi:10.1007/978-1-4615-4175-2_1
8. Adolfsson, H. Transition Metal-Catalyzed Epoxidation of Alkenes. In *Modern Oxidation Methods;* Bäckvall, J.-E., Ed.; Wiley-VCH: Weinheim, Germany, 2004; pp 21–49. doi:10.1002/3527603689.ch2
9. Yamada, T.; Takai, T.; Rhode, O.; Mukaiyama, T. *Bull. Chem. Soc. Jpn.* **1991,** *64,* 2109–2117. doi:10.1246/bcsj.64.2109
10. Kaneda, K.; Haruna, S.; Imanaka, T.; Hamamoto, M.; Nishiyama, Y.; Ishii, Y. *Tetrahedron Lett.* **1992,** *33,* 6827–6830. doi:10.1016/s0040-4039(00)61786-0
11. Ikawa, T.; Fukushima, T.; Muto, M.; Yanagihara, T. *Can. J. Chem.* **1966,** *44,* 1817–1825. doi:10.1139/v66-273
12. Serra, A. C.; Rocha Gonsalves, A. M. d'A. *Tetrahedron Lett.* **2011,** *52,* 3489–3491. doi:10.1016/j.tetlet.2011.04.120
13. Lesieur, M.; Battilocchio, C.; Labes, R.; Jacq, J.; Genicot, C.; Ley, S. V.; Pasau, P. *Chem. – Eur. J.* **2019,** *25,* 1203–1207. doi:10.1002/chem.201805657
14. Ahlqvist, G. P.; Burke, E. G.; Johnson, J. A.; Jamison, T. F. *Polym. Chem.* **2021,** *12,* 489–493. doi:10.1039/d0py01676d
15. Gambacorta, G.; Sharley, J. S.; Baxendale, I. R. *Beilstein J. Org. Chem.* **2021,** *17,* 1181–1312. doi:10.3762/bjoc.17.90
16. Gemoets, H. P. L.; Hessel, V.; Noël, T. Reactor Concepts for Aerobic Liquid phase Oxidation: Microreactors and Tube Reactors. *Liquid Phase Aerobic Oxidation Catalysis: Industrial Applications and Academic Perspectives;* Wiley-VCH Verlag GmbH: Weinheim, Germany, 2016; pp 397–419. doi:10.1002/9783527690121.ch23
17. Kasakado, T.; Fukuyama, T.; Nakagawa, T.; Taguchi, S.; Ryu, I. *Beilstein J. Org. Chem.* **2022,** *18,* 152–158. doi:10.3762/bjoc.18.16
18. Saito, Y.; Nishizawa, K.; Laroche, B.; Ishitani, H.; Kobayashi, S. *Angew. Chem., Int. Ed.* **2022,** *61,* e202115643. doi:10.1002/anie.202115643
19. Takumi, M.; Sakaue, H.; Nagaki, A. *Angew. Chem., Int. Ed.* **2022,** *61,* e202116177. doi:10.1002/anie.202116177
20. Ashikari, Y.; Tamaki, T.; Takahashi, Y.; Yao, Y.; Atobe, M.; Nagaki, A. *Front. Chem. Eng.* **2022,** *3,* 819752. doi:10.3389/fceng.2021.819752
21. Ashikari, Y.; Maekawa, K.; Ishibashi, M.; Fujita, C.; Shiosaki, K.; Bai, H.; Matsuyama, K.; Nagaki, A. *Green Process. Synth.* **2021,** *10,* 722–728. doi:10.1515/gps-2021-0069
22. Ashikari, Y.; Tamaki, T.; Kawaguchi, T.; Furusawa, M.; Yonekura, Y.; Ishikawa, S.; Takahashi, Y.; Aizawa, Y.; Nagaki, A. *Chem. – Eur. J.* **2021,** *27,* 16107–16111. doi:10.1002/chem.202103183
23. Tamaki, T.; Nagaki, A. *Tetrahedron Lett.* **2021,** *81,* 153364. doi:10.1016/j.tetlet.2021.153364
24. Mallia, C. J.; Baxendale, I. R. *Org. Process Res. Dev.* **2016,** *20,* 327–360. doi:10.1021/acs.oprd.5b00222
25. Yamamoto, T.; Tonomura, O.; Nagaki, A. *J. Chem. Eng. Jpn.* **2020,** *53,* 73–77. doi:10.1252/jcej.19we083
26. Vanoye, L.; Wang, J.; Pablos, M.; de Bellefon, C.; Favre-Réguillon, A. *Catal. Sci. Technol.* **2016,** *6,* 4724–4732. doi:10.1039/c6cy00309e
27. Zhou, Y.; He, W.; Fang, Z.; Guo, K. *ChemistrySelect* **2018,** *3,* 13530–13533. doi:10.1002/slct.201803038
28. Hone, C. A.; Kappe, C. O. *Top. Curr. Chem.* **2019,** *377,* 2. doi:10.1007/s41061-019-0233-8
29. Gérardy, R.; Emmanuel, N.; Toupy, T.; Kassin, V.-E.; Tshibalonza, N. N.; Schmitz, M.; Monbaliu, J.-C. M. *Eur. J. Org. Chem.* **2018,** 2301–2351. doi:10.1002/ejoc.201800149
30. Hone, c. A.; Roberge, d. M.; Kappe, C. O. *ChemSusChem* **2017,** *10,* 32–41. doi:10.1002/cssc.201601321
31. Wentzel, B. B.; Alsters, P. L.; Feiters, M. C.; Nolte, R. J. M. *J. Org. Chem.* **2004,** *69,* 3453–3464. doi:10.1021/jo030345a
32. Yahiaoui, A.; Belbachir, M.; Soutif, J. C.; Fontaine, L. *Mater. Lett.* **2005,** *59,* 759–767. doi:10.1016/j.matlet.2004.11.017

Inductive heating and flow chemistry – a perfect synergy of emerging enabling technologies

Conrad Kuhwald, Sibel Türkhan and Andreas Kirschning[*]

Abstract

Inductive heating has developed into a powerful and rapid indirect heating technique used in various fields of chemistry, but also in medicine. Traditionally, inductive heating is used in industry, e.g., for heating large metallic objects including bending, bonding, and welding pipes. In addition, inductive heating has emerged as a partner for flow chemistry, both of which are enabling technologies for organic synthesis. This report reviews the combination of flow chemistry and inductive heating in industrial settings as well as academic research and demonstrates that the two technologies ideally complement each other.

Introduction

Several decades ago, inductive heating was introduced as an indirect technique in various applications, including industrial manufacturing, synthetic chemistry [1-3], and medicine (Figure 1) [4-7]. Compared to microwave heating [8,9], the other major indirect heating technique, inductive heating has several advantages. Technically, the system is composed of an inductive coil and an alternating current (AC) generator. The material to be heated is usually located in the interior of the coil or in its vicinity, so that the heat is not generated by convection across a surface. Compared to heating under microwave irradiation, the system does not need to be encased for safety reasons. Inductive heating of materials is extremely fast with the best de-

termined power transfer value of all heating technologies [10]. It has therefore found wide industrial application for heating large metallic objects and workpieces. It is used for bending tubes, bonding, welding, sintering, and annealing of metals and alloys [11]. In addition to steel and alloys, glass or silicon are also heated or melted under inductive heating conditions [12]. In the last decade, inductive heating has also been used for bonding, heating rubber, deforming plastic, or shrinking work-pieces [13-15]. These materials are not conductive like steel, copper, or alloys, so another mechanism must take hold to introduce heat. This is often achieved by embedding small super-paramagnetic ferromagnetic or ferrimagnetic nanoparticles into

these materials. For this purpose, superparamagnetic iron oxide nanoparticles (SPION) are most commonly used, of which the main forms are magnetite (Fe_3O_4) and its oxidized form maghemite (γ-Fe_2O_3). Although cobalt and nickel are also highly magnetic materials, they are less common due to their inherent toxicity and ease of oxidation.

Figure 1: Inductive heating, a powerful tool in industry and the Life Sciences.
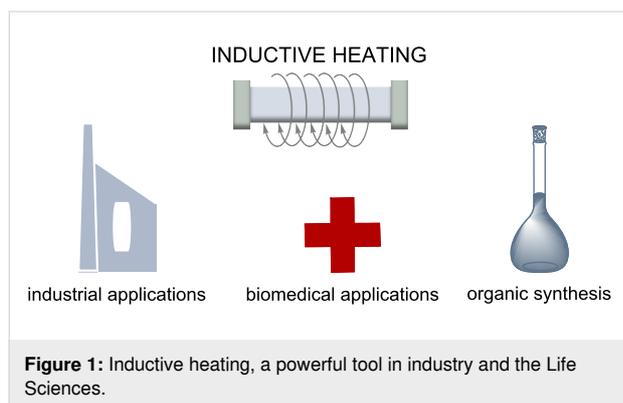
Another branch of research involving SPIONs focuses on developments in nanoscience, nanomedicine, and nanoparticle-assisted imaging, diagnosis, and drug delivery [4-7], an area that is not covered in this report.

Review
1 Theoretical background of electromagnetic induction

To better understand the mechanisms of inductive heating, some basic physical principles are first explained. This type of heating depends on various structural, morphological, chemical, and physical properties of the materials to be heated. When a suitable receiver is placed in an alternating electromagnetic field, this energy is converted into heat, apart from minor losses due to convection, conduction, and thermal radiation. This conversion of energy into heat takes place according to three different principles, which depend on the properties of the material.

1.1 Hysteresis loop

The orbital motion and electron spin profile of a material determine its magnetic properties. Ferromagnetic (FM) materials have unpaired electron spins that couple in space and provide a strong magnetic force. However, ferromagnetic materials consist of multiple domains. In a magnetic field, electron spins align within a domain, but commonly not in all domains. As such, ferromagnetic materials consume the energy to grow domains in the direction of the field. However, the multidomain state becomes energetically unfavorable once the material under consideration reaches a certain size such that the energy

required to form a domain wall is higher than the energy required to maintain the magnetostatic energy of a single domain. In ferromagnetic single-domain materials, the spins align in the same direction and act as a giant magnetic moment [16,17]. The coupling of these spins to the crystal lattice is called hysteresis. When a magnetic field is applied, the electromagnetic energy of the atoms is transferred to the lattice in the form of heat, which is undesirable for many applications of magnetic materials. This process is therefore referred to as magnetic loss. The amount of energy loss per cycle of magnetic field generation is interpreted as the magnetization of a material in a hysteresis loop, which is defined as magnetic hysteresis loss (Figure 2). It is characterized by three parameters: 1) the saturation magnetization (M_s), at which the material reaches its maximum in the magnetic field, 2) the remanent magnetization (M_r), which is retained by the material when the magnetic field is removed, and 3) the coercivity (H_c), which is the magnetic field required to demagnetize the sample and determines the heat release to the surrounding media. These three parameters are critical to the heat release of magnetic nanoparticles and can vary for different particle types. Coercivity is an inherent property of magnetic nanoparticles that reaches a maximum at a critical diameter of magnetic nanoparticles from multidomain to single domain structures. In hysteresis curves, the area between M_r and H_c is correlated with the energy absorbed per mass. For ferromagnetic materials, the area indicates that their magnetic heating mechanism depends on hysteresis losses.

Figure 2: Electric displacement field of a ferromagnetic and superparamagnetic material.
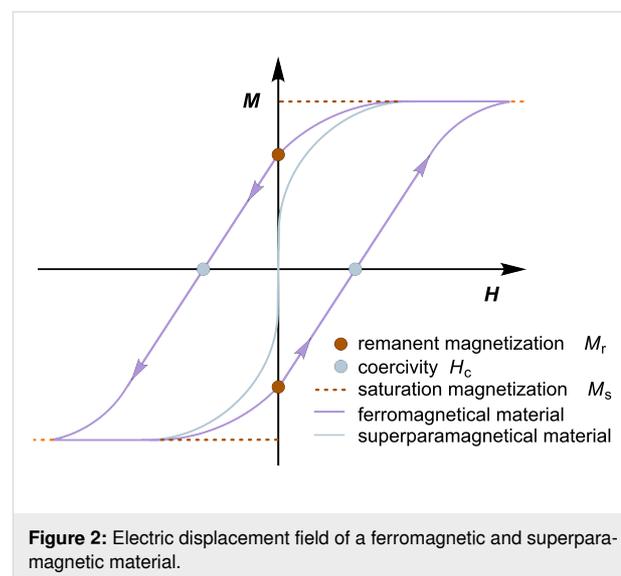
1.2 Néel relaxation

Magnetic particles consisting of a single domain have a remanent magnetization (M_r) of zero; therefore, they lack the hysteresis contribution in the heating process (Figure 2). Their mechanism of electromagnetic energy dissipation is described

by the Néel relaxation mechanism [18]. This phenomenon is called superparamagnetism (SPM) and occurs with decreasing particle size when reaching the nanoscale. The energy barrier of such superparamagnetic nanoparticles to reverse magnetization is directly related to magnetic anisotropy and particle volume [19,20]. In external magnetic fields, these spins rotate in the direction of the magnetic field direction and the axis of magnetic moment fluctuates along the magnetocrystalline anisotropy axis. Néel has described the relationship between the relaxation time of the thermal fluctuations of the magnetic moments of the individual domains and the uniaxial anisotropy. In Néel relaxation, the energy barrier for the remanence of magnetization decreases with smaller particle volume. The Néel relaxation process can be observed in dry, powdered single-domain nanoparticles or in immobilized nanoparticles, e.g., when embedded in tumor tissue.

1.3 Joule effect
Eddy currents or Foucault currents are generated by an oscillating electromagnetic field that penetrates the resistance of a magnetically conducting receiver and releases energy through the Joule effect [21,22]. The heating power in eddy currents is directly correlated with the square of the applied frequency and field amplitude. In contrast to the two previous effects, the distribution of current density is not homogeneous when a conductor is introduced into an oscillating electric current. It decreases exponentially starting from the surface with increasing distance, e.g., into the depth of the material. The fact that the heat is not evenly distributed, but is mainly located on the surface, is called the skin-depth effect. It should be noted that this effect decreases significantly with increasing frequency. Two further parameters to be considered for inductively heated materials are the Curie temperature (TC) and the blocking temperature (TB). They mark the phase transition from ferromagnetic to paramagnetic and from ferromagnetic to superparamagnetic materials, respectively. These values represent the thermal limit up to which the materials can be inductively heated, since above this point they lose their permanent magnetism [23].
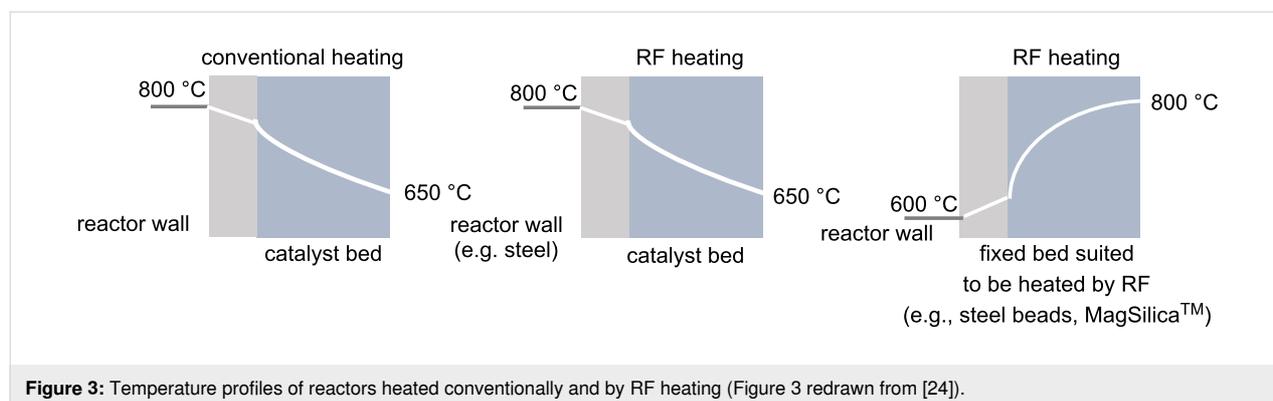
2 Inductive heating in industrial applications under flow conditions
## 2.1 General remarks
Energy efficiency is one of the most important cost factors in industrial processes, especially for high temperature reactions in fixed-bed reactors. In general, conductive particles or (super-para)magnetic nanoparticles are suitable as fixed-bed materials for heat generation by applying an external oscillating electromagnetic field. Due to the high specific surface area of these bulk materials, rapid heat transfer by radio frequency (RF) heating is possible (Figure 3). RF-induced heating offers several advantages for use in high-temperature reactions. Advantageously, the heat is generated directly within the reactors, bypassing the problem of thermal gradients. Another advantage of generating heat directly at or near the catalyst surface arises from the potential for hot spots to form, which can substantially exceed the volume temperature of the surrounding reaction medium and lead to significant accelerations of chemical reactions. It is also important that the reactor wall is not exposed to the high temperatures in this process, which has safety implications. Finally, the desired temperature is reached more quickly compared to convective heating and better temperature control can be ensured, e.g., by IR pyrometers.

2.2 Application of trickle bed reactor systems for isopulegol production
Berenguer-Murcia et al. [25] developed a near isothermal micro trickle bed reactor operated by radiofrequency (RF; 300 kHz) heating of nickel ferrite particles (110 µm) deposited in the fixed bed. To achieve near-isothermal conditions at a reactor length of 50 mm, at least three heating zones were set up. The fixed bed was composed of alternating catalyst and heating zones. The heating zones consisted of a mixture of nickel ferrite particles and glass spheres with a particle size of 110 µm. Conventionally heated trickle bed reactors using externally located heating devices suffer from uneven temperature distribution in the reactor bed and the formation of hot spots that can lead to rapid deactivation of the catalyst.

Figure 3: Temperature profiles of reactors heated conventionally and by RF heating (Figure 3 redrawn from [24]).

The authors selected the synthesis of isopulegol (**2**) from citronellal (**1**) as test reaction (Scheme 1). Thus, citronellal (**1**) was cyclized to isopulegol in the heating zone. This was achieved at 80 °C in 1,4-dioxane using a Zeolite-encapsulated magnetic nickel ferrite nanoparticles (NiFe$_2$O$_4$@TiO$_2$@ZSM-5) catalyst, an aluminosilicate zeolite, which gave best results due to its high Brønsted acidity [26]. Using inductive heating resulted in a highly improved catalytic system that showed long-term stability. This example is of relevance for the fragrance and flavour industries, as isopulegol (**2**) can be transformed into menthol in one step by catalytic hydrogenation.

Scheme 1: Continuous flow synthesis of isopulegol (**2**) from citronellal (**1**).
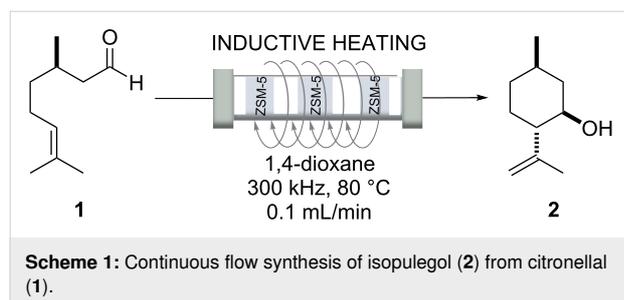
2.3 Dry and steam methane reforming

The commencement of the energy transformation is associated with the search for alternative and more environmentally friendly energy sources [27]. The dry reforming of methane is a particularly interesting process in this context (Scheme 2, reaction 1). A second variant is the steam methane reforming process. Since complex solids such as wood, sewage sludge or municipal waste cannot be evaporated, they are reformed using supercritical water on a heterogeneous catalyst at 250–300 bar, 400–550 °C, and a large excess of water [28]. The former process is the preferred route for large-scale production of syngas from biogas [29], while the latter is the main catalytic route [30].

The intrinsic problem with these processes is the extremely high temperature required, typically above 700 °C (ambient pressure) [27]. Since most such processes do not operate at ambient pressure, much higher temperatures around 950 °C are actually required. At these high temperatures, the selectivity of the process is a challenge. Possible side reactions such as hydrogenation of CO and CO$_2$, decomposition of CH$_4$, and the Boudouard reac-

tion lead to the formation of elemental carbon [31]. Another problem is the Curie temperature (T_C) associated with the material. Depending on the composition of the stainless steel, this is around 750 °C [32]. In 2017, Mortensen's team performed the reaction for the first time with inductively heated Ni-Co NP alloys deposited on a magnesium aluminate (MgAl$_2$O$_4$) spinel [33]. The alloy prepared specifically for this case contained 12.6 wt % Ni and 9.0 wt % Co with a Curie temperature above 800 °C. By using a high Co content (T_C = 1115 °C), they were able to maintain ferromagnetic properties even at very high temperatures. Since the addition of nickel further catalyzes this reaction, complete conversions with low carbon formation could be obtained at low flow rates. At higher flow rates, reaction kinetics was the limiting factor. Later, it was found that by doping the alloy with small amounts of copper, almost complete conversion (95%) could be achieved at lower electromagnetic fields and higher flow rates (Q = 152 NL/h) [34]. Not only was less carbon formation observed with this new material, but also little to no reduction in catalytic activity. Although this is not yet the most efficient process that could be used on a large scale, it is a remarkable application for inductive heating.

2.4 CO$_2$ storage and release under RF heating

The climatic changes are associated, among other factors, with increasing emissions of CO$_2$ into the atmosphere. The group of Rebrov et al. investigated the storage of CO$_2$ in CaO via the calcination process using inductive heating (Scheme 3) [35].

$$CO_2 + CaO \rightleftharpoons CaCO_3 \qquad \Delta H°_{298} = -178 \text{ kJ/mol}$$

Scheme 3: Calcination and RF heating.

The cycle can be divided into two individual processes: First, the carbonation step, in which the CaO absorbs the CO$_2$ to form the calcium carbonate at 650–680 °C, and second, the subsequent calcination step, in which the CaO-based sorbent is sintered at temperatures of 850–950 °C to release the captured CO$_2$ and form CaO again. The inductive method is a very easy to implement and cost-effective system that can be installed in production plants. A higher desorption rate (15.4%) and a lower degree of sintering of the sorbent were observed with the IH

$$(1) \quad CH_4 + CO_2 \rightleftharpoons 2\,CO + 2\,H_2 \qquad \Delta H°_{298} = 247 \text{ kJ/mol}$$

$$(2) \quad CH_4 + H_2O \rightleftharpoons CO + 3\,H_2 \qquad \Delta H°_{298} = 206 \text{ kJ/mol}$$

Scheme 2: Dry (reaction 1) and steam (reaction 2) methane reforming.

method compared to conventional heating methods, coupled with shorter cycle and start-up times. Rebrov et al. also suggested that the system can be used during periods of low power consumption to reduce the load on the electrical system.

## 2.5 Preparation of hydrocarbons (the Fischer–Tropsch process)

Monodisperse Fe@FeCo core shell nanoparticles as well as Fe(0) nanoparticles with a Ru(0) layer exhibit large heating capability when exposed to an external oscillating electromagnetic field. These particles combine magnetic and surface catalytic properties and thus have been employed in the Fischer–Tropsch process. The heating performance is characterized by the specific absorption rate (SAR) of the material. The tested materials showed high SAR values when brought into an electromagnetic field of 50 mT at a frequency of 54 kHz. Under these conditions the particles were able to catalyze the hydrogenation of CO. The presence of ruthenium increased the catalytic activity and allowed the catalytic process to be carried out at lower reaction temperatures, which was explained by the fact that the surface temperature of the nanoparticles was in fact significantly higher than 200 °C. It was also not necessary to implement an additional heating device for the outer reactor wall. Thus, this process represents a promising example of "cold magnetic catalysis" as it is termed in the paper [36].

2.6 Methane production ("Sabatier" process)

One of the largest challenges for sustainable power generation is to create a system in which all energy sources can be converted into each other efficiently and according to demand. In the so-called "power to gas" (PtG) technology, an efficient catalytic approach has been missing to date [37,38]. A very challenging catalytic process, which is gaining importance in this context, is the Sabatier reaction.

In this reaction, CO_2 and H_2 are converted to CH_4 (Scheme 4). This process can be used as a catalytic cycle in combination with electrolysis of water to produce the hydrogen exactly when the demand requires it. The reactions are very powerful and can represent an important access to synthetic fuels. This is important not only in the context of energy storage, CO_2 reduction, and climate change prevention, but also because they provide a country-independent source of energy. However, for use in a continuous flow system, the catalyst must have extremely high SAR and catalytic activity. Recently, a series of promising systems have been produced for this purpose. These include ($Fe_{2.2}C$) NPs [39], (ICNPs@Ni; 29 wt % Ni), and (ICNPs@Ru 1 wt % Ru) on a silica-alumina support (SiRAlox). The Ru nanoparticles far outperformed the previously known catalysts. A methane yield of 93% with complete selectivity could be achieved with high flow rates (125 mL/min; reactor dimensions according to SI: 2 cm diameter and 1 cm height of catalyst filling) in an external electromagnetic field of 28 mT. Heating can be problematic when exothermic reactions are performed. To prevent catalyst deactivation, the group of Giambastiani et al. developed homogeneously sized Ni nanoparticles (4 ± 1 nm) decorated on an oxidized carbon felt (OCF) matrix [40]. A laser pyrometer was used to measure the temperature of the catalyst bed in the quartz reactor. The inductor was controlled by a proportional-integral-derivative (PID) controller, which regu-
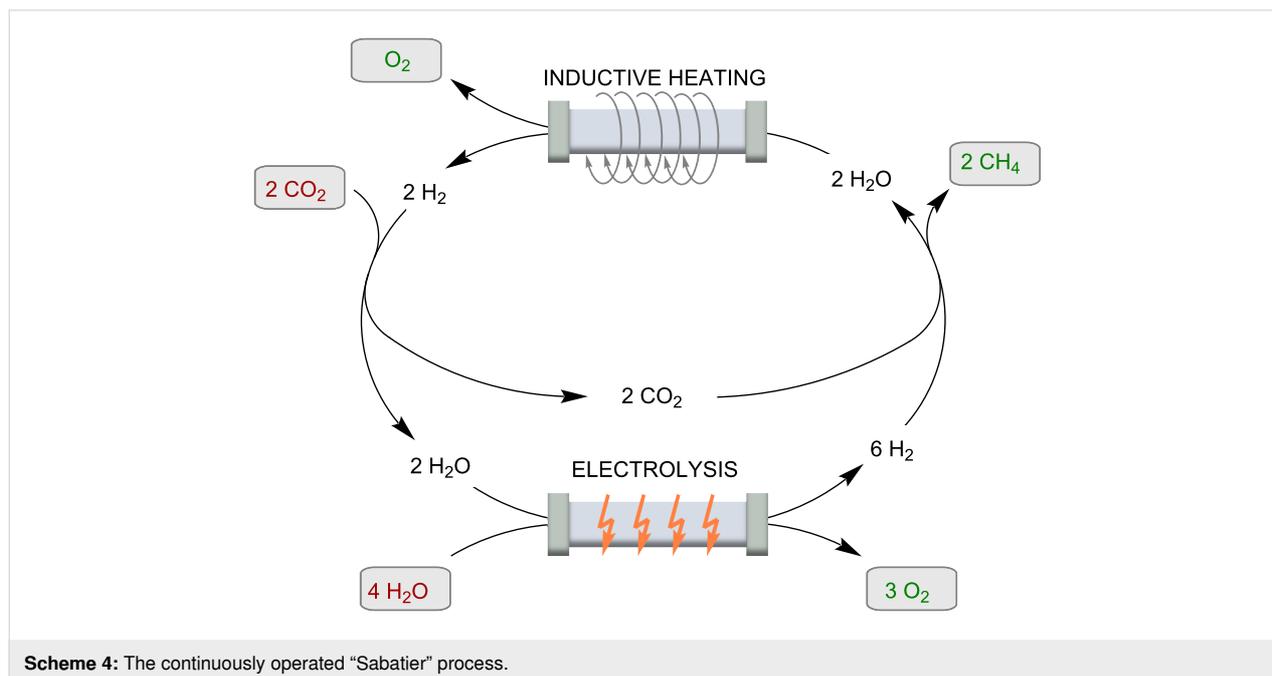

Scheme 4: The continuously operated "Sabatier" process.

lates the temperature. This feedback loop allowed the temperature of the catalyst bed to be fine-tuned and adjusted in real time to suit the conditions.

2.7 Biofuel production

The increasing demand for renewable energy sources goes hand in hand with the sustainable and efficient use of naturally occurring waste. Two factors that mainly affect the conversion rate of biodiesel are the use of catalysts and the heating process chosen. Inductive heating is applied to improve the pyrolysis of bio-oils, a process used to obtain high quality biofuels. Inductive heating is advantageous in this process because a rapid and uniform heating of the biomass and catalyst is important for product quality. Compared to a conventional heating process, the authors found that a higher quality of bio-oil with a higher yield of aromatic hydrocarbons and a lower oxygen content is obtained in a process with RF heating [41].

A potential energy source for biofuel production is napier grass. The group of Lin investigated the yield and pyrolytic products of HF heating in the pyrolysis of napier grass (Scheme 5) [42]. The yield of liquid products increased with heating rates up to 150 °C/min. Pine sawdust and its major components, lignin and cellulose, were pyrolyzed by RF heating at high temperatures ranging from 500 °C to 700 °C. The authors found that higher temperature resulted in higher gas yield and lower liquid yield. The results could be relevant to the forestry and paper industries, which produce large amounts of lignin as a byproduct. The authors compared the fast pyrolysis of poplar wood and switchgrass by RF heating. The highest yield of bio-oil was obtained for switchgrass at a pyrolysis temperature as low as 450 °C.

Scheme 5: Biofuel production from biomass using inductive heating for pyrolysis.
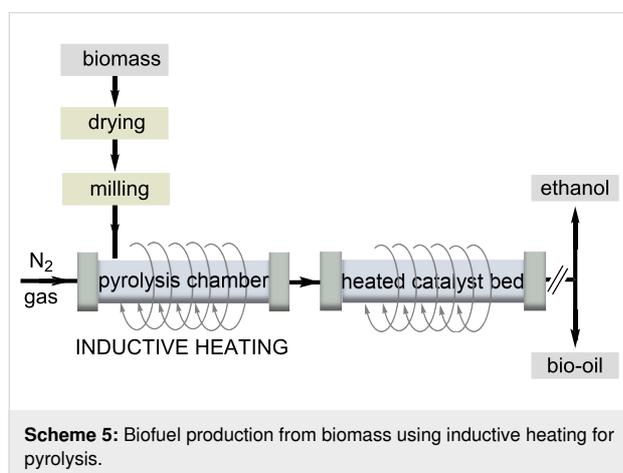
2.8 Water electrolysis

Electrolysis of water as a power-to-hydrogen (PtH) concept is not new, but has become one of the most important topics being discussed today. Due to the energy of hydrogen–hydrogen bonding, water electrolysis enables chemical storage of renewable electricity. Chatenet, Carrey and co-workers showed that the electrocatalytic reaction of hydrogen formation from water can be improved by using RF heating (Scheme 6) [43]. Thus, nickel-coated iron carbide NP (FeC-Ni) was developed to drastically reduce the overpotential at 20 mA/cm^2 (≈200 mV for OER). This kinetic enhancement corresponds to a temperature increase of 200 °C, although the actual temperature only increased by 5 °C. The authors suggested that the use of RF heating may allow water splitting near the equilibrium voltage at room temperature. Although it was expected that the magnetic field applied by inductive heating would disturb the flowing current, mainly positive effects were observed.


Scheme 6: Water electrolysis using an inductively heated electrolysis cell.
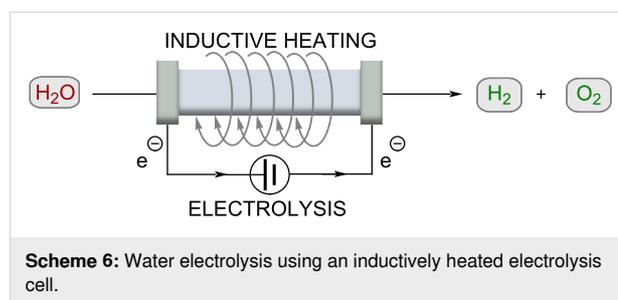
3 Micro- and mesoflow technology and indirect heating

3.1 Microwave-accelerated reactions under flow conditions

Reactions that take 20 minutes or longer under classical batch conditions can be accelerated considerably under continuous flow conditions by rapid heating, because flow chemistry usually involves the use of pressure-stable reactors, which leads to shortened residence times. Inductive heating, in addition to microwave irradiation [44-46] heating, can serve as an indirect and rapid heating technology that, when combined with pressure-resistant microstructured flow reactors, enables "flash" heating so that even supercritical conditions can be achieved. In this context, Poliakoff and co-workers used supercritical water to perform several industrially relevant and continuously guided conversions, using microwave irradiation as an indirect heating method [47]. Other examples in which the two enabling technologies microwave and flow were combined are the Dimroth rearrangement exemplified for the conversion of 1,3-thiazine **3** to the corresponding 3-substituted hydropyrimidine **4** (Scheme 7, reaction 1) [48].

A noteworthy example was recently published by Organ and co-workers [49]. A three-component reaction of an aldehyde **5**, a secondary amine **6**, and a terminal alkyne **7**, afforded aryl-propargylamines **8** in up to 84% yield under flow conditions
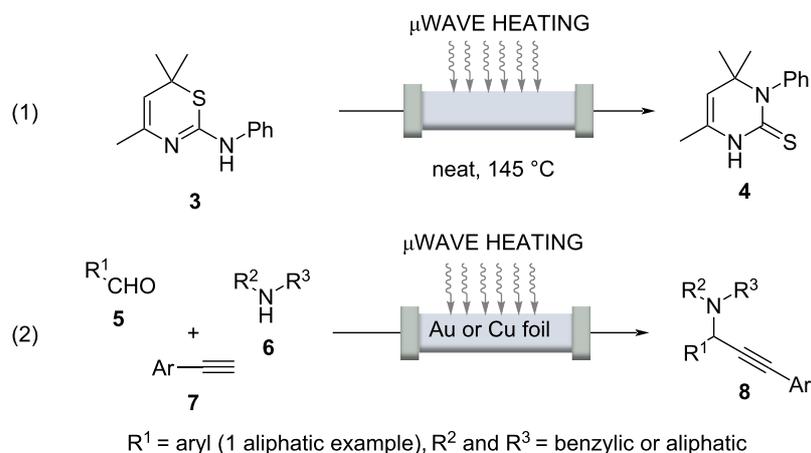
Scheme 7: Dimroth rearrangement (reaction 1) and three-component reaction (reaction 2) to propargyl amines **8** under continuous flow conditions with microwave assistance.

(Scheme 7, reaction 2). Microwave irradiation interacted with a thin foil of Cu or Au that served as catalyst inside the glass capillary. The work must be highlighted in that the actual temperature of the glass/metal surface could be determined locally using a high-resolution IR camera. It was found to be 950 °C and not 185 °C of the reaction mixture itself. These studies are noteworthy because it can be assumed that the temperatures determined by Organ locally on metal surfaces can also be transferred to inductively heated materials including superparamagnetic nanoparticles.
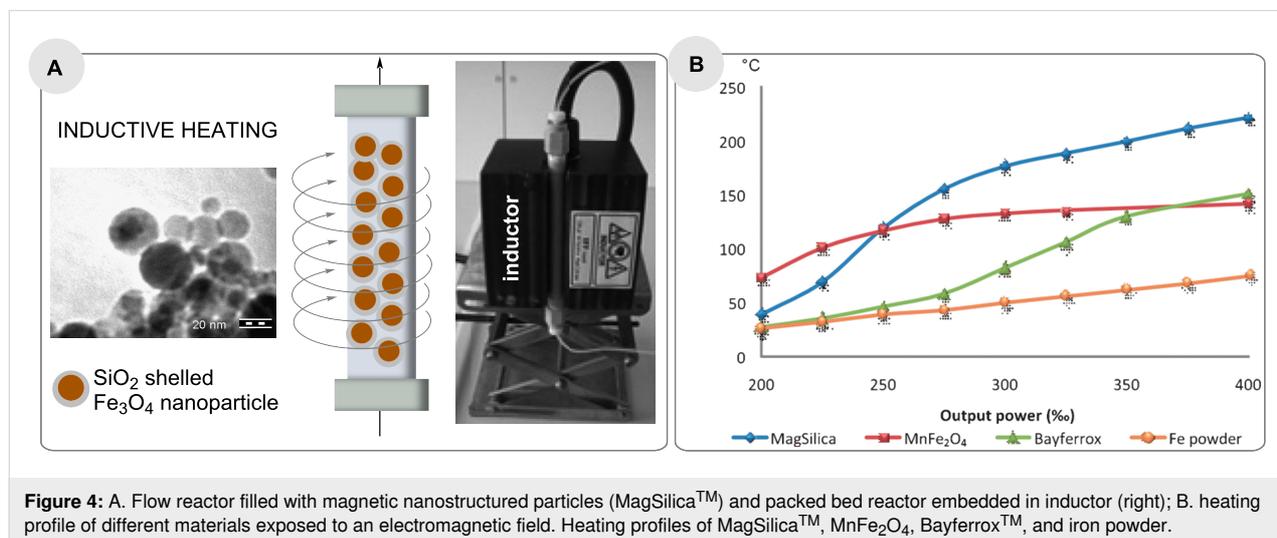
3.2 Reactions under flow conditions accelerated by inductive heating

3.2.1 First steps and comparison with other techniques: As mentioned in the introduction, various physical phenomena enable rapid heating of inductive materials such as steel or

copper, or fixed-bed materials composed of steel beads as well as superparamagnetic nanoparticles in an oscillating electromagnetic field. Kirschning and co-workers introduced nanostructured particles based on Fe_2O_3/Fe_3O_4 coated with silicon dioxide (core-shell nanostructured particles), called MagSilica^{TM} to be used as fixed-bed materials in many different continuous flow processes (Figure 4A) [50].

These materials are excited very rapidly in a medium frequency (25 kHz) electromagnetic field, heating reaction mixtures in packed bed reactors to temperatures up to 250 °C, which was measured at the reactor outlet (Figure 4B)).

The heat is generated only at the surface of the iron oxide nanoparticles (eddy currents) and this is dissipated to the surrounding environment, which is why the bulk temperature must be

Figure 4: A. Flow reactor filled with magnetic nanostructured particles (MagSilica^{TM}) and packed bed reactor embedded in inductor (right); B. heating profile of different materials exposed to an electromagnetic field. Heating profiles of MagSilica^{TM}, MnFe$_2$O$_4$, Bayferrox^{TM}, and iron powder.
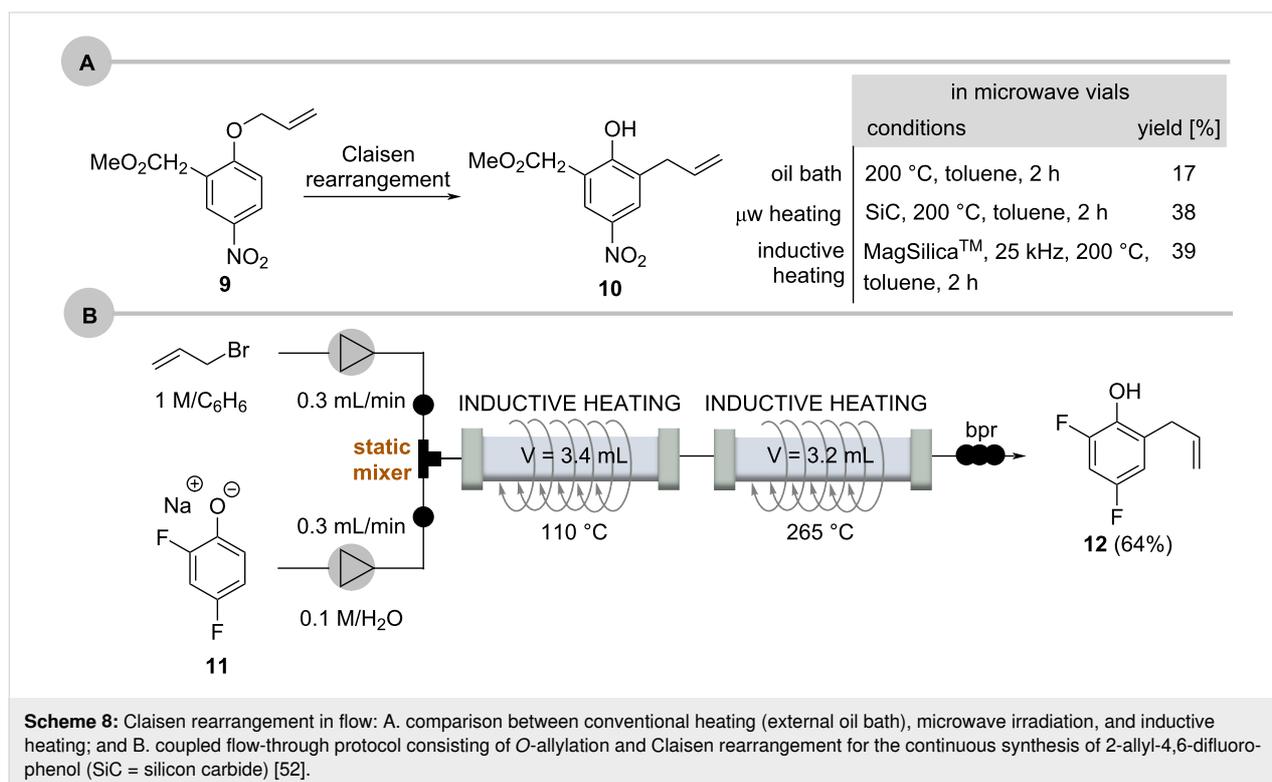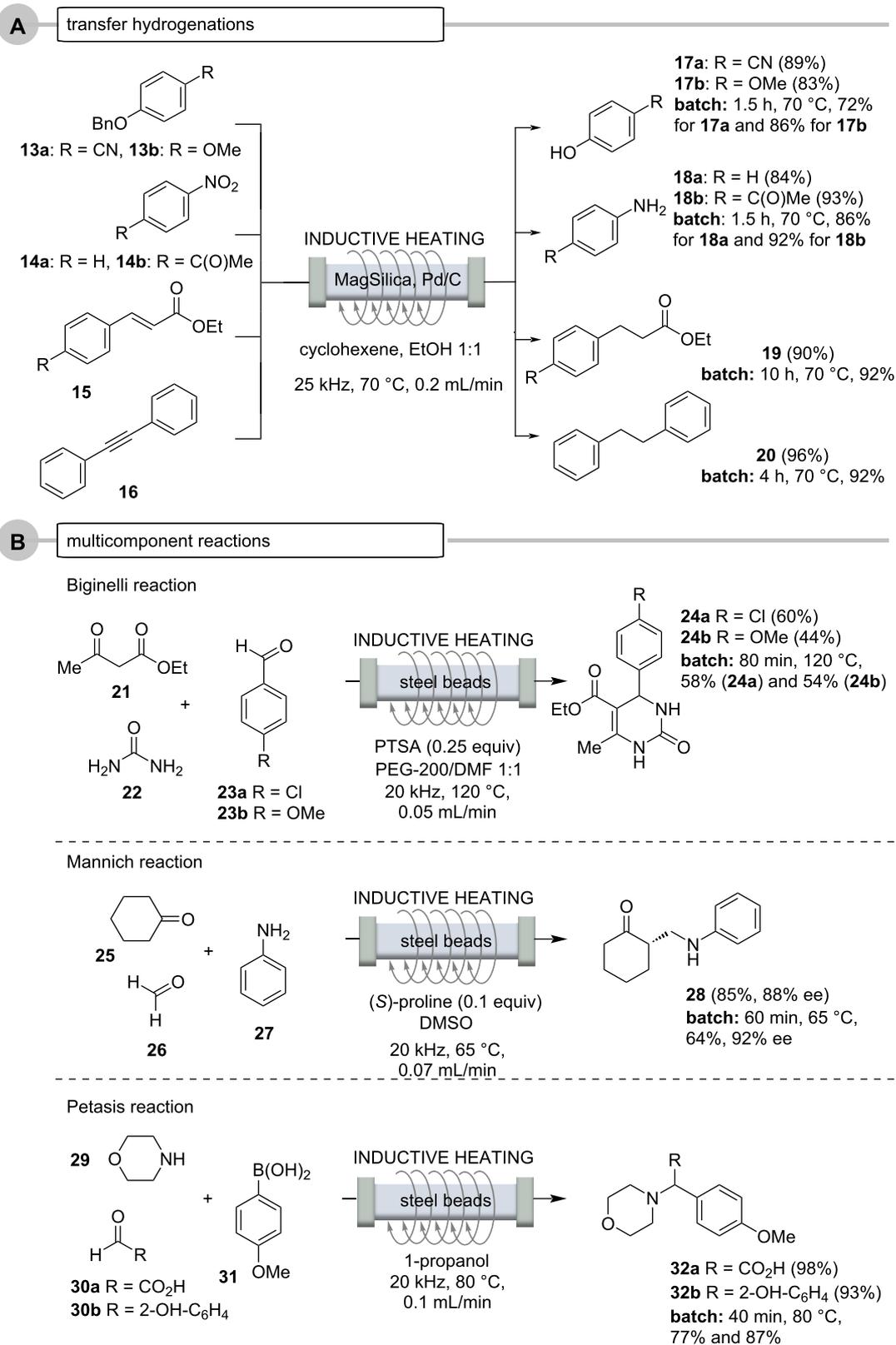
much lower than the surface temperature of the nanostructured particles (Figure 4B).

The Claisen rearrangement of the electron-deficient aryl allyl ether **9** was chosen to compare the versatility and performance of inductive heating with conventional and microwave heating (Scheme 8A) [50]. The effectiveness of inductive heating is clearly comparable to microwave-induced heating. In continuation of these studies a two-step sequence was developed which showed that Claisen rearrangements can be accelerated in water as solvent (Scheme 8B) [51]. The phenolate salt **11** was mixed with allyl bromide in a static mixer and inductively heated to 110 °C at 110–160 bar to form the *O*-allyl phenol which was heated in a second reactor to 265 °C where the Claisen rearrangement under near-critical conditions occurred to yield 2-allyl-4,6-difluorophenol (**12**) in 64% yield. In this example, the two reactors made of steel were heated directly by the external electromagnetic field.
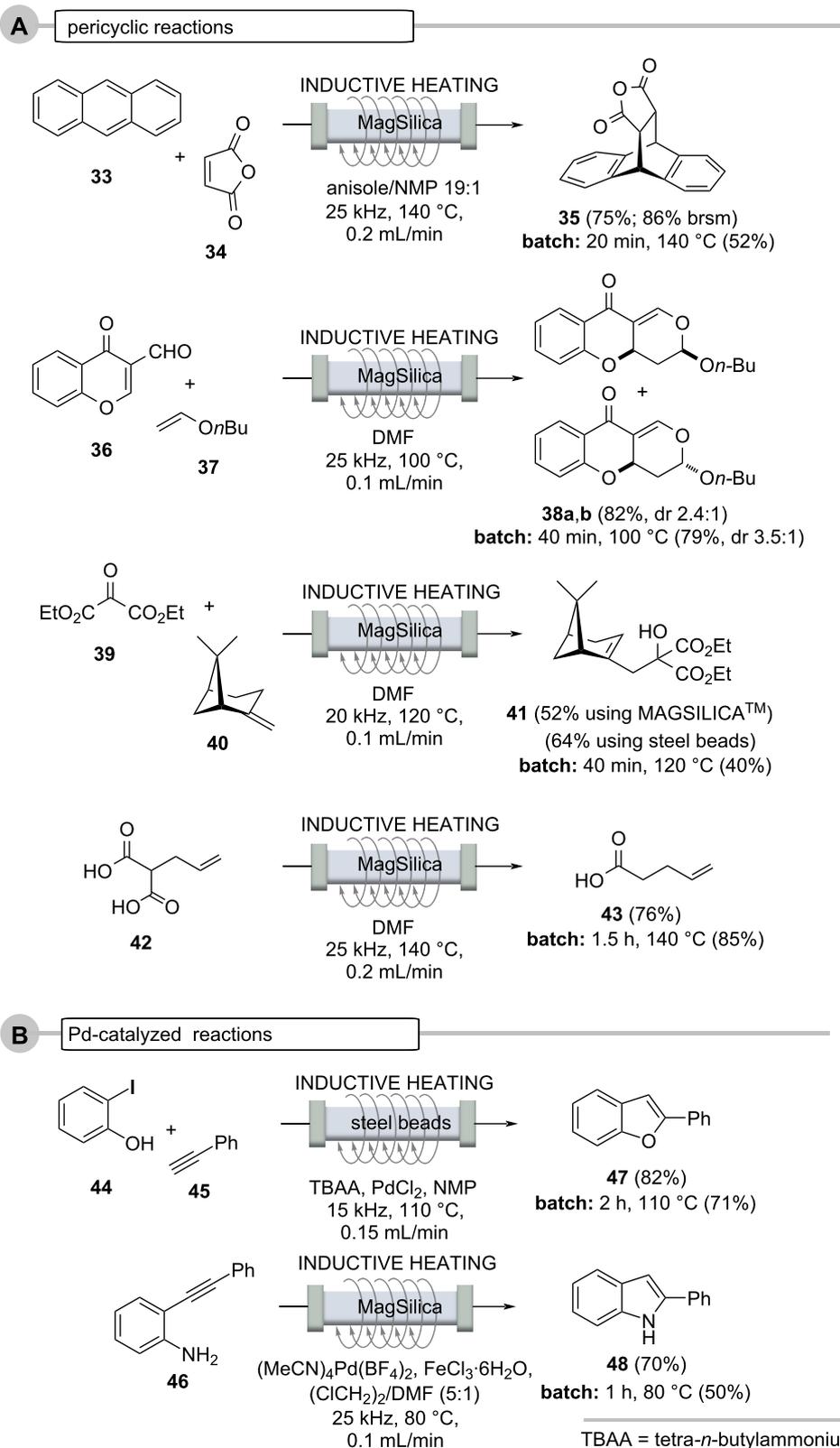
Other comparisons include the Pd-mediated transfer hydrogenations using ethanol in cyclohexene (Scheme 9, case A), multicomponent reactions (Scheme 9, case B), pericyclic reactions (Scheme 10, case A) and Pd-catalyzed reactions (Scheme 10, case B) [53]. Noteworthy, packed bed fillings used for the transfer hydrogenations (Pd) are reusable for several reductions without the need to adjust the overall reaction conditions (flow rate and residence time, temperature etc.).

Multicomponent reactions (MCRs) are of particular interest in the field of flow chemistry because this enabling technique can be easily automated. Thus, protocols can be iteratively repeated by simply changing building blocks so that compound libraries can be quickly accessed [54,55]. The formation of heterocycles traditionally often requires very harsh conditions, so that high pressure and high temperature can greatly accelerate many of these transformations. This indeed is the domain of flow chemistry. The Biginelli [56,57], Mannich [58] and Petasis [55,59-61] reactions are typical representative examples and these have been transferred into flow protocols (Scheme 9B). Steel beads serve as fix-bed materials to inductively heat up glass reactors. For the Biginelli reaction solubility of the starting urea (**22**) as well as the products **24a** and **24b** were an issue being overcome by using a solvent mixture of PEG/DMF 1:1. Also the proline-catalyzed asymmetric Mannich reaction was achieved with cyclohexanone (**25**), formaldehyde (**26**), and aniline (**27**) and 10 mol % of the organocatalyst to yield β-aminoketone **28** in 85% yield (88% ee), in less than 1 h. Although a significantly higher yield was achieved compared to the batch experiment, a slight reduction in enantioselectivity was observed. The Petasis or Petasis boron-Mannich (PBM) reaction of glyoxalic acid (**30a**) or salicylic aldehyde (**30b**), with morpholine (**29**) and *p*-methoxyphenylboronic acid (**31**) furnished α-aminocarboxylic acid **32a** and phenol **32b** in excellent yield (98% and 93%), again much higher than the yields found for the batch protocol (77% and 87%).

Scheme 8: Claisen rearrangement in flow: A. comparison between conventional heating (external oil bath), microwave irradiation, and inductive heating; and B. coupled flow-through protocol consisting of *O*-allylation and Claisen rearrangement for the continuous synthesis of 2-allyl-4,6-difluorophenol (SiC = silicon carbide) [52].

A transfer hydrogenations

13a: R = CN, **13b**: R = OMe

14a: R = H, **14b**: R = C(O)Me

15

16

INDUCTIVE HEATING

MagSilica, Pd/C

cyclohexene, EtOH 1:1

25 kHz, 70 °C, 0.2 mL/min

17a: R = CN (89%)
17b: R = OMe (83%)
batch: 1.5 h, 70 °C, 72%
for **17a** and 86% for **17b**

18a: R = H (84%)
18b: R = C(O)Me (93%)
batch: 1.5 h, 70 °C, 86%
for **18a** and 92% for **18b**

19 (90%)
batch: 10 h, 70 °C, 92%

20 (96%)
batch: 4 h, 70 °C, 92%

B multicomponent reactions

Biginelli reaction

21

22

23a R = Cl
23b R = OMe

INDUCTIVE HEATING

steel beads

PTSA (0.25 equiv)
PEG-200/DMF 1:1
20 kHz, 120 °C,
0.05 mL/min

24a R = Cl (60%)
24b R = OMe (44%)
batch: 80 min, 120 °C,
58% (**24a**) and 54% (**24b**)

Mannich reaction

25

26

27

INDUCTIVE HEATING

steel beads

(*S*)-proline (0.1 equiv)
DMSO
20 kHz, 65 °C,
0.07 mL/min

28 (85%, 88% ee)
batch: 60 min, 65 °C,
64%, 92% ee

Petasis reaction

29

30a R = CO$_2$H
30b R = 2-OH-C$_6$H$_4$

31

INDUCTIVE HEATING

steel beads

1-propanol
20 kHz, 80 °C,
0.1 mL/min

32a R = CO$_2$H (98%)
32b R = 2-OH-C$_6$H$_4$ (93%)
batch: 40 min, 80 °C,
77% and 87%

Scheme 9: Continuous flow reactions and comparison with batch reaction (oil bath). A. Pd-catalyzed transfer hydrogenations using ethanol in cyclohexene [53], B. multicomponent reactions.

A pericyclic reactions

33 + **34**

INDUCTIVE HEATING
MagSilica

anisole/NMP 19:1
25 kHz, 140 °C,
0.2 mL/min

35 (75%; 86% brsm)
batch: 20 min, 140 °C (52%)

36 + **37**

INDUCTIVE HEATING
MagSilica

DMF
25 kHz, 100 °C,
0.1 mL/min

38a,b (82%, dr 2.4:1)
batch: 40 min, 100 °C (79%, dr 3.5:1)

EtO_2C CO_2Et + **40**

39

INDUCTIVE HEATING
MagSilica

DMF
20 kHz, 120 °C,
0.1 mL/min

41 (52% using MAGSILICA™)
(64% using steel beads)
batch: 40 min, 120 °C (40%)

42

INDUCTIVE HEATING
MagSilica

DMF
25 kHz, 140 °C,
0.2 mL/min

43 (76%)
batch: 1.5 h, 140 °C (85%)

B Pd-catalyzed reactions

44 **45**

INDUCTIVE HEATING
steel beads

TBAA, $PdCl_2$, NMP
15 kHz, 110 °C,
0.15 mL/min

47 (82%)
batch: 2 h, 110 °C (71%)

46

INDUCTIVE HEATING
MagSilica

$(MeCN)_4Pd(BF_4)_2$, $FeCl_3 \cdot 6H_2O$,
$(ClCH_2)_2$/DMF (5:1)
25 kHz, 80 °C,
0.1 mL/min

48 (70%)
batch: 1 h, 80 °C (50%)

TBAA = tetra-*n*-butylammonium acetate

Scheme 10: Continuous flow reactions and comparison with batch reaction (oil bath). A. pericyclic reactions and B. Pd-catalyzed reactions.

Pericyclic reactions such as the Diels–Alder and hetero-Diels–Alder cycloadditions, the Alder-En reaction, as well as the decarboxylation of α-alkylated malonic acids, are also suitable for flow protocols in combination with inductive heating (Scheme 10, case A) [53]. The yields but especially the residence times of the reactions outperformed those of the analogous experiments carried out under batch conditions by far [62-64].

The heating method was also successfully tested on various thermally conducted pericyclic reactions (Scheme 10, case A), such as in (hetero)-Diels–Alder reactions (anthracene (**33**) and maleic anhydride (**34**) to the cycloaddition adduct **35** and chromene carbaldehyde **36** and enol ether **37** to the diastereomeric pyrano-chromenes **38**), Alder-En reactions (oxomalonate diethyl ester (**39**) and β-pinene (**40**) to give the α-pinene derivative **41**), and the thermal decarboxylation of the malonic acid derivative **42** to give pent-4-enecarboxylic acid (**43**). In many cases, the flow protocol provided improved yields compared to the corresponding batch syntheses.

Palladium-catalyzed cross-coupling reactions require higher temperatures and thus can be realized in an inductively heated flow system [65-71]. This is exemplified for the tandem synthesis of benzofuran **47** and phenylindole **48** (Scheme 10, case B) starting from phenol **44** and aniline derivative **46**, respectively. The latter reaction was carried out in a glass reactor filled with MagSilica[TM] [53].

3.2.2 Using chemically active fixed-beds (stoichiometric reagents): Flow chemistry can be advantageously combined with the use of chemically active fixed-bed materials, especially heterogeneous catalysts. Here, too, the reactor material can either be heated directly by induction or there are additives in the fixed-bed material that interact with the oscillating electromagnetic field. Recently, Rebrov and co-workers disclosed the direct amide formation of a carboxylic acid and anilline using high energy ball milling to prepare the sulfated TiO_2 (50 wt %)/$NiFe_2O_4$ (50 wt %) catalyst that serves as fixed-bed material (Scheme 11, case A) [72,73]. The reaction was carried out at 150 °C and an internal pressure of 7 bar. Remarkably, the process could be operated for 15 h with a slight decrease of effciency. Importantly, the catalyst activity can completely be restored when heating the packed bed to 400 °C exposed to an air flow. The importance of this study is the fact that no activating agents are required and water is the only byproduct.

Organometallic chemistry and heating are not among the most intuitively sensible combinations. However, prior to the formation of an organometallic species, e.g., from the metals magnesi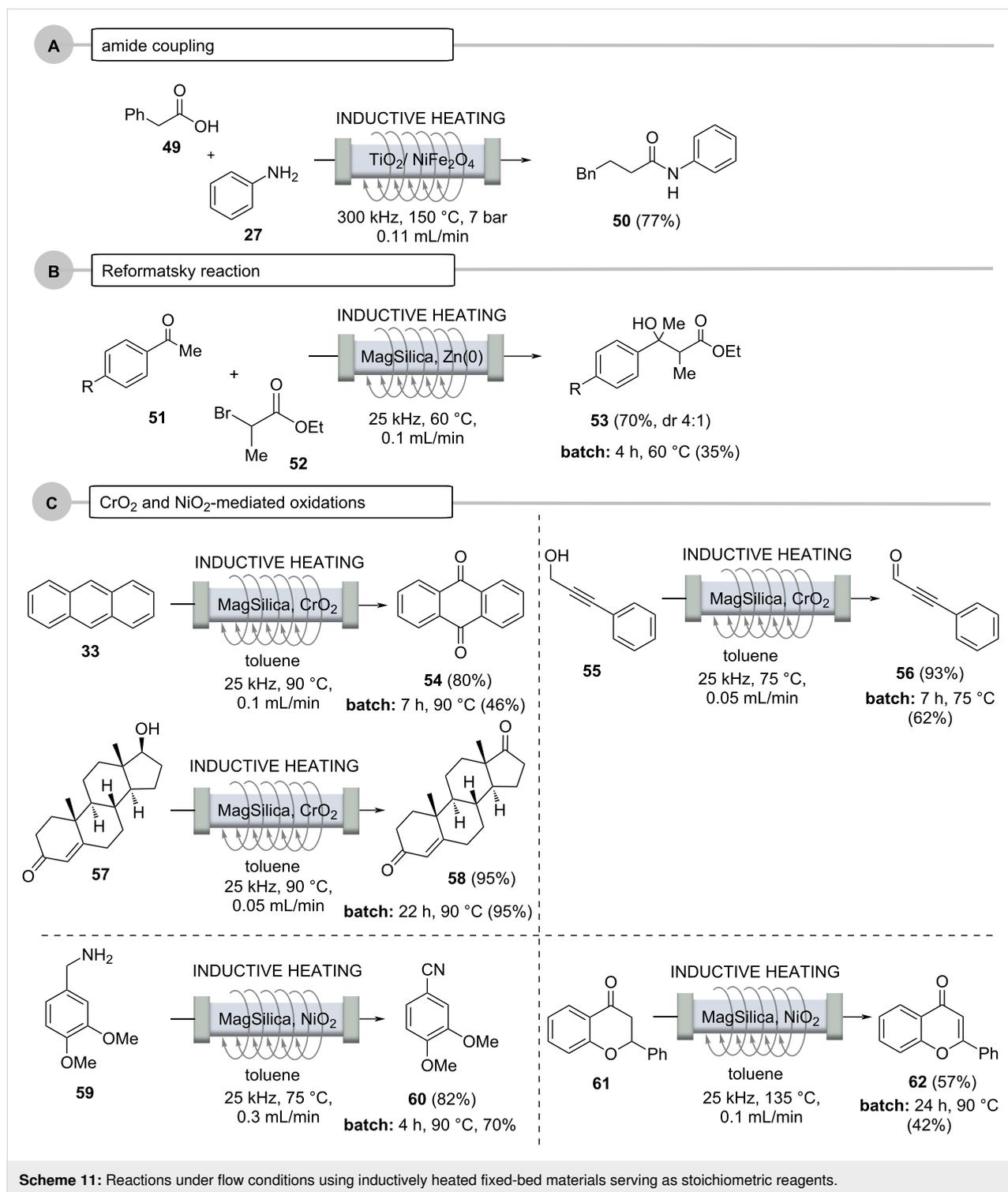um or zinc, (thermal) activation is required. This was demonstrated for the Reformatzky reaction (Scheme 11, case B) [53,74], in which zinc powder was mixed with MagSilica[TM] and positioned inside the flow reactor. For example, 2-bromopropanoic acid ethyl ester (**52**) and acetophenone **51** were reacted in a heated fixed-bed reactor with the mediation of zinc to give the Reformatsky product **53**, and, as commonly observed, in significantly improved yields compared to the corresponding batch processes.

Oxidations, especially metal oxide-based variants, are among the most frequently performed chemical reactions. Interesting examples are MagTrieve[TM], which contains CrO_2 and nickel peroxide (NiO_2). Both were mixed with MagSilica[TM] and used as fixed-bed materials (Scheme 11, case C) [75].

At this point, it is important to note that CrO_2, despite its paramagnetic properties, does not heat up in an oscillating electromagnetic field because it does not exhibit conductive properties, so it had to be mixed with MagSilica[TM]. Several oxidations were performed, including those of anthracene (**33**), propargyl alcohol **55** and testosterone (**57**), which proceeded smoothly with 80%, 93%, and 95% yields, respectively, in a fraction of the time required for the corresponding batch processes. In a simplified purification protocol, potential metal impurities were then removed using a magnet. This approach could facilitate the use of metal oxides in industry for a broader range of oxidative applications. NiO_2, on the other hand, was used to achieve the dehydrogenation of amines (to nitriles) and to perform the α,β dehydrogenation of ketones **61**.

3.2.3 Using chemically active fixed beds (catalysts): Copper metal in the form of wires or turnings can also be inductively heated when placed inside flow reactors (Scheme 12, case A). There, it performs a second role by also becoming a source for a copper catalyst, either by being released into solution or by acting as a surface-active species capable of promoting "click" reactions between alkynes and azides [76-81]. The process can be coupled with in situ generation of the azide from the corresponding bromide. The 1,2,3-triazoles are formed in up to 99% yield and in less than 10 minutes residence time, which includes azide formation prior to the cycloaddition step. Interestingly, this process could not be successfully repeated under conventional batch conditions. Organ's findings [49] suggest that the inductive heating technique creates local hot spots, either on the copper surface due to skin depth effects or alternatively in copper nanoparticles released into solution, likely leading to a dramatic acceleration of the cycloaddition reaction.

Reactions with soluble metal complexes or metal nanoparticles, utilized in transition-metal catalysis, are often avoided, especially if the metal contamination in the product exceeds certain

Scheme 11: Reactions under flow conditions using inductively heated fixed-bed materials serving as stoichiometric reagents.

limits. This is particularly true for the pharmaceutical industry. A continuous flow protocol for oxidations of alcohols to aldehyes or ketones using gold nanoparticles in the presence of oxygen gas or atmospheric air was achieved by modifying the silica shell of nanostructured MagSilica[TM] with gold nanoparticles (Scheme 12, case B). After heating these modified SPIONs

in an electromagnetic field, a continuous process could be established by oxidation with molecular oxygen introduced into the reaction stream via a tube-in-tube membrane reactor, a process which should be very attractive for industrial applications, as oxygen or air act as cheap and environmentally friendly oxidants [82].
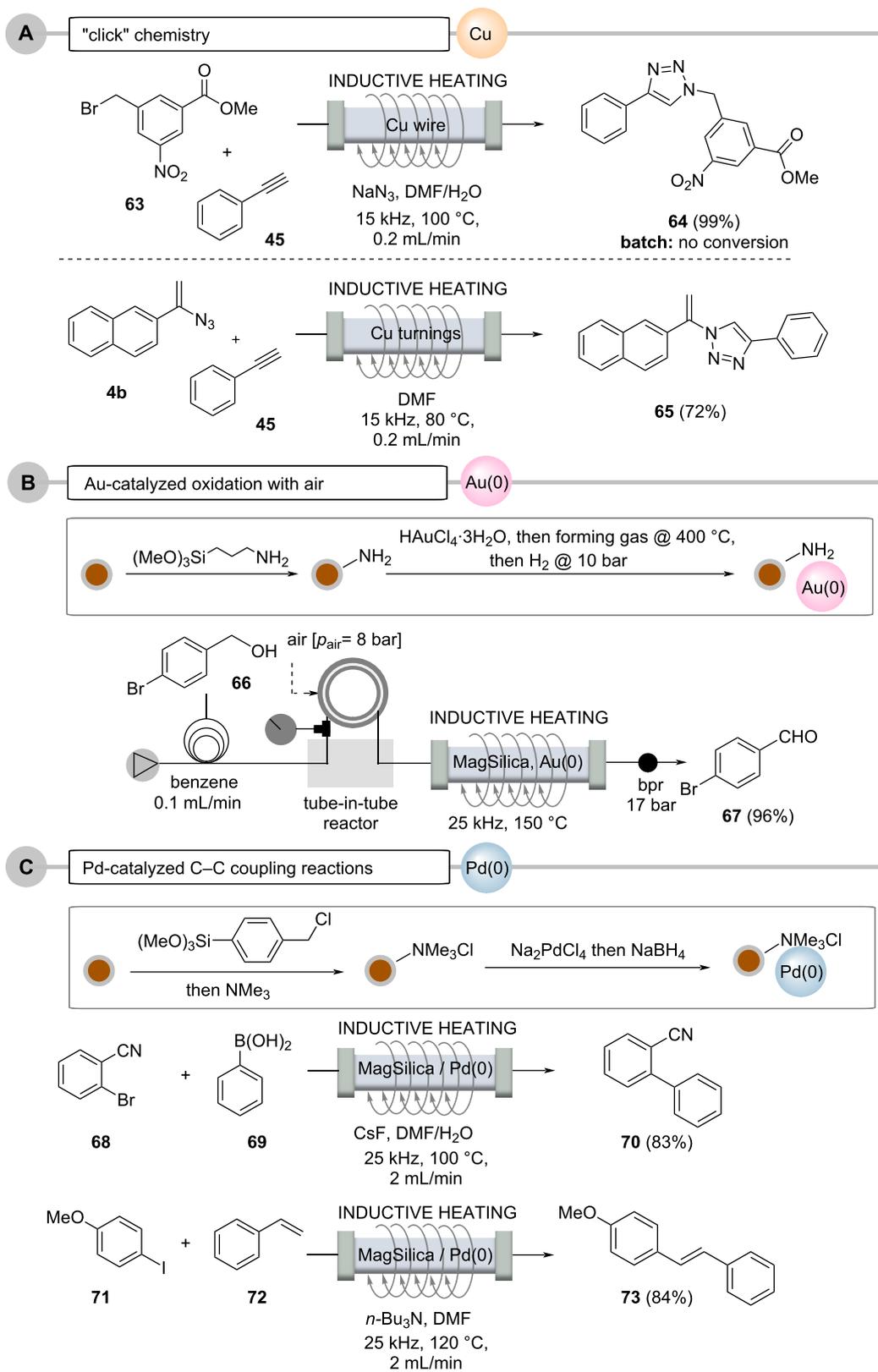
Scheme 12: Reactions under flow conditions using inductively heated fixed-bed materials serving as catalysts: A. with copper metal, B. with Au-doped MagSilica^TM, and C. with Pd-doped MagSilica^TM.

An interesting combination of SPIONs and transition-metal catalysis opens up when both concepts are combined architecture-wise [83]. For instance, catalytically active metal nanoparticles, e.g., consisting of Pd(0), can be deposited on the silicate surface of MagSilica^TM, so that the required heat for Pd(0)-mediated catalysis can be generated directly by the functionalized nanostructured particles (Scheme 12, case C) [50].

This was achieved by reductive precipitation of Pd(0) nanoparticles from ammonium-bound tetrachloropalladate [84,85], which showed good catalytic activity in various cross-coupling reactions under flow conditions. In these reactions, the leaching of palladium was as low as 34 ppm for Suzuki–Miyaura reactions and 100 ppm for Heck reactions. Importantly, the functionalized nanoparticles could be reused several times without observing a decrease in catalytic activity.

3.2.4 Multistep processes: The inductive heating technology has also been used in multistep processes targeting drugs or important molecules in the fragrance industry.

The first example deals with a metal-free carbon–carbon-bond formation process between tosylhydrazones generated from the corresponding aldehydes **74** and boronic acids **76**, yielding a reduced arylation product **77** [86,87]. Mechanistically, either diazo or carbene intermediates can be proposed, as Barluenga has outlined, and migration of the aryl group leads to an alkyl-boronic acid, which is hydrolyzed by protodeboronation, yielding the arylation product **77**. A two-step flow protocol began with the carbonyl compounds (e.g., **74**), and the first flow step yielding tosylhydrazones that were transferred directly to the second reactor to be coupled with boronic acids (Scheme 13). Both steps required heating, which was per-

formed by electromagnetic induction of a fixed-bed material based on steel beads. A continuous two-step flow process over a period of almost two days yielded the arylation product in 88% yield, demonstrating the robustness of the process [87].

The use of water as a green solvent is a greatly increasing field of research. But besides its reduced environmental footprint, water features unique physicochemical properties at supercritical conditions. The five step synthesis of a typical antipsychotic drug iloperidone (**80**) is an impressive example of how supercritical water can be utilized as a privileged solvent in organic transformations (Scheme 14) [88]. Because of space limitations, we here only highlight the last five steps, which all involve inductive heating between 110–180 °C and four out of five steps are performed in supercritical water. Phenol **79** and the *N*-alkylated product **78** were mixed and pumped through a 1/8" stainless steel reactor, heated to 180 °C at 4.5 MPa for 7.5 min. These conditions allowed to suppress the decomposition of the *N*-alkylation product **78** by using a 1/8"-reactor. The subsequent purification was realized by a clever catch and release protocol based on a silica column, yielding iloperidone (**80**, 67%).

The tricyclic antidepressant hydrochloride of amitriptyline (**84**) was the target of a multistep continuous flow protocol in which, for one reaction step, inductive heating was used to achieve water elimination triggered exclusively under thermal conditions [54]. The flow process started with a multilithiation sequence which included a carboxylation and a Parham cyclization and hence a Grignard alkylation of ketone **82** using reagent **81**. The resulting alcohol **83** was subjected to thermolysis that led to water elimination. This step proceeded in just 30 s by employing the inductive heating technique. The crude elimination
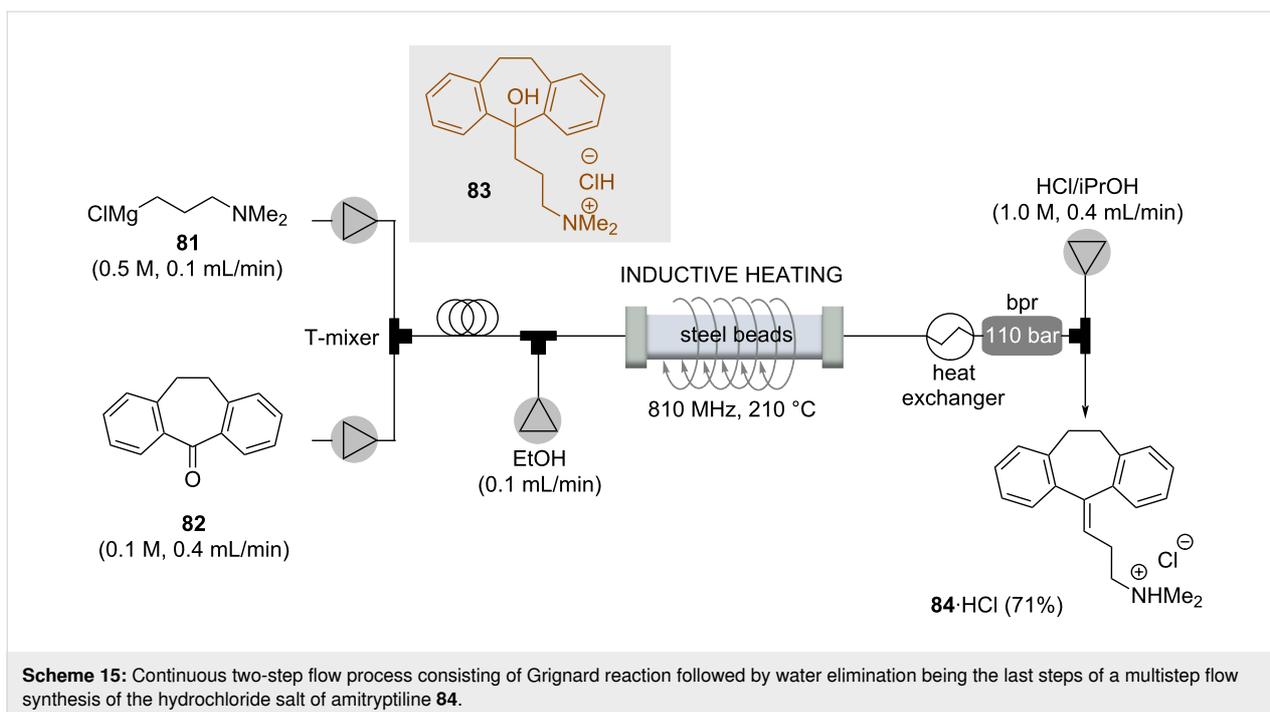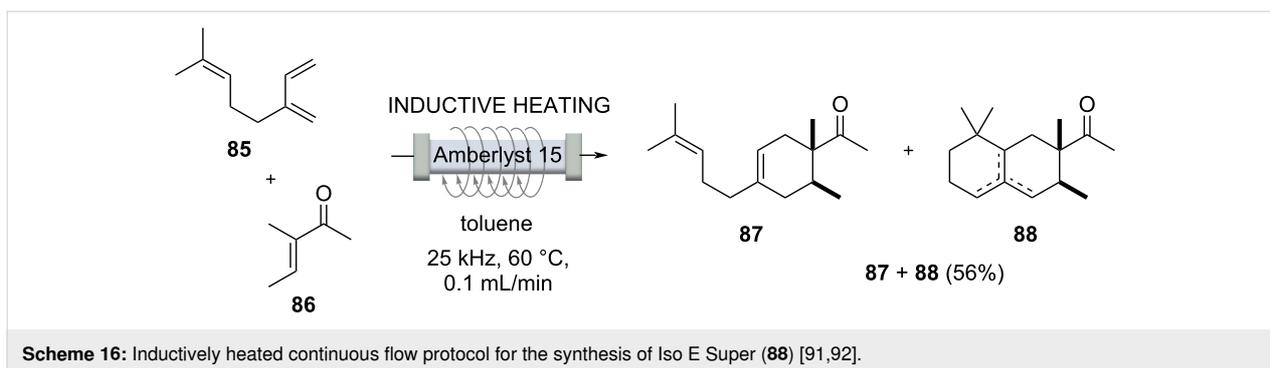
Scheme 13: Two step flow protocol for the preparation of 1,1'-diarylalkanes **77** from ketones and aldehydes **74**, respectively, and boronic acids **76**.

Scheme 14: *O*-Alkylation, the last step in the multistep flow synthesis of Iloperidone (**80**) accompanied with a "catch and release" purification protocol.
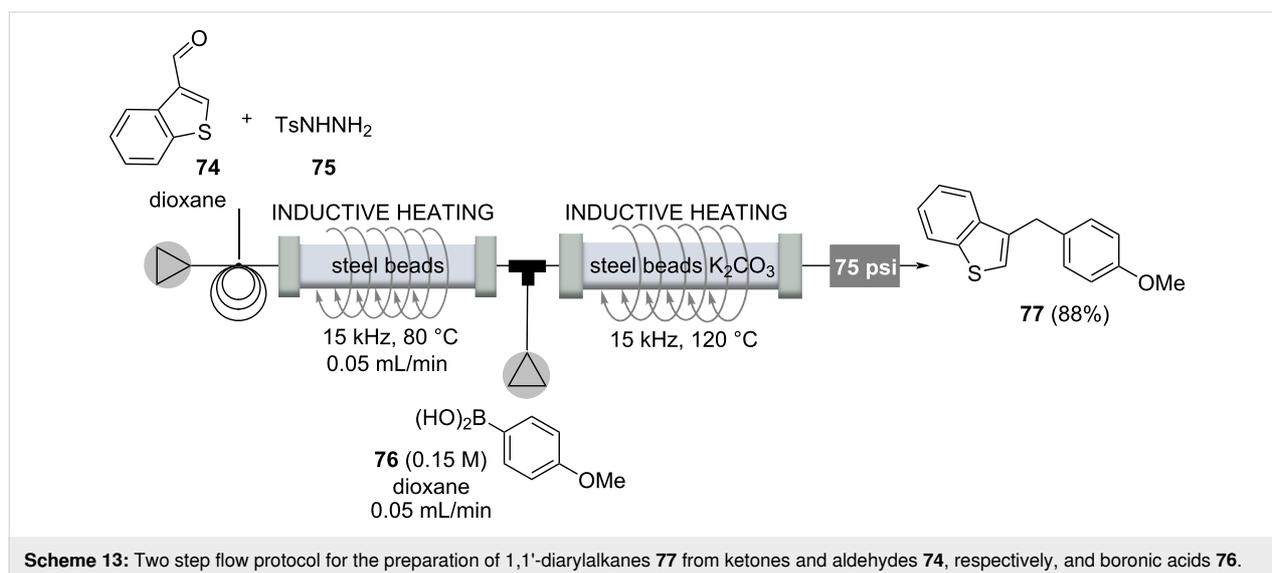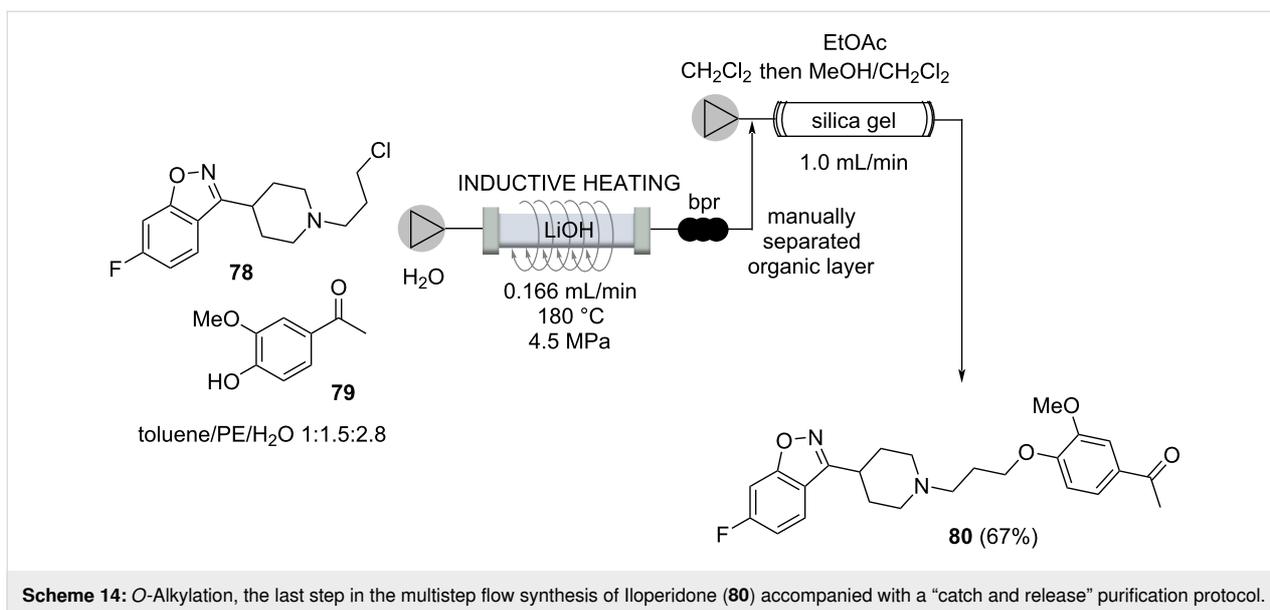
product was then mixed with a 1 M HCl solution in iPrOH that initiated crystallization of the hydrochloride salt of amitryptiline (**84**) (Scheme 15).

Iso E Super® (**88**) [89] is one of the most successful synthetic fragrances ever developed [90]. It is a component of a variety of perfumes with varying ratios and is the first example of a single ingredient sold as perfume in the fragrance industry. Structurally, it is related to natural terpenes. Starting from myrcene (**85**), an inductively heated process was developed, initiated

with a Diels–Alder cycloaddition that furnished ambrelux (**87**) (Scheme 16). This was cyclized under acidic conditions with Amberlyst 15™ ion exchange resin embedded inside the flow reactor. However, successful conversion to an industrial process was hindered by the fact that polymerization of the starting material myrcene (**85**) could not be suppressed, leading to fouling of the catalyst and consequently to inactivation. The polymerization could be suppressed by preloading the reactor with the vinyl methyl ketone **86** before starting the process. Nevertheless, it could not be sustained over a longer period of time. By

Scheme 15: Continuous two-step flow process consisting of Grignard reaction followed by water elimination being the last steps of a multistep flow synthesis of the hydrochloride salt of amitryptiline **84**.

Scheme 16: Inductively heated continuous flow protocol for the synthesis of Iso E Super (**88**) [91,92].

splitting the process into two independent operations, a yield of 56% (**87** + **88**) was obtained for the Diels–Alder cycloaddition, and suppressed polymerization at room temperature. This mixture was then converted in a second step and an Amberlyst 15[TM]-catalyzed cyclization at 60 °C gave **88** with a selectivity of 95%. Reactions such as polymerizations that inhibit the catalyst are side reactions that are very difficult to control, but this example sheds light on an often overlooked limitation of flow processes.

Musk-like fragrances occupy a special position among perfumes. An illustrative multistep protocol with practical relevance to the fragrance and flavor industry is a three-step flow-through protocol leading to macrocycles with musk-like olfactoric properties, which was realized under extreme conditions. These include the use of safety-hazardous reaction mixtures, the handling of explosive intermediates, and their pyrolysis at high temperatures (Scheme 17) [93]. Cyclohexanone (**25**) was mixed with conc. formic acid, and a mixture of H_2O_2 (30%)/HNO_3

Scheme 17: Three-step continuous flow synthesis of macrocycles **89** and **90** with musk-like olfactoric properties.
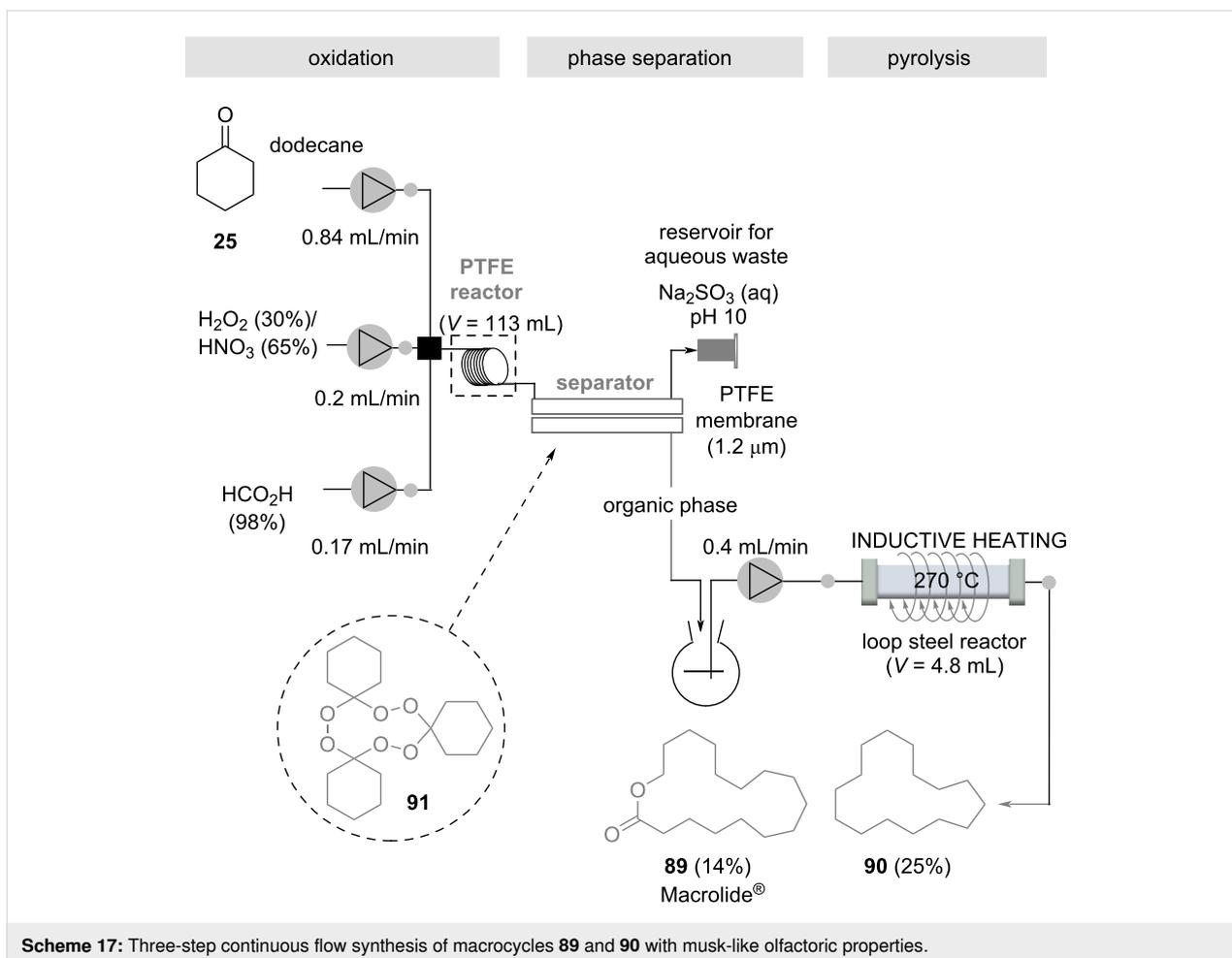
(65%) in a PTFE reactor at rt. This led to the formation of the cyclic triperoxide **91** in 48% (isolated) yield. Interestingly, the equilibrium favors the formation of the trimer **91** over the corresponding dimeric diperoxide. The reaction mixture was then transferred to a continuous phase separator equipped with a semipermeable membrane, from where the organic phase was transferred to a stainless steel loop reactor. Here, the macrocyclic triperoxide **91** was subjected to pyrolysis at 270 °C. This was done by inductive heating and the residence time was only 12 minutes. The Macrolide® **89** was obtained in 14% together with the aliphatic macrocyclic **90**, the latter can be oxidatively converted into the corresponding ketone, which is of practical importance in the fragrance industry. It is clear that this process could not be established as a batch protocol due to the hazardous conditions.

Conclusion

Inductive heating and flow chemistry are an ideal combination for performing continuously operated high-temperature and high-pressure syntheses. The technical setup is quite simple compared to corresponding microwave devices, the heating process is very efficient, and energetically extremely favorable. Remarkable examples in the field of fundamental chemical processes in a world that requires new solutions for energy supply show the power of inductive heating. In addition, academic examples draw attention to the use of continuously operated chemical processes with induction heating for the fields of bulk chemical production and the fragrance and flavor industries, as well as, eventually, the pharmaceutical industry. The authors are certain that this combination of enabling technologies holds great future opportunities.

Acknowledgements

ORCID® iDs

Conrad Kuhwald - https://orcid.org/0000-0001-9319-4526
Andreas Kirschning - https://orcid.org/0000-0001-5431-6930

References

1. Kirschning, A.; Kupracz, L.; Hartwig, J. *Chem. Lett.* **2012**, *41,* 562–570. doi:10.1246/cl.2012.562
2. Wang, W.; Tuci, G.; Duong-Viet, C.; Liu, Y.; Rossin, A.; Luconi, L.; Nhut, J.-M.; Nguyen-Dinh, L.; Pham-Huu, C.; Giambastiani, G. *ACS Catal.* **2019**, *9,* 7921–7935. doi:10.1021/acscatal.9b02471
3. Reddy, L. H.; Arias, J. L.; Nicolas, J.; Couvreur, P. *Chem. Rev.* **2012**, *112,* 5818–5878. doi:10.1021/cr300068p
4. Norris, M. D.; Seidel, K.; Kirschning, A. *Adv. Ther.* **2019**, *2,* 1800092. doi:10.1002/adtp.201800092
5. Chen, G.; Roy, I.; Yang, C.; Prasad, P. N. *Chem. Rev.* **2016**, *116,* 2826–2885. doi:10.1021/acs.chemrev.5b00148
6. Wadajkar, A. S.; Menon, J. U.; Kadapure, T.; Tran, R. T.; Yang, J.; Nguyen, K. T. *Recent Pat. Biomed. Eng.* **2013**, *6,* 47–57. doi:10.2174/1874764711306010007
7. Lee, N.; Yoo, D.; Ling, D.; Cho, M. H.; Hyeon, T.; Cheon, J. *Chem. Rev.* **2015**, *115,* 10637–10689. doi:10.1021/acs.chemrev.5b00112
8. Kappe, C. O. *Angew. Chem., Int. Ed.* **2004**, *43,* 6250–6284. doi:10.1002/anie.200400655
9. Lidström, P.; Tierney, J.; Wathey, B.; Westman, J. *Tetrahedron* **2001**, *57,* 9225–9283. doi:10.1016/s0040-4020(01)00906-1
10. Benkowsky, G. *Induktionserwärmung. Härten, Glühen, Schmelzen, Löten, Schweissen; Grundlagen und praktische Anleitungen für Induktionserwärmungsverfahren, insbesondere auf dem Gebiet der Hochfrequenzerwärmung,* 5th ed.; Verlag Technik: Berlin, Germany; p 12.
11. Liedtke, D. *Wärmebehandlung von Eisenwerkstoffen I;* Expert Verlag: Renningen, Germany, 2014.
12. Thompson, K.; Gianchandani, Y. B.; Booske, J.; Cooper, R. F. *J. Microelectromech. Syst.* **2002**, *11,* 285–292. doi:10.1109/jmems.2002.800929
13. Lammel, C.; Dilger, K. *Adhaes.–Kleben Dichten* **2000**, *44,* 11.
14. Wlach, S.; Wachinger, G.; Meer, T.; Lammel, C. Verfahren zum Verbinden eines ersten Materials mit einem zweiten Material im Flugzeugbau. WO Patent WO2009/047010, April 16, 2009.
15. Peterson, T. R.; Walker, M. A. Multipass induction heating for thermoplastic welding. U.S. Patent US5486684, Jan 23, 1996.
16. Ruta, S.; Chantrell, R.; Hovorka, O. *Sci. Rep.* **2015**, *5,* 9090. doi:10.1038/srep09090
17. Hergt, R.; Dutz, S.; Müller, R.; Zeisberger, M. *J. Phys.: Condens. Matter* **2006**, *18,* S2919–S2934. doi:10.1088/0953-8984/18/38/s26
18. Néel, L. *J. Phys. Radium* **1950**, *11,* 49–61. doi:10.1051/jphysrad:0195000110204900
19. Dutz, S.; Hergt, R. *Int. J. Hyperthermia* **2013**, *29,* 790–800. doi:10.3109/02656736.2013.822993
20. Kneller, E. F.; Luborsky, F. E. *J. Appl. Phys.* **1963**, *34,* 656–658. doi:10.1063/1.1729324
21. Appino, C.; de la Barrière, O.; Fiorillo, F.; LoBue, M.; Mazaleyrat, F.; Ragusa, C. *J. Appl. Phys.* **2013**, *113,* 17A322. doi:10.1063/1.4795744
22. Moses, A. J. Eddy Current Losses in Soft Magnetic Materials. *Wiley Encyclopedia of Electrical and Electronics Engineering;* John Wiley & Sons: New York, NY, USA, 2016; pp 1–22. doi:10.1002/047134608x.w4531.pub2
23. Turner, R. C.; Fuierer, P. A.; Newnham, R. E.; Shrout, T. R. *Appl. Acoust.* **1994**, *41,* 299–324. doi:10.1016/0003-682x(94)90091-4
24. Houlding, T. K.; Rebrov, E. V. *Green Process. Synth.* **2012**, *1,* 19–31. doi:10.1515/greenps-2011-0502
25. García-Aguilar, J.; Fernández-García, J.; Rebrov, E. V.; Lees, M. R.; Gao, P.; Cazorla-Amorós, D.; Berenguer-Murcia, Á. *Chem. Commun.* **2017**, *53,* 4262–4265. doi:10.1039/c7cc01138e
26. Fuentes, M.; Magraner, J.; De Las Pozas, C.; Roque-Malherbe, R.; Pariente, J. P.; Corma, A. *Appl. Catal.* **1989**, *47,* 367–374. doi:10.1016/s0166-9834(00)83242-x
27. Lavoie, J.-M. *Front. Chem. (Lausanne, Switz.)* **2014**, *2,* 81. doi:10.3389/fchem.2014.00081
28. Abdullah, B.; Abd Ghani, N. A.; Vo, D.-V. N. *J. Cleaner Prod.* **2017**, *162,* 170–185. doi:10.1016/j.jclepro.2017.05.176

29. Jang, W.-J.; Shim, J.-O.; Kim, H.-M.; Yoo, S.-Y.; Roh, H.-S.
Catal. Today **2019,** *324,* 15–26. doi:10.1016/j.cattod.2018.07.032

30. Iulianelli, A.; Liguori, S.; Wilcox, J.; Basile, A. *Catal. Rev.: Sci. Eng.*
2016, *58,* 1–35. doi:10.1080/01614940.2015.1099882

31. Abiev, R. S.; Sladkovskiy, D. A.; Semikin, K. V.; Murzin, D. Y.;
Rebrov, E. V. *Catalysts* **2020,** *10,* 1358. doi:10.3390/catal10111358

32. Lozinskii, M. G. *Industrial Applications of Induction Heating;* Pergamon
Press: New York, NY, USA, 1969; p 690.

33. Mortensen, P. M.; Engbæk, J. S.; Vendelbo, S. B.; Hansen, M. F.;
Østberg, M. *Ind. Eng. Chem. Res.* **2017,** *56,* 14006–14013.
doi:10.1021/acs.iecr.7b02331

34. Vinum, M. G.; Almind, M. R.; Engbæk, J. S.; Vendelbo, S. B.;
Hansen, M. F.; Frandsen, C.; Bendix, J.; Mortensen, P. M.
Angew. Chem., Int. Ed. **2018,** *57,* 10569–10573.
doi:10.1002/anie.201804832

35. Sotenko, M.; Fernández, J.; Hu, G.; Derevschikov, V.; Lysikov, A.;
Parkhomchuk, E.; Semeykina, V.; Okunev, A.; Rebrov, E. V.
Chem. Eng. Process. **2017,** *122,* 487–492.
doi:10.1016/j.cep.2017.05.009

36. Meffre, A.; Mehdaoui, B.; Connord, V.; Carrey, J.; Fazzini, P. F.;
Lachaize, S.; Respaud, M.; Chaudret, B. *Nano Lett.* **2015,** *15,*
3241–3248. doi:10.1021/acs.nanolett.5b00446

37. Gahleitner, G. *Int. J. Hydrogen Energy* **2013,** *38,* 2039–2061.
doi:10.1016/j.ijhydene.2012.12.010

38. Götz, M.; Lefebvre, J.; Mörs, F.; McDaniel Koch, A.; Graf, F.;
Bajohr, S.; Reimert, R.; Kolb, T. *Renewable Energy* **2016,** *85,*
1371–1390. doi:10.1016/j.renene.2015.07.066

39. Bordet, A.; Lacroix, L.-M.; Fazzini, P.-F.; Carrey, J.; Soulantica, K.;
Chaudret, B. *Angew. Chem., Int. Ed.* **2016,** *55,* 15894–15898.
doi:10.1002/anie.201609477

40. Wang, W.; Duong-Viet, C.; Xu, Z.; Ba, H.; Tuci, G.; Giambastiani, G.;
Liu, Y.; Truong-Huu, T.; Nhut, J.-M.; Pham-Huu, C. *Catal. Today* **2020,**
357, 214–220. doi:10.1016/j.cattod.2019.02.050

41. Kurniati, S.; Soeparman, S.; Yuwono, S. S.; Hakim, L.; Syam, S.
Energies (Basel, Switz.) **2019,** *12,* 383. doi:10.3390/en12030383

42. Lee, M.-K.; Tsai, W.-T.; Tsai, Y.-L.; Lin, S.-H. *J. Anal. Appl. Pyrolysis*
2010, *88,* 110–116. doi:10.1016/j.jaap.2010.03.003

43. Niether, C.; Faure, S.; Bordet, A.; Deseure, J.; Chatenet, M.; Carrey, J.;
Chaudret, B.; Rouet, A. *Nat. Energy* **2018,** *3,* 476–483.
doi:10.1038/s41560-018-0132-1

44. Strauss, C. R. *Chem. Aust.* **1990,** *57,* 186.

45. Cablewski, T.; Faux, A. F.; Strauss, C. R. *J. Org. Chem.* **1994,** *59,*
3408–3412. doi:10.1021/jo00091a033

46. Chen, S.-T.; Chiou, S.-H.; Wang, K.-T.
J. Chem. Soc., Chem. Commun. **1990,** 807.
doi:10.1039/c39900000807

47. Yan, C.; Fraga-Dubreuil, J.; Garcia-Verdugo, E.; Hamley, P. A.;
Poliakoff, M.; Pearson, I.; Coote, A. S. *Green Chem.* **2008,** *10,* 98–103.
doi:10.1039/b710041h

48. Glasnov, T. N.; Vugts, D. J.; Koningstein, M. M.; Desai, B.;
Fabian, W. M. F.; Orru, R. V. A.; Kappe, C. O. *QSAR Comb. Sci.* **2006,**
25, 509–518. doi:10.1002/qsar.200540210

49. Shore, G.; Yoo, W.-J.; Li, C.-J.; Organ, M. G. *Chem. – Eur. J.* **2010,** *16,*
126–133. doi:10.1002/chem.200902396

50. Ceylan, S.; Friese, C.; Lammel, C.; Mazac, K.; Kirschning, A.
Angew. Chem., Int. Ed. **2008,** *47,* 8950–8953.
doi:10.1002/anie.200801474

51. Oltmanns, M.; Kirschning, A. *Synlett* **2020,** *31,* 1942–1946.
doi:10.1055/s-0040-1705945

52. Mingos, D. M. P.; Baghurst, D. R. *Chem. Soc. Rev.* **1991,** *20,* 1–47.
doi:10.1039/cs9912000001

53. Ceylan, S.; Coutable, L.; Wegner, J.; Kirschning, A. *Chem. – Eur. J.*
2011, *17,* 1884–1893. doi:10.1002/chem.201002291

54. Kupracz, L.; Kirschning, A. *Adv. Synth. Catal.* **2013,** *355,* 3375–3380.
doi:10.1002/adsc.201300614

55. Saengchantara, S. T.; Wallace, T. W. *J. Chem. Soc., Perkin Trans. 1*
1986, 789–794. doi:10.1039/p19860000789

56. Galliford, C. V.; Scheidt, K. A. *Angew. Chem., Int. Ed.* **2007,** *46,*
8748–8758. doi:10.1002/anie.200701342

57. Dondoni, A.; Massi, A. *Acc. Chem. Res.* **2006,** *39,* 451–463.
doi:10.1021/ar068023r

58. Kappe, C. O. *Tetrahedron* **1993,** *49,* 6937–6963.
doi:10.1016/s0040-4020(01)87971-0

59. Mukherjee, S.; Yang, J. W.; Hoffmann, S.; List, B. *Chem. Rev.* **2007,**
107, 5471–5569. doi:10.1021/cr0684016

60. Odedra, A.; Seeberger, P. H. *Angew. Chem.* **2009,** *121,* 2737–2740.
doi:10.1002/ange.200804407

61. Alza, E.; Rodríguez-Escrich, C.; Sayalero, S.; Bastero, A.;
Pericàs, M. A. *Chem. – Eur. J.* **2009,** *15,* 10167–10172.
doi:10.1002/chem.200901310

62. Phutdhawong, W.; Buddhasukh, D.; Pyne, S. G.; Rujiwatra, A.;
Pakawatchai, C. *Synth. Commun.* **2006,** *36,* 881–883.
doi:10.1080/00397910500466025

63. Jenner, G.; Ben Salem, R.; El'yanov, B.; Gonikberg, E. M.
J. Chem. Soc., Perkin Trans. 2 **1989,** 1671–1675.
doi:10.1039/p29890001671

64. Israeli, M.; Pettit, L. D. *J. Chem. Soc., Dalton Trans.* **1975,** 414–417.
doi:10.1039/dt9750000414

65. Negishi, E.-i., Ed. *Handbook of Organopalladium Chemistry for Organic
Synthesis;* John Wiley & Sons: New York, NY, USA, 2003.
doi:10.1002/0471212466

66. Diederich, F.; Stang, P. J., Eds. *Metal-Catalyzed Cross-Coupling
Reactions;* Wiley-VCH: Weinheim, Germany, 1998.
doi:10.1002/9783527612222

67. Mennecke, K.; Kirschning, A. *Synthesis* **2008,** 3267–3272.
doi:10.1055/s-2008-1067274

68. Nikbin, N.; Ladlow, M.; Ley, S. V. *Org. Process Res. Dev.* **2007,** *11,*
458–462. doi:10.1021/op7000436

69. Phan, N. T. S.; Khan, J.; Styring, P. *Tetrahedron* **2005,** *61,*
12065–12073. doi:10.1016/j.tet.2005.07.109

70. Liu, S.; Fukuyama, T.; Sato, M.; Ryu, I. *Org. Process Res. Dev.* **2004,**
8, 477–481. doi:10.1021/op034200h

71. Odell, L. R.; Lindh, J.; Gustafsson, T.; Larhed, M. *Eur. J. Org. Chem.*
2010, 2270–2274. doi:10.1002/ejoc.201000063

72. Liu, Y.; Rebrov, E. V. *Catalysts* **2021,** *11,* 146.
doi:10.3390/catal11020146

73. Nagarajan, S.; Ran, P.; Shanmugavelan, P.; Sathishkumar, M.;
Ponnuswamy, A.; Suk Nahm, K.; Gnana kumar, G. *New J. Chem.*
2012, *36,* 1312–1319. doi:10.1039/c2nj40119c

74. Ocampo, R.; Dolbier, W. R., Jr. *Tetrahedron* **2004,** *60,* 9325–9374.
doi:10.1016/j.tet.2004.07.018

75. Fürstner, A. *Synthesis* **1989,** 571–590. doi:10.1055/s-1989-27326

76. Wegner, J.; Ceylan, S.; Friese, C.; Kirschning, A. *Eur. J. Org. Chem.*
2010, 4372–4375. doi:10.1002/ejoc.201000628

77. Kupracz, L.; Hartwig, J.; Wegner, J.; Ceylan, S.; Kirschning, A.
Beilstein J. Org. Chem. **2011,** *7,* 1441–1448. doi:10.3762/bjoc.7.168

78. Moses, J. E.; Moorhouse, A. D. *Chem. Soc. Rev.* **2007,** *36,*
1249–1262. doi:10.1039/b613014n

79. Wen, J.; Wu, K.; Yang, D.; Tian, J.; Huang, Z.; Filatov, A. S.; Lei, A.; Lin, X.-M. *ACS Appl. Mater. Interfaces* **2018,** *10,* 25930–25935. doi:10.1021/acsami.8b06927

80. Ötvös, S. B.; Fülöp, F. *Catal. Sci. Technol.* **2015,** *5,* 4926–4941. doi:10.1039/c5cy00523j

81. Bao, J.; Tranmer, G. K. *Chem. Commun.* **2015,** *51,* 3037–3044. doi:10.1039/c4cc09221j

82. Chaudhuri, S. R.; Hartwig, J.; Kupracz, L.; Kodanek, T.; Wegner, J.; Kirschning, A. *Adv. Synth. Catal.* **2014,** *356,* 3530–3538. doi:10.1002/adsc.201400261

83. Kirschning, A.; Jas, G. Applications of Immobilized Catalysts in Continuous Flow Processes. *Immobilized Catalysts;* Topics in Current Chemistry, Vol. 242; Springer: Berlin, Heidelberg, 2004; pp 209–239. doi:10.1007/b96877

84. Solodenko, W.; Wen, H.; Leue, S.; Stuhlmann, F.; Sourkouni-Argirusi, G.; Jas, G.; Schönfeld, H.; Kunz, U.; Kirschning, A. *Eur. J. Org. Chem.* **2004,** 3601–3610. doi:10.1002/ejoc.200400194

85. Mennecke, K.; Cecilia, R.; Glasnov, T. N.; Gruhl, S.; Vogt, C.; Feldhoff, A.; Vargas, M. A. L.; Kappe, C. O.; Kunz, U.; Kirschning, A. *Adv. Synth. Catal.* **2008,** *350,* 717–730. doi:10.1002/adsc.200700510

86. Barluenga, J.; Tomás-Gamasa, M.; Aznar, F.; Valdés, C. *Nat. Chem.* **2009,** *1,* 494–499. doi:10.1038/nchem.328

87. Kupracz, L.; Kirschning, A. *J. Flow Chem.* **2013,** *3,* 11–16. doi:10.1556/jfc-d-12-00021

88. Hartwig, J.; Kirschning, A. *Chem. – Eur. J.* **2016,** *22,* 3044–3052. doi:10.1002/chem.201504409

89. Hall, J. B.; Sanders, J. M. Perfume compositions and perfurme articles containing one isomer of an octahydrotetramethyl acetonaphthone. U.S. Pat. Appl. US3929677A, Dec 30, 1975.

90. Stepanyuk, A.; Kirschning, A. *Beilstein J. Org. Chem.* **2019,** *15,* 2590–2602. doi:10.3762/bjoc.15.252

91. Stepanyuk, A. Master Thesis; Leibniz University Hannover, Hannover, Germany, 2019.

92. van der Linde, M.; Master Thesis; Leibniz University Hannover, Hannover, Germany, 2020.

93. Seemann, A.; Panten, J.; Kirschning, A. *J. Org. Chem.* **2021,** *86,* 13924–13933. doi:10.1021/acs.joc.1c00663

Synthesis of odorants in flow and their applications in perfumery

Merlin Kleoff[*1], Paul Kiler[2] and Philipp Heretsch[*3]

Abstract

Continuous flow technology is a key technology for sustainable manufacturing with numerous applications for the synthesis of fine chemicals. In recent years, the preparation of odorants utilizing the advantages of flow reactors received growing attention. In this review, we give an overview of selected methods for the synthesis of odorants in flow, including heterogeneously catalyzed reactions, gas reactions, and photochemical C–H functionalization processes. After a brief introduction on types of odorants, the presented odorant syntheses are ordered according to the main odor families "fruity", "green", "marine", "floral", "spicy", "woody", "ambery", and "musky" and their use and importance for perfumery is briefly discussed.

Introduction

The history of odorants goes back to ancient cultures such as the Egyptian around 5000 BC where resins of incense, opoponax, and myrrh were burnt for religious purposes [1]. Today, "the art of perfumery is closely connected to [synthetic] chemistry", as outlined by Jean-Claude Ellena, the former master perfumer of Hermès [2]. In fact, the development of perfumes and cosmetics is strongly driven by the development of new odorants with unprecedented scents or superior physical properties [3-8]. Ernest Beaux, creator of Chanel *No. 5*, even

claimed that "the future of perfumery is in the hand of chemistry" [3]. In addition, the industrial synthesis of odorants is the only way to provide them in sufficient quantities when natural sources are rare, or their production is unethical as it is the case for ingredients obtained from animals such as musk or civet [9,10].

In recent years, flow chemistry has enriched organic synthesis as an enabling technology to realize reactions that are impos-

sible in batch or to provide products in higher purity avoiding expensive purification procedures [11-18]. Given the superior heat-, mass-, and phototransfer in microreactors, flow chemistry has been outlined as a central tool for sustainable manufacturing [18]. Utilizing the virtue of flow chemistry, more and more methods for the preparation of odorants in flow are developed. Recently, Baxendale and co-workers reviewed techniques and apparatus tailored to the synthesis of flavors and fragrances [19]. In this review, we want to give an overview of selected flow protocols for the synthesis of various odorants and highlight their role for perfumery. All quotations of percentages of these raw materials in perfumes are in the concentrate formula, before dilution, and are taken from GC/MS analyses.

Review
Classification of odorants

As there are many different types of scents, there are various classifications for fragrances. In this review, fragrances are ordered from "fruity" to "musky" following the olfactory spectrum wheel developed by Kraft and co-workers (Figure 1) [3,4]. It has to be noted that this is only a simple and subjective classification; most odorants belong to multiple categories.

Figure 1: The olfactory spectrum wheel ordering different types of odorants from fruity to musky.
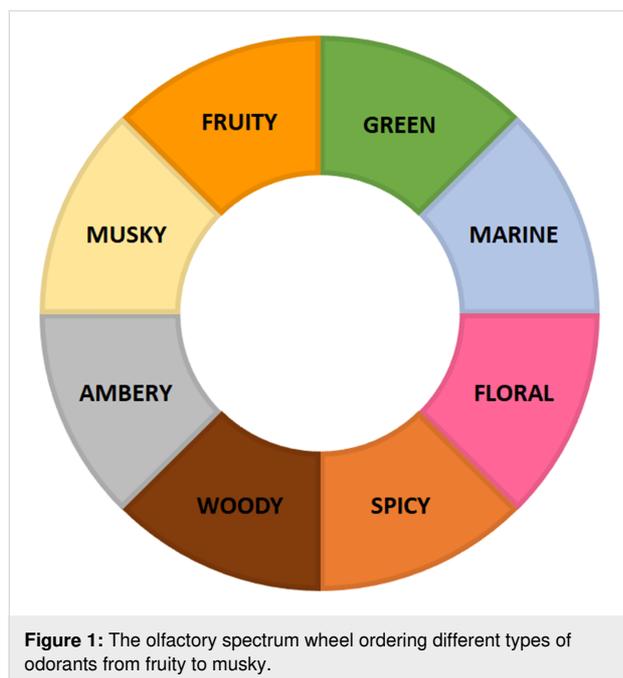
Depending on the vapor pressure and consequently the perceptibility of an odorant on a paper strip (the so called "substantivity"), it can be ordered in a pyramid (Figure 2) as a "top note" (substantivity of up to a few hours), a "middle note" (substantivity of many hours), or a "base note" (substantivity of days up to weeks) [2,20]. Typically, fresh and citric odorants, e.g., limonene, are top notes, while warm and sweet odorants

such as vanillin are base notes [21]. However, these classical categories have been partially overcome by synthetic odorants. For example, hedione (methyl dihydrojasmonate), one of the most important odorants of modern perfumery, has a fresh, citric and slightly floral scent – but is commonly categorized as a middle note with a substantivity of 72 h [22].

Figure 2: Classification of odorants as "top note", "middle note" and "base note" depending on their substantivity.
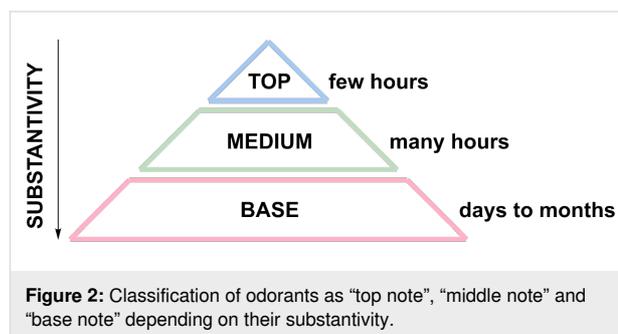
Most professional perfumes are well-balanced mixtures of top, middle, and base notes. While top notes have a "diffusive" effect on a perfume increasing its volatility, base notes may serve as "fixatives" reducing the volatility of a perfume and, thus, increasing its longevity. Notably, there are odorants (in particular amber notes) which are base notes serving as fixatives but also enhancing the perceptibility of a perfume [23].

Fruity odorants

One of the most important odorants giving raspberries their characteristic scent is the so-called "raspberry ketone" (**5**) having a "sweet, fruity, and warm odor" which is frequently used for fruity perfumes and as a flavor [9]. It is prominently used in, e.g., Tom Ford: *Tuscan Leather* along with notes of leather, muguet, and thyme, defining the character of this scent. The related methyl ether **6** ("raspberry ketone methyl ether") is also used as odorant but is, in contrast to raspberry ketone (**5**), "intensely sweet, floral" and only "slightly fruity" [9]. Kappe and co-workers disclosed an access to both odorants in a two-step synthesis (Scheme 1) [24]. In the first step, 4-aryl-3-buten-2-ones **3** and **4** are prepared via aldol condensation of the corresponding aldehydes **1** and **2** and acetone in 78–90% yield with a productivity of up to 0.35 kg/h for enone **4**.

In the second step, the obtained 4-aryl-3-buten-2-ones **3** and **4** are selectively hydrogenated in flow using a packed-bed reactor with Raney nickel as catalyst affording raspberry ketone (**5**) in 91% yield and raspberry ketone methyl ether (**6**) in 94% yield, respectively. For compound **6**, both individual steps were combined for a two-step aldol condensation/hydrogenation flow sequence providing raspberry ketone methyl ether (**6**) on a gram scale in 75% overall yield. Interestingly, also alternative flow protocols for the synthesis of 4-aryl-3-buten-2-ones **3** and **4**
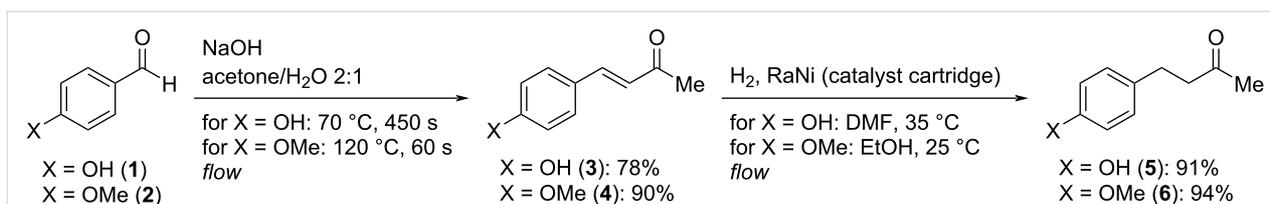
Scheme 1: Synthesis of raspberry ketone (**5**) and raspberry ketone methyl ether (**6**) in two steps in flow.

were first developed on small scale under microwave batch conditions to reach short reaction times of 1–10 min and subsequently translated to scalable flow processes [24].

While raspberries have a fruity and "berry" scent which is typically associated with the color red, the scent of citrus fruits is placed more between the fruity and the green notes. Among the odorants found in citrus fruits, such as oranges and grapefruits, (+)-nootkatone (**8**) is one of the most powerful odorants having a "sweet, citrusy" scent and a good substantivity [9]. However, (+)-nootkatone (**8**) is relatively expensive as it has to be extracted from grapefruits or prepared by, e.g., oxidation of (+)-valencene (**7**) (using toxic di-*tert*-butyl chromates), which is isolated from the essential oil of oranges [9]. In 2014, Neuenschwander and Jensen reported a flow setup for the catalyst and solvent-free oxidation of (+)-valencene (**7**) with molecular oxygen at elevated temperatures providing (+)-nootkatone (**8**) in 10% yield (Scheme 2). In this setup, neat (+)-valencene (**7**) is

mixed with a stream of oxygen resulting in the formation of a segmented gas–liquid flow. In segmented flow a higher surface-to-volume ratio is achieved and toroidal currents occur within the liquid slugs which result in a continuous mixing of the liquid slugs. Therefore, the reaction proceeds up to 100 times faster in flow than under conventional batch conditions [25].

Although, pure isoamyl acetate (**10**) has a "pronounced, fruity-fresh odor" which is "slightly nauseating", it is "in dilution reminiscent of pear, banana, [and] apple" making it useful for perfumery in small doses [9]. For instance, it is appearing in both vintage Geoffrey Beene: *Grey Flannel* and Georgio Armani: *Acqua di Gioia eau fraiche* at 0.04%. Žnidaršič-Plazl and co-workers developed a method for the acetylation of isoamyl alcohol (**9**) catalyzed by *Candida antarctica* lipase B (Scheme 3) [26]. A biphasic system consisting of *n*-heptane and an aqueous buffer solution is used and efficiently mixed in a Corning AFR[TM] Low Flow reactor providing a fine dispersion of the reaction mixture and, thus, a large interface between the phases. Subsequently, the biphasic system is directly separated, employing a PTFE membrane separator, to afford a solution of isoamyl acetate in *n*-heptane, while the aqueous layer containing the lipase could be recycled. At 60 °C with a residence time of 8.6 min isoamyl acetate (**10**) is obtained in 59% yield according to GC analysis [26]. Related methods for the enzyme-catalyzed acetylation of isoamyl alcohol (**9**) have been developed utilizing biphasic systems, supercritical carbon dioxide as a sol-
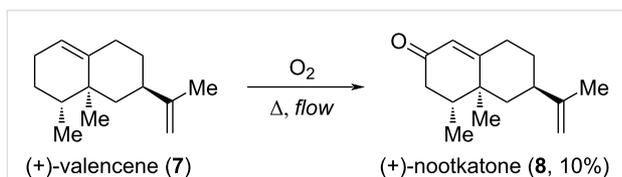
Scheme 2: Autoxidation of (+)-valencene (**7**) to (+)-nootkatone (**8**) under catalyst and solvent-free conditions in a segmented flow.
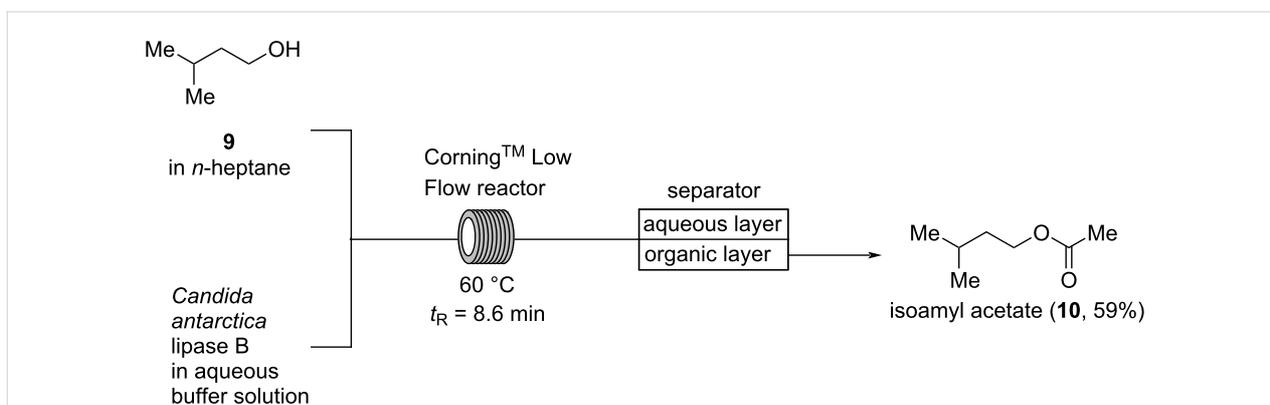
Scheme 3: Enzyme-catalyzed acetylation of isoamyl alcohol (**9**) in a biphasic *n*-heptane/water mixture utilizing a Corning[TM] Low Flow reactor.
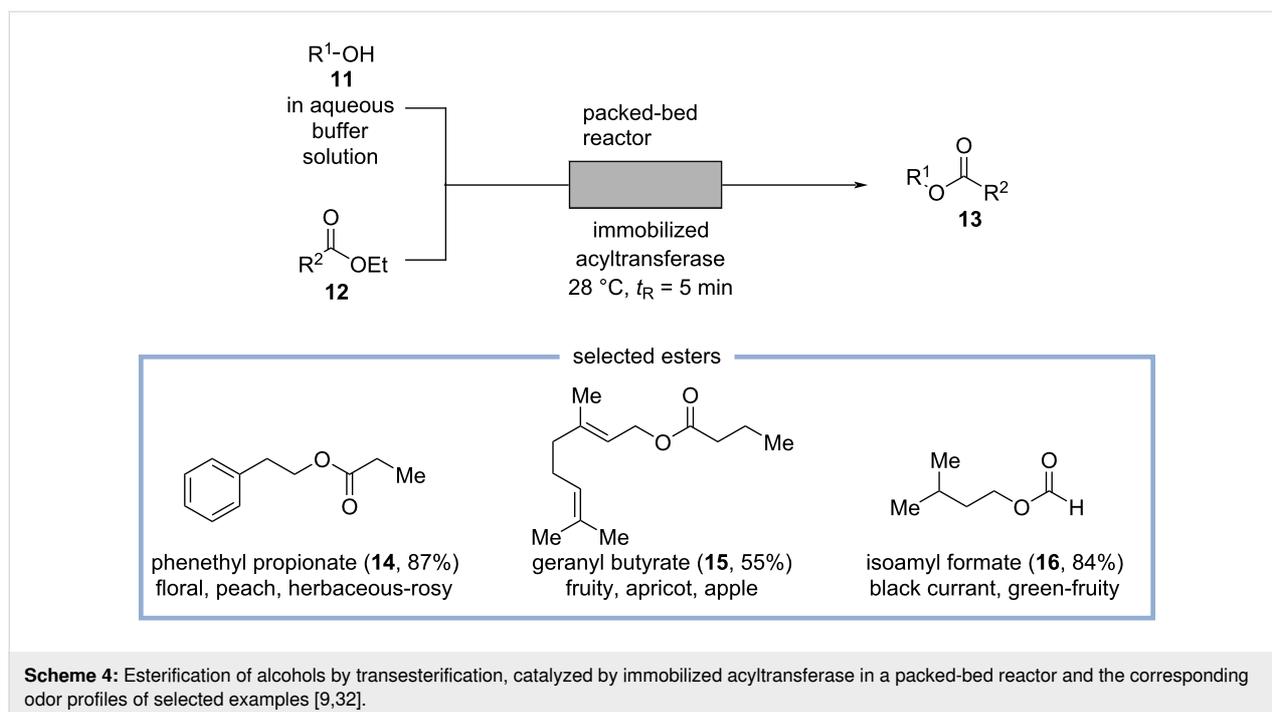
vent, or packed-bed reactors with immobilized enzymes [27-31].
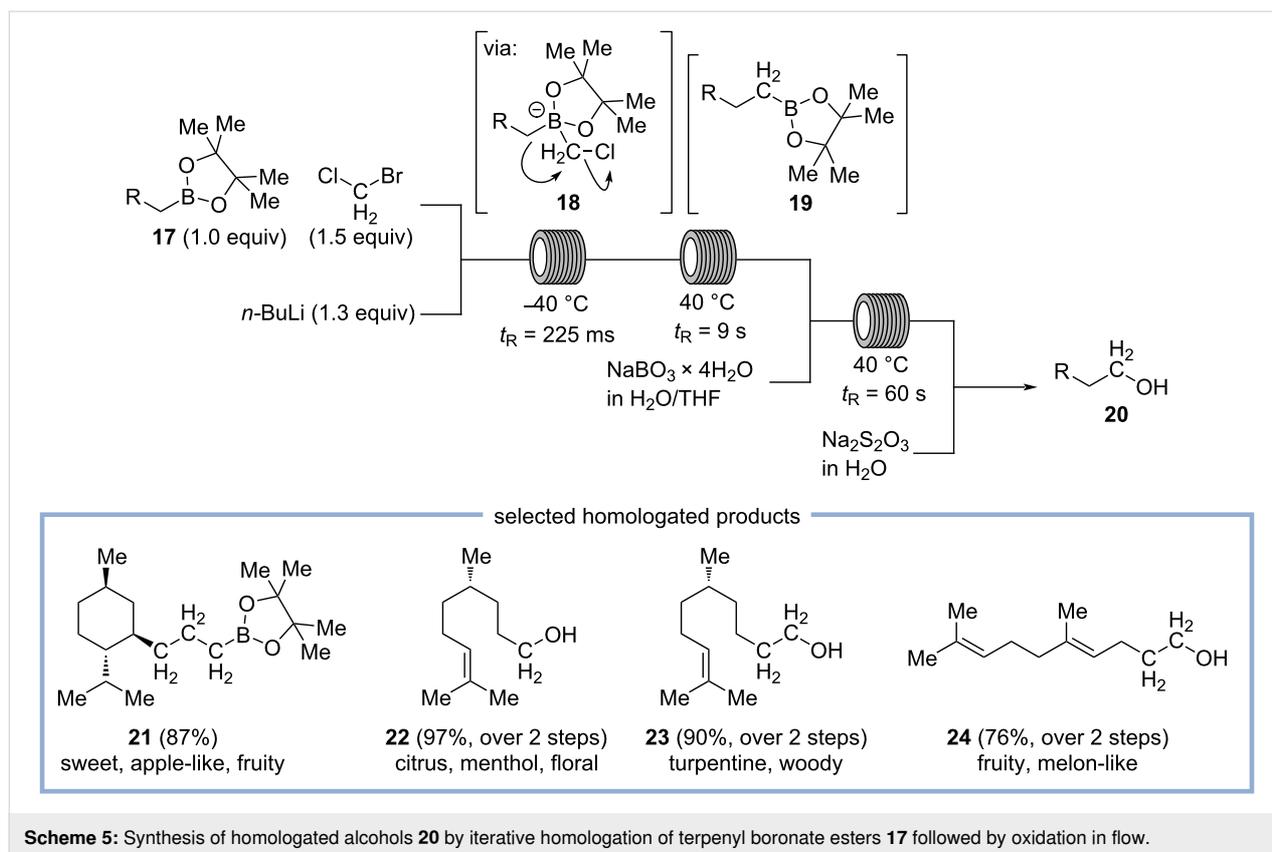
More recently, Paradisi and co-workers disclosed a more general access to a variety of esters with mainly fruity and floral odorants by transesterification of acyl donors of structure **12** to the corresponding alcohols **11** using an immobilized transferase obtained from *Mycobacterium smegmatis* (Scheme 4) [32]. A solution of the acyl donor **12** in ethyl acetate and an aqueous buffer solution of the corresponding alcohols **11** are mixed in a T-piece and the resulting segmented flow is pumped through a packed-bed reactor containing the immobilized transferase. The reaction mixture is directly analyzed by GC, or, as demonstrated for the preparation of phenylethyl acetate, further diluted with ethyl acetate, and the biphasic system is separated in flow providing phenylethyl acetate in 82% isolated yield. Using this method, a variety of 2-phenylethyl-, cinnamyl-, geranyl-, *n*-hexyl-, and isoamyl esters with mainly fruity odor profiles are obtained in moderate to excellent yields. Some selected esters (**14–16**) and their odor profiles are shown in Scheme 4 [32].

Related methods for the esterification of natural occurring alcohols, such as geraniol, utilizing immobilized enzyme-catalysis in packed-bed reactors were developed by the groups of de Souza and Yadav [33,34].

Very recently, Kirschning and co-workers presented a general method for the Matteson reaction in flow, allowing iterative homologation of various terpene boronate esters **17**, which are

subsequently oxidized to the corresponding alcohols **20** (Scheme 5) [35]. In the first step, a solution of terpenyl pinacol boronates **17** and bromochloromethane in tetrahydrofuran is mixed with *n*-butyllithium in *n*-hexane at −40 °C. By using a specifically designed, 3D-printed micromixer made from stainless steel, ultrafast mixing of both solutions is achieved within milliseconds initializing bromine–lithium exchange of bromochloromethane to generate (chloromethyl)lithium. This carbenoid species readily reacts with terpenyl pinacol boronates **17**, resulting in the formation of intermediate **18**, which undergoes 1,2-anionotropic rearrangement to the homologated pinacol boronate **19**. As the rearrangement is a much slower process, the reaction mixture is passed through a second reactor at elevated temperature with a residence time of 9 s to allow full conversion to the homologated pinacol boronate **19**. This species can then be directly pumped to a second homologation reactor module (and then, if desired, even to a third) to reiterate homologation. The resulting reaction mixture is either collected directly to provide the homologated pinacol boronates **19**, e.g., menthol-derived compound **21**, which was found to have a "rather sweet, slightly apple-like, fruity odor". Alternatively, the reaction mixture is pumped to an oxidation module in which the pinacol boronates are mixed with a solution of sodium perborate in water/tetrahydrofuran to perform oxidation to the corresponding alcohols **20** at 40 °C in 60 s. In order to quench remaining oxidants, the reaction mixture is combined with an aqueous solution of sodium thiosulfate before it is collected. Among the prepared alcohols, a few compounds were found to have interesting olfactory properties. Alcohol **22** has a citrus

Scheme 4: Esterification of alcohols by transesterification, catalyzed by immobilized acyltransferase in a packed-bed reactor and the corresponding odor profiles of selected examples [9,32].

Scheme 5: Synthesis of homologated alcohols **20** by iterative homologation of terpenyl boronate esters **17** followed by oxidation in flow.
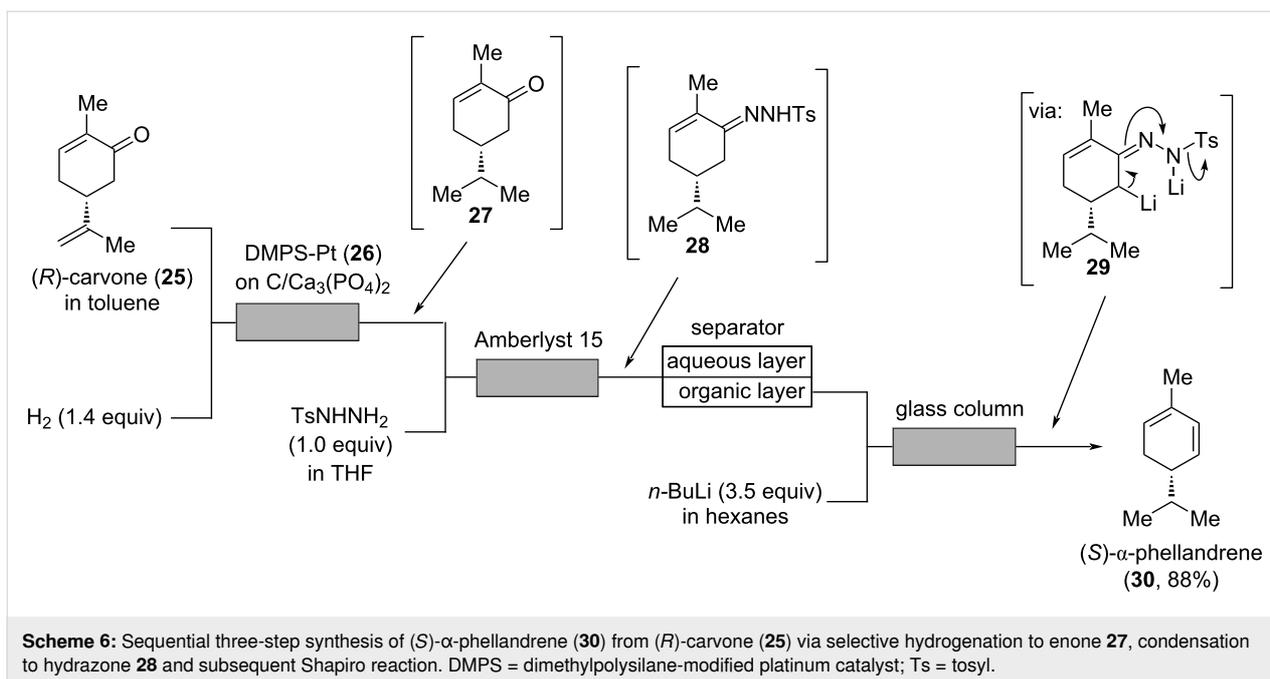
and menthol note, while its homolog **23** shows a turpentine-like, woody scent. In contrast, alcohol **24**, which is a homolog of geraniol, has a strong fruity, melon-like odor profile [35].

Green odorants

To the family of green odorants belong those having a scent that is reminiscent of leaves and grasses, but also odorants that are minty, camphorous, or resinous. Peppermint is a fresh, cold, and quite clean top note that is mostly employed in men's fragrances, both in classical (Davidoff: *Cool Water* at approx. 0.2%) and modern fragrances (Chanel: *Allure Homme Sport*, Jean-Paul Gaultier: *Le Mâle* at approx. 0.01%). However, small doses of mint notes give a desirable sparkle even to female fragrances, e.g., Parfums de Marly: *Delina Exclusif*, and for topnote blends for tuberose flower accords used in fragrances. The most important mint notes are certainly menthone and menthol, but occasionally (S)-α-phellandrene gives better results in a perfume [9].

"When absolutely pure", (S)-α-phellandrene "has a pleasant, fresh-citrusy, and peppery-woody odor with a discretely mint note" [9]. Very recently, Kobayashi, Ishitani, and co-workers described a three-step sequential continuous flow process for the synthesis of (S)-α-phellandrene (**30**) from (R)-carvone (**25**, Scheme 6) [36].

In the first step, a solution of (R)-carvone (**25**) in toluene is merged with a stream of hydrogen and the resulting segmented flow is passed through a column reactor containing a dimethylpolysilane-modified platinum catalyst (DMPS-Pt, **26**), immobilized on carbon/calcium phosphate. At a temperature of 25 °C using 1.4 equivalents of hydrogen with a pressure of 1 bar, a good selectivity for the hydrogenation of the external alkene is achieved providing enone **27**. The reaction mixture containing enone **27** is then mixed with tosylhydrazone and passed through a column with sulfonic acidic resin Amberlyst-15 to catalyze the formation of hydrazone **28**. As one equivalent of water is formed in this condensation process, which is detrimental for the subsequent Shapiro reaction, water is continuously removed by in-line separation of the reaction mixture using a PTFE-membrane separator. The organic layer is then mixed with a solution of *n*-butyllithium in hexanes to initiate the Shapiro reaction of hydrazone **28** proceeding supposedly via dilithiated intermediate **29**. As the nitrogen produced in the reaction increases the volume of the reaction mixture and therefore is drastically shortening the residence time, a cooled glass column with the flow direction oriented against gravity is utilized. In this way, nitrogen bubbles can move to the top of the column, while the liquid reaction mixture remains below. At the outlet of the column, the reaction mixture is directly collected in a stirred flask containing water to quench the reac-
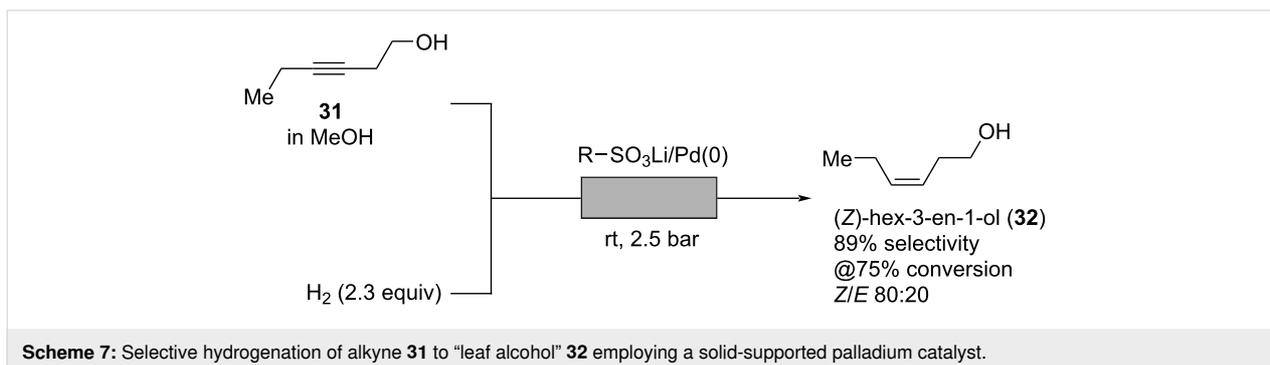
Scheme 6: Sequential three-step synthesis of (*S*)-α-phellandrene (**30**) from (*R*)-carvone (**25**) via selective hydrogenation to enone **27**, condensation to hydrazone **28** and subsequent Shapiro reaction. DMPS = dimethylpolysilane-modified platinum catalyst; Ts = tosyl.

tion. After filtration through activated aluminum, (*S*)-α-phellandrene (**30**) is obtained in a high yield of 88% over three steps on a 30 g scale corresponding to a productivity of 0.887 mol/day [36].

The smell of leaves and freshly cut green grass can mainly be traced back to (*Z*)-hex-3-en-1-ol (**32**) (so-called "leaf alcohol"), an important odorant with an intense green and grassy odor "often used along with geranium oil, galbanum, oakmoss, lavender, and mint oils" [4,9]. The freshness that comes from green notes such as (*Z*)-hex-3-en-1-ol, 2,4-dimethylcyclohex-3-ene-1-carbaldehyde, and (*E*,*Z*)-2,6-nonadien-1-al are nearly ubiquitous in modern perfumery for both women and men, even appearing in dark or woody fragrances such as Hugo Boss: *Soul*. In 2012, Barbaro and co-workers developed a synthesis for alkene **32** by selective hydrogenation of the corresponding alkyne (Scheme 7) [37]. Instead of using a Lindlar catalyst containing toxic lead salts, selectivity is achieved by the improved

reaction control in flow. A solution of alkyne **31** in methanol is mixed with a stream of hydrogen and pumped at room temperature and 2.5 bar through a tubular glass column containing a Dowex-supported palladium catalyst. Optimization of process parameters revealed that at a conversion of 75% a good selectivity of 89% for hydrogenation of alkyne **31** to alkene **32** is achieved affording a mixture of (*Z*)- and (*E*)-isomers in a ratio of 80:20 [37].

Floral odorants

Floral notes, such as rose, jasmine, orange blossom, or lavender, are typically middle notes defining the "heart" of many perfumes. To create a jasmine note, the synthetic odorant jasmonal (**35**) can be used which has an "oily-herbaceous and somewhat floral odor, reminiscent of many types of natural flowers, but mostly of jasmine, gardenia, and tuberose." It is "used very extensively in perfumes" and "soap perfumes" to introduce "jasmine-like floralcy when accompanied by more

Scheme 7: Selective hydrogenation of alkyne **31** to "leaf alcohol" **32** employing a solid-supported palladium catalyst.

volatile chemicals of floral character", while assisting "in fixation of the fragrance" due to its relatively high boiling point of 285 °C. It is industrially produced by an aldol condensation of heptanal (**34**, obtained from castor oil) and benzaldehyde (**33**). In the industrial process, stoichiometric amounts of sodium- or potassium hydroxide are used resulting in the formation of large quantities of undesired side products, e.g., enone **36**, the aldol condensation product of two molecules of heptanal [9,38].

Therefore, Gholami and co-workers developed a flow protocol for the synthesis of jasmonal (**35**) by aldol condensation of heptanal (**34**) and benzaldehyde (**33**) utilizing a magnesium-aluminum mixed oxide catalyst in a fixed bed reactor (Scheme 8A) [38]. To suppress the formation of side product **36**, an excess of benzaldehyde is used. At 140 °C and with a long residence time of 76 h, a moderate heptanal (**34**) conversion of 36% was achieved providing jasmonal (**35**) in a selectivity of 41% [38].

One of the least expensive floral odorants is acetophenone (**38**), having a "pungent-sweet odor, in dilution resembling that of hawthorn or a harsh orange-blossom type". Acetophenone appears in vintage Geoffrey Beene: *Grey Flannel* at 0.14%, and Shiseido: *Zen* and Gap: *Om* at approx. 0.014%. In 2013,

Roberge, Kappe, and co-workers investigated the C–H oxidation of ethylbenzene (**37**) to acetophenone with oxygen as an oxidant (Scheme 8B) [39]. The process is performed at 120 °C at 10 bar with a residence time of 6 min, and catalyzed homogenously utilizing the established "MC-system" (manganese/cobalt/bromide) in a heated tube reactor. Remarkably, acetophenone is obtained in a good yield of 66% and in 96% purity without purification, while other oxidation products are formed in only small quantities further exemplifying the selectivity of the flow process [39].

Spicy odorants

Similar to green notes in breadth and variety of odor profiles, are many spice oils and related molecules used in fragrances. Many of these molecules found in natural spice oils are terpenes, which belong to the top notes. Some molecules get to the middle notes, and, very rarely, spice materials reach the base notes. Thyme is occasionally used in soapy perfumes and detergents "where its power and freshness can introduce a hint of medicinal notes" [10]. This material is employed in, e.g., Tom Ford: *Tuscan Leather* to introduce a slightly medicinal and spicy note complementing the leathery and smoky notes (so called "white" thyme appears at approx. 0.25% in *Tuscan*

Scheme 8: A) Synthesis of jasmonal (**35**) by crossed aldol condensation of benzaldehyde (**33**) and heptanal (**34**) in a packed bed reactor containing a magnesium/aluminum mixed oxide catalyst. B) C–H oxidation of ethylbenzene (**37**) to acetophenone (**38**) enabled by a MC-system as catalyst and molecular oxygen. BPR = back pressure regulator; MFC = mass flow controller.
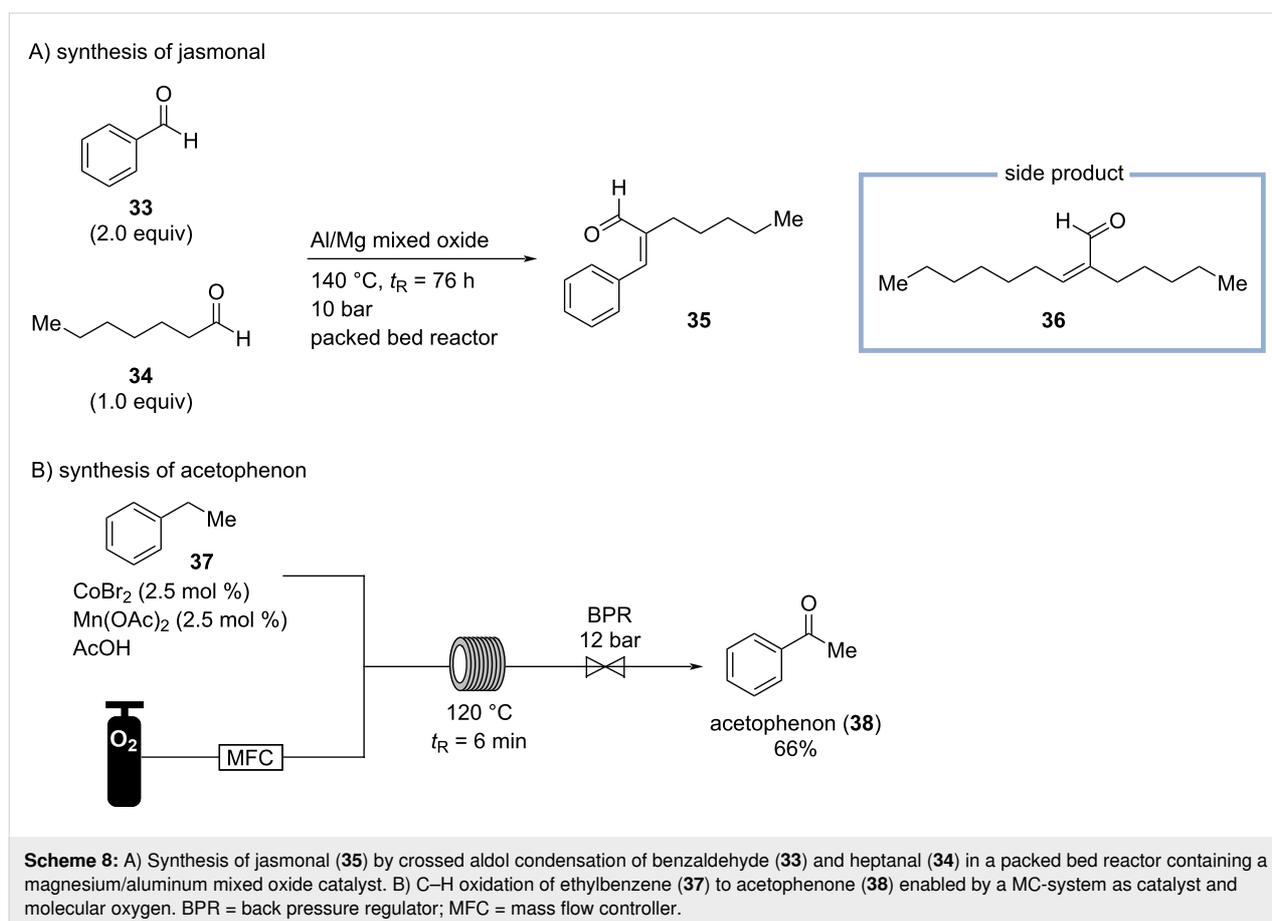
Leather). One of the main ingredients of thyme is thymol (**41**) which has a sweet-medicinal and warm odor; interestingly, it is also strongly antiseptic [9]. In 2005, Poliakoff and co-workers developed a synthesis of thymol by alkylation of *m*-cresol (**39**) in supercritical carbon dioxide (scCO$_2$) using γ-Al$_2$O$_3$ in a packed-bed reactor (Scheme 9) [40].

Scheme 9: Synthesis of thymol (**41**) from *m*-cresol (**39**) and isopropyl alcohol via Fries-type rearrangement of ether **40**.
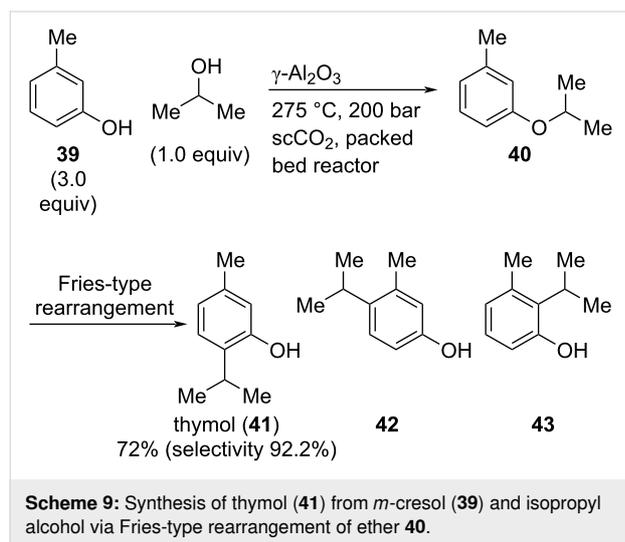
In the presence of Brønsted-acidic Nafion SAC-13, alkylation of *m*-cresol with isopropanol proceeds via a Friedel–Crafts-type mechanism in much lower selectivity. In contrast, the authors proposed that employing γ-Al$_2$O$_3$ as Lewis acid catalyst, reaction of **39** and isopropanol leads to isopropyl ether **40**. This intermediate undergoes a Fries-type rearrangement resulting in the formation of thymol (**41**) along with its regioisomers **42** and **43**. However, using an excess of isopropanol and a relatively low concentration of the organic substrates in scCO$_2$ (5% w/w), thymol (**41**) is produced in a good yield (72%) and selectivity (92.2%) as shown by GC. Interestingly, it was found that a higher substrate concentration is disadvantageous, as water is

formed in the process which decreases the activity of the catalyst. Thus, at a higher substrate concentration, the water removal by scCO$_2$ is not sufficient, thereby lowering both, yield and selectivity, of the process [40].

The first synthesis of coumarin by Perkin in 1868 was a breakthrough in the history of natural odorant synthesis [2]. Coumarin (**46**) has a sweet, slightly spicy, and hay-like scent [9,41]. It was extensively used in Houbigant: *Fougère Royal* (1882, appearing at approx. 10%), a perfume which has lent its name to a whole family of perfumes (*fougère perfumes*) [2]. Despite the molecular size of coumarin, it is often considered as a base note, but higher dosages can bring it into the middle notes.

In 2015, Guo and co-workers reported a flow procedure for the synthesis of coumarin (**46**) following the Perkin synthesis (Scheme 10) [42]. Salicylaldehyde (**44**) is mixed with a solution of potassium acetate and acetic acid in acetic anhydride. The reaction mixture is pumped through two separated tube reactors at 150 °C and 240 °C, respectively, proceeding with a combined residence time of 22.5 min. The authors propose that the reaction does not follow the mechanism of the Perkin process but proceeds via acylation of salicylaldehyde (**44**) to intermediate **45**, which forms coumarin (**46**) in an intramolecular aldol cyclization. Therefore, *O*-acylation of salicylaldehyde (**44**) is completed at 150 °C before the aldol condensation is initiated at 240 °C. While at lower temperatures, the aldol condensation proceeded incompletely, increasing the temperature to 250 °C lead to clogging of the reactor probably due to formation of phenolic resins as byproducts. In contrast, when the reaction is performed at 240 °C in one tube reactor, the reaction gives incomplete conversion and the yield of coumarin (**46**) drops to 21%. The authors proposed that under these conditions the reaction proceeds via the Perkin process, which is significantly slower than the *O*-acylation/aldol sequence [42].

Scheme 10: Preparation of coumarin (**46**) by reaction of salicylaldehyde (**44**) with potassium acetate, acetic acid, and acetic anhydride at elevated temperature in two separated tube reactors.
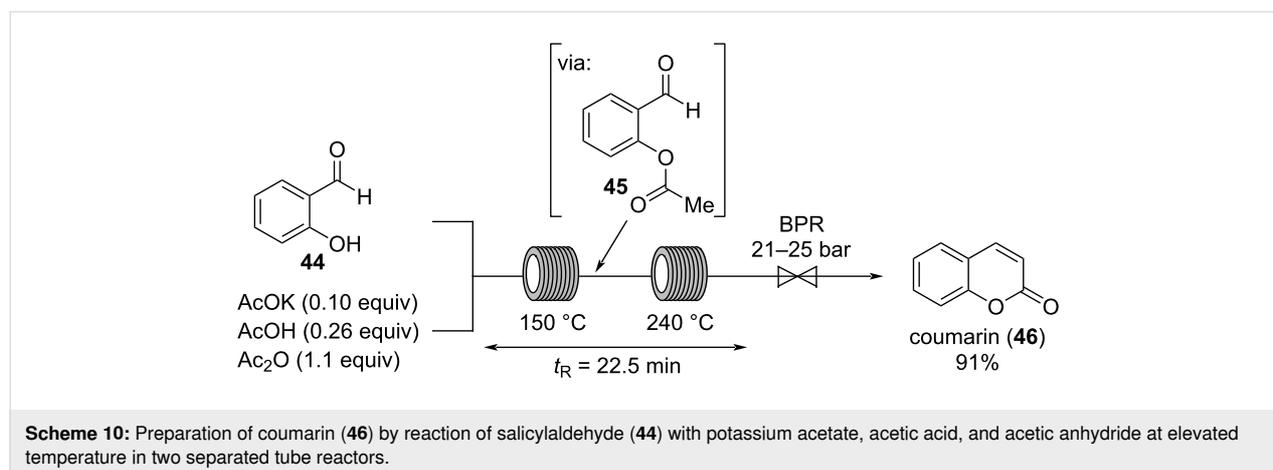
An odorant that is somewhat similar to coumarin is phthalide (**50**), having a sweet and powdery scent reminiscent of coconut and tonka bean [43]. Phthalide can be considered as a top note type of coumarin. Recently, Noël and co-workers developed a method for the photochemical, decatungstate-catalyzed C–H oxidation of activated and unactivated alkanes, including the transformation of isodihydrobenzofuran (**47**) to phthalide (**50**, Scheme 11) [44]. In this reaction, the decatungstate anion is activated by irradiation in a 3D-printed tube reactor using LED light with a wavelength of λ = 365 nm. It is assumed, that the photoexcited state of the decatungstate anion generates carbon-centered radical **48** which is trapped in a segmented flow with molecular oxygen provided by a mass flow controller. Peroxide **49** is formed as intermediate which further reacts to phthalide (**50**) in 71% yield. This method efficiently utilizes the advantages of flow chemistry for photoreactions and reactions with gases providing shorter reaction times and improved scalability [44].

Woody odorants

Woody odorants are widely used, especially in masculine perfumes. Some woody essential oils like cedarwood are relatively inexpensive, however, sandalwood oil has been overharvested for decades, and is now extremely expensive. Hence, for both expense and variety of woody type notes, there is a great demand of synthetic woody odorants. Among them, woody acetate (Vertenex, **54**) is an inexpensive ester with a "sweet, almost creamy-woody odor". Typically, woody acetate (**54**) is sold as a mixture of the *cis*- and the *trans*-isomer. Interestingly, the *cis*-isomer of **54** has a "pronounced fruity note over the woody sweetness", while the *trans*-isomer is weaker having a "dry, leathery" scent [9]. The commonly used concentration of woody acetate (**54**) in a perfume is 3–10%. Thus, Brenna and co-workers developed a *cis*-selective synthesis of **54** via a biocatalytic process in flow (Scheme 12) [45]. In the first step, a mixture of cyclohexanone **51**, NADH, and isopropanol in an aqueous phosphate buffer (pH ≈ 7) is pumped through a contin-

Scheme 11: Synthesis of phthalide (**50**) by photoinduced decatungstate catalysis.

Scheme 12: Synthesis of woody acetate (**54**) by reduction of cyclohexanone **51** and subsequent acetylation; ADH200 = alcohol dehydrogenase.
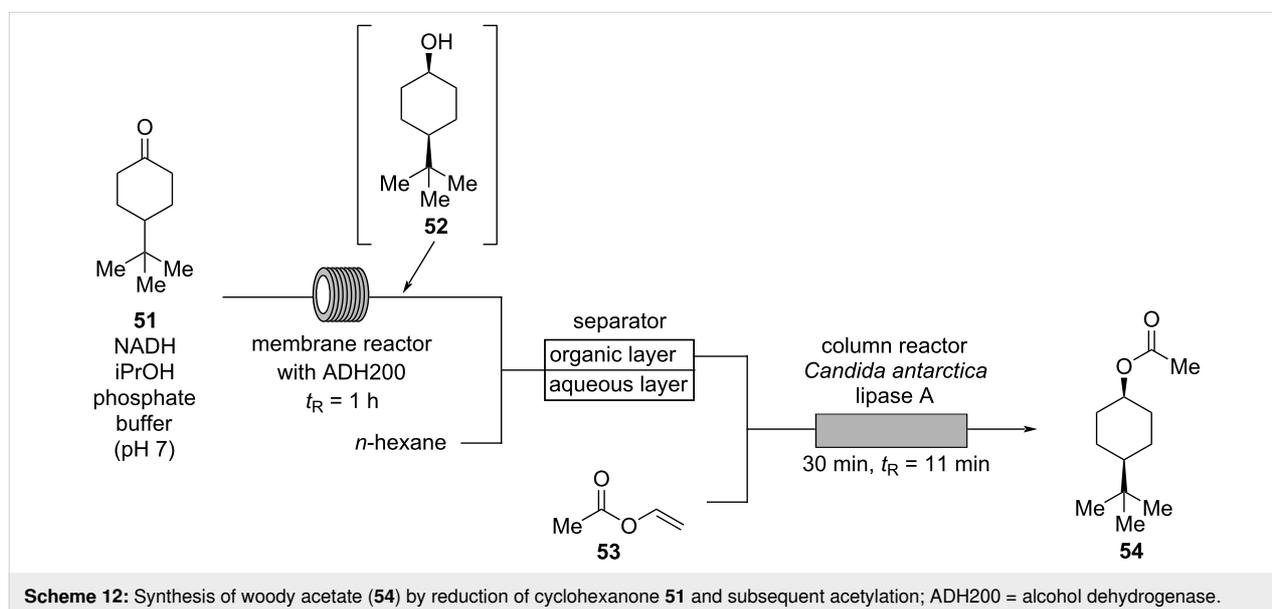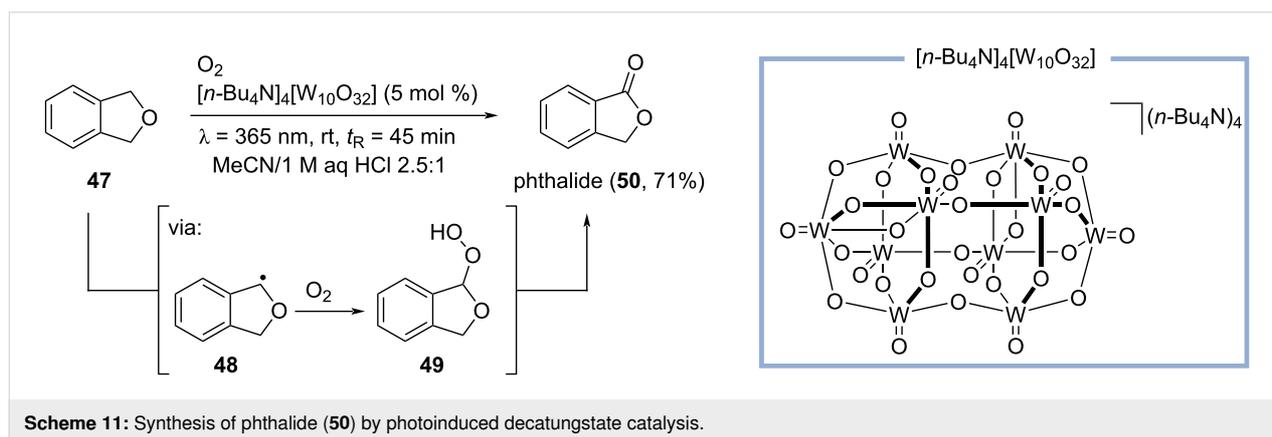
uously stirred membrane reactor at 30 °C with a residence time of 1 h containing alcohol dehydrogenase (ADH200). In this process, cyclohexanone **51** is selectively reduced to the corresponding *cis*-alcohol **52** and subsequently mixed with *n*-hexane providing a biphasic mixture which is continuously separated in a membrane separator. The organic layer is mixed with vinyl acetate (**53**) and pumped through a column reactor containing *Candida antarctica* lipase A. At 30 °C and with a residence time of 11 min, acetylation of *cis*-alcohol **52** is mediated. After distillation, *cis*-woody acetate **54** is obtained in 89% isolated yield (de > 99%) on a gram scale [45].

Additionally, Noël and co-workers prepared (+)-sclareolide (3a,6,6,9a-tetramethyl-1,4,5,5a,7,8,9,9b-octahydronaphtho[8,7-*d*]furan-2-one), a rarely used aromatic odorant reminiscent of cedar and tobacco, by C–H oxidation of (−)-ambroxan (1,5,5,9-tetramethyl-13-oxatricyclo[8.3.0.0(4,9)]tridecane) using the same method as described above for the synthesis of phthalide (**50**, see Scheme 11) [44]. However, this synthesis is more of academic value for the research on C–H functionalizations as, in fact, (−)-ambroxan is industrially prepared by reduction of (+)-sclareolide [4].

Musky odorants

Originally, musk was obtained from the gland of the musk deer and used as a powerful base note. Due to the high price of musks of natural origin, the vast majority of them is produced by chemical synthesis. Today, a plethora of synthetic musks with a broad structural and olfactory diversity are available, and commonly, musk molecules comprise between 20–40% of a fragrance. Typically, musk odorants are sweet, waxy, and "animalic", bringing warmth and erogenous mystery to a perfume. However, many modern musks can also be fresh (e.g., Galaxolide, 4,6,6,7,8,8-hexamethyl-1,3,4,6,7,8-hexahydrocyclopenta[*g*]isochromene), fruity (e.g., Helvetolide, 2-(1-(3,3-dimethylcyclohexyl)ethoxy)-2-methylpropyl propionate, has a distinct pear note), powdery (e.g., Tonalide, 1-(5,6,7,8-tetrahydro-3,5,5,6,8,8-hexamethyl-2-naphthalinyl)ethanone), or show even unexpected notes, such as a metallic character reminiscent of hot iron (Habanolide, (12*E*)-oxacyclohexadec-12-en-2-one) [3,4,9,46,47].

Although, all musks of natural origin are macrocyles, most synthetic musks are polycyclic musks (PCM), while the fourth synthetic generation of musks are linear molecules [3,4]. In 1999, juniper lactone (**56**) was isolated from the flowers of orchids among with the structurally related and better known Ambrettolide [(*Z*)-7-hexadecen-16-olide], having a sweet odor with "great tenacity and fixative power" [9,48]. Notably, and already in 1970, Story and co-workers described that cyclic ketones can be reacted with hydrogen peroxide under acidic conditions to the corresponding triperoxides which form macrocyclic structures at high temperatures, e.g., juniper lactone (**56**) [49]. Despite the elegance of this access, the safety of this process is questionable complicating the large-scale production in batch. Very recently, Kirschning and co-workers developed a flow protocol to overcome these limitations and prepared various macrolactones from triperoxides by pyrolysis in an inductively heated flow reactor (Scheme 13) [50,51]. Due to the commercial relevance of juniper lactone (**56**), they designed a flow setup for a scalable and safe two-step synthesis of **56** from cyclohexanone.

Scheme 13: Synthesis of juniper lactone (**56**) by pyrolysis of triperoxide **55** generated by oxidation of cyclohexanone in flow.
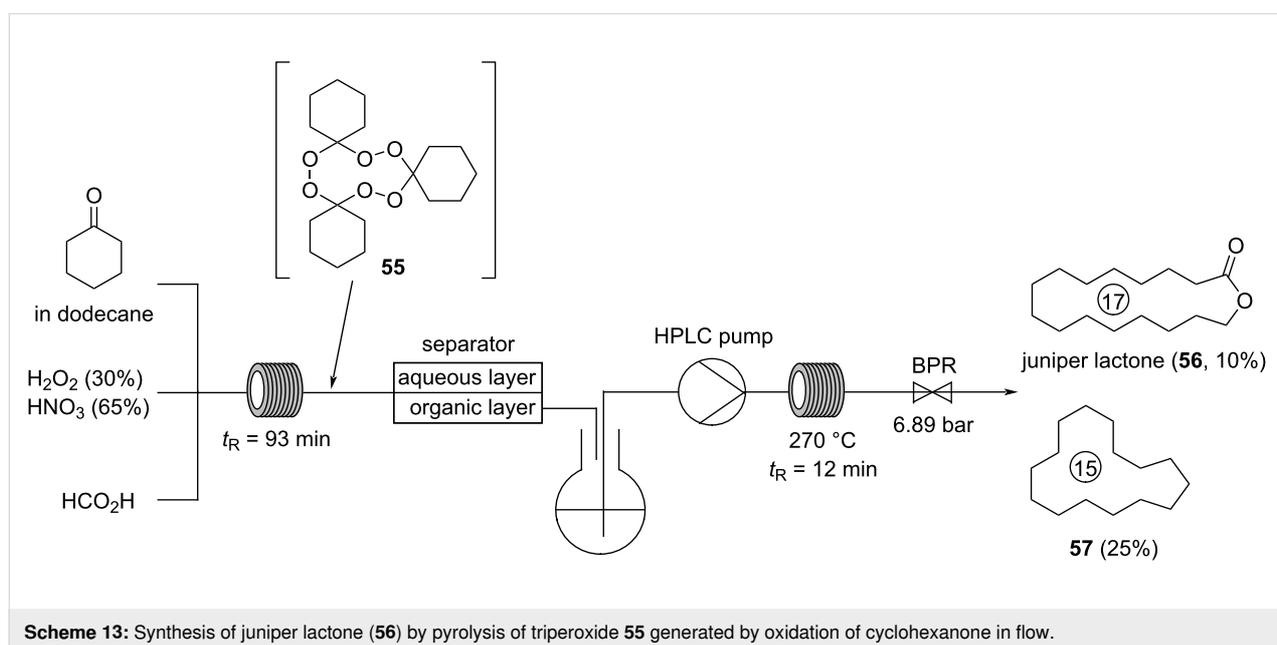
In the first step, a solution of cyclohexanone in dodecane is mixed in a Q-piece with hydrogen peroxide, nitric acid, and formic acid and subsequently pumped at room temperature through a PTFE tube reactor with a residence time of 93 min. The resulting biphasic mixture is separated using a membrane reactor with a PTFE membrane. While the aqueous layer is directly quenched with an aqueous solution of sodium sulfite, the organic layer containing triperoxide **55** in dodecane is collected in a flask and directly pumped using an HPLC pump in an inductively heated tube reactor made from stainless steel 316L. In this reactor, the second step, i.e. pyrolysis of triperoxide **55** is achieved at 270 °C with a residence time of 12 min. The reaction mixture is collected and analyzed by GC/MS indicating formation of juniper lactone (**56**) in a yield of 10% along with cyclopentadecane (**57,** 25% yield) and other byproducts. Although, juniper lactone (**56**) is obtained in a relatively low yield, this protocol allows its scalable and straightforward synthesis from simple and inexpensive starting materials. The dangers associated with organic peroxides are significantly reduced by conducting both generation and pyrolysis of triperoxide **55** in flow reactors, while phase separation of the biphasic mixture containing triperoxide **55** is realized in a PTFE membrane reactor [50].

Since many macrocyclic musks (or their precursors) contain internal olefins, they are frequently prepared by ring-closing metathesis [3,4]. It is well described that metathesis reactions can be significantly accelerated in flow, as the boiling point of the solvent employed can be exceeded using back pressure regulators (BPRs) and formed gases (e.g., ethylene) can be easily removed employing tube-in-tube reactors [11]. Therefore, Roberge, Fogg, and co-workers investigated the advantages of continuously stirred tank reactors (CSTR) and tube reactors in comparison to the corresponding batch reaction for the ring-closing metathesis of diene **58**, producing macrocyclic olefin **60** (Scheme 14) [52]. Although, macrocycle **60** is not a commer-

cial product, the corresponding saturated lactone **61** (Exaltolide), is "delicately animal, musky, and sweet" and regarded by many perfumers as one of the most elegant musks [9].

In batch and employing 1 mol % catalyst loading, the reaction reaches a maximum conversion of 82% at 80 °C after 10 min. When diene **58** and catalyst **59** are pre-mixed and pumped through a tube reactor, the ethylene released from the reaction results in a segmented flow. Therefore, the formed ethylene is not released from the tube reactor, hampering the reaction to reach full conversion as observed under batch conditions. In contrast, when a continuously stirred tank reactor was used, its head space was continuously flushed with argon to keep the concentration of ethylene in solution as low as possible. In this case, full conversion to macrocyclic olefin **60** (99% yield, detected be GC-FID) could be achieved after 20 min at 80 °C using 1 mol % of catalyst **59** [52].

Due to the fact that ethylene formed in the ring-closing metathesis can result in the formation of unstable ruthenium methylidene species, causing degeneration of the metathesis catalyst, the continuous removal of ethylene from the reaction mixture can be highly beneficial. Therefore, Skowerski and co-workers constructed a tube-in-tube reactor for the ring-closing metathesis of dienes **62** and **63** to macrocycles **65** or **66**, respectively, mediated by ruthenium catalyst **64** (Scheme 15) [53]. The substrate and the catalyst are mixed in a Q-piece and pumped through a tube reactor in which a smaller tube consisting of semipermeable Teflon AF2400 is placed. To the inner tube, vacuum is applied removing efficiently the ethylene that is formed in the reaction. Using a low concentration of the substrate to facilitate ring-closure and employing a moderate temperature of 70 °C and a residence time of 30 min, macrocycles **65** and **66** are obtained in excellent yields with a preference for the *E*-isomers as determined by GC/MS analysis.
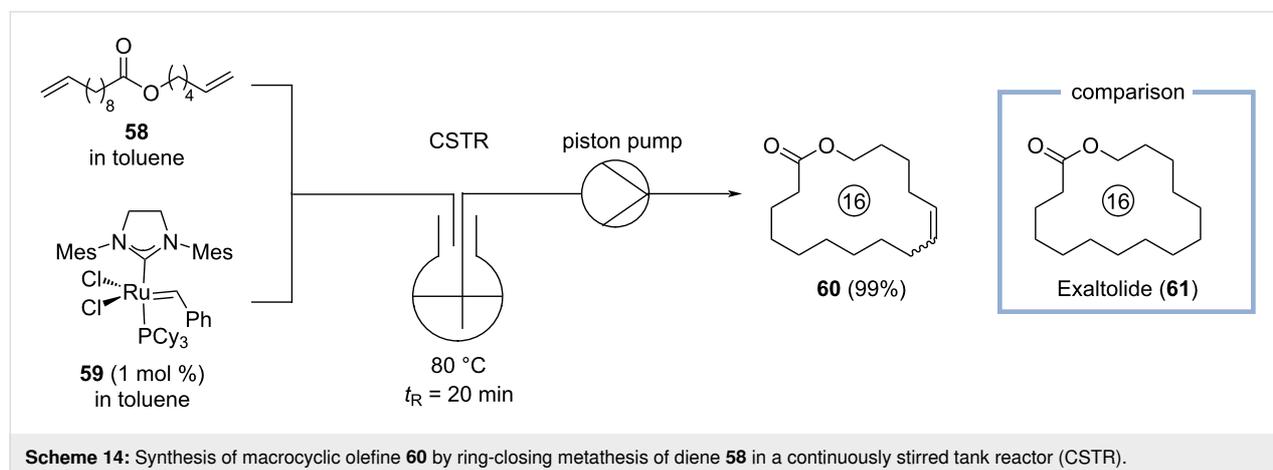
Scheme 14: Synthesis of macrocyclic olefine **60** by ring-closing metathesis of diene **58** in a continuously stirred tank reactor (CSTR).
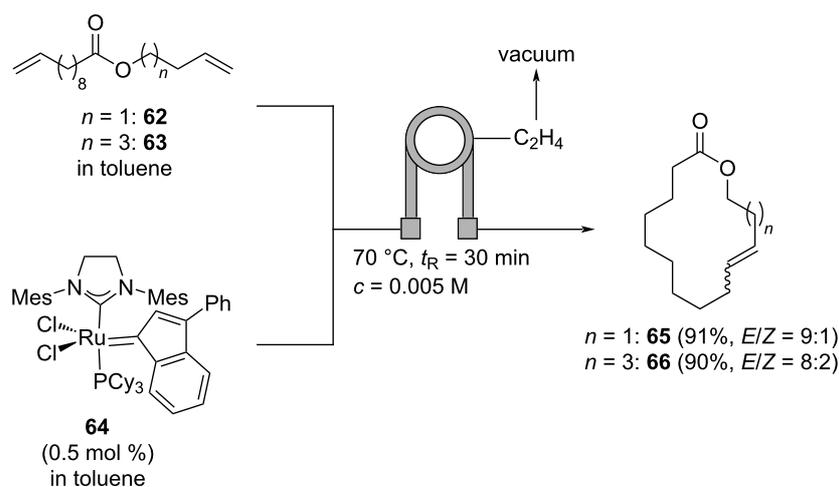
Scheme 15: Synthesis of macrocycles **65** and **66** by ring-closing metathesis of dienes **62** or **63**, respectively, in a tube-in-tube reactor removing the formed ethylene.

Although, macrocycles **65** and **66** are, to the best of our knowledge, not used as musks in perfumery, this work demonstrates the value of tube-in-tube reactors for the preparation of musk-like structures (in fact, **66** (*n* = 3) is an isomer of the widely used musk Habanolide, (12*E*)-oxacyclohexadec-12-en-2-one) [53].

Civetone (**69**) is the key ingredient of natural civet, which is the glandular secretion of civet cats. Civet is an extremely long-lasting ingredient giving a fragrance a warm and animalic touch while enhancing floral notes [9]. Natural civet has been used in large quantities in classical perfumes such as Guerlain: *Jicky*

(1889, used at approx. 0.6–1.0%) or Coty: *Chypre* (1917) [7]. Due to the high price of natural civet and as the civet cats suffer from captivity and the torturous (and sometimes even deadly) "extracting process" of the civet oil, most perfumers deny using natural civet [10]. Therefore, synthetic replicates of civet have been developed which are constructed around civetone (**69**) as key ingredient. In most syntheses of civetone (**69**), the internal double bond is prepared in a ring closing metathesis providing a mixture of civetone (**69**) and the undesired *E*-isomer. More recently, Browne, Mauduit, and co-workers developed a *Z*-selective synthesis of civetone (**69**) in a tube-in-tube reactor (Scheme 16) [54]. Solutions of dialkene **67** and the
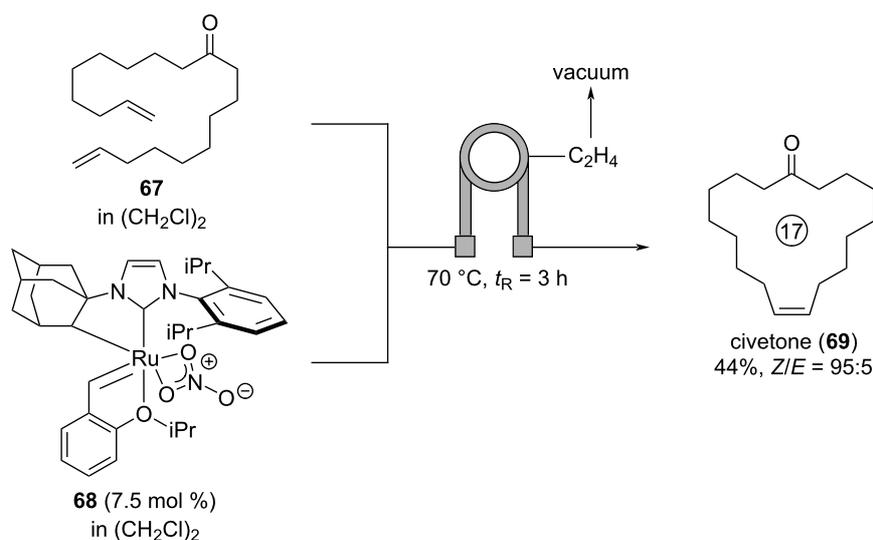
Scheme 16: *Z*-Selective synthesis of civetone (**69**) enabled by metathesis catalyst **68** in a tube-in-tube reactor.

Z-selective ruthenium catalyst **68** in 1,2-dichloroethane are mixed and pumped through a tube-in-tube reactor continuously removing the ethylene formed in the ring-closing metathesis. At 70 °C and with a residence time of 3 h, civetone (**69**) is formed in 44% isolated yield with a *Z/E* ratio of 95:5. Additionally, the authors developed an alternative synthesis of civetone (**69**) by metathesis of ethyl 9-decenoate and subsequent Dieckmann cyclization in flow, followed by a saponification and decarboxylation process in batch providing (*Z*)-civetone in 48% yield over three steps and with a *Z*-selectivity of >98% [54].

In contrast, Amorelli, Collins, and co-workers performed a ring-closing metathesis for the synthesis of macrocycle **72** from diene **70** at high temperatures of 150 °C in only 5 min without removal of formed ethylene (Scheme 17) [55]. Under these conditions, the employed Stewart–Grubbs catalyst **71** is completely decomposed but its decomposition products could efficiently be removed by passing the reaction mixture through a cartridge containing a mixture of silica and charcoal providing **72** in 32% yield at a productivity of 0.2 g/h. The macrocycle **72** was already synthesized by International Flavors & Fragrances (IFF) in 2013 and found to have a "strong musky odor" with "highly desirable properties in the top and middle notes that were described as feminine, smooth, creamy, warm, and comfortable" [55].

Conclusion

Flow chemistry has evolved as a valuable tool for organic synthesis that simplifies upscaling and, in some cases, allows to overcome limitations in batch, while being safer and more sustainable. These advantages have been utilized for the preparation of various odorants, reaching from fruity and green odorants, which are typically small and volatile molecules, to macrocyclic musks with higher molar masses and boiling points.

In flow, photocatalyzed oxidations with molecular oxygen proceed in higher yields and with shorter reaction times, as it has been used for the synthesis of, e.g., phthalide (**50**). In contrast, when ethylene is formed in a ring-closing metathesis reaction for the preparation of macrocyclic musks, the efficient removal of ethylene by the means of a tube-in-tube reactor or a continuously stirred tank reactor (CSTR) can promote the reaction and suppress decomposition of the catalyst. In addition, reactions involving organometallics at low temperatures or instable intermediates, e.g., endoperoxide (**55**), benefit from the superior reaction control and safety profile of flow reactors. Many of the transformations in this review demonstrate the utilization of solid-supported reagents in cartridges that allow to avoid separation of the reagent after performing the respective reaction.

Given these examples, we believe that the adoption of flow techniques has a great potential to facilitate the synthesis of new scents with exciting odor profiles, while simplifying upscaling of the reaction to an industrial process.

Conflicts of Interest
Paul Kiler is senior perfumer and owner of PK Perfumes. However, none of the perfumes discussed in this review are sold by or are associated with Paul Kiler or his clients.

Scheme 17: Synthesis of macrocyclic olefine **72** by ring-closing metathesis of diene **70**.

ORCID® iDs

Merlin Kleoff - https://orcid.org/0000-0001-7350-542X
Paul Kiler - https://orcid.org/0000-0002-7316-575X
Philipp Heretsch - https://orcid.org/0000-0002-9967-3541
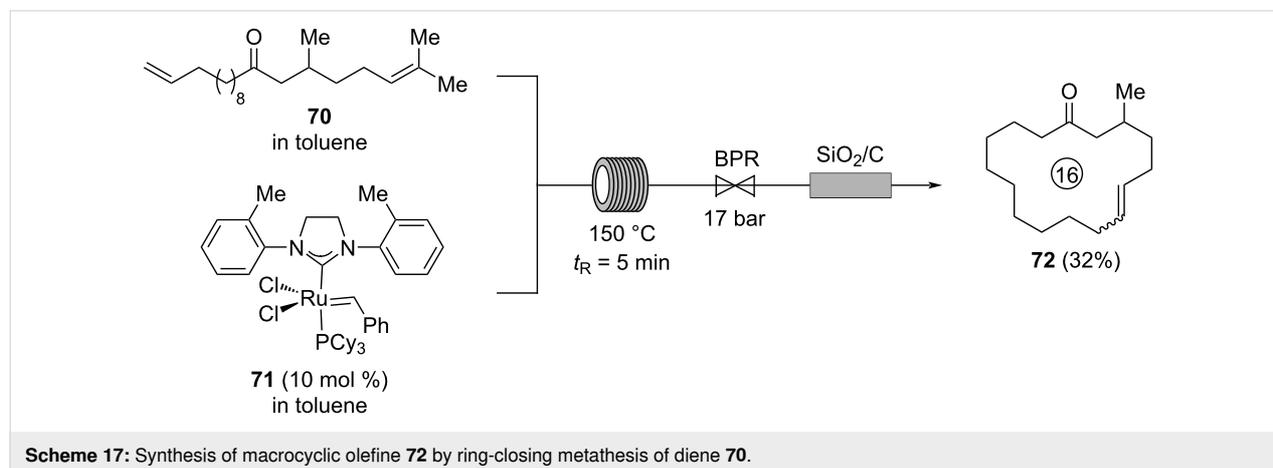
References

1. Ohloff, G. *Riechstoffe und Geruchssinn – Die molekulare Welt der Düfte;* Springer: Berlin, Heidelberg, 1990. doi:10.1007/978-3-662-09768-7
2. Ellena, J.-C. *Parfum – Ein Führer durch die Welt der Düfte,* 2nd ed.; CH Beck: München, Germany, 2016.
3. Kraft, P.; Bajgrowicz, J. A.; Denis, C.; Fráter, G. *Angew. Chem., Int. Ed.* **2000,** *39,* 2980–3010. doi:10.1002/1521-3773(20000901)39:17<2980::aid-anie2980>3.0.co;2-%23
4. Armanino, N.; Charpentier, J.; Flachsmann, F.; Goeke, A.; Liniger, M.; Kraft, P. *Angew. Chem., Int. Ed.* **2020,** *59,* 16310–16344. doi:10.1002/anie.202005719
5. Stepanyuk, A.; Kirschning, A. *Beilstein J. Org. Chem.* **2019,** *15,* 2590–2602. doi:10.3762/bjoc.15.252
6. Sell, C. S. *Fundamentals of Fragrance Chemistry;* Wiley-VCH: Weinheim, Germany, 2019.
7. Schäfer, B. *Naturstoffe der chemischen Industrie;* Springer: Berlin, Heidelberg, 2006. doi:10.1007/978-3-662-61017-6
8. Malkar, R. S.; Yadav, G. D. *Curr. Catal.* **2020,** *9,* 32–58. doi:10.2174/2211544708666190613163523
9. Arctander, S. *Perfume and Flavor Chemicals;* Allured Publishing Corporation: Carol Stream, IL, USA, 1994.
10. Arctander, S. *Perfume and Flavor Materials of Natural Origin;* Orchard Innovations: New York, NY, USA, 2020.
11. Plutschack, M. B.; Pieber, B.; Gilmore, K.; Seeberger, P. H. *Chem. Rev.* **2017,** *117,* 11796–11893. doi:10.1021/acs.chemrev.7b00183
12. Noël, T.; Cao, Y.; Laudadio, G. *Acc. Chem. Res.* **2019,** *52,* 2858–2869. doi:10.1021/acs.accounts.9b00412
13. Cambié, D.; Bottecchia, C.; Straathof, N. J. W.; Hessel, V.; Noël, T. *Chem. Rev.* **2016,** *116,* 10276–10341. doi:10.1021/acs.chemrev.5b00707
14. Gutmann, B.; Cantillo, D.; Kappe, C. O. *Angew. Chem., Int. Ed.* **2015,** *54,* 6688–6728. doi:10.1002/anie.201409318
15. Yoshida, J.-i.; Kim, H.; Nagaki, A. *J. Flow Chem.* **2017,** *7,* 60–64. doi:10.1556/1846.2017.00017
16. Williams, J. D.; Kerr, W. J.; Leach, S. G.; Lindsay, D. M. *Angew. Chem., Int. Ed.* **2018,** *57,* 12126–12130. doi:10.1002/anie.201807393
17. Harenberg, J. H.; Weidmann, N.; Wiegand, A. J.; Hoefer, C. A.; Annapureddy, R. R.; Knochel, P. *Angew. Chem., Int. Ed.* **2021,** *60,* 14296–14301. doi:10.1002/anie.202103031
18. Wiles, C.; Watts, P. *Green Chem.* **2014,** *16,* 55–62. doi:10.1039/c3gc41797b
19. Gambacorta, G.; Sharley, J. S.; Baxendale, I. R. *Beilstein J. Org. Chem.* **2021,** *17,* 1181–1312. doi:10.3762/bjoc.17.90
20. Mata, V. G.; Gomes, P. B.; Rodrigues, A. E. *AIChE J.* **2005,** *51,* 2834–2852. doi:10.1002/aic.10530
21. Butler, H. *Poucher's Perfumes, Cosmetics and Soaps;* Kluwer Academic Publishers: Dordrecht, Boston, London, 2000. doi:10.1007/978-94-017-2734-1
22. Hedione; The Good Scent Company database. http://www.thegoodscentscompany.com/data/rw1015272.html (accessed April 16, 2021).
23. Narula, A. P. S. *Chem. Biodiversity* **2014,** *11,* 1629–1638. doi:10.1002/cbdv.201300403
24. Viviano, M.; Glasnov, T. N.; Reichart, B.; Tekautz, G.; Kappe, C. O. *Org. Process Res. Dev.* **2011,** *15,* 858–870. doi:10.1021/op2001047
25. Neuenschwander, U.; Jensen, K. F. *Ind. Eng. Chem. Res.* **2014,** *53,* 601–608. doi:10.1021/ie402736j
26. Novak, U.; Lavric, D.; Žnidaršič-Plazl, P. *J. Flow Chem.* **2016,** *6,* 33–38. doi:10.1556/1846.2015.00038
27. Žnidaršič-Plazl, P.; Plazl, I. *Process Biochem. (Oxford, U. K.)* **2009,** *44,* 1115–1121. doi:10.1016/j.procbio.2009.06.003
28. Cvjetko, M.; Vorkapić-Furač, J.; Žnidaršič-Plazl, P. *Process Biochem. (Oxford, U. K.)* **2012,** *47,* 1344–1350. doi:10.1016/j.procbio.2012.04.028
29. Pohar, A.; Plazl, I.; Žnidaršič–Plazl, P. *Lab Chip* **2009,** *9,* 3385–3390. doi:10.1039/b915151f
30. Romero, M. D.; Calvo, L.; Alba, C.; Habulin, M.; Primožič, M.; Knez, Ž. *J. Supercrit. Fluids* **2005,** *33,* 77–84. doi:10.1016/s0896-8446(04)00114-7
31. dos Santos, P.; Meireles, M. A. A.; Martínez, J. *J. Supercrit. Fluids* **2017,** *127,* 71–80. doi:10.1016/j.supflu.2017.03.019
32. Contente, M. L.; Tamborini, L.; Molinari, F.; Paradisi, F. *J. Flow Chem.* **2020,** *10,* 235–240. doi:10.1007/s41981-019-00063-8
33. Salvi, H. M.; Kamble, M. P.; Yadav, G. D. *Appl. Biochem. Biotechnol.* **2018,** *184,* 630–643. doi:10.1007/s12010-017-2572-7
34. Adarme, C. A. A.; Leão, R. A. C.; de Souza, S. P.; Itabaiana, I., Jr.; de Souza, R. O. M. A.; Rezende, C. M. *Mol. Catal.* **2018,** *453,* 39–46. doi:10.1016/j.mcat.2018.04.007
35. Kuhwald, C.; Kirschning, A. *Org. Lett.* **2021,** *23,* 4300–4304. doi:10.1021/acs.orglett.1c01222
36. Miller, S. J.; Ishitani, H.; Furiya, Y.; Kobayashi, S. *Org. Process Res. Dev.* **2021,** *25,* 192–198. doi:10.1021/acs.oprd.0c00391
37. Moreno-Marrodan, C.; Barbaro, P.; Catalano, M.; Taurino, A. *Dalton Trans.* **2012,** *41,* 12666–12669. doi:10.1039/c2dt31626a
38. Gholami, Z.; Tišler, Z.; Vondrová, P.; Velvarská, R.; Štěpánek, K. *Catalysts* **2020,** *10,* 1033. doi:10.3390/catal10091033
39. Gutmann, B.; Elsner, P.; Roberge, D.; Kappe, C. O. *ACS Catal.* **2013,** *3,* 2669–2676. doi:10.1021/cs400571y
40. Amandi, R.; Hyde, J. R.; Ross, S. K.; Lotz, T. J.; Poliakoff, M. *Green Chem.* **2005,** *7,* 288–293. doi:10.1039/b418983c
41. Coumarin; The Good Scent Company database. http://www.thegoodscentscompany.com/data/rw1003832.html (accessed May 2, 2021).
42. Li, X.; Chen, A.; Zhou, Y.; Huang, L.; Fang, Z.; Gan, H.; Guo, K. *J. Flow Chem.* **2015,** *5,* 82–86. doi:10.1556/1846.2014.00043
43. Phthalide; The Good Scent Company database. http://www.thegoodscentscompany.com/data/rw1274731.html (accessed March 31, 2022).
44. Laudadio, G.; Govaerts, S.; Wang, Y.; Ravelli, D.; Koolman, H. F.; Fagnoni, M.; Djuric, S. W.; Noël, T. *Angew. Chem., Int. Ed.* **2018,** *57,* 4078–4082. doi:10.1002/anie.201800818
45. Tentori, F.; Brenna, E.; Crotti, M.; Pedrocchi-Fantoni, G.; Ghezzi, M. C.; Tessaro, D. *Catalysts* **2020,** *10,* 102. doi:10.3390/catal10010102
46. David, O. R. P. *Eur. J. Org. Chem.* **2017,** 4–13. doi:10.1002/ejoc.201601249
47. David, O. R. P. *Chem. – Eur. J.* **2020,** *26,* 7537–7555. doi:10.1002/chem.202000577

48. Hirose, S.; Joichi, A.; Nakamura, S.; Awano, K. *Flavour Fragrance J.* **1999,** *14,* 183–184.
doi:10.1002/(sici)1099-1026(199905/06)14:3<183::aid-ffj804>3.0.co;2-s

49. Busch, P.; Story, P. R. *Synthesis* **1970,** 181–183.
doi:10.1055/s-1970-21592

50. Seemann, A.; Panten, J.; Kirschning, A. *J. Org. Chem.* **2021,** *86,* 13924–13933. doi:10.1021/acs.joc.1c00663

51. Davey, P. N.; Ellwood, S.; Ellings, J. A. Novel process. UK Pat. Appl. GB2512836A, Oct 15, 2014.

52. Monfette, S.; Eyholzer, M.; Roberge, D. M.; Fogg, D. E. *Chem. – Eur. J.* **2010,** *16,* 11720–11725. doi:10.1002/chem.201001210

53. Skowerski, K.; Czarnocki, S. J.; Knapkiewicz, P. *ChemSusChem* **2014,** *7,* 536–542. doi:10.1002/cssc.201300829

54. Morvan, J.; McBride, T.; Curbet, I.; Colombel-Rouen, S.; Roisnel, T.; Crévisy, C.; Browne, D. L.; Mauduit, M. *Angew. Chem., Int. Ed.* **2021,** *60,* 19685–19690. doi:10.1002/anie.202106410

55. Morin, É.; Sosoe, J.; Raymond, M.; Amorelli, B.; Boden, R. M.; Collins, S. K. *Org. Process Res. Dev.* **2019,** *23,* 283–287. doi:10.1021/acs.oprd.8b00450

Continuous flow synthesis of azobenzenes via Baeyer–Mills reaction

Jan H. Griwatz[‡1,2], Anne Kunz[‡1,2] and Hermann A. Wegner[*1,2]

Full Research Paper

Address:
[1]Institute of Organic Chemistry, Justus Liebig University, Heinrich-Buff-Ring 17, 35392 Giessen, Germany and [2]Center for Material Research (ZfM/LaMa), Justus Liebig University, Heinrich-Buff-Ring 16, 35392 Giessen, Germany

Email:
Hermann A. Wegner[*] - hermann.a.wegner@org.chemie.uni-giessen.de

* Corresponding author   ‡ Equal contributors

Abstract

Azobenzene, as one of the most prominent molecular switches, is featured in many applications ranging from photopharmacology to information or energy storage. In order to easily and reproducibly synthesize non-symmetric substituted azobenzenes in an efficient way, especially on a large scale, the commonly used Baeyer–Mills coupling reaction was adopted to a continuous flow setup. The versatility was demonstrated with a scope of 20 substances and the scalability of this method exemplified by the synthesis of >70 g of an azobenzene derivative applied in molecular solar thermal storage (MOST) systems.

Introduction

Although the red-colored azobenzenes (AB) have been known for years as dyes, their applications nowadays span from energy and information storage [1-5], organocatalysis [6], photobiology and photopharmacology [7], host–guest chemistry [8], molecular mechanics [9,10], to molecular machines [11]. This popularity is due to the ability of ABs to isomerize from their energetically more stable (*E*)- to the meta-stable (*Z*)-isomer by irradiation with light [12]. During this isomerization, not only the geometry is altered from the planar (*E*)-AB to its twisted (*Z*)-AB form, but also its properties change (e.g., dipole moment and polarity) [13,14]. Furthermore, the (*Z*)-AB can be reversibly switched back by visible light or thermally [15]. To synthesize ABs a variety of reactions can be chosen from, each having both advantages and disadvantages. The best synthesis must be individually selected for the respective use [16]. There are various ways to access symmetric and non-symmetric AB compounds in a convenient way in batch size, as it has been summarized in detail [16]. One example is the reliable synthesis of symmetric ABs in high yields via a Cu-catalyzed oxidative coupling of aniline derivatives [17]. This synthesis can be

also used for the formation of non-symmetric AB, however, only for a selected set of anilines. One of the most applied methods to access non-symmetric azobenzenes is based on the condensation of nitrosobenzenes with anilines (Scheme 1). This so-called Baeyer–Mills reaction, which was first published by Baeyer in 1874 and further investigated by Mills, proceeds best for electron-rich anilines with electron-poor nitrosobenzenes. The reactivity can be rationalized by the proposed mechanism, which involves nucleophilic attack of the aniline on the nitrosobenzene derivatives in acidic or basic media (Scheme 1) [18-21]. However, in order to use azobenzenes as functional materials, access to a large-scale process is necessary. In this context continuous flow synthesis is frequently discussed as potential solution to address this challenge. This technique is neither limited by the size of the reaction vessel nor the stirring as the reagents are pumped continuously through the reactor. The set-up also allows precise control of the reaction time and temperature, which can lead to higher yields and purity [22]. Flow chemistry to prepare azobenzenes has been previously applied to the Cu-catalyzed synthesis of symmetric substituted AB derivatives [23,24]. However, non-symmetric substituted ABs are not accessible by this method in an efficient way. Herein, we report a continuous flow synthesis of non-symmetric AB compounds via the Baeyer–Mills reaction, which allows to obtain large quantities of products from different substrates in a fast and efficient manner.

Scheme 1: Baeyer–Mills reaction of AB (**1a**) involving nucleophilic attack of aniline (**2a**) to nitrosobenzene (**3**).
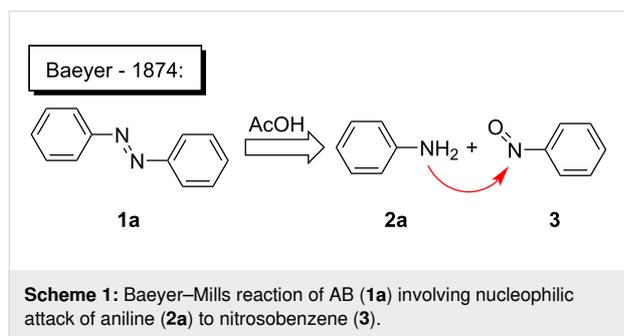
Results and Discussion

For optimization of the Baeyer–Mills coupling in continuous flow the reaction to generate unsubstituted AB (**1a**) was performed with freshly distilled aniline (**2a**) and commercially available nitrosobenzene (**3**), dissolved separately in acetic acid. Both starting materials had the same concentration and were pumped by a Vapourtec E-Series system (for details, see experimental part in Supporting Information File 1). After mixing, the solution was passed through a tube reactor, in which the temperature as well as the residence time can be easily modified. Afterwards the respective reaction mixture was collected and analyzed (Figure 1). In order to optimize the reaction, both the temperature and the residence time were successively changed

to achieve the highest conversion to AB. The residence time was increased from 5.0 to 50.0 min and the temperature was raised stepwise from 25 °C up to 90 °C (Figure 1). After the set residence time an aliquot was collected, diluted with acetonitrile, and subsequently examined by HPLC analysis (for details, see Supporting Information File 1).

Figure 1: Flow setup for optimization of the Baeyer–Mills reaction with aniline (**2a**) and nitrosobenzene (**3**). In this setup the temperature of the tube reactor as well as the residence time can be individually varied (Figure 2).
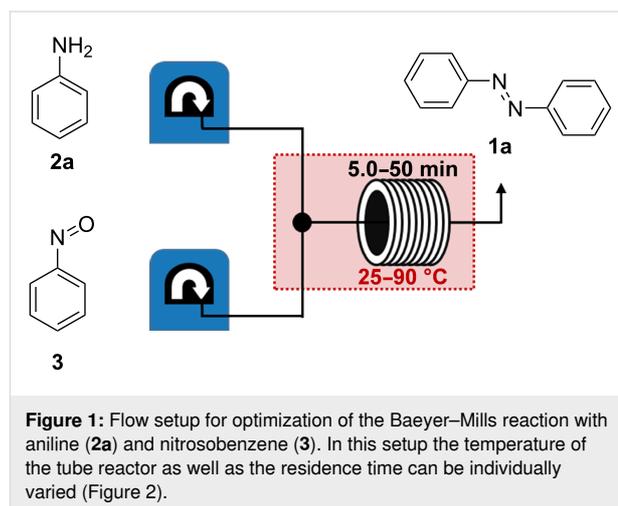
At lower temperature, AB (**1a**) could be detected, but only a low conversion of the starting materials was observed (Figure 2). At higher temperature, the product/starting material ratio was improved but was still not satisfactory. Therefore, not only the temperatures, but also the residence time was gradually changed (Figure 2). At 70–90 °C and a residence time of 50.0 min the best results were observed. However, heating to 80–90 °C provided increasing amounts of azoxybenzene, which is a known side product of the Bayer–Mills reaction [25]. Hence, these parameters (70 °C, 50.0 min) were chosen to do

temperature θ/°C	5.0	10.0	16.7	50.0
25	5	5	12	31
40	12	20	29	52
50	19	31	45	67
60	31	42	58	77
70	42	56	69	83
80	53	67	76	81
90	55	69	79	86

Figure 2: Optimization of the Baeyer–Mills reaction of nitrosobenzene (**3**) with aniline (**2a**) to AB (**1a**). The numbers in the figure result from the ratio of the integral of the HPLC peak of AB (**1a**) to the integral of AB (**1a**), nitrosobenzene (**3**), and aniline (**2a**) at a wavelength of 254 nm (see Supporting Information File 1 for details).

the synthesis on a preparative scale. The setup was slightly modified to include an aqueous workup and extraction of the organic phase. For this purpose, a third pump was implemented which adds cyclohexane to the reaction mixture after the tube reactor (Figure 3). The reaction solution with cyclohexane was continuously fed into a separating funnel containing brine. After phase separation, drying of the organic phase with $MgSO_4$, and evaporation of the solvent, AB (**1a**) could be obtained in 98% yield under the previously optimized conditions. By collection of the reactor output for 2 h, 582 mg of AB were obtained.

Figure 3: Flow setup after prior optimization with unsubstituted aniline (**2a**) and nitrosobenzene (**3**) to AB (**1a**).
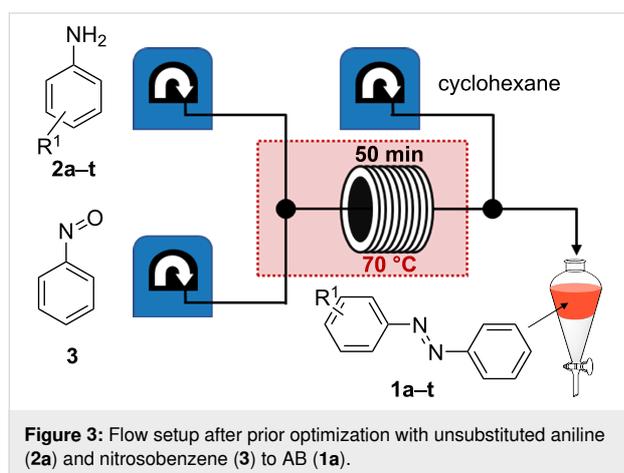
Further purification was not necessary as the product was satisfactorily pure with the described workup. After successful optimization of the synthesis of unsubstituted AB (**1a**) the setup was also tested for a large number of other azobenzene derivatives to determine the scope of the method (Table 1). All aniline derivatives **2a–s** were commercially available and the corresponding azobenzenes **1a–s** were synthesized according to the general procedure in continuous flow as described before. The optimized flow and workup conditions gave the products in high purity for most of the synthesized AB derivatives (see Supporting Information File 1 for details). Only in a few cases flash column chromatography was necessary to isolate the pure products (see Table 1). As expected, the method worked excellently for most of the electron-rich anilines due to their increased nucleophilicity.

A comparison of *ortho-*, *meta-* and *para-*substituted derivatives revealed that for electron-rich anilines, the *para-*substituted ABs are formed in better yields as their *ortho-* and *meta-*analogues. For example, the synthesis of AB **1i** from *m*-anisidine (**2i**) gave only 7% yield, due to the formation of large amounts of azoxybenzene and purification issues therefrom. The moderate product yields from the *ortho-*substituted aniline derivatives are presumably caused by the higher steric hindrance of the nucleophilic attack. Low yields in case of electron-poor aniline

Table 1: Substrate scope of the Baeyer–Mills reaction under the optimized conditions in continuous flow.

entry	aniline **2**	product **1**	yield [%]
1	**2a**	**1a**	98
2	**2b**	**1b**	89
3	**2c**	**1c**	77
4	**2d**	**1d**	94

Table 1: Substrate scope of the Baeyer–Mills reaction under the optimized conditions in continuous flow. (continued)
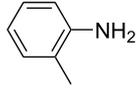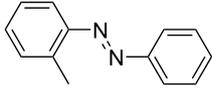
5	**2e**	**1e**[a]	79
6	**2f**	**1f**[a]	67
7	**2g**	**1g**	>99
8	**2h**	**1h**	96
9	**2i**	**1i**[a]	7
10	**2j**	**1j**[a]	72
11	**2k**	**1k**[a]	23
12	**2l**	**1l**[a]	65
13	**2m**	**1m**	70
14	**2n**	**1n**	99
15	**2o**	**1o**	7
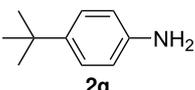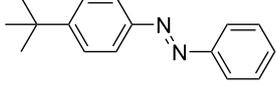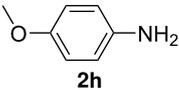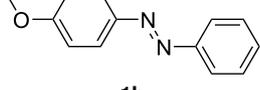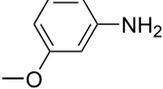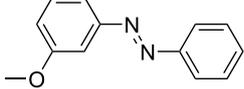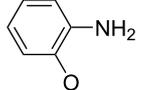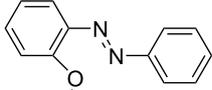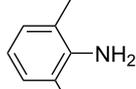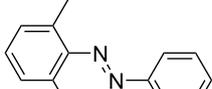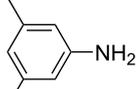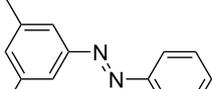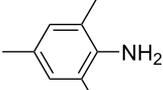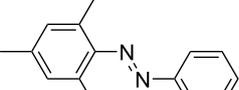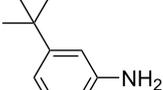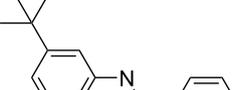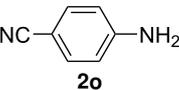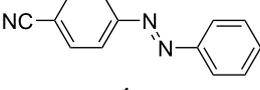
Table 1: Substrate scope of the Baeyer–Mills reaction under the optimized conditions in continuous flow. (continued)
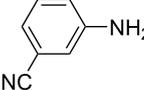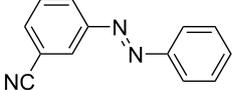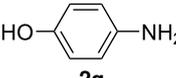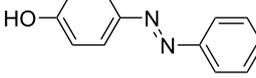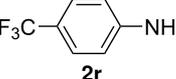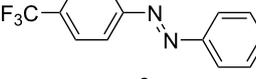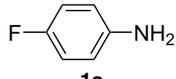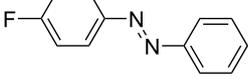
|		
16	**2p**	**1p** 54
17	**2q**	**1q** 68
18	**2r**	**1r**[a] 33
19	**1s**	**1s** 95

[a]Purified by chromatography.

derivatives can be explained by the reduced nucleophilicity. To exemplarily demonstrate the optimization for electron-poor derivatives, the synthesis of *p*-cyano-substituted AB **1o** was repeated at higher temperatures. Thereby the yield of **1o** could be increased to 17% (90 °C) and 19% (110 °C), respectively. However, since larger amounts of azoxybenzene were formed, column chromatography became necessary relativizing this improvement in yield (see Supporting Information File 1 for spectra). Substrates, which did not result in AB formation, were anilines with a nitro-substituent. Moreover, some further cases of *ortho*-substituted anilines were unsuccessful, for which steric effects could serve as an explanation (see Supporting Information File 1 for details). In comparison with published batch syntheses, the herein reported continuous flow synthesis usually gives similar or improved yields and eliminates the shortcomings in scalability.

For the applications of ABs as molecular materials often larger amounts are required, for example, as active compounds in molecular solar thermal energy storage (MOST) systems. Therefore, we utilized the set-up for the preparation of large amounts of AB **1t** (Scheme 2). This AB analogue was first synthesized by Masutani et al. in 2014 and was examined by them as well as in further studies by other groups regarding their potential for MOST applications, e.g., in a fluidic chip device by Wang et al. [1,26,27]. For the large-scale synthesis both, aniline **2t** as well as nitrosobenzene (**3**), were dissolved in acetic acid and, as described before, pumped through the flow setup (Figure 3). Every 12 h, the organic phase was separated from the aqueous phase, dried over MgSO₄, and the solvent was subsequently re-

moved. The solvent was recycled to minimize waste. After a total runtime of 3 days 72 g of AB **1t** were obtained as pure red oil which corresponds to a yield of >99%. Therefore, the method should be suitable for the preparation of easily several 100 grams of azobenzene compounds.

Scheme 2: Large-scale synthesis of AB **1t** from aniline **2t** and nitrosobenzene (**3**) in >99% yield within 3 days.
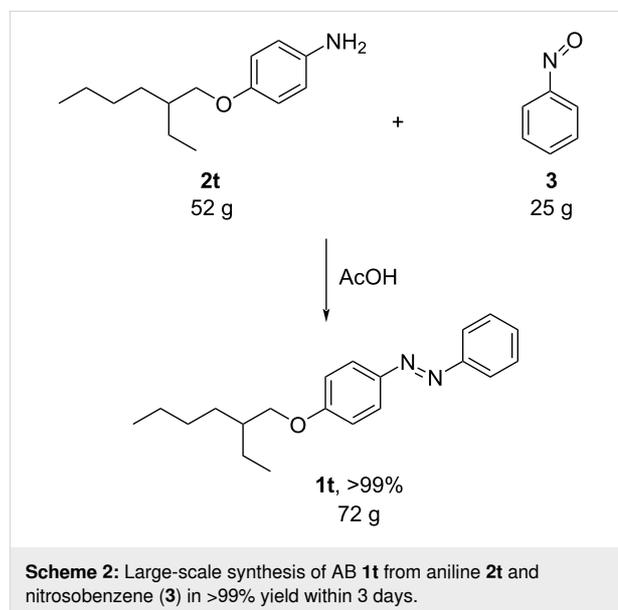
Conclusion

In summary, the Baeyer–Mills reaction was successfully transferred to a continuous flow setup. The method can be used for various anilines as starting materials to access the desired ABs. A scope of 20 different anilines (**2a–t**) resulting in the corre-

sponding azobenzenes **1a–t** was investigated and especially electron-rich azobenzenes were prepared in yields up to >99%. Furthermore, the setup was demonstrated to be applicable for a large-scale synthesis, where azobenzene **1t** was obtained in 72 g within 3 days without the need of further purification. With this process a large number of non-symmetric substituted azobenzenes can be prepared in high yields and large quantities which opens new possibilities for applications of AB as molecular materials in general.

Supporting Information

Supporting Information File 1
General information, experimental data of all isolated products, ^{1}H and ^{13}C NMR spectra, and structures of unsuccessful substrates.
[https://www.beilstein-journals.org/bjoc/content/supplementary/1860-5397-18-78-S1.pdf]

Acknowledgements

Funding

ORCID® iDs

Jan H. Griwatz - https://orcid.org/0000-0003-2028-0938
Anne Kunz - https://orcid.org/0000-0002-2142-2689
Hermann A. Wegner - https://orcid.org/0000-0001-7260-6018

References

1. Wang, Z.; Losantos, R.; Sampedro, D.; Morikawa, M.-a.; Börjesson, K.; Kimizuka, N.; Moth-Poulsen, K. *J. Mater. Chem. A* **2019,** *7,* 15042–15047. doi:10.1039/c9ta04905c
2. Liu, Z. F.; Hashimoto, K.; Fujishima, A. *Nature* **1990,** *347,* 658–660. doi:10.1038/347658a0
3. Ikeda, T.; Tsutsumi, O. *Science* **1995,** *268,* 1873–1875. doi:10.1126/science.268.5219.1873
4. Gerkman, M. A.; Han, G. G. D. *Joule* **2020,** *4,* 1621–1625. doi:10.1016/j.joule.2020.07.011
5. Dong, L.; Feng, Y.; Wang, L.; Feng, W. *Chem. Soc. Rev.* **2018,** *47,* 7339–7368. doi:10.1039/c8cs00470f
6. Liu, H.-d.; Zheng, A.-x.; Gong, C.-b.; Ma, X.-b.; Hon-Wah Lam, M.; Chow, C.-f.; Tang, Q. *RSC Adv.* **2015,** *5,* 62539–62542. doi:10.1039/c5ra10343f
7. Hüll, K.; Morstein, J.; Trauner, D. *Chem. Rev.* **2018,** *118,* 10710–10747. doi:10.1021/acs.chemrev.8b00037
8. Liu, M.; Yan, X.; Hu, M.; Chen, X.; Zhang, M.; Zheng, B.; Hu, X.; Shao, S.; Huang, F. *Org. Lett.* **2010,** *12,* 2558–2561. doi:10.1021/ol100770j
9. Konieczkowska, J.; Bujak, K.; Nocoń, K.; Schab-Balcerzak, E. *Dyes Pigm.* **2019,** *171,* 107659. doi:10.1016/j.dyepig.2019.107659
10. Zhang, Y.; Sun, X.; An, X.; Sui, A.; Yi, J.; Song, X.-m. *Dyes Pigm.* **2021,** *186,* 109018. doi:10.1016/j.dyepig.2020.109018
11. Norikane, Y.; Tamaoki, N. *Org. Lett.* **2004,** *6,* 2595–2598. doi:10.1021/ol049082c
12. Hartley, G. S. *Nature* **1937,** *140,* 281. doi:10.1038/140281a0
13. Harada, J.; Ogawa, K.; Tomoda, S. *Acta Crystallogr., Sect. B: Struct. Sci.* **1997,** *53,* 662–672. doi:10.1107/s0108768197002772
14. Mostad, A.; Rømming, C. *Acta Chem. Scand.* **1971,** *25,* 3561–3568. doi:10.3891/acta.chem.scand.25-3561
15. Bandara, H. M. D.; Burdette, S. C. *Chem. Soc. Rev.* **2012,** *41,* 1809–1825. doi:10.1039/c1cs15179g
16. Merino, E. *Chem. Soc. Rev.* **2011,** *40,* 3835–3853. doi:10.1039/c0cs00183j
17. Zhang, C.; Jiao, N. *Angew. Chem., Int. Ed.* **2010,** *49,* 6174–6177. doi:10.1002/anie.201001651
18. Mills, C. *J. Chem. Soc., Trans.* **1895,** *67,* 925–933. doi:10.1039/ct8956700925
19. Baeyer, A. *Ber. Dtsch. Chem. Ges.* **1874,** *7,* 1638–1640. doi:10.1002/cber.187400702214
20. Ueno, K.; Akiyoshi, S. *J. Am. Chem. Soc.* **1954,** *76,* 3670–3672. doi:10.1021/ja01643a021
21. Dommaschk, M.; Peters, M.; Gutzeit, F.; Schütt, C.; Näther, C.; Sönnichsen, F. D.; Tiwari, S.; Riedel, C.; Boretius, S.; Herges, R. *J. Am. Chem. Soc.* **2015,** *137,* 7552–7555. doi:10.1021/jacs.5b00929
22. Plutschack, M. B.; Pieber, B.; Gilmore, K.; Seeberger, P. H. *Chem. Rev.* **2017,** *117,* 11796–11893. doi:10.1021/acs.chemrev.7b00183
23. Qin, H.; Liu, C.; Lv, N.; He, W.; Meng, J.; Fang, Z.; Guo, K. *Dyes Pigm.* **2020,** *174,* 108071. doi:10.1016/j.dyepig.2019.108071
24. Georgiádes, Á.; Ötvös, S. B.; Fülöp, F. *ACS Sustainable Chem. Eng.* **2015,** *3,* 3388–3397. doi:10.1021/acssuschemeng.5b01096
25. Tombari, R. J.; Tuck, J. R.; Yardeny, N.; Gingrich, P. W.; Tantillo, D. J.; Olson, D. E. *Org. Biomol. Chem.* **2021,** *19,* 7575–7580. doi:10.1039/d1ob01450a
26. Masutani, K.; Morikawa, M.-a.; Kimizuka, N. *Chem. Commun.* **2014,** *50,* 15803–15806. doi:10.1039/c4cc07713j
27. Wang, Z.; Moïse, H.; Cacciarini, M.; Nielsen, M. B.; Morikawa, M.-a.; Kimizuka, N.; Moth-Poulsen, K. *Adv. Sci.* **2021,** *8,* 2103060. doi:10.1002/advs.202103060

Heterogeneous metallaphotoredox catalysis in a continuous-flow packed-bed reactor

Wei-Hsin Hsu[1,2], Susanne Reischauer[1,2], Peter H. Seeberger[1,2], Bartholomäus Pieber[*1] and Dario Cambié[*1]

Abstract

Metallaphotoredox catalysis is a powerful and versatile synthetic platform that enables cross-couplings under mild conditions without the need for noble metals. Its growing adoption in drug discovery has translated into an increased interest in sustainable and scalable reaction conditions. Here, we report a continuous-flow approach to metallaphotoredox catalysis using a heterogeneous catalyst that combines the function of a photo- and a nickel catalyst in a single material. The catalyst is embedded in a packed-bed reactor to combine reaction and (catalyst) separation in one step. The use of a packed bed simplifies the translation of optimized batch reaction conditions to continuous flow, as the only components present in the reaction mixture are the substrate and a base. The metallaphotoredox cross-coupling of sulfinates with aryl halides was used as a model system. The catalyst was shown to be stable, with a very low decrease of the yield (≈1% per day) during a continuous experiment over seven days, and to be effective for C–O arylations when carboxylic acids are used as nucleophile instead of sulfinates.

Introduction

The amount and impact of visible-light-mediated protocols in organic synthesis have increased dramatically since the late 2000s [1]. The main driving force of this phenomenon is the novel reactivity afforded by visible-light photocatalysts that enable new reaction pathways that were previously difficult or impossible to realize [2]. Technical advancements, such as the rise of light-emitting diodes (LEDs) and new reactor technolo-

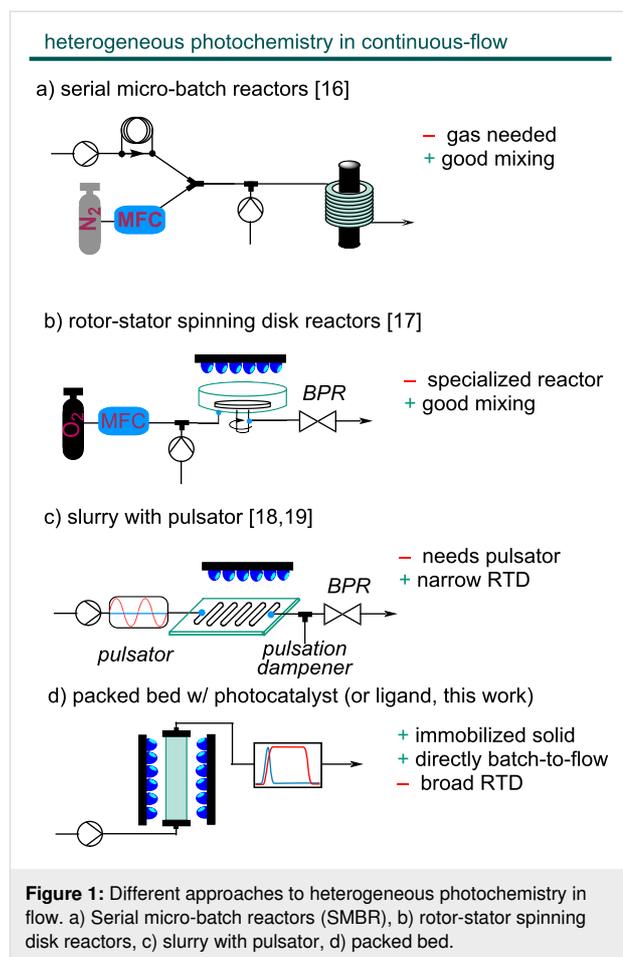gies were similarly important incentives to popularize light-mediated organic synthesis [3]. The adoption of flow chemistry ensured short photon path lengths and overcame issues related to scalability and productivity caused by the limited light penetration in large batch reactors (Lambert–Beer law), thereby making photocatalysis a promising option for industrially relevant processes [4,5]. This is underlined by several photochemi-

cal and photocatalytic transformations that have been performed on industrial scales in continuous-flow reactors [6-8].

A particularly appealing branch of photocatalytic organic synthesis is the combination with other modes of catalysis in dual catalytic approaches [9]. Especially the combination with other transition metal catalysts (metallaphotoredox catalysis), such as nickel complexes, resulted in a vast number of new methods to achieve cross-couplings under mild conditions [10]. However, the conditions of these methods are often hard to translate to flow [11,12] and significant changes to the optimized batch protocol are usually required [13,14]. The most common obstacle in the batch-to-flow translation of metallaphotoredox reactions is their frequent heterogeneous nature, most commonly due to poorly soluble inorganic bases, catalysts or additives [5,15]. Solid reagents and catalysts cause severe problems, such as reactor clogging under continuous-flow conditions. To prevent reactor fouling in (gas-)solid-liquid heterogeneous photoreactions, different solutions have been proposed [16], including the use of serial micro-batch reactors (SMBR, Figure 1a) [17], rotor-stator spinning disk reactors (Figure 1b) [18], and the combination of oscillatory pumps with microstructured reactors (Figure 1c) [19,20].
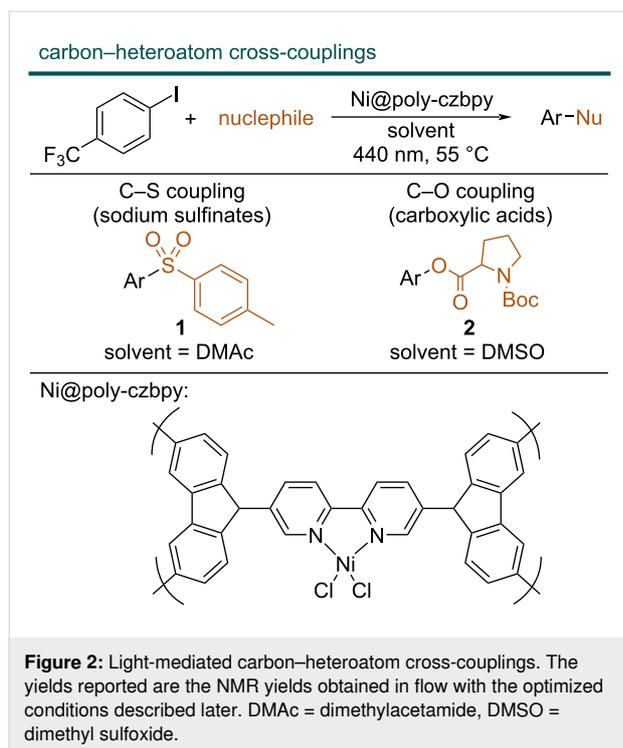
When the (photo)catalyst is the solid material in a heterogeneous reaction, packed-bed reactors are the most appealing solution for flow processes [5] (Figure 1d): The heterogeneous catalyst remains located in a specific part of the reactor through which the reaction mixture is pumped, which reduces material damage through attrition and the confinement of the catalysts in the packed bed lifts the need for solid separation. If the catalyst is sufficiently (photo-)stable, a higher turnover number can be achieved [16]. Issues related to the low surface-to-volume ratio that prevents efficient irradiation of heterogeneous photocatalysts in packed beds can be addressed by adding, for example, glass beads [21]. These considerations have justified the development of several strategies to immobilize transition-metal photocatalysts [22].

In the case of flow-metallaphotoredox catalysis packed-bed reactors were not applied to date. This is likely because these reactions are mainly carried out using homogeneous catalysis. Several studies have shown that the combination of solid photocatalysts (i.e., semiconductors) and homogeneous nickel complexes are feasible, but the fact that the nickel complex is in solution reduces the benefits of packed-bed reactor types [19,23,24]. Recently, several bifunctional heterogeneous catalysts that combine the photo- and the nickel catalyst in a single material have been reported [23,25-27]. For example, some of us have shown that a bipyridine ligand decorated with two carbazole groups can be polymerized to afford a heterogeneous

Figure 1: Different approaches to heterogeneous photochemistry in flow. a) Serial micro-batch reactors (SMBR), b) rotor-stator spinning disk reactors, c) slurry with pulsator, d) packed bed.

macroligand (poly-czbpy) that coordinates nickel and serves as an active catalyst for light-mediated carbon–heteroatom cross-couplings of sodium sulfinates, carboxylic acids and sulphonamides with aryl halides (Figure 2) [28]. Although recyclable, batch reactions are characterized by long reaction times (24 h).

Here, we present a detailed investigation of a continuous-flow strategy for these heterogeneous catalysts, using a packed-bed reactor. The use of a packed-bed reactor for these solid–liquid reactions is attractive as reaction and separation can be combined in one step. This is particularly notable in our case since, after complexing poly-czbpy with nickel (Ni@poly-czbpy), the simultaneous separation of both the photocatalyst and metal-catalyst is achieved. The combination of both catalytic activities in a single material is crucial to obtain this result, as a mixture of a heterogeneous photocatalyst with an immobilized metal catalyst would be problematic both in terms of packed bed uniformity and activity, while partially homogeneous systems would need downstream separations. We used in-line reaction monitoring to study several process parameters, such as time, temperature and the photon flux, to maximize the

Figure 2: Light-mediated carbon–heteroatom cross-couplings. The yields reported are the NMR yields obtained in flow with the optimized conditions described later. DMAc = dimethylacetamide, DMSO = dimethyl sulfoxide.

require any additives, such as a base, which allows for a straightforward proof-of-principle study on the long-term stability of the polymeric material under flow conditions. Compared to the original batch procedure, a reduction of the reaction concentration by a factor of two was necessary to ensure complete solvation of the sulfinate salt.

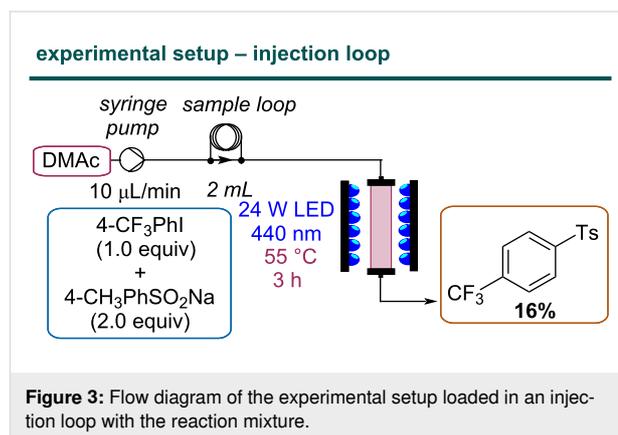**Figure 3:** Flow diagram of the experimental setup loaded in an injection loop with the reaction mixture.

Results and Discussion
Reactor assembly and model reaction
We started our investigations by preparing a packed-bed reactor using a glass column (6.6 mm i.d., 100 mm length) that can be used in a dedicated setup for heterogeneous flow photocatalysis carried out in a commercial photochemical flow reactor (from Vapourtec) [29-32]. To decrease the optical density of the bed, the column was loaded with a mixture of poly-5,5'-di(9*H*-carbazol-9-yl)-2,2'-bipyridine (poly-czbpy), glass beads and silica [33]. Once the column was ready, nickel was ligated to the polymerized ligand to afford the complexated catalyst (Ni@poly-czbpy). Based on previous batch optimizations we aimed for a ligand/metal ratio of 2:1 to ensure no unligated nickel is present as it negatively impacts the selectivity. By recirculating a solution of $NiCl_2$·glyme (4.3 mM) through the reactor for three hours (flow rate: 0.5 mL/min) most of the Ni was ligated to the macroligand (84% by ICP, see Supporting Information File 1).

To test the activity of the bed, a flow setup consisting of a syringe pump, a sample loop for injecting low volumes of the reaction mixture, and the photoreactor unit was assembled (Figure 3). The C–S coupling between 4-iodobenzotrifluoride and sodium *p*-toluenesulfinate was chosen as the model reaction [28]. In contrast to other protocols, this reaction does not

Once homogeneous conditions were achieved, the reaction mixture was injected into the reactor, which was radiated with 440 nm LEDs at 55 °C. A poor yield (16%) was obtained using a residence time of 3 hours. This result called for a more detailed investigation of crucial reaction parameters to understand if the limitation is of catalytic or technological nature.

Steady-state and automated reaction analysis
To systematically study the cross-coupling using the packed-bed reactor, we decided to equip the continuous-flow setup with a dedicated tool for in-line analysis. Such techniques enable rapid investigations of process-related parameters [34]. In particular, the presence of a trifluoromethyl group in the substrate enabled straightforward reaction monitoring via ^{19}F NMR. To this end, a 1 T benchtop NMR equipped with a flow cell was connected to the reactor outlet and used to acquire a series of spectra. In particular, a series of 128 repetitions with a 90° pulse width and a relatively long repetition time of 5.2 s (3.2 acquisition + 2s delay) was used to ensure accurate integrals. The processed FIDs were integrated and the following integration limits were used: starting material between −60.85 to −61.1 ppm, product between −61.1 and −61.35 ppm and an unidentified side-product at −60.5 to −60.7 ppm, no other peaks were detected in the fluorine spectra. The product yield calculated from the relative ratio of the product to the total integral area was comparable with the NMR yield calculated with hexafluorobenzene as internal standard in the high-field spectrometer (see Supporting Information File 1, Table S1). With the in-line analytical data in hand, it was clear that the sample loop
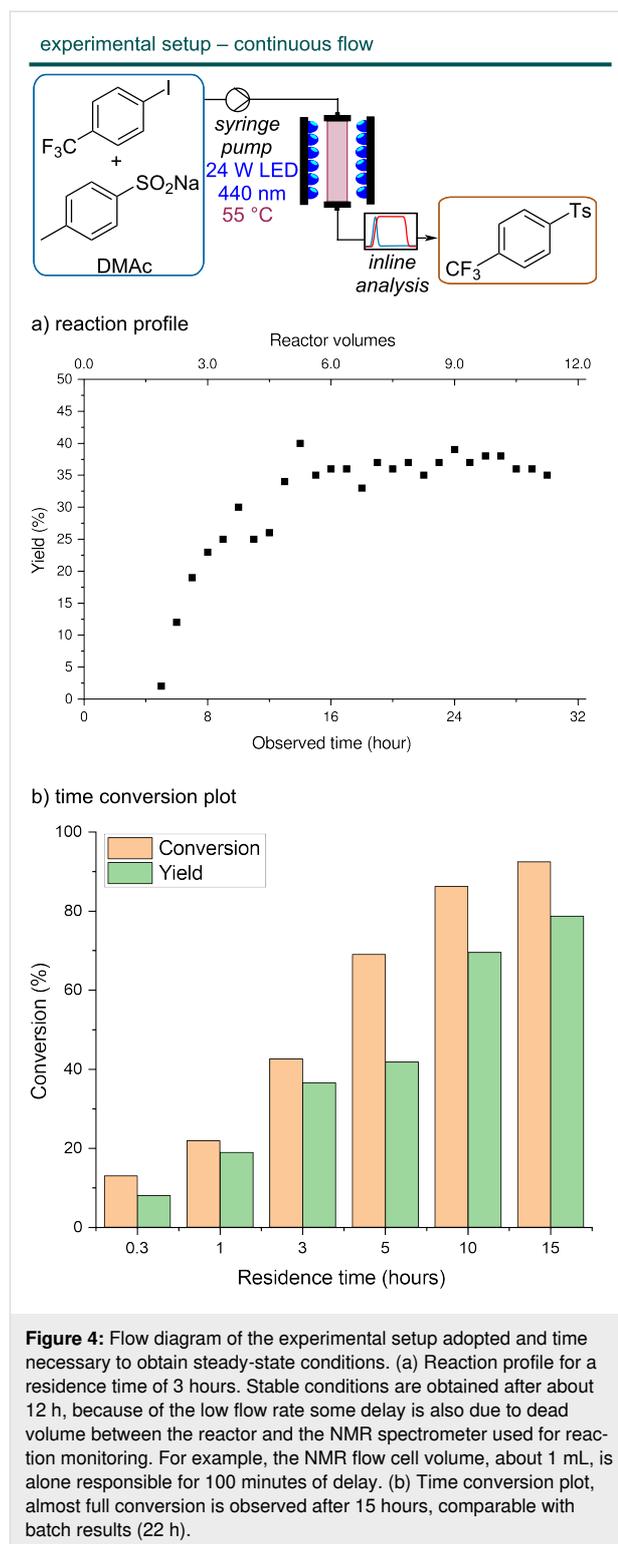
volume was too low to reach steady-state conditions. By switching to a continuous operation mode, we realized that a residence time of around 3 hours was necessary to reach steady-state conditions and the yield improved significantly (36%) (Figure 4a). This corresponds to approximately five reactor volumes, even though the volume of the NMR flow cell and the tubing between the reactor and the flow cell is also responsible for this delay.

As a next step, we intended to perform a residence time screening. However, the five reactor volumes needed to reach steady-state conditions meant that, depending on the residence time, up to several hours were needed to acquire each data point. To accelerate the acquisition of experimental results, we decided to equip our reactor with an in-line benchtop NMR spectrometer at the reactor outlet. First, we verified that the NMR yield calculated directly from the benchtop ^{19}F NMR spectrum was in good agreement with the high-field NMR yields calculated with an internal standard (see Supporting Information File 1, Table S1). Then, a program was developed to monitor the reaction yield over time by automatically acquiring, processing and integrating the ^{19}F NMR spectrum of the reaction mixture flowing in the spectrometer (see relevant code in Supporting Information File 3). In particular, the python packages flowchem [35] and nmrglue [36] were used to control the spectrometer and process the free induction decay (FID) files, respectively. The reaction was run until stable conditions were obtained, defined as seven consecutive spectra in which the coefficient of variation (CV) of the auto-integrated product yield was below 3%.

Residence time, photon flux and temperature studies

Having developed an automated analysis system, we proceeded with a residence time screening. A reaction time of 15 hours was necessary to reach almost quantitative conversion (92%) (Figure 4b). These results suggest that neither a higher local concentration of light-absorbing species nor the improved light distribution significantly improves the transformation compared with the batch reaction.

Next, we investigated if the reaction rate significantly depends on the received photon flux (Table 1). For these studies, we chose a residence time of 3 hours (i.e., 10 μL/min flow rate) as a compromise between conversion (high enough to observe changes with the different conditions tested) and residence time (as short as possible to reduce the amount of time needed for the experiments). Changing the light intensity had a minor impact on the reaction rate (Table 1, entries 2–4). This observation suggests that the turnover determining step is likely not of photochemical nature.

Figure 4: Flow diagram of the experimental setup adopted and time necessary to obtain steady-state conditions. (a) Reaction profile for a residence time of 3 hours. Stable conditions are obtained after about 12 h, because of the low flow rate some delay is also due to dead volume between the reactor and the NMR spectrometer used for reaction monitoring. For example, the NMR flow cell volume, about 1 mL, is alone responsible for 100 minutes of delay. (b) Time conversion plot, almost full conversion is observed after 15 hours, comparable with batch results (22 h).

Based on this consideration, we turned to the reactor temperature as a means for process intensification. As expected, performing the reaction at a lower temperature proved detrimental (Table 1, entry 5). However, at higher temperatures, the colour of the polymer in the packed bed turned rapidly black (see Sup-

Table 1: Optimization of temperature and light intensity for the coupling of 4-iodobenzotrifluoride and sodium *p*-toluenesulfinate.

| Entry[a]	Light intensity	Temp. [°C]	Conversion [%]	Yield [%]
1	0%	55	0	n.d.
2	50%	55	66	61
3	75%	55	67	62
4	**100%**	**55**	**72**	**67**
5	100%	40	60	54
6[b]	100%	70	64	55
7[c]	100%	55	62	51

[a]Data was collected by 37.6 MHz ^{19}F NMR; [b]the colour of the polymer in the column turned dark during irradiation (see Supporting Information File 1, Figure S4); [c]the data was collected after entry 5.

porting Information File 1, Figure S4), and lower yields were observed (Table 1, entries 6 and 7). The catalyst deactivation could be due to the formation of nickel-black [28], or via (photo-)thermal degradation of the polymer.

Packed-bed stability

To study the stability of the Ni@poly-czbpy packed-bed reactor and evaluate its suitability for scaling-out, a continuous experiment over seven days was performed using the conditions with 100% intensity, 55 °C and 3 hours residence time (Figure 5). After reaching steady-state conditions (12 h, in agreement with previous observations, see Figure 4a), only a minor decrease in the catalyst activity (about 1% per day) was observed throughout the experiment, demonstrating the good long-term stability of the heterogeneous catalyst. In particular, the catalyst turnover number (TON) calculated over the 7-day experiment is comparable with the TON observed in batch for a single reaction (35 vs 36, respectively). Since the catalyst is still highly active after 7 days, a higher TON could be achieved by extending the experiment duration. This observation constitutes a promising starting point for applications in large-scale synthesis or automated reaction optimization.

Based on literature precedents on catalyst leaching in packed-bed reactors [37,38], we assumed that the decreased activity could be linked to nickel leaching. Based on ICP results on the reactor outlet collected in the long-run experiment, after seven days of continuous reaction 0.42 mg of nickel (25% of the 1.66 mg initially complexed, see Figure 5) leached into the reaction solution. However, performing another round of complexation with NiCl$_2$·glyme did not restore the original activity of the catalyst in the packed bed. Together with the catalyst deactivation observed in the temperature study, this result points at a temperature-dependent ligand photodegradation as a likely deactivation mechanism. The amount of nickel leaching
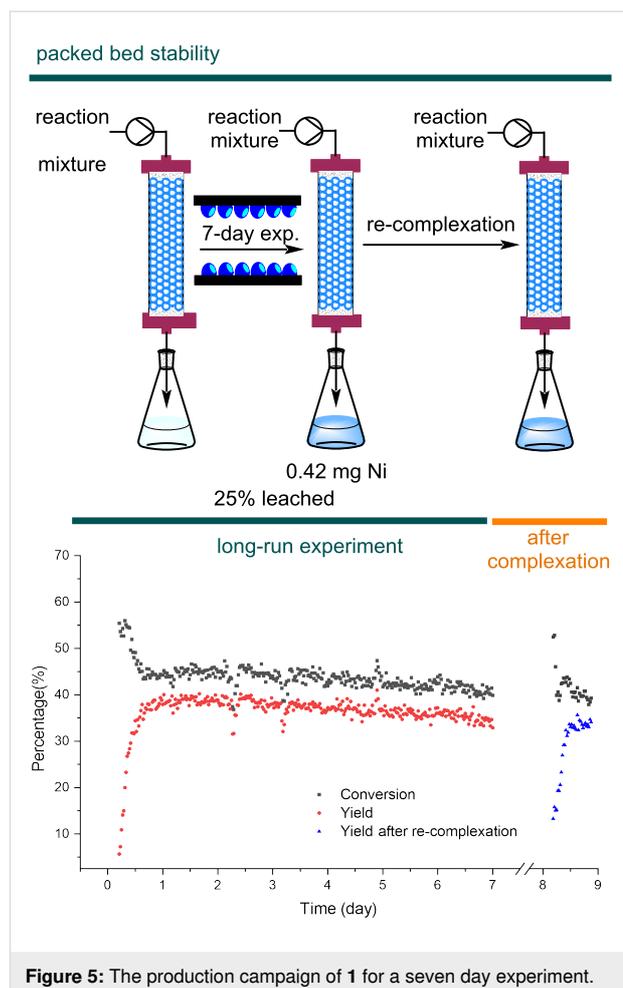
Figure 5: The production campaign of **1** for a seven day experiment.

observed is significant and, depending on the substrate, the metal contamination after chromatography might still be too high for use as API. If the remaining nickel content becomes an issue, a column packed with an immobilized scavenger could be used to further reduce the Ni content in the final product [39].

Reactor optimization

Flow maldistribution and poor mixing efficiency in the packed bed could cause the relatively long time necessary to reach steady-state conditions. Consequently, we evaluated a static mixer to improve the flow distribution in the packed bed [40-42]. The residence time distribution (RTD) of the reactor was measured via a pulsed tracer experiment (see Supporting Information File 2 for details) and compared with a modified reactor unit containing a helical static mixer (Figure 6) [43]. The addition of the static mixer had a limited impact on both the standard deviation of the mean residence time and the reaction outcome, most likely due to the low flow rate (10 μL/min) [43,44]. An alternative approach to obtain a narrower RTD is the reduction of the reactor diameter, as this would decrease the axial dispersion [45]. Replacing the glass column (i.d. 6.6 mm)

Figure 6: Photo of the packed column with a helical static mixer (polished SS316, 10 cm length, 15 mixing elements L/D = 1.04 from Stamixco AG).

with a PTFE capillary with a smaller inner diameter (i.d. 5/32",
3.9 mm) resulted in a narrower residence time distribution and
higher yields (see Table 2).

C–O coupling reaction

Finally, we evaluated the use of the capillary-based reactor for
the related C–O coupling of 4-iodobenzotrifluoride and
N-(Boc)-proline with *N-tert*-butylisopropylamine (BIPA) in
dimethyl sulfoxide (DMSO) (Scheme 1). In analogy with the
C–S coupling, a residence time of 3 hours was chosen for a test
experiment, resulting in 81% conversion and 61% NMR yield.
In this case a significant acceleration compared to the original
batch reaction time (24 h) was observed, likely thanks to the use
of the same reaction concentration as in the original batch report
[28]. This was unlike the C–S coupling, where the limited solu-

bility of the sulfinate salt required a dilution of the reaction
conditions to obtain a homogenous reaction mixture. As previ-
ously observed [28], the reaction concentration has a signifi-
cant impact on the efficiency of the nickel cycle in metallapho-
toredox reactions. It is therefore not surprising that a larger
acceleration of the reaction kinetics in flow versus batch was
observed for the C–O coupling as opposed to the C–S coupling.

Conclusion

In summary, we developed a packed-bed reactor for metalla-
photoredox catalysis in continuous flow. The heterogeneous
catalyst used, based on a bipyridine ligand decorated with two
carbazole groups, served as both photo- and nickel catalyst,
making the reactor packing simple and reproducible. Compared
with homogeneous approaches to metallaphotoredox catalysis,

Table 2: Comparison of different reactors.
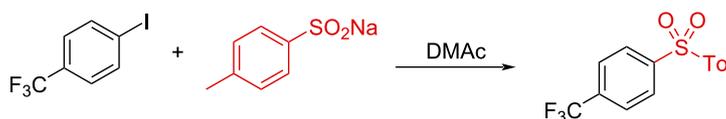
Entry	Reactor	Conversion [%]	Yield [%]	Mean residence time ± standard deviation [min]
1[a]	glass column	45	36	161 ± 58
2[b]	glass column + static mixer	45	37	171 ± 42
3	5/32" ID tube[c]	57	50	195 ± 32

[a]6.60 mm ID; [b]outfit of the reactor (Figure 6) [c]5/32" equals to 4.0 mm.
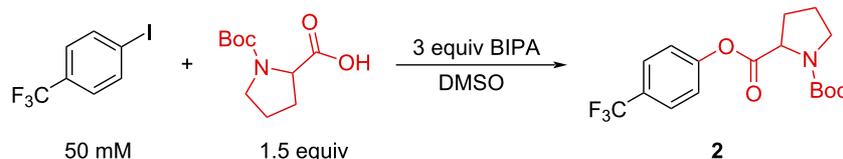
Scheme 1: C–O coupling between 4-iodobenzotrifluoride and *N*-(Boc)-proline.

this heterogeneous solution simplifies the catalyst separation and the translation of the optimized batch conditions to flow. Most notably, reactions previously optimized in batch could be performed in continuous flow directly with little (C–S coupling) to no (C–O coupling) changes to the reaction conditions. Overall, the lack of catalyst separation and the possibility of combining the reactor with in-line analytical feedback enables the flow synthesis of C–S and C–O coupled products in a simple, versatile and amenable to automation way.

Supporting Information

Supporting Information File 1
Details of packed-bed assembly, experimental procedures, reaction optimization and compounds characterization data.
[https://www.beilstein-journals.org/bjoc/content/supplementary/1860-5397-18-115-S1.pdf]

Supporting Information File 2
Residence time distribution calculation notebook.
[https://www.beilstein-journals.org/bjoc/content/supplementary/1860-5397-18-115-S2.zip]

Supporting Information File 3
NMR control and auto-integration notebook.
[https://www.beilstein-journals.org/bjoc/content/supplementary/1860-5397-18-115-S3.zip]

ORCID® iDs
Wei-Hsin Hsu - https://orcid.org/0000-0001-6433-290X
Susanne Reischauer - https://orcid.org/0000-0002-5032-2855
Peter H. Seeberger - https://orcid.org/0000-0003-3394-8466
Bartholomäus Pieber - https://orcid.org/0000-0001-8689-388X
Dario Cambié - https://orcid.org/0000-0003-2722-5106

Preprint
A non-peer-reviewed version of this article has been previously published as a preprint: https://doi.org/10.3762/bxiv.2022.56.v1

References
1. Shaw, M. H.; Twilton, J.; MacMillan, D. W. C. *J. Org. Chem.* **2016,** *81,* 6898–6926. doi:10.1021/acs.joc.6b01449
2. Marzo, L.; Pagire, S. K.; Reiser, O.; König, B. *Angew. Chem., Int. Ed.* **2018,** *57,* 10034–10072. doi:10.1002/anie.201709766
3. Buglioni, L.; Raymenants, F.; Slattery, A.; Zondag, S. D. A.; Noël, T. *Chem. Rev.* **2022,** *122,* 2752–2906. doi:10.1021/acs.chemrev.1c00332
4. Cambié, D.; Bottecchia, C.; Straathof, N. J. W.; Hessel, V.; Noël, T. *Chem. Rev.* **2016,** *116,* 10276–10341. doi:10.1021/acs.chemrev.5b00707
5. Plutschack, M. B.; Pieber, B.; Gilmore, K.; Seeberger, P. H. *Chem. Rev.* **2017,** *117,* 11796–11893. doi:10.1021/acs.chemrev.7b00183
6. Bottecchia, C.; Lévesque, F.; McMullen, J. P.; Ji, Y.; Reibarkh, M.; Peng, F.; Tan, L.; Spencer, G.; Nappi, J.; Lehnherr, D.; Narsimhan, K.; Wismer, M. K.; Chen, L.; Lin, Y.; Dalby, S. M. *Org. Process Res. Dev.* **2022,** *26,* 516–524. doi:10.1021/acs.oprd.1c00240
7. Steiner, A.; Roth, P. M. C.; Strauss, F. J.; Gauron, G.; Tekautz, G.; Winter, M.; Williams, J. D.; Kappe, C. O. *Org. Process Res. Dev.* **2020,** *24,* 2208–2216. doi:10.1021/acs.oprd.0c00239
8. Halperin, S. D.; Kwon, D.; Holmes, M.; Regalado, E. L.; Campeau, L.-C.; DiRocco, D. A.; Britton, R. *Org. Lett.* **2015,** *17,* 5200–5203. doi:10.1021/acs.orglett.5b02532
9. Skubi, K. L.; Blum, T. R.; Yoon, T. P. *Chem. Rev.* **2016,** *116,* 10035–10074. doi:10.1021/acs.chemrev.6b00018
10. Chan, A. Y.; Perry, I. B.; Bissonnette, N. B.; Buksh, B. F.; Edwards, G. A.; Frye, L. I.; Garry, O. L.; Lavagnino, M. N.; Li, B. X.; Liang, Y.; Mao, E.; Millet, A.; Oakley, J. V.; Reed, N. L.; Sakai, H. A.; Seath, C. P.; MacMillan, D. W. C. *Chem. Rev.* **2022,** *122,* 1485–1542. doi:10.1021/acs.chemrev.1c00383
11. Abdiaj, I.; Alcázar, J. *Bioorg. Med. Chem.* **2017,** *25,* 6190–6196. doi:10.1016/j.bmc.2016.12.041
12. González-Esguevillas, M.; Fernández, D. F.; Rincón, J. A.; Barberis, M.; de Frutos, O.; Mateos, C.; García-Cerrada, S.; Agejas, J.; MacMillan, D. W. C. *ACS Cent. Sci.* **2021,** *7,* 1126–1134. doi:10.1021/acscentsci.1c00303
13. Harper, K. C.; Moschetta, E. G.; Bordawekar, S. V.; Wittenberger, S. J. *ACS Cent. Sci.* **2019,** *5,* 109–115. doi:10.1021/acscentsci.8b00728
14. Lima, F.; Kabeshov, M. A.; Tran, D. N.; Battilocchio, C.; Sedelmeier, J.; Sedelmeier, G.; Schenkel, B.; Ley, S. V. *Angew. Chem., Int. Ed.* **2016,** *55,* 14085–14089. doi:10.1002/anie.201605548
15. Vaccaro, L.; Lanari, D.; Marrocchi, A.; Strappaveccia, G. *Green Chem.* **2014,** *16,* 3680–3704. doi:10.1039/c4gc00410h
16. Thomson, C. G.; Lee, A.-L.; Vilela, F. *Beilstein J. Org. Chem.* **2020,** *16,* 1495–1549. doi:10.3762/bjoc.16.125
17. Pieber, B.; Shalom, M.; Antonietti, M.; Seeberger, P. H.; Gilmore, K. *Angew. Chem., Int. Ed.* **2018,** *57,* 9976–9979. doi:10.1002/anie.201712568
18. Chaudhuri, A.; Zondag, S. D. A.; Schuurmans, J. H. A.; van der Schaaf, J.; Noël, T. *Org. Process Res. Dev.* **2022,** *26,* 1279–1288. doi:10.1021/acs.oprd.2c00012
19. Rosso, C.; Gisbertz, S.; Williams, J. D.; Gemoets, H. P. L.; Debrouwer, W.; Pieber, B.; Kappe, C. O. *React. Chem. Eng.* **2020,** *5,* 597–604. doi:10.1039/d0re00036a

20. Debrouwer, W.; Kimpe, W.; Dangreau, R.; Huvaere, K.; Gemoets, H. P. L.; Mottaghi, M.; Kuhn, S.; Van Aken, K. *Org. Process Res. Dev.* **2020,** *24,* 2319–2325. doi:10.1021/acs.oprd.0c00150

21. Bottecchia, C.; Erdmann, N.; Tijssen, P. M. A.; Milroy, L.-G.; Brunsveld, L.; Hessel, V.; Noël, T. *ChemSusChem* **2016,** *9,* 1781–1785. doi:10.1002/cssc.201600602

22. Abramov, A.; Bonardd, S.; Pérez-Ruiz, R.; Díaz Díaz, D. *Adv. Synth. Catal.* **2022,** *364,* 2–17. doi:10.1002/adsc.202101048

23. Vijeta, A.; Casadevall, C.; Reisner, E. *Angew. Chem.* **2022,** *134,* e202203176. doi:10.1002/ange.202203176

24. Wen, Z.; Wan, T.; Vijeta, A.; Casadevall, C.; Buglioni, L.; Reisner, E.; Noël, T. *ChemSusChem* **2021,** *14,* 5265–5270. doi:10.1002/cssc.202101767

25. Zhao, X.; Deng, C.; Meng, D.; Ji, H.; Chen, C.; Song, W.; Zhao, J. *ACS Catal.* **2020,** *10,* 15178–15185. doi:10.1021/acscatal.0c04725

26. Vijeta, A.; Casadevall, C.; Roy, S.; Reisner, E. *Angew. Chem., Int. Ed.* **2021,** *60,* 8494–8499. doi:10.1002/anie.202016511

27. Gisbertz, S.; Pieber, B. *ChemPhotoChem* **2020,** *4,* 456–475. doi:10.1002/cptc.202000014

28. Cavedon, C.; Gisbertz, S.; Vogl, S.; Richter, N.; Schrottke, S.; Teutloff, C.; Seeberger, P. H.; Thomas, A.; Pieber, B. *ChemRxiv* **2021**. doi:10.26434/chemrxiv-2021-kt2wr

29. Tobin, J. M.; Liu, J.; Hayes, H.; Demleitner, M.; Ellis, D.; Arrighi, V.; Xu, Z.; Vilela, F. *Polym. Chem.* **2016,** *7,* 6662–6670. doi:10.1039/c6py01393g

30. Kong, C. J.; Fisher, D.; Desai, B. K.; Yang, Y.; Ahmad, S.; Belecki, K.; Gupton, B. F. *Bioorg. Med. Chem.* **2017,** *25,* 6203–6208. doi:10.1016/j.bmc.2017.07.004

31. Wong, Y.-L.; Tobin, J. M.; Xu, Z.; Vilela, F. *J. Mater. Chem. A* **2016,** *4,* 18677–18686. doi:10.1039/c6ta07697a

32. Tobin, J. M.; McCabe, T. J. D.; Prentice, A. W.; Holzer, S.; Lloyd, G. O.; Paterson, M. J.; Arrighi, V.; Cormack, P. A. G.; Vilela, F. *ACS Catal.* **2017,** *7,* 4602–4612. doi:10.1021/acscatal.7b00888

33. Woźnica, M.; Chaoui, N.; Taabache, S.; Blechert, S. *Chem. – Eur. J.* **2014,** *20,* 14624–14628. doi:10.1002/chem.201404440

34. Rodriguez-Zubiri, M.; Felpin, F.-X. *Org. Process Res. Dev.* **2022,** *26,* 1766–1793. doi:10.1021/acs.oprd.2c00102

35. *Flowchem,* v. 0.0.8, 2022; Cambié, D.; Wolf, J.; Wei-Hsin, H. doi:10.5281/zenodo.6675694

36. Helmus, J. J.; Jaroniec, C. P. *J. Biomol. NMR* **2013,** *55,* 355–367. doi:10.1007/s10858-013-9718-x

37. Barreiro, E. M.; Hao, Z.; Adrio, L. A.; van Ommen, J. R.; Hellgardt, K.; Hii, K. K. (Mimi). *Catal. Today* **2018,** *308,* 64–70. doi:10.1016/j.cattod.2017.10.013

38. Cantillo, D.; Kappe, C. O. *ChemCatChem* **2014,** *6,* 3286–3305. doi:10.1002/cctc.201402483

39. Baxendale, I. R.; Ley, S. V.; Mansfield, A. C.; Smith, C. D. *Angew. Chem., Int. Ed.* **2009,** *48,* 4017–4021. doi:10.1002/anie.200900970

40. Hessel, V.; Löwe, H.; Schönfeld, F. *Chem. Eng. Sci.* **2005,** *60,* 2479–2501. doi:10.1016/j.ces.2004.11.033

41. Hardt, S.; Drese, K. S.; Hessel, V.; Schönfeld, F. *Microfluid. Nanofluid.* **2005,** *1,* 108–118. doi:10.1007/s10404-004-0029-0

42. Ghanem, A.; Lemenand, T.; Della Valle, D.; Peerhossaini, H. *Chem. Eng. Res. Des.* **2014,** *92,* 205–228. doi:10.1016/j.cherd.2013.07.013

43. Etchells, A. W., III; Meyer, C. F. Mixing in Pipelines. *Handbook of Industrial Mixing;* John Wiley & Sons: Hoboken, NJ, USA, 2003; pp 391–477. doi:10.1002/0471451452.ch7

44. Schwolow, S.; Hollmann, J.; Schenkel, B.; Röder, T. *Org. Process Res. Dev.* **2012,** *16,* 1513–1522. doi:10.1021/op300107z

45. Yazdanpanah, N.; Cruz, C. N.; O'Connor, T. F. *Comput. Chem. Eng.* **2019,** *129,* 106510. doi:10.1016/j.compchemeng.2019.06.035